

Advanced Characterization of the Tensile and Compressive Behavior of PP and PP Composites

Dissertation

by

Michael Jerabek

prepared at the

Polymer Competence Center Leoben GmbH

and the

Institute of Materials Science and Testing of Plastics

submitted to the

University of Leoben



Academic Advisor

O.Univ.-Prof. Dr.mont. Reinhold W. Lang
University of Leoben, Austria

Supervisor

Dr.mont. Zoltan Major
University of Leoben, Austria

Referees

O.Univ.-Prof. Dr.mont. Reinhold W. Lang
University of Leoben, Austria

Univ.-Prof. Dr.tech. Béla Pukánszky
University of Budapest, Hungary

Leoben, January 2009

I declare in lieu of oath, that I wrote this dissertation and performed the associated research myself, using only the support indicated in the acknowledgements and literature cited.

Leoben, January 2009

Dipl.-Ing. Michael Jerabek

ACKNOWLEDGEMENTS

First, I would like to thank Prof. Reinhold W. Lang for the thorough reviewing of the dissertation and the associated papers. I am particularly grateful to him for the numerous discussions on scientific matters and interpretations of experimental results, for the fruitful dialogues on the general concept and scope of the dissertation and also for helping me to further improve my scientific style of writing. I am also very grateful to Prof. Béla Pukánszky, for his acceptance as the second referee of my doctoral committee. Moreover, I appreciate his contribution and support in two of the papers very much. The critical questions and comments in our discussions pushed me further to new insights and perspectives of the work and the related interpretations of the results.

My deepest appreciation goes to Dr. Zoltan Major, who offered me the possibility to work in this interesting field of research and for the great support during the last five years. The various fruitful discussions and ideas contributed considerably to the success of this work.

I also wish to express my gratitude to Prof. Krishnaswamy Ravi-Chandar, for giving me the possibility to work at the Center for Mechanics of Solids, Structures and Materials at the University of Texas at Austin under his leadership during my PhD thesis. I would like to emphasize that I appreciated the support and friendly environment a lot and I am very grateful for the support in two of the papers.

I am indebted to Borealis Polyolefine GmbH (Linz, A) for acting as a project partner and for supplying the materials investigated in this dissertation. Particularly, I would like to thank DI Harald Herbst for his valuable contribution to the understanding of the micromechanics of the PP composites.

Special thanks go to my former colleague DI Daniel Tscharnuter, who helped me in the theoretical modeling and the realization of a novel approach for viscoelastic materials. Moreover, I am also grateful to my former colleague Dr. Robin Steinberger, who supported me with his knowledge and expertise in the daily experimental work. The discussions with him particularly at the beginning of the project helped me a lot to get my ideas as a young researcher in the right order.

I would like to thank my former student colleagues Simon Gastl, DI Herwig Thiel and Bernd Schritteser, who conducted numerous experimental tests, also within their Bachelor Thesis. Due to the accurate and reliable measurements and their personal dedication it was possible to obtain the required information from the test results.

I would like to express my gratitude also to Peter Moharitsch, who prepared an incredible number of specimens of highest quality. Moreover, he not only supported me in designing new test fixtures and devices, but he also machined and built these parts. For the smooth work in the laboratory, my special thanks go to Werner Lindner. He always knew an easy and fast solution even in the case of serious problems.

Last but not least, my gratitude goes to my longtime partner Susanne Kahlen, without her understanding this work would not have been possible. She gave me unlimited freedom on numerous evenings and weekends and took care of our daughter Melanie, to finish the experiments and this work, as it has been a very intensive time.

Major parts of this research work were performed at the Polymer Competence Center Leoben GmbH (PCCL, Austria) within the research projects I-1.7, II-1.03 and S.04 within the framework of the Kplus-program of the Austrian Ministry of Traffic, Innovation and Technology with contributions by *the University of Leoben* and *Borealis Polyolefine GmbH*. The PCCL is funded by the Austrian Government and the State Governments of Styria and Upper Austria.

ABSTRACT

A basic understanding of the micro-mechanisms of deformation and failure related to the mechanical properties of polypropylene (PP) and particulate filled PP composites is of crucial importance for appropriate material and structural component modeling. Especially PP composite materials offer a great potential for tailor-made properties by specific selection and definition of filler type, content and surface modification. As the polymeric matrix exhibits viscoelastic behavior, mechanical composite properties also strongly depend on time, rate of testing, temperature and stress state. Thus, the main objective of the dissertation was to investigate the effect of several of these parameters on the behavior of neat and particulate filled PP. As to the filler types, two glass beads with different size distributions and talc were used in two volume fractions.

Digital image correlation (DIC) was utilized to obtain the effective value of Poisson's ratio for this class of relatively soft materials. Due to the lack of information on the reliability of the strain measurement result, the limits of accuracy of this optical strain measurement system under different environmental conditions were investigated, and the technique was applied to the characterization of PP and PP composites in the pre- and post-yield regime. As to the accuracy, a fine speckle pattern and a light intensity just below overexposure provided best results. While vibrations related to the operation of the testing machine were of minor influence in reducing the strain measurement accuracy, more pronounced effects were found for the operation of the temperature chamber. For the DIC system it could be shown that it allows for the proper strain determination in the pre- and post-yield regime. To account for the pressure dependence of the neat PP, several methods for uniaxial, plane strain and multiaxial compression testing were investigated and compared in the pre- and post-yield regime. A procedure for the determination of the compressive modulus was introduced and results were shown. To enable the detection of instability associated with friction and barreling and to calculate true stress-true strain curves, the measurement of transverse expansion of the specimen at large strains was necessary. Significant strain softening was observed in the post yield regime

for uniaxial compression tests, while with increasing confinement levels strain softening was reduced and in some cases strain hardening was observed. For the highest confinement level (approaching hydrostatic compression), plastic deformation was entirely suppressed, with all imposed deformations being reversible, thus making any classification in terms of strain hardening or softening obsolete.

Based on the successful implementation of the DIC system as an accurate full-field strain measurement device, the tensile behavior of PP composites filled with glass beads and talc was studied over a wide range of strain rates and temperatures. The interpretation of the results in terms of particle size and shape proved the importance of interfacial interactions in the determination of composite properties measured at large deformations. Debonding stress decreased with increasing particle size leading to a decreased composite yield stress. Because of their different temperature dependence, the debonding stress, which is substantially below the yield stress at low temperatures, approached the yield stress with increasing temperature. In the low temperature regime, debonding, crazing and micro-cracking were determined as the dominating deformation micro-mechanisms, leading to brittle fracture, which changed to shear yielding and crazing of the matrix as the main mechanisms leading to ductile failure as temperature increased. Changing of the dominating mechanism was observed also in composites filled with talc, which led to different composition dependences in various temperature regimes. Yield stress values decreased with increasing filler loading at low temperatures, but true reinforcement was observed as the temperature increased. The effect of interfacial interactions was expressed in quantitative terms by using a model proposed by Pukánszky and Vörös. The changing load-bearing capacity of fillers with different particle characteristics could be clearly related to the dominating deformation micro-mechanisms and to their changes with experimental conditions. To prove the obtained results and to quantify the debonding stress, volume strain measurements using the DIC system were also conducted as a function of strain rate and temperature. While local cavitation mechanisms (micro-voiding, crazing, and micro-cracking) and subsequent debonding of the particles dominated as failure mechanisms at high

strain rates and at room temperature, a more significant contribution of local shear yielding was observed with a reduced contribution of cavitation mechanisms at low strain rates or at 80 °C. This change in the dominating micro-mechanisms of deformation resulted in smaller volume strains during the tensile loading of the composites than for the respective neat matrix. Moreover, a novel approach is introduced for the detection of debonding using volume strain measurements, which takes into account the dilatational and deviatoric behavior of the neat matrix polymer and the composite, respectively. The results are supported by acoustic emission measurements carried out simultaneously with the same specimens.

As to the local stress state around the filler particles, the pressure dependent yield behavior of the neat PP was characterized applying various test methods from uniaxial tension and compression to multiaxial tension and confined compression. The experimental results were evaluated in terms of effective stress, to determine the equivalent stress vs. mean stress correlation and the pressure sensitivity index. An excellent linear relationship of equivalent stress vs. mean stress was found for all temperatures studied. To determine the pressure sensitivity as an intrinsic material parameter, normalized yield stresses were calculated with respect to the uniaxial tensile test. As expected, increasing pressure sensitivity values were found with increasing temperature, which was explained in terms of the free volume theory. The 3D Drucker-Prager yield function was fitted to the yield stresses and an average error between the predictions and the measurement of 8 % was obtained.

In addition, the long-term compressive relaxation behavior of neat PP and the PP composites was investigated, utilizing the uniaxial and confined compression test. As the full strain and stress field was determined in confined compression, all four viscoelastic material functions were deduced from the experimental results. As expected, the shear and the bulk relaxation moduli were found to increase with the addition of particles. In agreement with earlier results on other polymers, it turned out that the relaxation response is significantly retarded at higher confinement levels when compared to the uniaxial relaxation test. Furthermore, it was shown that the effect of filler particles on the long-term behavior depends on the specific uniaxial or multiaxial stress state.

KURZFASSUNG

Ein grundlegendes Verständnis der Mikro-Mechanismen der Deformation und des Versagens in Polypropylen (PP) und in partikel-gefüllten PP-Composites ist von entscheidender Bedeutung für die Modellierung des mechanischen Material- und Bauteilverhaltens. Insbesondere bei PP-Composites können durch geeignete Auswahl von Füllstofftype, Volumengehalt und Adaptierung der Partikeloberfläche, maßgeschneiderte Materialeigenschaften erzielt werden. Aufgrund der Viskoelastizität der PP-Matrix sind aber auch bei derartigen PP-Composites die mechanischen Eigenschaften abhängig von Zeit, Belastungsgeschwindigkeit, Temperatur und Spannungszustand. Das Hauptziel dieser Dissertation war somit, den Einfluss dieser Parameter auf das Verhalten von ungefülltem und gefülltem PP grundlegend zu untersuchen. Als Füllstoffe wurden 2 Typen von Glaskugeln mit unterschiedlichen Größenverteilungen und Talkum verwendet, wobei jeder dieser Füllstoffe für die Herstellung von Composites jeweils in zwei unterschiedlichen Volumenanteilen eingesetzt wurde.

Um genaue und zuverlässige Werte für die Querkontraktionszahl und Volumendehnung im reversiblen und irreversiblen Deformationsbereich für relativ weiche Materialien wie PP zu erhalten, wurde die Messmethode der digitalen Bildkorrelation angewendet. Da keine systematischen Untersuchungen über die Genauigkeit dieses Messsystems abhängig von relevanten Prüf- und Testparametern bekannt sind, wurden Untersuchungen bezüglich der jeweiligen Anwendungsgrenzen durchgeführt. Es stellte sich heraus, dass ein möglichst fein appliziertes Prüfkörpermuster und eine maximale Beleuchtungsintensität (ohne Überbelichtung einzelner Pixel), optimal in Bezug auf Messgenauigkeit sind. Ein Einfluss von Schwingungen der Prüfmaschine auf die Genauigkeit des Bildkorrelations-Messsystems konnte nicht detektiert werden, während ein signifikanter Effekt durch Schwingungen der Temperierkammer nachgewiesen werden konnte.

Um den Einfluss des Spannungszustandes an ungefülltem PP zu untersuchen, wurden uni-axiale und multi-axiale Druckprüfmethoden angewendet und die Ergebnisse im reversiblen als auch irreversiblen Dehnungsbereich verglichen. Um

genaue und reproduzierbare Werte für den Druckmodul zu erhalten, wurde eine neue Auswertemethode erarbeitet. Bei den uniaxialen Druckversuchen wurde auch die Querdehnung der Prüfkörper gemessen, einerseits um den Beginn einer plastischen Instabilität (Ausbauchen) zu detektieren und andererseits um „wahre“ Spannungs-Dehnungskurven zu berechnen. Während im irreversiblen Dehnungsbereich bei uniaxialer Druckbelastung abnehmende Spannungswerte festgestellt wurden, konnte bei multi-axialer Druckbelastung eine Spannungsverfestigung über den gesamten untersuchten Dehnungsbereich ermittelt werden. Bei sehr hohen Drücken (und näherungsweise hydrostatischen Druckverhältnissen) war jegliche irreversible plastische Deformation des Prüfkörpers unterdrückt.

Weiters wurden mit Hilfe des optischen Dehnungsmesssystems eine vollständige Charakterisierung der partikel-gefüllten PP-Composites unter einachsiger Zugbelastung abhängig von Dehnrates und Temperatur durchgeführt. Die Abhängigkeit der Messergebnisse in Bezug auf Partikelgröße und Form, unterstreicht die Bedeutung der Partikel/Matrix-Interaktion vor allem im irreversiblen Deformationsbereich. Die kritische Ablösespannung, die zum Versagen der Partikel/Matrix-Grenzfläche führt, nimmt mit zunehmender Partikelgröße ab. Die stärker ausgeprägte Temperaturabhängigkeit der makroskopischen Streckspannung gegenüber der Ablösespannung, führt bei tiefen Temperaturen (unter der Glasübergangstemperatur (T_g)) zu einem Versagen der Grenzfläche deutlich vor Erreichen der Streckspannung. Hingegen sind bei erhöhten Temperaturen Streckspannungen und Ablösespannungen nahezu gleich. Aus diesem Grund nahm die Streckspannung der untersuchten Werkstoffe bei tiefen Temperaturen mit zunehmendem Füllstoffgehalt ab, während die Streckspannung bei erhöhten Temperaturen unabhängig vom Füllstoffanteil war (bei Glaskugeln) bzw. mit steigendem Füllstoffanteil sogar zunahm (bei Talkum). Gleichzeitig wurde eine Änderung in den vorherrschenden mikro-mechanischen Deformationsmechanismen von Partikel/Matrix-Grenzflächenversagen, Hohlraumbildung, Crazing und Mikrorissbildung bei tiefen Temperaturen (unter T_g) zu Scherfließen und Crazing bei Raumtemperatur und darüber (über T_g) festgestellt. Die quantitative Beurteilung der Effektivität der einzelnen Füllstoffe erfolgte mittels eines von Pukánszky und Vörös vorgeschlagenen Modells. Damit konnte die

temperaturabhängige Partikel/Matrix-Interaktion eindeutig den jeweiligen dominanten Mikrodeformationen zugeordnet werden. Um diese Ergebnisse zusätzlich zu validieren, wurde mit Hilfe des optischen Dehnungsmesssystems präzise Messungen der Volumendehnung durchgeführt. Bei niedrigen Temperaturen oder hohen Dehnraten waren hohlraumbildende Deformationsmechanismen (Mikro-Kavitation, Crazing und Mikro-Rissbildung) gefolgt von Partikel/Matrix-Grenzflächenversagen dominant, während bei hohen Temperaturen oder langsamen Dehnraten Scherfließen und von geringer Bedeutung auch Kavitationsmechanismen vorherrschend waren. Durch diese signifikanten Änderungen in den dominanten lokalen Deformationsmechanismen wurden an den Composites Volumendehnungen ermittelt, die in gewissen Dehnungsbereichen (sowohl reversibles als auch irreversibles Regime) kleinere Werte für die Volumendehnung ergaben als für die ungefüllte Matrix. Durch die Anwendung einer neu entwickelten Methodik, welche sowohl die dilatorische als auch deviatorische Deformation der Matrix und der Composites berücksichtigt, konnten quantitative Werte für die Ablösespannung die zum Partikel/Matrix-Grenzflächenversagen führt ermittelt und mit Schallemissionsmessungen verglichen werden.

Um die Abhängigkeit der mechanischen Eigenschaften der ungefüllten PP-Matrix vom Spannungszustand zu charakterisieren, wurden verschiedenste Prüfmethoden wie uniaxialer Zug und Druck, biaxialer Zug und multiaxialer Druck angewendet. Der Zusammenhang zwischen effektiver (deviatorischer) und mittlerer (hydrostatischer) Spannung ermöglicht die Berechnung der Spannungsabhängigkeit der Fließspannung. Bei allen untersuchten Temperaturen wurde eine lineare Beziehung zwischen der deviatorischen und der mittleren Spannung gefunden. Um die Spannungsabhängigkeit als echten Materialkennwert zu bestimmen, wurden für alle Temperaturen normalisierte effektive Spannungen bezogen auf die Zug-Fließspannung berechnet. Dabei wurde eine steigende Abhängigkeit der Fließspannung vom Spannungszustand mit zunehmender Temperatur festgestellt, die dem ansteigenden freien Volumen zugeordnet werden kann. Die Anwendung des 3D-Fließkriteriums von Drucker-Prager ergab eine gute Übereinstimmung zwischen den experimentellen Daten und diesem Fließkriterium.

Schließlich wurde auch das Langzeitverhalten unter uni-axialer und multiaxialer Druckbelastung untersucht. Im multiaxialen Druckversuch wurden alle vier viskoelastischen Materialfunktionen bestimmt, wobei die Composites im Vergleich zur ungefüllten Matrix erwartungsgemäß höhere Werte für die Moduli aufwiesen. Vergleiche der Resultate des uniaxialen mit dem multiaxialen Druckversuch ergaben ein signifikant verzögertes Relaxationsverhalten für den multiaxialen Spannungszustand. Weiters konnte gezeigt werden, dass die Effektivität der Partikel vom jeweiligen Spannungszustand der Belastung abhängen.

TABLE OF CONTENT

ACKNOWLEDGEMENTS.....	I
ABSTRACT	III
KURZFASSUNG	VI
TABLE OF CONTENT.....	X
PART I: OUTLINE AND SUMMARY	1
1. SCOPE, CONTENT AND STRUCTURE.....	2
2. OBJECTIVES AND METHODOLOGY	5
3. BACKGROUND AND CURRENT STATUS	8
4. MAJOR RESULTS AND DISCUSSION	12
5. CONCLUSIONS AND OUTLOOK.....	23
REFERENCES.....	27
PART II: COLLECTION OF PAPERS	30
<i>PAPER 1: STRAIN DETERMINATION OF POLYMERIC MATERIALS USING DIGITAL IMAGE CORRELATION</i>	<i>31</i>
<i>PAPER 2: ADVANCED COMPRESSION TESTING OF POLYMERIC MATERIALS.....</i>	<i>57</i>
<i>PAPER 3: MECHANICS AND MODELING OF THE TENSILE YIELD BEHAVIOR OF PARTICULATE FILLED PP COMPOSITES.....</i>	<i>86</i>
<i>PAPER 4: FILLER/MATRIX-DEBONDING AND MICRO-MECHANISMS OF DEFORMATION IN PARTICULATE FILLED PP COMPOSITES UNDER TENSION</i>	<i>110</i>
<i>PAPER 5: MULTIAXIAL YIELD BEHAVIOR OF POLYPROPYLENE</i>	<i>137</i>
<i>PAPER 6: RELAXATION BEHAVIOR OF NEAT AND PARTICULATE FILLED POLYPROPYLENE IN UNIAXIAL AND MULTIAXIAL COMPRESSION.....</i>	<i>164</i>

PART I:
OUTLINE AND SUMMARY

1. SCOPE, CONTENT AND STRUCTURE

Particulate filled polymeric composites have been used in increasing quantities in various applications, e.g., automotive industry, appliances, mobile phones, garden furniture, etc. (Markarian, 2004; Morieras, 2001). While in the past fillers were added to the polymer to reduce the price of the final product, in recent years the growing demand for customized and function-integrated products requires the use of more tailored composite materials. In general, the wide field of properties of polymeric materials is substantially extended by using appropriate fillers along with the proper choice of filler type and content. Latest developments have expanded the possible range of properties further, using hybrid composites containing two or more different fillers (Leong et al., 2003; Pal Singh et al., 2009). Fillers in general, increase the stiffness (Fu et al., 2008) and the heat deflection temperature (Yuan et al., 2004), and decrease the specific heat and increase the heat conductivity (Weidenfeller et al., 2005; Weidenfeller et al., 2004), and in most cases reduce the deformability (Dubnikova et al., 2004) of the composite. The long-term creep and relaxation tendency may also be significantly reduced by spherical as well as anisotropic fillers (Yang et al., 2007; Zhou et al., 2007). To obtain some reinforcing effect in the composite either very small particles or a minimum aspect ratio is needed (Pukánszky and Fekete, 1999). Usually significant weakening of the material can be observed, if the particles are orientated perpendicularly to the direction of the force (Christie, 1986).

The properties of particulate filled composites are basically determined by the behavior of the matrix, the properties of the filler, composition, structure (spatial distribution and orientation) and interfacial interaction (Pukánszky, 1995). Although such heterogeneous systems are of scientific and practical interest, their behavior under external load is not fully understood. Further research is needed to understand and to predict the debonding of the particles properly. In neat polypropylene (PP), the observed deformation mechanisms are void formation, crazing and micro-cracking associated with brittle fracture and shear-yielding frequently related to ductile failure (Friedrich, 1983; Narisawa and Ishikawa, 1990). In addition to the deformation behavior of the neat matrix, the dominant micro-

deformation process in the composite is usually debonding accompanied by void growth and coalescence, so that ultimately brittle or ductile failure may occur (Dubnikova et al., 1997).

As an inherent characteristic of viscoelastic materials, the different deformation processes of the matrix and the composite, respectively, depend significantly on time, temperature and stress state (Ward, 1971). For neat PP, at low temperatures or high deformation rates brittle fracture is observed, while at elevated temperatures or moderate loading rates ductile fracture occurs. As to the full characterization of the mechanical properties of viscoelastic materials, tests under different confinement levels are crucial to determine the stress state dependent onset of yielding (Pae, 1977). For a complete description of the failure micro-mechanisms in particulate filled composites, a thorough understanding of the matrix behavior is essential. Thus, the behavior of neat PP and PP composites was studied over a wide range of strain rates and temperatures in tension. In addition, the long-term relaxation behavior under different confinement levels was characterized. The onset of yielding of the neat PP was characterized in detail, which allowed for a proper prediction of the composite properties, when included in common micromechanical models.

The matrix material investigated was a development grade PP. For the composites, the same PP was used as matrix material, and two glass beads with different size distributions (large and small mean diameters) and talc were used as spherical and plate-like fillers, respectively. Each of these fillers was added to the neat PP in two different volume fractions (3.5 v% and 7.0 v%).

This dissertation consists of two main parts. Part I provides an overview of the work, briefly describing the overall objectives and the methodology (Chapter 2) along with the background and current relevant scientific knowledge (Chapter 3), summarizes the major results (Chapter 4), and ends with conclusions and an outlook for future work (Chapter 5). Part II consists of a collection of papers prepared for publication and providing information as to the details of the research performed and the results achieved. The six papers in total deal with various aspects related to test method development and implementation (Papers 1 and 2), the micro-mechanisms of deformation and failure of PP and the PP composites in

tension (Papers 3 and 4), the multiaxial yield behavior of neat PP (Paper 5) and the relaxation behavior of neat PP and PP composites (Paper 6). The papers are entitled as follows:

Paper 1: Strain Determination of Polymeric Materials using Digital Image Correlation

Paper 2: Advanced Compression Testing of Polymeric Materials

Paper 3: Mechanics and Modeling of the Tensile Yield Behavior of Particulate Filled PP Composites

Paper 4: Filler/Matrix Debonding and Micro-Mechanisms of Deformation in Particulate Filled PP Composites under Tension

Paper 5: Multiaxial Yield Behavior of Polypropylene

Paper 6: Relaxation Behavior of Neat and Particulate Filled Polypropylene in Uniaxial and Multiaxial Compression

2. OBJECTIVES AND METHODOLOGY

The main objective of this dissertation was (1) to adequately describe the multiaxial behavior of the viscoelastic PP matrix in tension and compression, (2) to determine the dominant micro-mechanisms of deformation and failure under tension loading as a function of strain rate and temperature in the PP composites, (3) to quantify the stress level, at which damage (matrix/particle debonding) occurs, and (4) to analyze the viscoelastic long-term behavior of the PP composites and to compare the results to those obtained for the neat PP matrix. To achieve these goals, advanced measurement techniques and methods were utilized in the entire work. Hence, the first two papers are related to the development and implementation of a comprehensive test methodology, while the following four papers deal with detailed investigations related to the characterization of the material behavior. The specific sub-goals of these papers are summarized as follows:

The objectives of *Paper 1* were to analyze the effects of various parameters related to a digital image correlation system test set-up on the accuracy of the overall longitudinal tensile strain result, on the one hand, and to characterize the pre- and post-yield regime of PP under tension, on the other. In *Paper 2* the experimental and procedures that allow for a comprehensive characterization of the compressive stress-strain behavior of plastics including uniaxial and multiaxial loadings of various confinement levels are described and discussed. In addition to details of the test set-up, information on proper test and data reduction procedures is provided.

The determination of the dominant micro-mechanism of deformation and failure were investigated in PP composites under tension loading as a function of temperature and strain rate in *Paper 3*. Glass beads of two different size distributions and talc were used as fillers to investigate the effect of mean particle size, shape and orientation. The load-bearing capacity of the filler and thus the strength of interfacial interaction were investigated with respect to the viscoelastic behavior of the matrix. In *Paper 4* the tests conducted and described in *Paper 3*

were evaluated using the digital image correlation system discussed in *Paper 1*. To quantify the onset of debonding, a novel approach utilizing volume strain measurement results is introduced, and the results are compared with those obtained by acoustic emission measurements. Moreover, volume strain curves of PP and PP composites were determined and analyzed as a function of strain rate and temperature, to determine the dominating micro-mechanism of deformation and failure under various conditions and to relate the behavior of the composite to that of the matrix.

As to the characterization of the pressure dependent yield behavior of the neat PP, various test methods were conducted covering the whole stress range from biaxial and uniaxial tensile tests in the low pressure regime to fully confined compression tests in the high pressure regime. These aspects are dealt with in *Paper 5*. The applied methodology and the experiments conducted provide data to generate true multiaxial yield stress values in a 3-dimensional stress state, representing the deformation behavior of the matrix material in the neat bulk state. These results complement those obtained in uniaxial and plane strain compression tests and allow for the characterization of the pressure dependence of the deformation and yield behavior of polymers as well as the deduction of a fully 3-dimensional yield criterion. Moreover, uniaxial and confined compression tests were also conducted in the relaxation mode to determine the viscoelastic long-term behavior of the neat PP and the PP composites, and are described in *Paper 6*. A specific advantage of the confined compression test is that it provides a full description of the strain and stress field in the specimen and thus allows for the determination of all four viscoelastic material functions ($G(t)$, $K(t)$, $E(t)$, $\nu(t)$). A comparison of uniaxial and confined data reveals the influence of pressure on the long-term relaxation behavior.

Overall, it is clear that meeting the objectives necessitates the development and successful implementation of a combination of three major elements:

- (1) the employment of novel measurement techniques (e.g., digital image correlation),
- (2) novel and improved test methods (e.g., various compression set-ups), and

- (3) a proper methodology for the detection of the onset of debonding along with the identification of the main mechanisms of deformation and failure on a micro- and macro-scale, respectively.

3. BACKGROUND AND CURRENT STATUS

So far a comprehensive characterization of the material in the sense described in the previous chapter was averted due to the lack of appropriate measurement devices and test procedures. For example, in the reversible deformation regime (pre-yield regime), the accurate determination of Poisson's ratio and volume strain in uniaxial tensile experiments for relatively soft materials as PP necessitates the application of non-contact measurement methods of high strain accuracy, which have become available only recently (Hild and Roux, 2006). Alternately, a proper characterization of the irreversible deformation regime associated with necking (yield- and post-yield regime), which initiates at some position of the specimen, also requires a device allowing for the determination of the strain distribution along the specimen measurement length. Finally, to deduce the relevant micro-mechanisms of deformation and failure (cavitation vs. shear modes), accurate volume strain measurements are needed covering a sufficient wide range of overall specimen deformation in the pre- and the post-yield regime.

Today various types of digital image correlation (DIC) systems allowing for a contact-less determination of longitudinal and transverse strains even including full-field determination of sufficient accuracy are offered commercially. However, hardly any studies are available systematically comparing the strain results of these DIC devices with those obtained by conventional clip-on extensometers in terms of accuracy and reliability (Robert et al., 2006).

As to the characterization and determination of the micro-mechanisms of deformation and failure of particulate filled composites, tensile tests provide good insight. Thus, various investigations are available on the yield behavior of filled composites as a function of particle size and content (Fu et al., 2008), particle surface modification and particle shape (Móczó and Pukánszky, 2008). The majority of these studies claims that particle debonding is a main micro-mechanism of deformation and failure in these material systems, with the onset of debonding from the polymer matrix occurring in the pre-yield regime (Renner et al., 2005; Vollenberg et al., 1988). In terms of structure and composition it was

found, that the debonding stress is proportional to the square root of the particle size and the modulus of the neat matrix, and appropriate models have been proposed to describe this dependence (Vollenberg et al., 1988; Pukánszky and Vörös, 1993).

While a significant effort was put into studying the effects of the composite structure and composition on yield behavior for specific test conditions, only few investigations dealt with the effects of strain rate and temperature on the deformation behavior covering both the pre- and post-yield regime (Lapcik et al., 2008; Zhou et al., 2002). As the mechanical behavior of polymers strongly changes in the regime of the glass transition temperature (T_g), corresponding changes of the dominant micro-deformation mechanism have been reported (Friedrich, 1983). Via the above mentioned matrix modulus dependence of debonding, debonding may be expected to also depend on test temperature (particularly when considering temperatures below and above T_g) and strain rate. However, no studies are available investigating such aspects.

Among the various measurement methods to determine the onset of debonding, e.g., “kink” in the stress-strain curve (Vollenberg et al., 1988), acoustic emission (Dányádi et al., 2006; Renner et al., 2007), in-situ experiments (Bai et al., 2003), and volume strain determination, the latter has been used most frequently (Meddad and Fisa, 1997; Naqui and Robinson, 1993; Yilmazer and Farris, 1983). Compared to any potential micro-mechanisms of deformation in neat PP, the debonding process creates additional volume in the case of composites. As to potential micro-mechanisms of deformation in the matrix, several specific mechanisms affecting volume strain by cavitation have been proposed for semicrystalline materials such as PP, including void formation, crazing and micro-cracking possibly accompanied by amorphous chain compaction, molecular orientation and crystalline order destruction/reformation (Addiego et al., 2006).

As a consequence, and depending on the method applied, the different approaches described in the literature resulted in large variations of debonding stress values (Renner, 2005). To accurately determine the debonding stress, both the dilatational and the deviatoric behavior of the matrix and the composite must be properly considered. The former provides information on the volumetric

deformation behavior in the pre-yield (Poisson's ratio) and in the yield- and post-yield regime (cavitation), while the latter is related to the yield- and post-yield regime only.

The investigation of the compressive behavior of polymeric materials in general has not nearly received the same attention as the tensile behavior. This is also the case for PP and PP composites. On the other hand, it is well known that the stress-strain behavior of these materials under tension and compression differs quite significantly, both macroscopically in terms of the stress-strain relationship and in terms of the micro-mechanisms of deformation and failure (Mohanraj et al., 2006; Sauer, 1977). Moreover, as to test devices and procedures for compressive testing, several methods have been developed and are described in standards (ISO 604, 2002) and in the literature (Kuhn, 1985; Ma and Ravi-Chandar, 2000; Williams, 1967). While initial load introduction deficiencies are not present in tension loading, the accuracy of the test specimen geometry and frictional effects between the specimen surface and the compression plates may significantly affect compression test results. However, no systematic investigation on the effect of various test set-ups and test parameters has been conducted, and a comprehensive comparison of various compression test methodologies is still lacking.

In this context of great importance is that in heterogeneous particulate filled composites a multiaxial stress distribution develops around the particles on the micro-scale even when uniaxial tension is applied on the macro-scale. Hence, to obtain a better understanding of the local deformation mechanisms in composites as well as for adequate micromechanical modeling, knowledge of the pressure dependent yield surface is also of crucial importance.

To determine the onset of yielding as a function of mean pressure, various test set-ups have been proposed and were utilized (Bardia and Narasimhan, 2006; Quinson et al., 1997). The majority of investigations in terms of pressure related material functions (e.g., modulus, yield stress, yield strain) has been performed under plane-stress conditions ($\sigma_3=0$) (Fasce et al., 2008; Ghorbel, 2008), and only few studies provide material properties in the 3D stress space (Pae, 1977). As the yielding behavior of polymers is not symmetrical in terms of any stress, 2D yield

criteria (e.g., modified von Mises, modified von Tresca) are not capable to predict the intrinsic polymeric behavior since they assume a constant yield function along the hydrostatic axis (Kolupaev and Bolchoun, 2008). As a consequence, several test methods in the tension and compression regime were applied to cover a wide range of stress states from biaxial tension to fully multiaxial confined compression and to apply the 3D Drucker-Prager yield function to the experimental test results (Drucker and Prager, 1952).

Furthermore, while many investigations exist for the monotonic behavior of PP composites (Fu et al., 2008; Móczó and Pukánszky, 2008) the long-term creep or relaxation response of these materials has not received sufficient attention. This is true not only for uniaxial creep or relaxation, but particularly for the case of confined compression. A specific advantage of relaxation experiments over creep experiments is that a direct, analytically exact determination of the relaxation modulus is possible without interconversion of viscoelastic material functions (Tschoegl, 1989).

Finally, for appropriate material and component modeling, knowledge of all four viscoelastic material functions (bulk-, shear- and uniaxial relaxation modulus, Poisson's ratio) is important (Tschoegl, 1997). While the confined compression test enables the simultaneous determination of the bulk- and shear relaxation modulus without assuming the constitutive behavior a-priori (Qvale and Ravi-Chandar, 2004) no such study seems to exist at least for PP and PP composites.

4. MAJOR RESULTS AND DISCUSSION

This chapter provides a brief overview of the major aspects and results of this dissertation as they are described in detail in the papers collected in Part II.

4.1 Strain Determination of Polymeric Materials using Digital Image Correlation (Paper 1)

The contactless optical strain measurement method referred to as digital image correlation (DIC) was applied to neat PP. The effects of test set-up parameters were analyzed in terms of two quality indicators, indicating the strain scatter from subset to subset (local strain scatter) and from picture to picture (global strain scatter), also considering practical aspects. The optimal parameters in terms of test set-up were excellent contrast with respect to the light intensity (i.e., maximum light intensity avoiding overexposure), a shutter time of 20 ms, and a speckle pattern with a very fine structure. While a minor effect of the operation of the test machine (i.e., vibrations) on the strain accuracy was detected, a significant decrease of the two quality indicators was obtained for the operation of the temperature chamber.

In the pre- and post-yield regime, the overall average and local strains were determined using the DIC system. As expected, a significant difference particularly in the yield and post-yield regime develops when comparing conventional engineering stress-strain curves and true stress-strain curves (Fig. 1). Plotting the strain contour plots as a function of position on the specimen surface allowed for the determination of the entire strain field as a function of the position on the specimen surface. Utilizing this information in combination with one of the quality indicators, the onset of yielding was defined and detected at a lower strain value than the nominal yield point.

In the pre-yield regime the transverse strain was measured via the DIC system and via a mechanically attached clip-on extensometer. Due to the significant creep indentation of the attachment pins of the clip-on extensometer, the lateral contraction exceeded the values obtained by the contactless DIC measurement.

Overall it could be shown that the DIC system allows for the proper strain determination both in the pre- and post-yield regime, and in terms of longitudinal and transverse strains as well as in terms of global average and local strains.

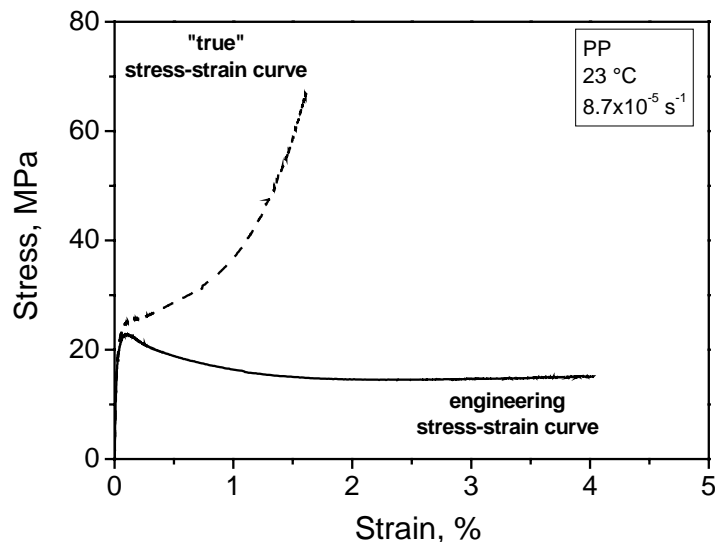


Fig.1: Nominal and “true” stress-strain curves of PP.

4.2 Advanced Compression Testing of Polymeric Materials (Paper 2)

The compression behavior of neat PP was investigated in the pre-yield and post-yield regime using a recently developed compression device. As to the characterization of the compressive modulus in uniaxial compression tests as one of the two characteristic values describing isotropic materials, an “apparent” compressive modulus was calculated related to the peak value of the first stress-strain derivative. Due to the initial load introduction deficiencies, the strain level at which the peak value was determined, was found to be considerably beyond the recommended strain range according to ISO 604. Determination of various “apparent” compressive moduli as a function of the diameter-to-length ratio of the specimen allows for an extrapolation to infinite specimen lengths and thus resulted in an “effective” value of the compressive modulus.

In the post-yield regime, the transverse expansion of the specimen in uniaxial compression tests was determined using an optical video extensometer. To account for frictional effects between the specimen surface and the compression

plates, PTFE tapes were applied on the specimen surfaces. Without the PTFE tape, barreling of the specimen was noticed. True strain-true stress curves were calculated based on the measurement of the transverse strain and on the assumption of $\nu=0.5$ (constant volume during deformation). The results illustrated the variation of true stress-strain data between experiment based and assumption based ($\nu=0.5$) approaches.

In addition to loading rate and temperature, hydrostatic pressure significantly influences the mechanical response of PP. Thus, uniaxial compressive tests and plane strain and confined compression experiments were conducted in order to compare the material behavior under these conditions and under uniaxial tensile conditions. As is shown in Fig. 2, significant differences were determined in the post-yield regime. In the fully confined compression set-up, yielding was inhibited entirely up to a stress level of about 600 MPa, with all deformations imposed on to the specimen being fully reversible.

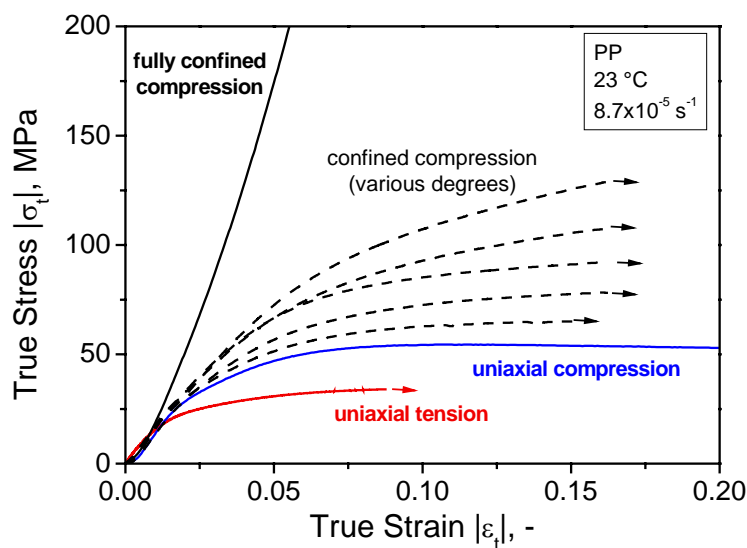


Fig. 2: True stress-true strain curves of uniaxial tensile, uniaxial, plane strain and confined compression tests, showing the strong impact of hydrostatic pressure on the obtained stress-strain response.

4.3 Mechanics and Modeling of the Tensile Yield Behavior of Particulate Filled PP Composites (Paper 3)

The tensile behavior of particulate filled PP composites containing two different glass bead grades (different mean diameter) and talc were investigated as a function of strain rate (from $8.7 \times 10^{-5} \text{ s}^{-1}$ to $8.7 \times 10^{-3} \text{ s}^{-1}$) and temperature (from $-30 \text{ }^\circ\text{C}$ to $80 \text{ }^\circ\text{C}$). As to the effect of particle size on the yield behavior, lower yield stress values were found for the composite containing the large glass beads than for those containing the small glass beads. This finding was related to the smaller debonding stresses for the larger glass bead composites. The micro-deformation mechanisms were found to change from being dominated by crazing and micro-cracking and debonding below ambient temperatures, to being dominated by shear yielding and crazing at room temperature and at elevated temperatures. According to the model by Pukánszky and Vörös (Pukánszky and Vörös, 1993), the debonding stress is directly linked to the square root of the uniaxial modulus and approaches the macroscopic yield stress of the respective composite at elevated temperatures.

Talc was added as filler, to investigate the effect of particle shape and orientation. At low temperatures, the yield stress observed for the talc filled PP composite was smaller than that of the neat matrix, while at elevated temperatures the talc composite exhibited higher yield stress values. This behavior may be related to an increasing debonding stress/yield stress relation and is apparently compensated at room and elevated temperatures by the development of a hard interphase and by the load carried by bonded filler particles. A similar change in the dominant micro-mechanisms of deformation and failure as described above for the glass bead composites was also found to occur with talc as filler.

To quantify the effect of interfacial interaction between filler particles and matrix, the model by Pukánszky and Vörös (Pukánszky and Vörös, 1993) was applied to the experimental yield stress values. Parameter B in this model is a measure of the effectivity of the filler particles and thus for the filler/matrix interaction. This parameter is depicted in Fig. 3 as a function of temperature. For the talc filler, an increase of B with increasing temperature was found, related to the change in the

dominant micro-deformation process and the increasing debonding stress/yield stress ratio. As expected, for the two glass bead grades, up to 50 °C an increasing B value was found with higher effective values for the small glass beads related to the larger debonding stress. The decrease of B at 80 °C may be associated with the lower interfacial interaction and the increased molecular mobility in the interphase. Thus, increasing the temperature further, yielding of the matrix becomes dominant. However, further investigations to proof this explanation are necessary.

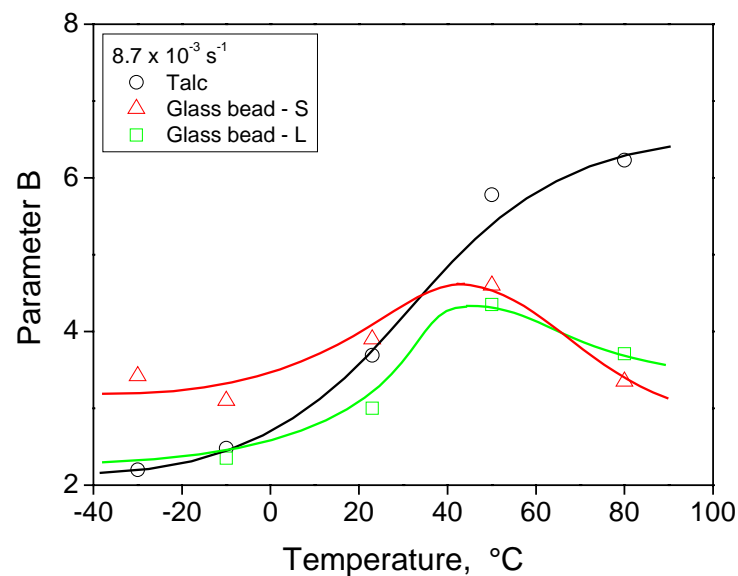


Fig. 3: Temperature dependence of parameter B according to the model by Pukánszky and Vörös for the three fillers used in PP composites.

4.4 Filler/Matrix-Debonding and Micro-Mechanisms of Deformation in Particulate Filled PP Composites Under Tension (Paper 4)

The volumetric behavior of PP and particulate filled PP composites was investigated using the contactless DIC system for accurate and reliable measurements of volume strains. As to the effect of particle size, larger volume strain values were found for the composite containing the large glass beads in the pre-yield and post-yield regime, which is in agreement with the findings described above. Interestingly, depending on the test conditions, smaller volume strain values were detected for the composite than for the neat matrix in some cases. In

contrast to low temperatures or high loading rates, at elevated temperatures or low loading rates the composites were found to exhibit smaller values of volume strain than the matrix, related to different dominant micro-deformation mechanisms in the matrix and composite, respectively. While shear yielding and crazing is dominant at room temperature for the neat matrix, the particles may truncate the formation of crazes in the pre-yield regime to some extent and may facilitate local shear yielding between debonded particles. In the case of talc as filler, the differences in the values of volume strain between the composite and the matrix even exceed those found for the two glass bead composites, exhibiting nearly a constant volume during deformation in the pre-yield regime at 80 °C.

To apply volume strain measurements for the determination of the onset of debonding in particulate filled composites, a novel approach was developed and compared to findings by acoustic emission experiments. In contrast to other approaches using volume strain to detect the debonding stress, the dilatational and deviatoric deformation of the composite and the matrix was considered and the onset of debonding was associated to the void formation, when the particles detach from the matrix. The results obtained corroborate the temperature dependence of the debonding stress as predicted by the model of Pukánszky and Vörös and revealed larger debonding stresses at room temperature than at elevated temperature. Furthermore, larger debonding stresses were determined for the small glass beads than for the large glass beads, with the highest debonding stresses exhibited by talc. In Fig. 4 the debonding stress is plotted against the logarithm of the specific surface area of filler, showing a linear as well as nonlinear correlation at 23 °C and 80 °C, respectively.

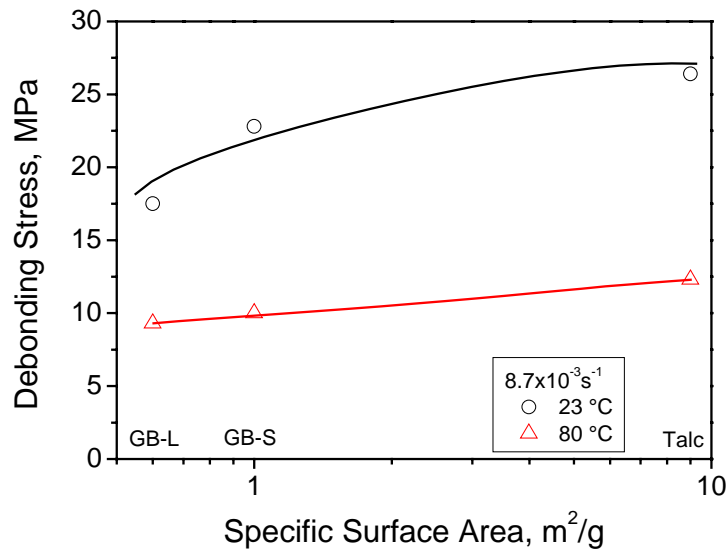


Fig. 4: Debonding stress of glass bead and talc plotted against specific surface area of filler determined at 23 °C and 80 °C.

Comparison of the results obtained by volume strain measurements to the acoustic emission method, revealed smaller debonding stresses for the latter approach. It is worth mentioning, that the data evaluation procedure applied for the acoustic emission measurements provides the stress level, where the maximum number of particles debond from the matrix so that this procedure cannot be used as indication for the onset of debonding. By modifying the data reduction, information on the onset of debonding may perhaps be obtained, and it is proposed to look at the potential of such a modified procedure.

4.5 Multiaxial Yield Behavior of Polypropylene (Paper 5)

The yield behavior of PP tested under different modes of deformation was evaluated in terms of equivalent stress and hydrostatic pressure to determine the pressure sensitivity index (PSI) as a function of temperature and to apply a fully three dimensional yield function (Drucker-Prager model (Drucker and Prager, 1952)) to the experimental test results. To compare different test set-ups, the equivalent stresses were calculated according to the definition given by Kachanov (Kachanov, 1974). As expected, a linear correlation between equivalent stress vs. mean stress was found for low as well as for room temperature and elevated

temperatures. A high mean pressure applied to the specimen exhibits a large value of the onset of yielding and thus a large equivalent stress. This behavior is related to the decreased free volume and molecular mobility, when a high constraint level is imposed on the material. In order to quantify the pressure sensitivity, the normalized equivalent stresses related to the uniaxial tensile tests were plotted against mean pressure, and the corresponding slope of the linear fit provides the value for the PSI. This value was found to increase with temperature, related to the increasing amount of free volume in the amorphous fraction of PP.

In contrast to 2D yield functions, the experimental test results also enabled the determination of a pressure dependent 3D yield criterion. A 3D Drucker-Prager yield surface was fitted to the experimental results using the best fit method (see Fig. 5). Apparently, the yielding behavior of PP is best described by a conical-shaped yield surface, shifted to significantly larger values in the compressive regime. A triaxial tensile yield stress of 72 MPa was found with a pressure coefficient (analogous to the cone angle) of 31.5 °. The average error between the experiments and the predictions by the yield surface was about 8 %, with the maximum error occurring in the biaxial tensile test. Intersection of the yield surface with the plane-stress plane ($\sigma_3=0$) is also illustrated in Fig. 5. The importance of a non axis-symmetric yield surface in terms of the third principal axis was demonstrated.

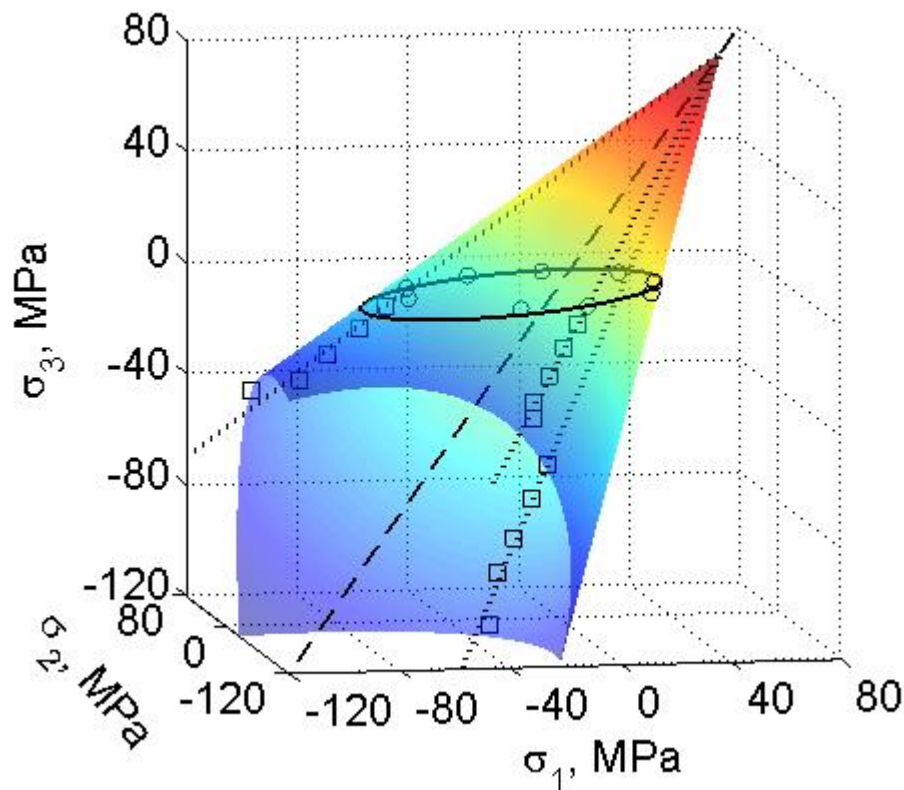


Fig. 5: Experimental yield stresses of PP determined via different test set-ups and the best fit Drucker-Prager yield function. Symbols: (o) plane-stress data, (\square) confined compression test results, (--) hydrostatic axis.

4.6 Relaxation Behavior of Neat and Particulate Filled Polypropylene in Uniaxial and Multiaxial Compression (Paper 6)

The long-term compressive relaxation behavior in uniaxial and confined compression was investigated for the neat and particulate filled PP. In order to increase the reproducibility of the confined compression test, a quality indicator was introduced, relating the applied load on the specimen to the hoop strain measured at the outer surface of the confining cylinder. A minimum coefficient of determination of 0.995 was found to provide reliable test results. To account for initial load introduction deficiencies, two corrections were conducted on the measured load and strain signals. Using this advanced testing procedure, the confined compression test provides the unique possibility, to determine all four viscoelastic material functions ($G(t)$, $K(t)$, $E(t)$, $\nu(t)$) within one test.

The shear and the bulk relaxation moduli, representing the two basic deformation modes for constant volume and constant shape, respectively, are directly provided by the confined compression method. As an example, the master curves of the individual tests performed at different temperatures are compared for the neat, and glass bead and talc filled PP in Fig. 6. A significantly larger amount of relaxation was found for the shear moduli than for the bulk moduli. Adding stiff particles to the neat PP resulted in an increase of the two moduli, the effect of talc being more pronounced, which was related to the mean aspect ratio of 8 of the talc particles and their alignment along the load direction.

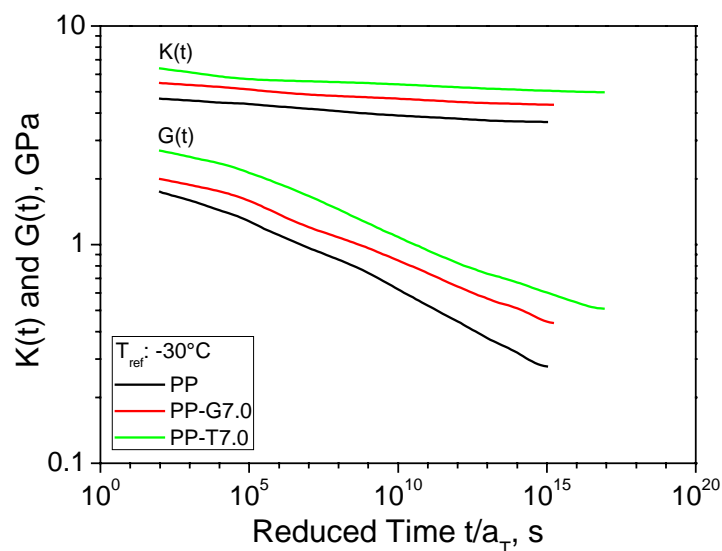


Fig. 6: Relaxation master curves for PP, PP-G7.0 and PP-T7.0 at a reference temperature of $-30\text{ }^{\circ}\text{C}$.

Interconversion of the shear and bulk relaxation moduli to the uniaxial modulus and comparison with uniaxial compression test results allowed for the determination of the effect of pressure on the long-term relaxation behavior. As it turned out in recent investigations, a minor effect of pressure was found below T_g , while the relaxation was significantly retarded above T_g for the confined compression set-up. Using normalized relaxation curves related to the initial value, provides information of the relaxation free from absolute values. While an exponential decay was found for the relaxation behavior in the unconfined mode, a power-law decay was observed in the confined mode. For the latter, similar relaxations were found for the neat and glass bead filled PP, while a reduced

relaxation was determined for the talc filled composite. In the confined mode, an equivalent behavior was found for all composites, showing a retarded relaxation compared to that of the neat PP. This behavior was related to different local stress states in the two test set-ups, which may allow for partial interfacial failure in the unconfined mode. Interconversion of the bulk and shear relaxation moduli to the time dependent Poisson's ratio revealed lower values for the composites than for the neat PP.

5. CONCLUSIONS AND OUTLOOK

In this dissertation, the mechanical behavior of neat PP and particulate filled PP composites was investigated in terms of micro-deformation mechanisms and interfacial interaction under tensile loading conditions, in terms of pressure dependent yielding, and in terms of long-term compressive relaxation. While the main objectives could essentially be achieved, new questions have come up requiring further investigations and future work.

In Papers 1 and 2, the test methodology applied for the extensive material characterization is described. Using two quality indicators, the optimal test set-up related to strain accuracy and practical aspects of the DIC system were determined. The DIC system was applied to measure the strain field in the pre-yield and post-yield regime of PP, and the overall average and local strains were determined. In the pre-yield regime, the longitudinal and transverse strains determined via the DIC system and via a mechanically attached extensometer were compared. A significant creep indentation of the mechanical extensometer pins on the specimen surface was noted, resulting in a considerable overestimation of the contraction of the specimen. Moreover, using one of the quality indicators allows for the evaluation of the onset of yielding, which was found to occur at strain values below the nominal yield point. However, further investigations are necessary to determine the accuracy of the DIC system as a function of the applied strain level on the specimen, and to compare the findings for the onset of yielding, which supposedly accounts for the first irreversible deformation of the specimen, to results by other test methods and procedures.

A detailed description of the advantages and drawbacks of various uniaxial, plane strain and confined compressive test methods are provided in paper two. In the pre-yield regime, an apparent compressive modulus was obtained using the peak value of the stress-strain derivative. Applying different specimen diameter-to-length ratios allowed for the extrapolation to infinite specimen length and thus provided an “effective” value of the compressive modulus. In the post-yield regime, vast differences in the true compressive stress-strain behavior were determined

depending on the degree of confinement. While PP in uniaxial compression exhibits significant strain softening in the post-yield regime, this tendency was reduced (plane strain compression) and then reverted to strain hardening with increasing confinement level. For the fully confined test condition, using a steel cylinder as confinement, no signs of plastic deformation up to a true longitudinal stress of 600 MPa were detected. To compare the pressure dependence of the pre-yield regime with that of the yield- and post-yield regime, further investigations need to be performed on the effective values of the compressive modulus as a function of the confinement level.

In Paper 3, the effect of particle size, shape and orientation on the yield stress in tensile loading was investigated as a function of loading rate and temperature. The dominant micro-deformation mechanisms were found to depend significantly on these two testing parameters. Looking first at the neat PP matrix material, the dominating deformation micro-mechanisms were found to be crazing and micro-cracking followed by brittle fracture at low temperatures or high loading rates, while shear yielding and to some degree crazing dominate at room temperature and at elevated temperatures or at moderate and slow loading rates. In the composites, debonding and crazing associated with micro-cracking, leading to brittle fracture were found for the low temperature regime. Limited particle debonding and shear yielding with some crazing of the matrix were found at elevated temperatures. The changing load-bearing capacity of fillers with different particle characteristics could be related to the dominating micro-mechanism of deformation. Future work regarding this topic should also concentrate on composites with higher filler contents and various particle shapes as well as on the effect of surface modification of the filler (i.e., enhanced particle-matrix interaction).

In Paper 4, tensile tests were carried out on the neat PP and on the PP composites at two temperatures (23 °C and 80 °C) in the strain rate range from $8.7 \times 10^{-3} \text{ s}^{-1}$ to $8.7 \times 10^{-5} \text{ s}^{-1}$ using the DIC system for accurate volume strain measurements. A significant increase in volume strain was recorded for composites containing the larger glass beads compared to those prepared with the smaller glass beads. The processes of local deformation in the matrix included various cavitation mechanisms (void formation, crazing and micro-cracking) and

shear yielding all being initiated prior to the yield point. The cavitation failure mechanisms (voiding, crazing, micro-cracking and debonding) were favoured by the lower temperature (23 °C) and higher strain rates. At the elevated temperature (80 °C) or lower strain rates the volume strain of the composites was even smaller than that of the matrix, indicating a change in the dominating micro-mechanisms of deformation from the various cavitation mechanisms to local shear yielding. The volume strain of composites containing talc was also smaller than that of the neat PP. The observed decrease in volume strain was explained by the compaction process in the amorphous phase and by the absence of debonding in this specific strain range. As to the determination of the debonding stress, a novel approach was introduced, which accounts for the dilatation and deviatoric behaviour of the matrix and composite, respectively. In agreement with the prediction of theoretical models and validated with acoustic emission measurements, the debonding stress was found to decrease with decreasing strain rate and increasing temperature. In this context, the rate of debonding (i.e. kinetics of debonding) and the subsequent plastic deformation of the matrix may be an interesting aspect to investigate in future work, which may also be required for the implementation in micromechanical damage evolution models.

Various test set-ups were utilized in Paper 5 to investigate the pressure dependent yield behavior of neat PP. As expected, vast differences in the true stress-strain behavior were determined depending on the degree of confinement. Evaluation of the equivalent stress at the yield point resulted in a linear correlation between the equivalent stress and the mean stress for all test temperatures, with the slope being the pressure sensitivity index (PSI). While the lowest equivalent stresses were obtained in the tensile regime with a positive mean tensile stress acting upon the specimen (i.e., uniaxial and biaxial tensile tests), the highest equivalent stresses were found for the confined compression test with the largest mean compressive stresses investigated in this study. As expected, the pressure dependency was found to increase with temperature, which was attributed to free volume effects in the amorphous phase and the associated influence on molecular mobility. The Drucker-Prager yield function was applied to the experimental test results, and a good agreement between the experiments and the predictions of the

yield criterion was found, with an average error of about 8 %. A triaxial tensile yield stress of 72 MPa was predicted and a pressure sensitivity angle of 31.5° was obtained. The effect of temperature and the addition of particles to PP may be investigated in future work, as well as the application of suitable methods for an accurate determination of the onset of yielding.

The long-term compressive relaxation behavior of neat PP and PP composites was characterized and described in Paper 6. The master curves of the shear and bulk relaxation moduli were determined utilizing the confined compression test set-up. By interconversion of the two viscoelastic material functions, the uniaxial relaxation modulus and the time dependent value of Poisson's ratio was calculated. Thus, a complete viscoelastic characterization of the material was achieved. Comparing the uniaxial relaxation modulus values directly measured in uniaxial compression to the uniaxial modulus values deduced from confined compression tests, it could be shown that the rate of relaxation is strongly reduced by the effect of the increased pressure in the confined compression set-up. As expected, particles increased all of the three modulus values and decreased Poisson's ratio compared to values obtained for neat PP. To provide a full description also in terms of quantitative measure of the pressure dependence of viscoelastic material functions, future investigations should focus on other confinement levels and strive towards establishing quantitative models for confined relaxation.

REFERENCES

- Addiego, F., Dahoun, A., G'Sell, C., Hiver, J.M. (2006). *Oil Gas Sci. Technol.* **61**, 715.
- Bai, S.L., Wang, M., Zhao, X.F. (2003). *Compos. Interfaces* **10**, 243.
- Bardia, P., Narasimhan, R. (2006). *Strain* **42**, 187.
- Christie, M. (1986). *Plast. Eng.* **42**, 41.
- Dányádi, L., Renner, K., Szabó, Z., Nagy, G., Móczó, J., Pukánszky, B. (2006). *Polym. Adv. Technol.* **17**, 967.
- Dubnikova, I.L., Berezina, S.M., Antonov, A.V. (2004). *J. Appl. Polym. Sci.* **94**, 1917.
- Dubnikova, I.L., Muravin, D.K., Oshmyan, V.G. (1997). *Polym. Eng. Sci.* **37**, 1301.
- Drucker, D.C., Prager, W. (1952). *Q. Appl. Math.* **10**, 157.
- Fasce, L.A., Pettarin, V., Marano, C., Rink, M., Frontini, P.M. (2008). *Polym. Eng. Sci.* **48**, 1414.
- Friedrich, K. (1983). *Adv. Polym. Sci.* **52/53**, 226.
- Fu, S.-Y., Feng, X.-Q., Lauke, B., Mai, Y.-W. (2008). *Composites Part B* **39**, 933.
- Ghorbel, E. (2008). *Int. J. Plast* **24**, 2032.
- Hild, F., Roux, S. (2006). *Strain* **42**, 69.
- International Standard. *Plastics - Determination of compressive properties ISO 604*, Third edition, 2002.
- Kachanov, L.M. (1974). "Fundamentals of the Theory of Plasticity", MIR Publishers, Moscow.
- Kolupaev, V.A., Bolchoun, A. (2008). *Forsch Ingenieurwes* **72**, 209.
- Kuhn, A.H. (2000). "ASM Handbook Volume 8: Mechanical Testing and Evaluation", ASM International.

- Lapcik, L., Jindrova, P., Lapcikova, B., Tamblyn, R., Greenwood, R., Rowson, N. (2008). *J. Appl. Polym. Sci.* **110**, 2742.
- Leong, Y.W., Mohd. Ishak, Z.A., Ariffin, A. (2003). *J. Appl. Polym. Sci.* **91**, 3327.
- Ma, Z., Ravi-Chandar, K. (2000). *Exp. Mech.* **40**, 38.
- Markarian, J. (2004). *Plast. Additives Compound* **6**, 26.
- Meddad, A., Fisa, B. (1997). *J. Appl. Polym. Sci.* **64**, 653.
- Móczó, J., Pukánszky, B. (2008). *J. Ind. Eng. Chem.* **14**, 535.
- Morieras G. (2001). *Ind. Miner.* **6**, 29.
- Mohanraj, J., Barton, D.C., Ward, I.M., Dahoun, A., Hiver, J.M., G'Sell, C. (2006). *Polymer* **47**, 5852.
- Naqui, S., Robinson, I.M. (1993). *J. Mater. Sci.* **28**, 1421.
- Narisawa, I., Ishikawa, M. (1990). *Adv. Polym. Sci.* **91/92**, 354.
- Pae, K.D. (1977). *J. Mater. Sci.* **12**, 1209.
- Pukánszky, B., Vörös, G. (1993). *Compos. Interfaces* **1**, 411.
- Pukánszky, B., Fekete, E. (1999). *Adv. Polym. Sci.* **139**, 109.
- Pukánszky, B. (1995). In: "Polypropylene. Structure, Blends and Composites" (Karger-Kocsis, J., ed.), Vol. (3/3), pp.1-70, Chapman and Hall, London.
- Quinson, R., Perez, J., Rink, M., Pavan, A. (1997). *J. Mater. Sci.* **32**, 1371.
- Qvale, D., Ravi-Chandar, K. (2004). *Mech. Time-Depend. Mater.* **8**, 193.
- Renner K., Henning S., Móczó, J., Yang, M.S., Choi H.J., Pukánszky, B. (2007). *Polym. Eng. Sci.* **45**, 1235.
- Renner, K., Yang, M.S., Móczó, J., Choi, H.J., Pukánszky, B. (2005). *Eur. Polym. J.* **41**, 2520.
- Robert, L., Nazaret, F., Cutard, T., Orteu, J.-J. (2007). *Exp. Mech.* **47**, 761.
- Sauer, J.A. (1977). *Polym. Eng. Sci.* **17**, 150.
- Singh, U.P., Biswas, B.K., Ray, B.C. (2009). *Mater. Sci. Eng., A* **501**, 94.

- Tschoegl, N.W. (1989). "The Phenomenological Theory of Linear Viscoelastic Behavior", Springer-Verlag, Heidelberg.
- Tschoegl, N.W. (1997). *Mech. Time-Depend. Mater.* **1**, 3.
- Vollenberg, P., Heikens, D., Ladan, H.C.B. (1988). *Polym. Compos.* **9**, 382.
- Ward, I.M. (1971). "Mechanical Properties of Solid Polymers", John Wiley & Sons Ltd., London.
- Weidenfeller, B., Höfer, M., Schilling, F.R. (2005). *Composites Part A* **36**, 345.
- Weidenfeller, B., Höfer, M., Schilling, F.R. (2004). *Composites Part A* **35**, 432.,
- Williams, J.G. (1967). *Trans. J. Plastics Inst.* **6**, 505.
- Yang, J., Zhang, Z., Friedrich, K., Schlarb, A.K. (2007). *Appl. Phys. Lett.* **91**, 11901.
- Yilmazer, U., Farris, R.J. (1983). *Polym. Compos.* **4**, 1.
- Yuan, Q., Jiang, W., An, L., Li, R.K.Y. (2004). *Polym. Adv. Technol.* **15**, 409.
- Zhou, T.H., Ruan, W.H., Yang, J.L., Rong, M.Z., Zhang, M.Q., Zhang, Z. (2007). *Compos. Sci. Technol.* **67**, 2297.
- Zhou, Y., Mallick, P.K. (2002). *Polym. Eng. Sci.* **42**, 2449.

PART II:

COLLECTION OF PAPERS

PAPER 1[°]**STRAIN DETERMINATION OF POLYMERIC MATERIALS
USING DIGITAL IMAGE CORRELATION**

M. Jerabek^{a*}, Z. Major^b, R.W. Lang^b

^a Polymer Competence Center Leoben GmbH, Roseggerstrasse 12, 8700 Leoben, Austria

^b Institute of Materials Science and Testing of Plastics, University of Leoben, Franz-Josef-Strasse 18, 8700 Leoben, Austria

ABSTRACT

Application of digital image correlation (DIC) to polymeric materials has been proven to be a powerful tool for non-contact strain measurement. In this paper the limits of accuracy of this optical strain measurement system under different environmental conditions were investigated, and the technique was applied to the characterization of polypropylene (PP) and PP composites (PP-C) in the pre- and post-yield regime. As to the accuracy, a fine speckle pattern and a light intensity just below overexposure provided best results. While vibrations related the operation of the testing machine were of minor influence in reducing the strain measurement accuracy, more pronounced effects were found for the operation of the temperature chamber. In characterizing the transverse strain behavior of PP-C, DIC results exhibited smaller values compared to transverse strains determined utilizing a mechanical clip-on extensometer. The latter effect is attributed to viscoelastic creep surface indentation of the extensometer pins, which mechanically interact with the specimen via the clip-on spring forces of the extensometer. For the DIC system it could be shown that it allows for the proper strain determination both in the pre- and post-yield regime, and in terms of

[°] Paper will be submitted to Polymer Testing.

* Corresponding author. Tel.: +43 3842 42962 21; fax: +43 3842 42962 6
E-Mail address: Jerabek@pccl.at

longitudinal and transverse strains as well as in terms of global average and local strains.

Keywords: Digital Image Correlation; Parameters; Polypropylene; True stress-true strain; Mechanical extensometer;

1. INTRODUCTION

In addition to traditional extensometry, optical strain measurement devices have been increasingly applied in recent years for various materials to characterize their mechanical behavior [1-5]. In contrast to clip-on or contact extensometers, which are mechanically attached to the test specimen, optical measurement devices operate contactless. Optical techniques are particularly suitable for soft polymeric materials, as local stress concentrations arising from the indentation of the specimen and the weight of an attached mechanical extensometer are entirely avoided.

In principle two optical strain measurement systems can be distinguished; devices with a fixed gauge length measuring the strain between two edges commonly referred to as video extensometer [6], and full-field strain analysis (FFSA) systems referred to as digital image correlation (DIC) [7]. DIC is based on the principle of comparing speckle pattern structures on the surface of the deformed and the undeformed sample or between any two deformation states. For this purpose a virtual grid of subsets of a selected size and shape, consisting of certain pixel gray value distributions is superimposed on the preexisting or artificially sprayed-on surface pattern and followed during deformation by an optical camera system. In this manner information on the in-plane local strain distribution is gained without assuming the constitutive behavior of the material a priori. Furthermore, this method is independent of specimen geometry and can also be applied to complex parts and geometries [8-12] to gain information on the deformation behavior of real service components.

For traditional extensometry the limits of resolution and accuracy are well known and can easily be determined. In the case of optical measurement devices the situation is more complicated, since resolution and accuracy depend on the whole

measurement system including the objective, the camera and the light system. The number of pixels per mm, which represent an important characteristic as to the resolution of optical systems, strongly depends on the distance between camera and the specimen. Of specific importance, environmental conditions like vibrations of the test equipment or glass panels between specimen and camera when testing at non-ambient temperatures may have a significant influence on the obtained strain accuracy. Moreover, out-of-plane movements of the specimen affect the apparent size of the specimen and thus may also alter the strain result in 2D measurements. Finally, the range of the depth of sharpness is limited and determines the operating distance to the measured object, if significant out-of-plane movements occur.

Knowledge of the intrinsic material behavior of polymeric materials from the small strain range up to ultimate failure is of crucial importance for developing adequate material laws for numerical modeling and for a deeper understanding of the microscopic deformation mechanisms. Up to the yield point polymers deform relatively homogeneously, therefore good agreement between results of mechanical extensometers and DIC systems may be expected. At large strains, in the yield and post-yield regime, inhomogeneous deformations are observed in many polymers [13], which are not adequately recorded by traditional extensometry. However, for a proper calculation of true strain and true stress in the highly deformed neck, the local longitudinal strain as well as the local transverse strain values are needed.

As DIC provides a full description of longitudinal and transverse strain distributions also in the highly strained neck region of the specimen, true strain and true stress as well as Poisson's ratio and volume strain can be calculated also providing information on the local strain history at each position of the specimen surface. Thus DIC allows for a determination of modulus and Poisson's ratio in the pre-yield regime, and true stress-strain relationships in the post-yield regime.

The objectives of this paper are (1) to analyze the effects of various parameters related to the DIC test set-up (light intensity, camera shutter time, speckle pattern structure, machine and temperature chamber vibrations) on the accuracy of the overall longitudinal tensile strain result (average value for the standardized gauge

length of 50 mm), (2) to characterize the pre- and post-yield regime of polypropylene (PP) under tension, and (3) to compare the results obtained by DIC with those obtained by a conventional mechanical transverse extensometer.

2. MATERIALS AND EXPERIMENTAL

A development grade PP homopolymer (PP) and a particulate filled PP (PP-C) commercial grade with the same homopolymer as matrix were selected as model materials for all experiments. The materials were manufactured and delivered by Borealis Polyolefine GmbH Linz (Linz, Austria) as injection molded tensile specimens according to ISO 3167, type B.

The tensile tests were performed on an electro-mechanical universal testing machine of the type Instron 5500 (Instron LTD; High Wycombe, UK). Unless otherwise indicated in the result section, the crosshead displacement in the experiments was usually set to a rate of 0.01 mm/s corresponding to a strain rate of $8.7 \times 10^{-5} \text{ s}^{-1}$. Although all tests were carried out at an ambient temperature of 23 °C, a conventional temperature chamber used for non-ambient temperature tests was also mounted on the frame of the testing machine to study the effect of a glass panel between DIC camera and specimen and perhaps additional vibrations on the DIC results.

The initial specimen length between the wedge grips was 115 mm. The axial strain was measured by a mechanical clip-on extensometer of the type Instron 2630-112 with an initial gage length of 50 mm; the transverse strain was recorded via a clip-on extensometer of the type Instron 2620-603 with an initial gage length of 10 mm. The DIC measurement was carried out with the ARAMIS 3D optical deformation analysis system developed by GOM (Gesellschaft für optische Messtechnik mbH; Braunschweig, D). To allow for a sufficient optical signal detection and to avoid heating of the specimen during testing, the light directed onto the specimen was provided by the cold light system Dedocool (Dedo Weigert Film GmbH; Munich, D).

The 3D DIC system consists of two high speed cameras for recording the images (type Basler 504k; Basler AG; Ahrensburg, D), a trigger box to control the

cameras, and a computer for data acquisition and evaluation. Image recording is done simultaneously with the acquisition of the analog inputs from the testing machine (e.g., force and displacement signal). To record the front of the specimen, the cameras were equipped with a 105 mm Nikon lens, and were mounted on a displaceable frame attached directly to the testing machine (Fig. 1^{*}). This configuration allows for a fixed camera position relative to the test machine and the specimen position, while being able to move the cameras easily to the left to open and close the temperature chamber. In this manner, the relative position of the two cameras to each other is also fixed and only one calibration procedure is needed for a series of experiments with different specimens and tests at different temperatures. However, the drawback of this set-up is that oscillations from the drive system of the test machine and from the fan of the temperature chamber are directly transferred to the cameras and may significantly influence the quality of the test results.

In contrast to 2D measurements with one camera, calibration of the DIC system is obligatory when performing 3D measurements, taking the relative position of the two cameras to each other into account. In this context, it should be pointed out that out-of-plane movements of the specimen relative to the camera position using a 2D system (as they occur for example in a simple uniaxial tensile test due to cross-sectional dilatation) may significantly influence the results [1,6]. An overview of specifics and the performance characteristics of 2D and 3D systems is provided in Table 1.

For a complete description of the strain field a random speckle pattern on the surface of the target object is necessary. To ensure a reproducible background for all tests, a matt white grounding was applied onto the specimen surfaces. The pattern was produced by a black graphite spray so that the specimens were homogeneously covered with densely yet distinctly spaced graphite. As shown in Fig. 2, the principle of any DIC system is to use the random gray value intensity distribution of the pattern on the object and to overlay a grid of subsets or facets on it. In the two pictures recorded simultaneously by the cameras, each subset

* All figures of this paper are collected at the end of the text.

has a unique intensity distribution. The calibration function enables the detection of the position of each subset in the 3D space. In a series of images recorded during a test, the pattern becomes deformed according to the specimen deformation, and the subsets can be detected in each image according to the intensity distribution calculated and determined in the reference image. As the size and shape of the subsets changes when the target object is strained, the strain field on the specimen surface in longitudinal and transverse direction may be obtained by continuously analyzing the speckle pattern and the deformed subsets. The algorithm applied to identify the subsets in each picture is of great importance for the accuracy of the strain field [14-16].

Table 1: Overview of 2D and 3D-DIC properties

	2D	3D
Number of cameras	1	2
Calibration requirement	No, however needed and possible to gain information on displacement	Yes
Influence of out-of-plane movements of the specimen	Significant influence on strain measurement	No influence on the strain measurement
Out-of-plane measurement	Not possible	Yes; measurement of the out-of-plane movement
Minimal measurement area	Down to 1 mm ²	Limited by the size and position of the cameras to each other

From the numerous software specific adjustable parameters of a DIC system the most important one affecting the result accuracy is the size of the subsets [17]. As the subset size determines and is equivalent to the minimum local gauge length, and since there is no systematic procedure, the definition of an adequate subset size is based on operator experience and judgment. In this investigation overlapping quadratic subsets with a size of 25 pixels and a step of 19 pixels between two subsets were used. Longitudinal and transverse strain values are obtained for each of the subsets, implying constant strain values within a given subset.

In order to obtain overall strain values from DIC measurements which are consistent with the tensile strain definition of ISO 527, the initial evaluation distance along the specimen should be set equal to the initial gauge length of

50 mm (Fig. 2). Overall (global) strain values can then be obtained from DIC measurements by simply averaging the strain values of all subsets in the initial gauge length area.

Data reduction

The nominal longitudinal $\varepsilon_{n,l}$ and nominal transverse strains $\varepsilon_{n,t}$ were calculated as

$$\varepsilon_{n,l} = \frac{l - l_0}{l_0} \quad (1)$$

and

$$\varepsilon_{n,t} = \frac{w - w_0}{w_0} \quad (2)$$

where l and l_0 are the actual and initial length and w and w_0 the actual and initial width of the specimen, respectively. For results presented in this paper, the initial gauge length of the evaluation area was varied and adapted to the corresponding measurement purpose.

True longitudinal strain, $\varepsilon_{t,l}$ was calculated as

$$\varepsilon_{t,l} = \ln(\varepsilon_{n,l} + 1) \quad (3)$$

The nominal stress σ_n and true stress σ_t is given by

$$\sigma_n = \frac{F}{A_0} \quad (4)$$

and

$$\sigma_t = \frac{F}{A} \quad (5)$$

where F is the applied force, and A_0 and A are the initial and actual cross-section of the specimen, respectively, the latter being determined by DIC.

Poisson's ratio is defined as

$$\nu = -\frac{\varepsilon_{n,t}}{\varepsilon_{n,l}} \quad (6)$$

3. RESULTS AND DISCUSSION

3.1. Effect of test set-up parameters

Among the test set-up parameters potentially affecting the quality of test results, the influence of light intensity, camera shutter time, speckle pattern structure, machine and temperature chamber vibrations were investigated in more detail. In general, when investigating the effect of one of these parameters, all other parameters were kept constant and set at the default value defined in preliminary experiments. Default values were maximum light just avoiding overexposure, a shutter time of 13 ms, a very fine speckle pattern structure, and the testing machine and the temperature chamber not in operation. Simultaneously subset size and step, the adjustment of the objective and the calculation procedure in the software program also were kept constant.

To learn about the importance of the above parameters, two indicators – the *mean value of strain standard deviations (SSD)* and the *standard deviation of mean strain values (MSV)* – were defined and deduced based on a statistical analysis. For this purpose, a series of 500 pictures was recorded for each parameter set using an evaluation area corresponding to a gauge length of 50 mm. The mean value of SSD was derived by first calculating the SSD for each picture taking all subsets within the evaluation area and then calculating the mean value of all 500 SSDs. Conversely, the standard deviation of MSV was derived by first calculating the mean value for each picture again taking all subsets within the evaluation area and then calculating the standard deviation of all 500 MSVs. Using these definitions, the mean value of SSD represents a measure of the *local strain scatter* from subset to subset within the evaluation area, while the standard deviation of MSV is a measure of the *global strain scatter* from picture to picture. The latter indicator determines the accuracy of strain measurement, which may be compared to equivalent values usually provided for conventional mechanical extensometers. In terms of improved signal and data reduction quality both indicator values should be as small as possible, keeping other more practical aspects of data generation and processing in mind.

The *effect of light intensity* in terms of increased brightness on the two characteristic indicator values defined above is shown in Fig. 3 for a series of four tests. While the mean value of SSD (local strain scatter) initially decreases with increasing brightness, the standard deviation of MSV (global strain scatter) overall increases. For the highest brightness value investigated (test number 4), overexposure – indicated by the high value of the standard deviation of MSV – is observed. Hence, the optimum set-up in terms of excellent contrast corresponds to the brightness of test number 3. For this brightness the accuracy of strain measurement (standard deviation of MSV) is about 1.25×10^{-3} %.

Figure 4 illustrates the influence of the shutter time in the range of 1 ms to 130 ms on the two quality indicators. Both characteristic values decrease with increasing shutter time up to 30 ms and essentially remain constant for higher shutter times. This may be attributed to the superposition of two opposing effects. On the one hand, an increasing shutter time and hence longer light exposure improves the quality of the detected average signal and thus acts to reduce both characteristic values. On the other, an increasing shutter time leads to a higher level of noise by the chips used in digital cameras, which tends to increase the values of SSD and MSV. The optimum set-up was deduced for a shutter time of 20 ms.

The influence of speckle pattern structure was investigated by applying three different sizes of speckles from very coarse to fine. As depicted in Fig. 5, fine speckles clearly lead to improved results (lowest values for SSD and MSV), which may be related to the enhanced gray scale value distribution from subset to subset.

The influence of any vibrations caused by the operation of the test machine or the temperature chamber on the strain signal quality was determined. In the experiment with the test machine in operation, the specimen investigated was mounted into the moving grip and not attached to the static grip. To simulate the moving specimen target (i.e., evaluation area) in a real tensile test, the measurement was performed at a displacement rate of 0.1 mm/s. In this case, the temperature chamber was not in operation. Conversely, when the temperature chamber was in operation, the test machine was shut off so that the specimen was also not moving in this instance. The results for the various test set-ups are shown

in Fig. 6. While the operating temperature chamber clearly decreases the signal quality both in terms of SSD and MSV values, a somewhat surprising result was found for the case of the operating test machine in that the value for MSV was reduced. It should be mentioned, however, that these results were only obtained in a limited number of tests. In any case, the MSV values were not significantly altered by the operating test machine thus providing evidence that this parameter in terms of affecting the signal quality can be neglected. In contrast, a significantly more pronounced effect in terms of reducing the strain signal quality results from the operating temperature chamber. Part of this influence is certainly related to the vibrations caused by the operating temperature chamber, which is attached to the test frame. Additional effects may be caused by the quality and relative position of the chamber window consisting of two or more separated glass panels.

In summarizing the above results on the effect of various test and machine parameters on the signal quality of the optical strain measurement system, it may be concluded that under practical test conditions of an operating test machine, the accuracy of strain measurement at ambient temperatures is about 0.0015 %, a value which is comparable to conventional clip-on extensometers. For non-ambient temperatures, i.e., when using a temperature chamber, the accuracy of strain measurement worsens to a value of about 0.006 %. At this point it should be mentioned, that additional problems may arise when using temperature chambers at low temperatures when ice formation on the specimen surface disturbs and possibly even invalidates the speckle pattern recognition.

3.2. Uniaxial tensile testing with the DIC system in the pre-yield regime

During a uniaxial tensile test a specimen is strained in the longitudinal direction and as long as the deformation is homogenous a constant strain can be measured along the specimen length. In this case a mechanical clip-on extensometer attached to the specimen directly provides accurate strain values by measuring relative displacements between the two extensometer knife edges and relating these to the extensometer reference gage length. Conversely, the DIC system determines absolute displacement values for each subset on the specimen surface. Plotted as a function of the position on the specimen surface, these local displacement values should result in a straight line for a homogeneous strain

distribution. Figure 7 illustrates such a result for the small strain region of PP in terms of a displacement contour plot (Fig. 7a), a schematic of the local displacement situation also indicating the data reduction procedure to obtain an overall average strain value (Fig. 7b), and the transformation of the displacement contour plot into a diagram of displacement vs. original position of a given subset field (Fig. 7c).

A nominal stress-strain diagram for PP exposed to uniaxial tension with strain determination using the DIC system is depicted in Fig. 8. The corresponding strain contour plots for the positions *a* to *g* in the stress-strain diagram are illustrated in Fig. 9. It is worth noting that no averaging or filtering was applied on the data, and hence the strain distribution depicted in the contour plots was calculated within the subsets. This represents highly local strain values which also depend on subset size and thus can be determined only with limited accuracy, resulting in a strain variation from 0.96 % to 1.33 % in Fig. 9a.

Figure 10 shows the local longitudinal strain of the strain contour plots in Fig. 9 as a function of the absolute position on the specimen surface in the unstrained state along the specimen center line. Overall the strain distribution along the specimen is seen to be rather uniform. The small undulations in the various lines of Fig. 10 are related to the inherent scatter of strain measurement of the system (variations caused by the mean value of SSD as discussed above), thus again providing information as to the limits of strain determination. Nevertheless, with increasing strain value and starting from the overall strain associated with position *d*, a slight strain gradient along the specimen length becomes increasingly apparent, with higher strains at position 0 mm compared to the position 50 mm. In fact, this strain gradient always allows for a clear prediction of the necking position at later stages of the specimen deformation.

Another example of a stress-strain diagram comparing the results of a strain determination in longitudinal direction (i.e., overall average strain) via the DIC system and conventional mechanical clip-on extensometer is shown in Fig. 11 for PP-C. As expected, both strain determination methods exhibit good agreement up to the yield point. However, beyond the onset of yielding, the clip-on extensometer delivers higher strains than the DIC system. This is related to the fact that the

original gauge length of the DIC system was set slightly shorter than the one of the mechanical extensometer to be able to use both systems simultaneously on the same specimen. The onset of yielding was actually triggered by the contact forces of the knife edges of the mechanical extensometer, and thus the strain was locally enhanced in a regime just outside the original gauge length of the DIC system but still at least partly within the range of the clip-on extensometer.

To compare results of measurements of transverse strain vs. longitudinal strain using mechanical extensometers and the DIC system, different specimens were used for each of the techniques to avoid any contact effects associated with the mechanical extensometer on the DIC measurement. The results are shown in Fig. 12 for two strain rates. First, transverse strains indicating a significantly stronger transverse contraction even in the pre-yield regime (below 5 %) were found for the mechanical extensometer, the difference being larger for the lower strain rate. Both of these observations are related to the creep indentation of the contact pins of the clip-on transverse extensometer into the specimen surface during the test. At lower test speeds the effect is enhanced. These results imply that Poisson's ratio measurements at least for this class of materials should make use of contactless optical strain measurement systems rather than of mechanically attached devices. Further details regarding the determination of Poisson's ratio for a wide variety of test conditions and set-ups are discussed in a separate paper [18].

3.3. Uniaxial tensile testing with the DIC system in the post-yield regime

The stress-strain response of PP over the entire deformation regime investigated with special focus on the onset of yielding (instability) and the post-yield regime is shown in Fig. 13. As mechanical extensometers affect the onset of yielding by contact forces and do not allow for proper strain measurements beyond yielding, these experiments were performed using the DIC system only. For the positions h to k in the global stress-strain diagram, the strain contour plots and strain distributions along the specimen center line, indicating the position dependent local strain values, are shown in Figs. 14 and 15, respectively. The highest values

of local strain of Fig. 15 were used to construct the stress vs. local strain curve in Fig. 13. Thus, Fig. 13 provides an indication of the strain range in the post-yield regime, depending on whether a global or a local strain definition is used. For example, for position k the two strain values differ by a factor of 1.8 (32 % vs. 58 %). Figs. 14 and 15 also indicate the position and illustrate the significant increase in strain in the localized region where the onset of subsequent necking was observed. Simultaneously, the material outside the necking region was found to experience a reduced strain increase. As the neck stabilizes at a certain constant local strain, it then propagates along the specimen so that the crosshead displacement determines the neck propagation velocity. In this state, the undrawn material outside the necking area remains essentially unaffected.

To determine the position of the onset of yielding indicated also in Fig. 13, the mean value of SSD is plotted vs. the local longitudinal strain in Fig. 16. As the value of SSD provides a measure for the local strain scatter, the onset of instability was defined as the point at which this value surpasses the longitudinal strain independent scatter level of about 8×10^{-4} . This position defining the onset of yielding (perhaps associated with the first occurrence of irreversible deformation) along with the position of the yield point are both shown in Figs. 13 and 16. According to this procedure, the onset of yielding occurs at strains significantly before the macroscopic yield point and neck instability.

4. CONCLUSIONS

The objective of this paper was to identify the effect of test set-up parameters on the accuracy of a DIC system, to compare results of this system with those obtained by conventional extensometer techniques, and to determine the strain field in an inhomogeneously deforming polymer in the post-yield regime. Tests were performed on a neat PP and a particulate filled PP composite.

To evaluate the strain result of the DIC system in terms of strain accuracy, two quality indicators (mean value of SSD and standard deviation of MSV) were introduced representing the local strain scatter from subset to subset and the global strain scatter from picture to picture. For the DIC system, the optimal test

set-up related to strain accuracy and practical aspects were excellent contrast with respect to the light intensity (i.e., maximum light intensity avoiding overexposure), a shutter time of 20 ms, and a speckle pattern with a very fine structure. While a minor effect of the operation of the test machine (i.e., vibrations) on the strain accuracy was detected, a significant decrease of the two quality indicators (SSD and MSV) was obtained for the operation of the temperature chamber.

The DIC system was applied to measure the strain field in the pre- and post-yield regime of PP, and the overall average and local strains were determined. In the pre-yield regime, the longitudinal and transverse strains determined via the DIC system and a mechanically attached extensometer, were compared. While no effect on the longitudinal strain result was observed, a significant creep indentation of the mechanical extensometer pins on the specimen surface was noted, resulting in a considerable overestimation of the contraction of the specimen. Thus, the use of contactless optical measurement devices are certainly advantageous for the determination of Poisson's ratio values for this class of materials.

In the yield and post-yield regime, the determination of proper strain values focused on an adequate use of the DIC system only. Significant differences were observed beyond the onset of necking when comparing the stress vs. average strain and stress vs. local strain curves. As to the evaluation of the onset of yielding, the mean value of SSD was plotted against local longitudinal strain and the significant increase in the SSD value above the strain independent strain scatter was related to the onset of instability, which was found to occur at lower strain values than the nominal yield point. Overall it could be shown that the DIC system allows for the proper strain determination both in the pre- and post-yield regime, and in terms of longitudinal and transverse strains as well as in terms of global average and local strains.

Acknowledgements

The research work of this paper was performed at the Polymer Competence Center Leoben GmbH (PCCL, Austria) within the framework of the Kplus-program of the Austrian Ministry of Traffic, Innovation and Technology with contributions by *the University of Leoben* and *Borealis Polyolefine*

GmbH. The PCCL is funded by the Austrian Government and the State Governments of Styria and Upper Austria.

References

- [1] E. Parsons, M.C. Boyce, D.M. Parks. An experimental investigation of the large-strain tensile behavior of neat and rubber-toughened polycarbonate. *Polymer* 2004;45:2665.
- [2] Z. Fang, T.J. Wang, H.M. Li. Large tensile deformation behavior of PC/ABS alloy. *Polymer* 2006;47:5174.
- [3] E.M. Parsons, M.C. Boyce, D.M. Parks, M. Weinberg. Three-dimensional large-strain tensile deformation of neat and calcium carbonate-filled high-density polyethylene. *Polymer* 2005;46:2257.
- [4] F. Addiego, A. Dahoun, C. G'Sell, J.M. Hiver. Volume Variation Process of High-Density Polyethylene During Tensile and Creep Tests. *Oil Gas Sci. Technol.* 2006;61:715.
- [5] O.D Almeida, F. Lagattu, J. Brillaud. Analysis by a 3D DIC technique of volumetric deformation gradients: Application to polypropylene/EPR/talc composites. *Composites Part A* 2008;39:1210.
- [6] E. Fauster, P. Schalk. Evaluation and calibration methods for the application of a video-extensometer to tensile testing of polymer materials. *Proc. SPIE* 2005;5679 (187).
- [7] F. Hild, S. Roux. Digital Image Correlation: from Displacement Measurement to Identification of Elastic Properties - a Review. *Strain* 2006;42:69.
- [8] W. Sun, E.L. Dong, M. Xu, B. Luo, X. He. Tensile test of membrane materials using digital image correlation method. *Proc. SPIE* 2007; 6423.
- [9] D.V. Hemelrijck, A. Makris, C. Ramault, E. Lamkanfi, W.V. Paepegem, D. Lecompte. Biaxial testing of fibre-reinforced composite laminates. *Proc I Mech E, Part L* 2008; 222: 1464.
- [10] E. Verhulp, E.V. Rietbergen, R. Huiskes. A three-dimensional digital image correlation technique for strain measurements in microstructures. *J. Biomech.* 2004;37:1313.

-
- [11] M.A. Sutton, J.H. Yan, S. Avril, F. Pierron, S.M. Adeb. Identification of Heterogeneous Constitutive Parameters in a Welded Specimen: Uniform Stress and Virtual Fields Methods for Material Property Estimation. *Exp. Mech.* 2008;48:451.
- [12] H.A. Bruck, G. Fowler, S.K. Gupta, T.M. Valentine. Using Geometric Complexity to Enhance the Interfacial Strength of Heterogeneous Structures Fabricated in a Multi-stage, Multi-piece Molding Process. *Exp. Mech.* 2004;44:261.
- [13] I.M. Ward. *Mechanical Properties of Solid Polymers.* Wiley-Interscience. 1971.
- [14] H.W. Schreier, M.A. Sutton. Systematic errors in digital image correlation due to undermatched subset shape functions. *Exp. Mech.* 2002;42:303.
- [15] H.W. Schreier, J.R. Braasch, M.A. Sutton. Systematic errors in digital image correlation caused by intensity interpolation. *Opt. Eng.* 2000;39:2915.
- [16] Y.F. Sun, H.J. Pang. Study of optimal subset size in digital image correlation of speckle pattern images. *Opt. Lasers Eng.* 2007;45:967.
- [17] B. Pan, H. Xie, Z. Wang, K. Qian, Z. Wang. Study on subset size selection in digital image correlation for speckle patterns. *Opt. Express* 2008;16:7037.
- [18] D. Tscharnuter, M. Jerabek, Z. Major, R.W. Lang. Poisson's ratio of Polypropylene and Polypropylene Compounds in various Strain Histories. To be published.

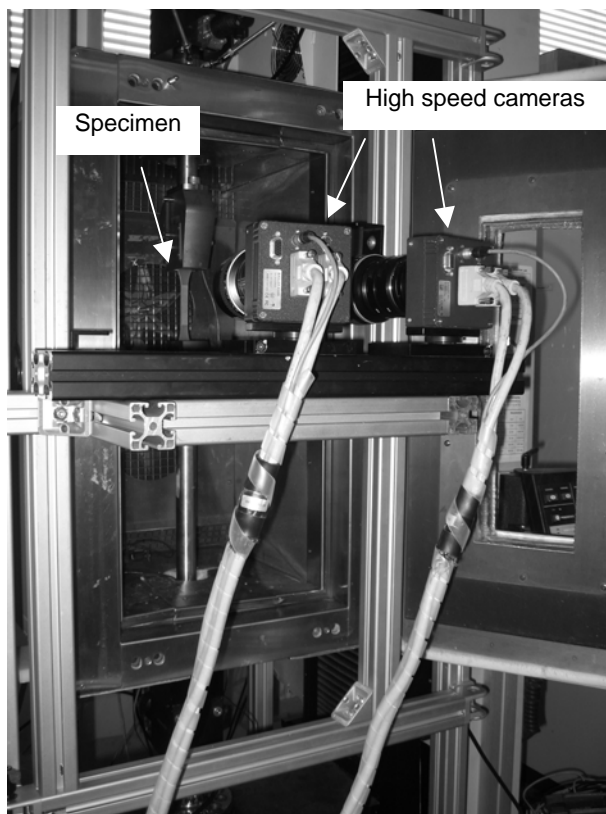


Fig. 1. Picture of the tensile set-up showing the specimen fixed in the grips and the two high speed cameras of the DIC system mounted on the displaceable frame ensuring a fixed relative position of the two cameras and the specimen.

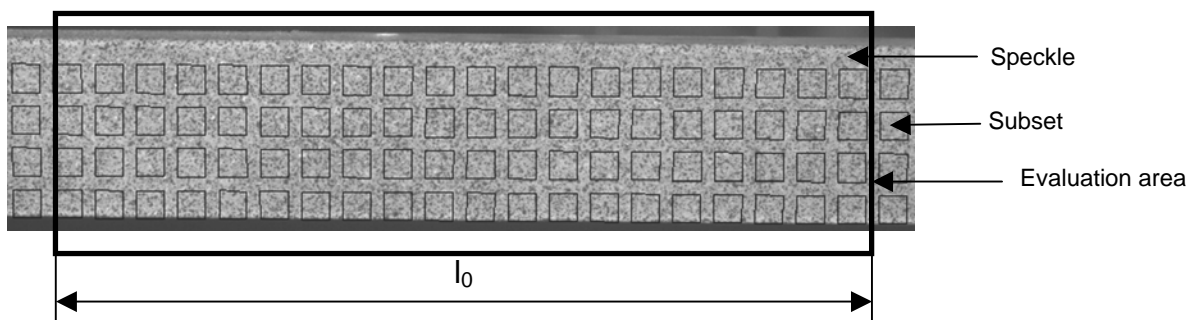


Fig. 2. Measurement range of the specimen illustrating the evaluation area (corresponding to the initial gauge length l_0), the random speckle pattern and the predefined subsets positioned by the software. For illustration purposes, only every second subset is plotted so that subset overlays are not shown.

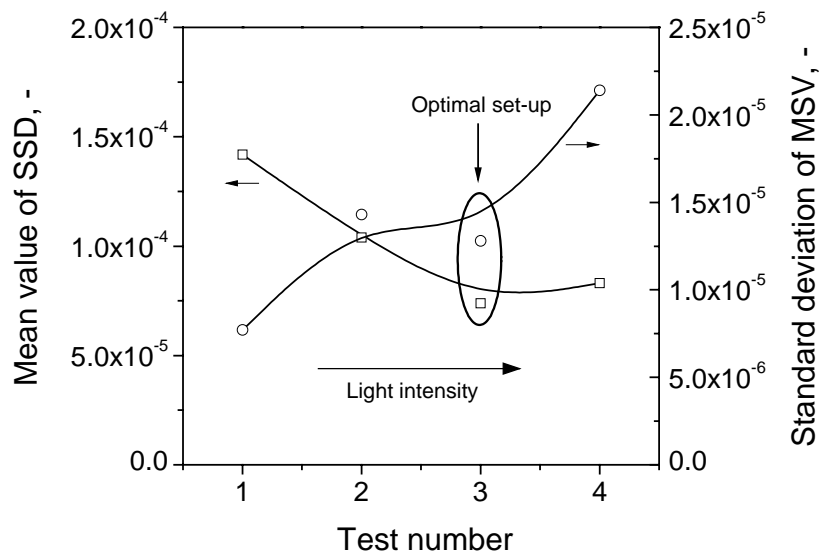


Fig. 3. Effect of light intensity (brightness) on the two quality indicator values SSD and MSV.

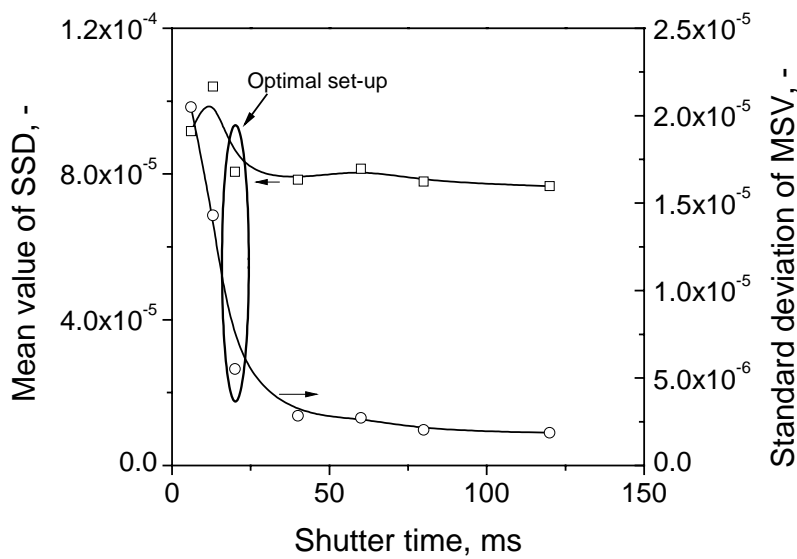


Fig. 4. Effect of shutter time (light exposure) on the two quality indicator values SSD and MSV.

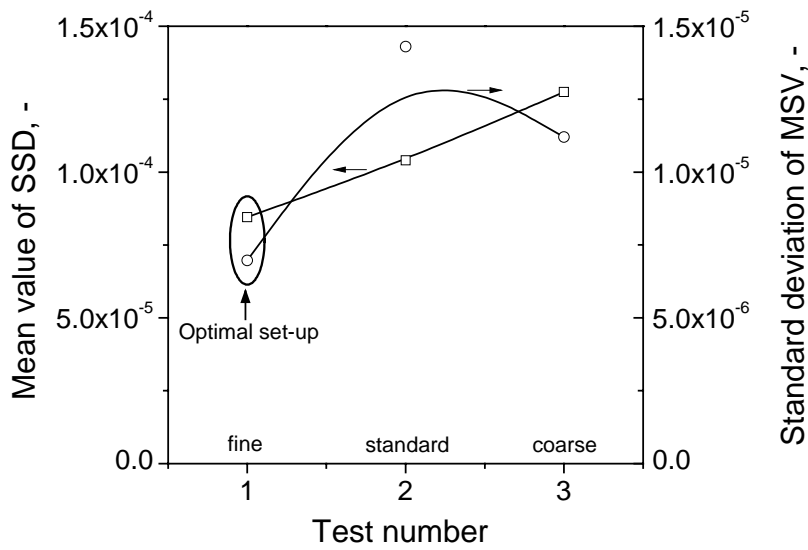


Fig. 5. Effect of speckle pattern structure on the two quality indicator values SSD and MSV.

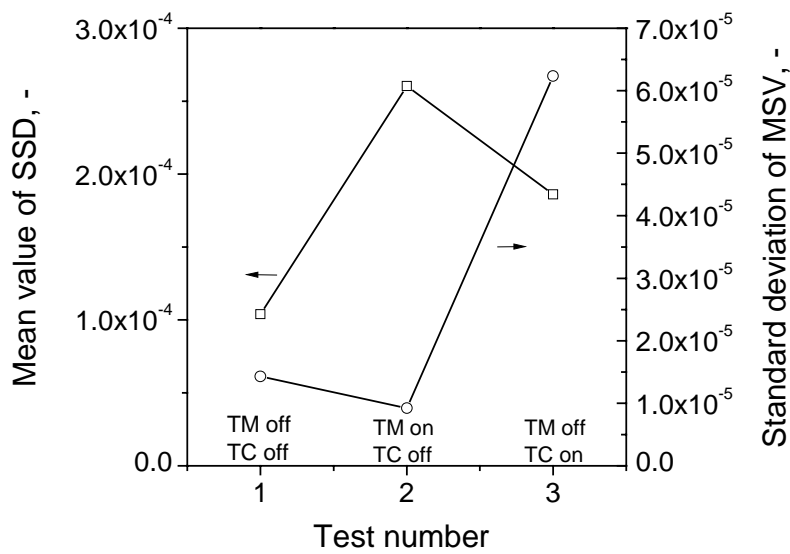


Fig. 6. Effect of operating test machine (TM) or temperature chamber (TC) on the two quality indicator values SSD and MSV.

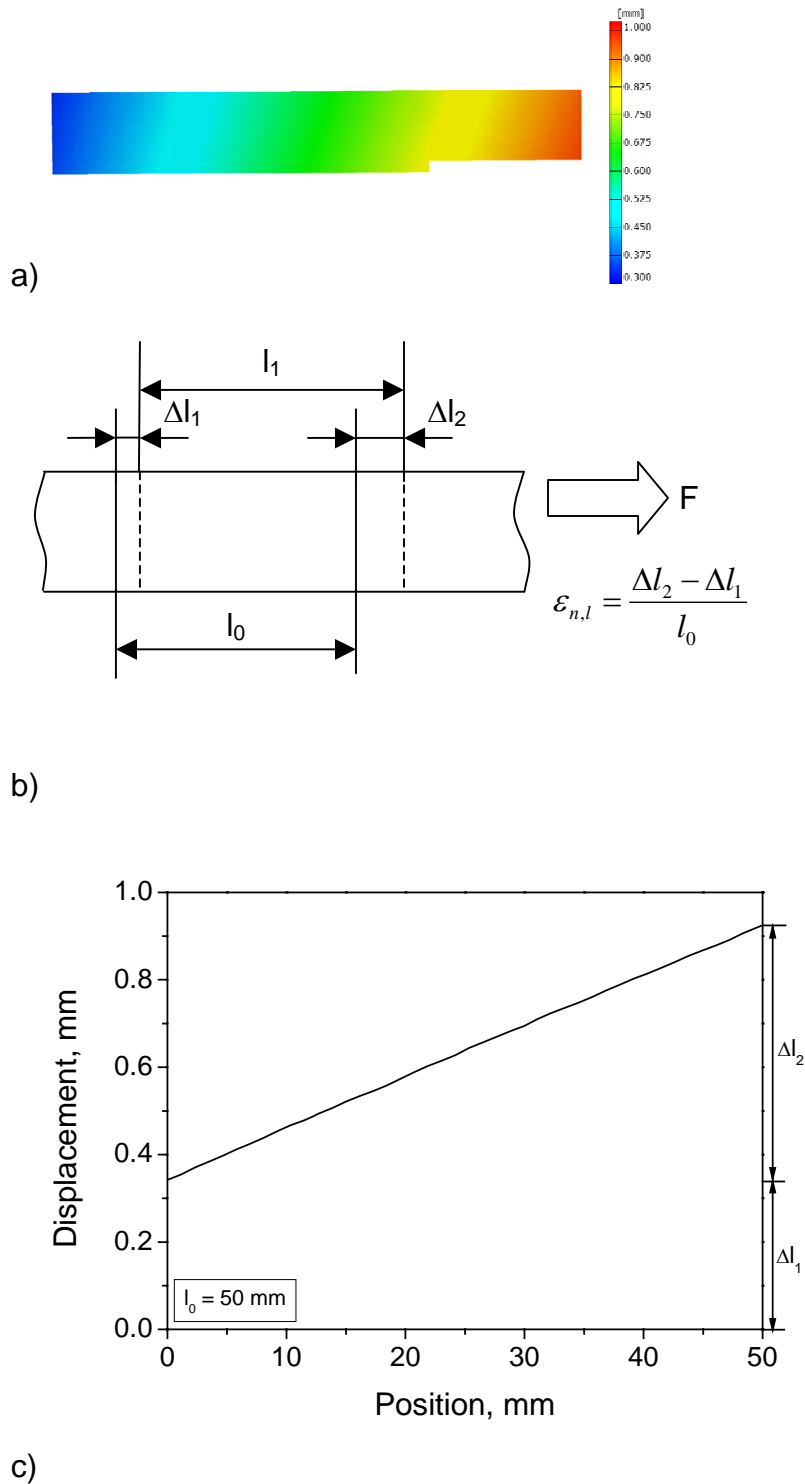


Fig. 7. Example of a displacement measurement result of PP in the small strain regime with the DIC system illustrating the data reduction scheme for the overall average strain $\epsilon_{n,l}$. a) Contour plot of the displacement, b) schematic of the measurement principle and the strain deduction, and c) displacement vs. absolute position on the specimen surface for the contour plot of figure a).

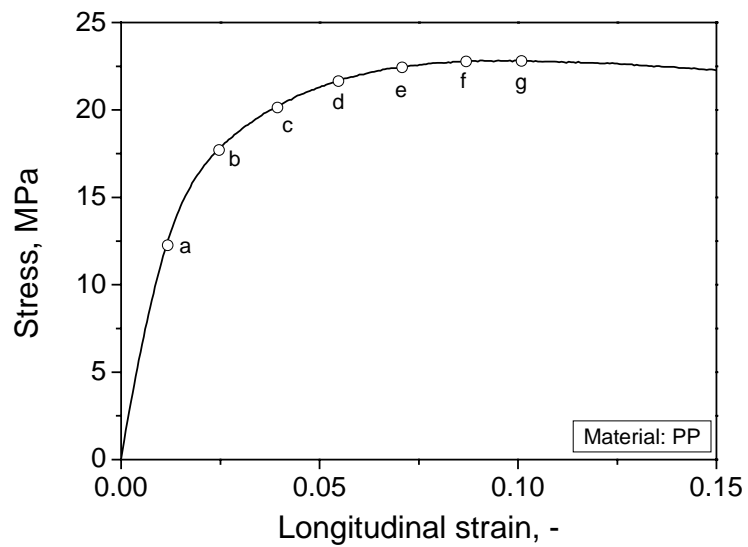


Fig. 8. Stress-strain curve of PP determined using the DIC system indicating the positions a to g taken for the strain contour and distribution plots in Figs. 9 and 10, respectively.

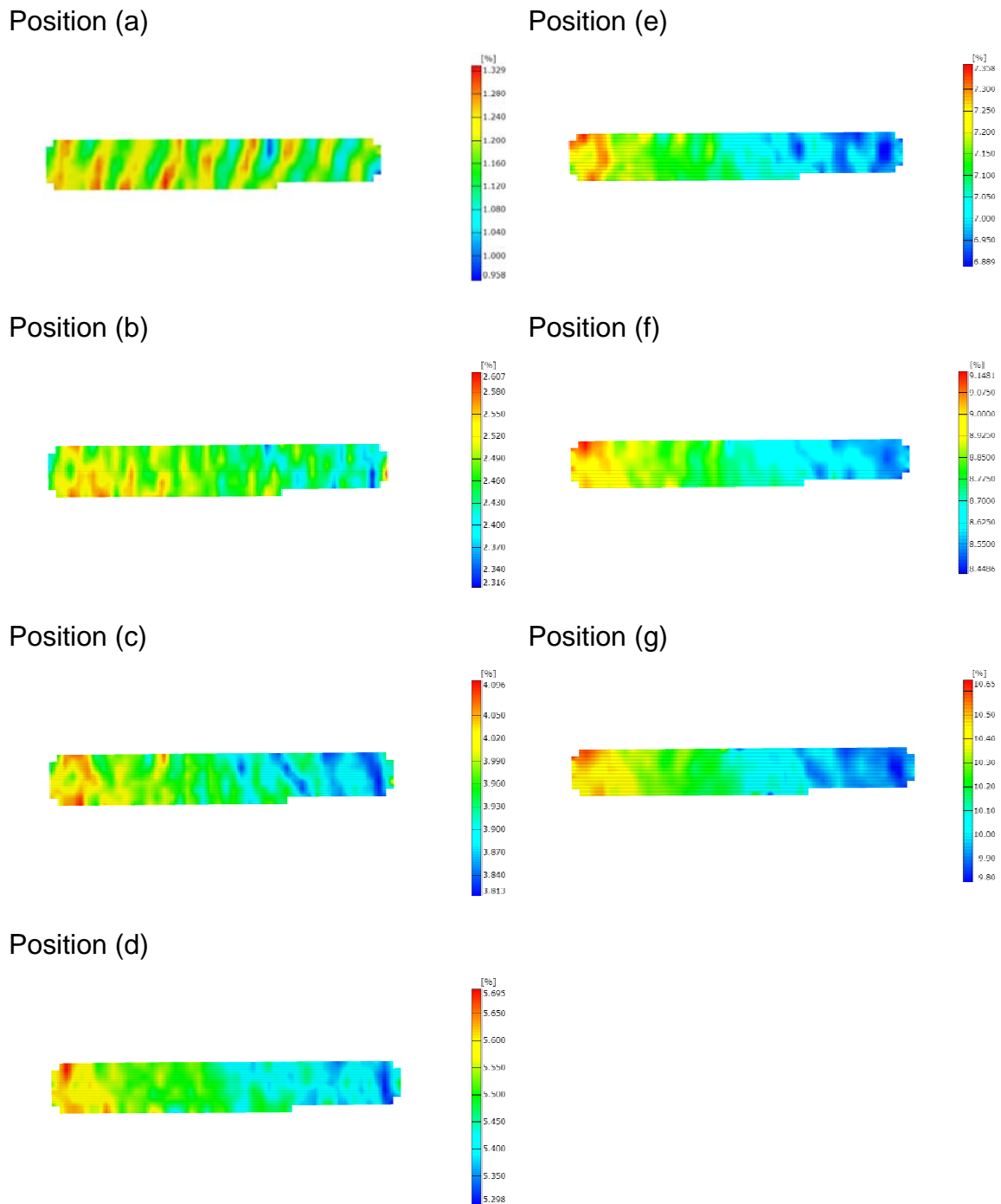


Fig. 9. Strain contour plots of the longitudinal strain during a tensile test of PP in the pre-yield regime up to the onset of yielding for the various deformation levels a to g indicated in Fig. 8.

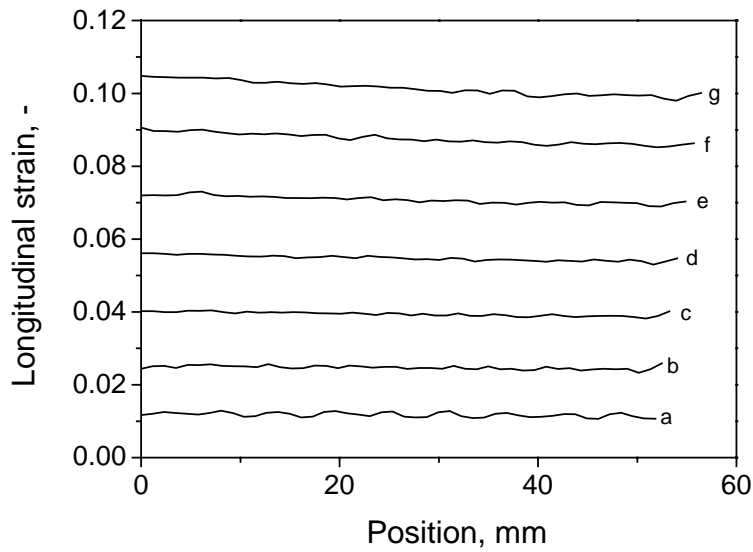


Fig. 10. Strain distribution along the specimen center line for the various deformation levels a to g indicated in Fig. 8.

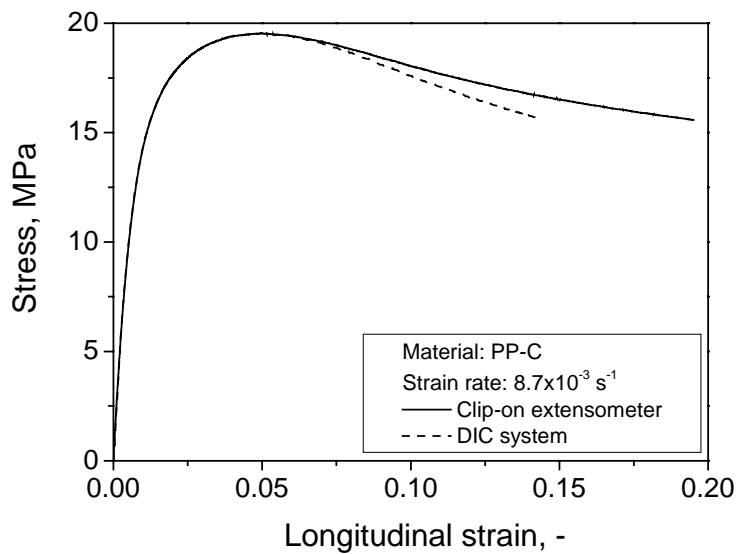


Fig. 11. Stress-strain curve of PP-C comparing the results of measurements of the overall average strain via the DIC system and a mechanical clip-on extensometer.

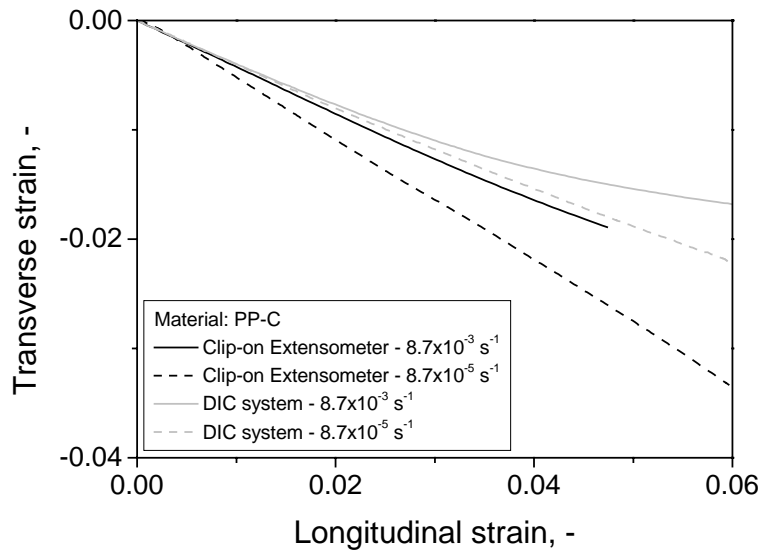


Fig. 12. Transverse strain vs. longitudinal strain curves of PP-C comparing the results of strain measurements using the DIC system and mechanical clip-on extensometers.

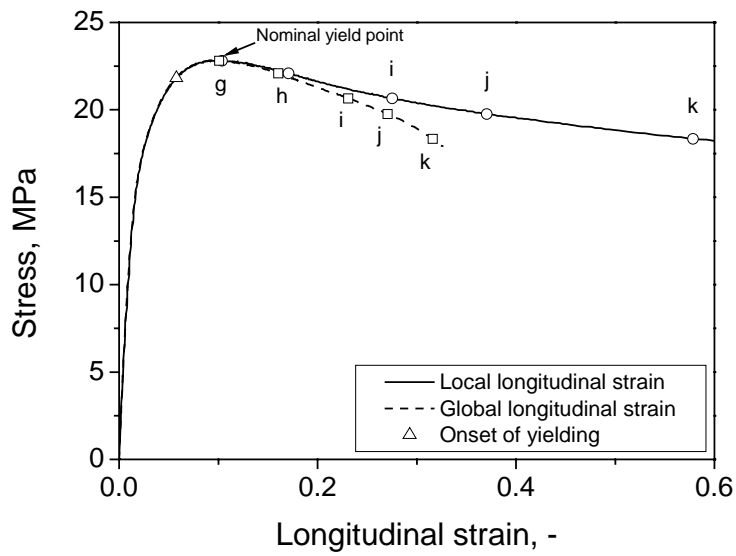


Fig. 13. Stress-strain curves based on local and global strain measurement.

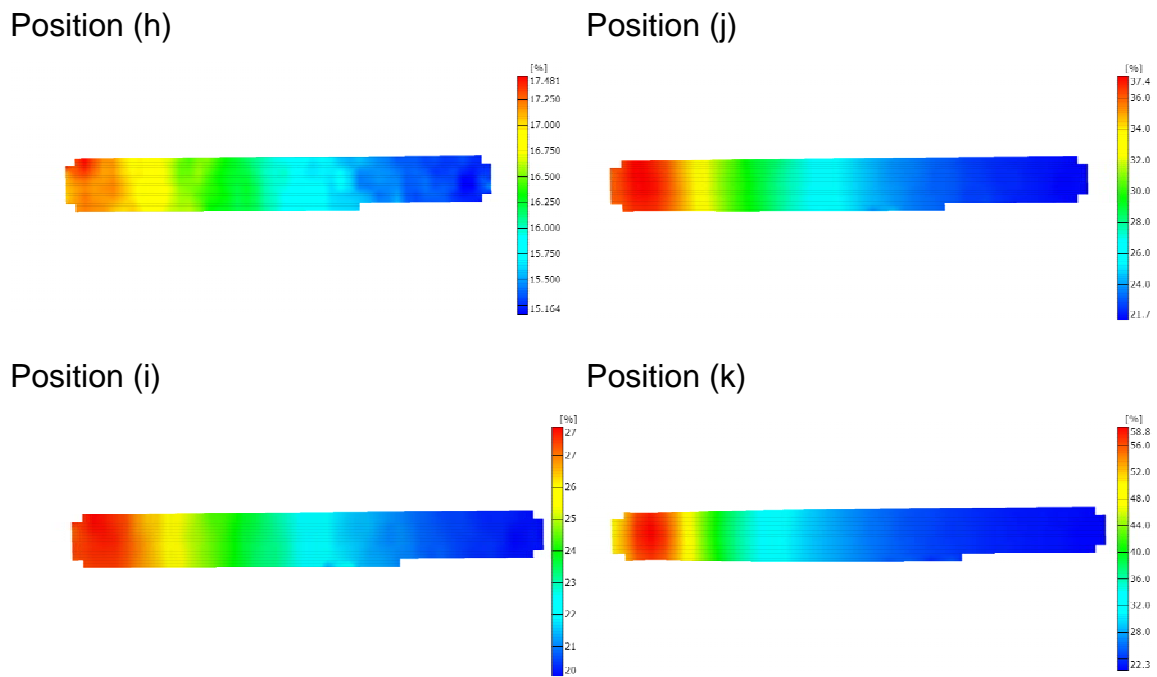


Fig. 14. Contour plots of the longitudinal strain taken at positions indicated in Fig. 16 beyond the yield point.

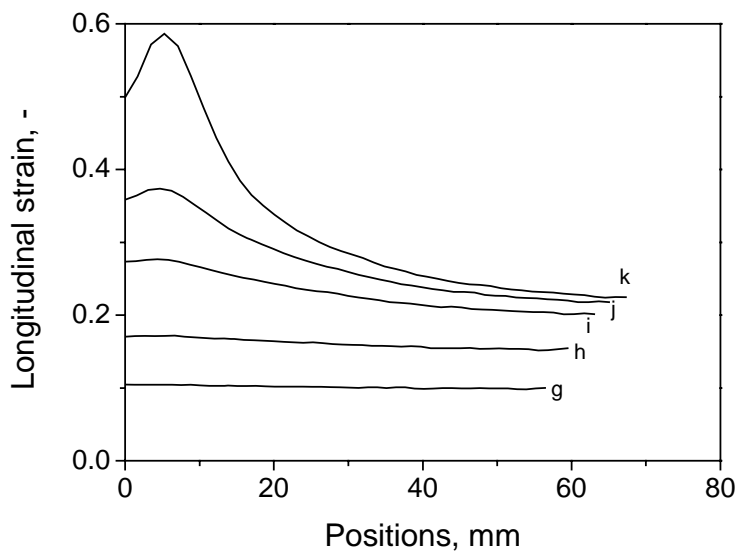


Fig. 15. Sections of the contour plots shown in Figs. 11g and 14 versus the relative position on the specimen.

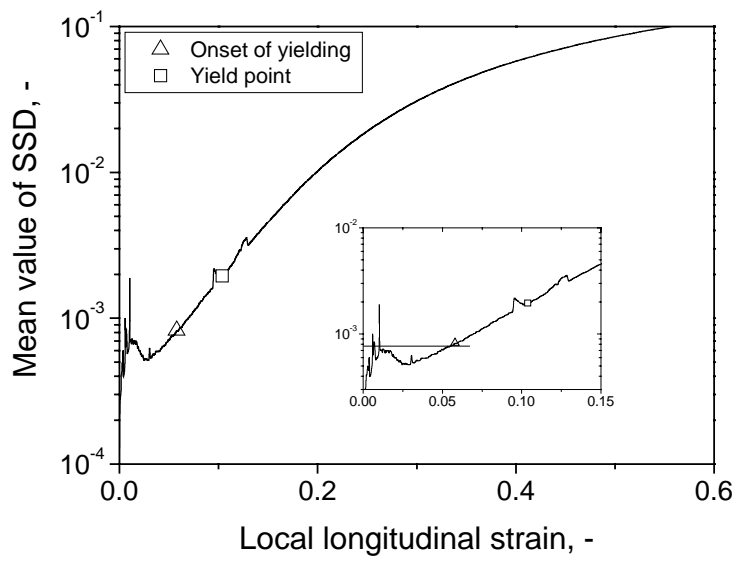


Fig. 16. Mean value of SSD vs. local longitudinal strain, depicting also the onset of yielding and the nominal yield point.

PAPER 2[°]**ADVANCED COMPRESSION TESTING OF POLYMERIC MATERIALS**

M. Jerabek^{a*}, Z. Major^b, R.W. Lang^b

^a Polymer Competence Center Leoben GmbH, Roseggerstrasse 12, 8700 Leoben, Austria

^b Institute of Materials Science and Testing of Plastics, University of Leoben, Franz-Josef-Strasse 18, 8700 Leoben, Austria

ABSTRACT

Several methods for uniaxial, plane strain and multiaxial compression testing were investigated and compared using polypropylene as a model material. An overview of various parameters affecting compression test results is provided with particular emphasis on friction between the specimen and the compression plate. A procedure for the determination of the compressive modulus is introduced and results are shown. To enable the detection of instability associated with friction and barreling and to calculate true stress – true strain curves, the measurement of transverse expansion of the specimen at large strains is necessary. Significant strain softening was observed in the post yield regime for uniaxial compression tests. With increasing confinement levels strain softening was reduced and in some cases strain hardening was observed. For the highest confinement level (approaching hydrostatic compression), plastic deformation was entirely suppressed, with all imposed deformations being reversible, thus making any classification in terms of strain hardening or softening obsolete.

Keywords: Compression test; Confinement level; Multiaxiality; Post yield behavior; Strain softening; Strain hardening; Poisson's ratio; Polypropylene;

[°] Paper is submitted to Polymer Testing

* Corresponding author. Tel.: +43 3842 42962 21; fax: +43 3842 42962 6
E-Mail address: Jerabek@pccl.at

1. INTRODUCTION

Polymeric materials and parts are frequently exposed to loading situations where compressive stresses occur and in many cases are even dominating. These compressive stresses may be either local or global, and they may be of different confinement levels (uniaxial and various degrees of multiaxiality). In terms of the type of loading, they may be monotonic, cyclic or long-term static.

Typical examples of compressive loading in practical applications of plastics include all structural components exposed to direct compressive or bending loads, rollers, gears, damping materials and alike [1]. On a regional and local scale, compressive stresses also play a major role in joint technologies (e.g., screw joints, clamping, fastening), in cutting processes and in tribological applications (i.e., friction, wear and scratch processes) also including fretting fatigue loads [2-5]. Another example for the development of local compressive stresses are polymer matrix composites, in which compressive stresses on a local scale develop around the reinforcing phase, even though the external load applied to the material may be a tensile load [6].

Considering that the behavior of polymeric materials under tension and compression may differ particularly in the yield and post-yield regime [7-9], the need to characterize the compressive behavior of plastics becomes evident. Moreover, the above examples indicate the importance of compressive testing in a comprehensive manner under various loading modes and underline the need for appropriate test methodologies. Last but not least, adequate material data and material laws for compression are especially needed in advanced component design procedures and for structural reliability assessments based on modern simulation tools.

In performing compressive tests, several difficulties are usually encountered. In particular, the contact situation related to the details of load introduction is of prime importance, both in the low and high strain regime. At low strain levels a convex nonlinear force-displacement curve may develop as a result of misalignment of the compression plate and the specimen surface, and to a lesser degree also as a consequence of the microscopic roughness of the two contact surfaces. At higher

strain levels, test set-up misalignment and off-axis loading may cause premature specimen failure by buckling. Finally, friction at the interface between specimen surface and compression plate becomes particularly important at high strain levels and in the post-yield regime, not only leading to a multiaxial stress state in the load introduction region even in uniaxial tests but also causing specimen barreling.

The objective of this paper is to describe a set of experimental procedures that allow for a comprehensive characterization of the compressive stress-strain behavior of plastics including uniaxial and multiaxial loading of various confinement levels. In addition to details of the test set-up, information on proper test and data reduction procedures is provided. The experiments were performed using polypropylene (PP) as a model material.

2. EXPERIMENTAL

2.1. Test Categories, Specimen Configurations and Material

To cover various degrees of confinement, three categories of tests were performed including uniaxial compression (two types of test set-up), plane strain compression (two types of test set-up) and fully confined compression.

Due to the higher stability and axis symmetry and in order to achieve comparability between the uniaxial and the fully confined test, a cylindrical specimen geometry was selected and used for these two test categories. For the plane strain compressive tests, rectangular plates were employed. Further details as to the specimen geometries are described in the respective sections on the test set-up below.

The material used in this study as a model material was a development grade polypropylene homopolymer PP(H), manufactured and delivered by Borealis Polyolefine GmbH (Linz, A) as injection molded plates, out of which all specimens were machined. The identical material was extensively characterized under monotonic tensile loading and in compressive relaxation tests [10, 11].

2.2. Testing and Test Instrumentation

All tests were carried out on an electro-mechanical driven universal testing machine of the type Instron 5500 (Instron LTD; High Wycombe, UK). Depending on the specimen length, the tests were performed at a testing rate ranging from 0.069 mm/s to 0.173 mm/s, corresponding to a local strain rate of $8.7 \times 10^{-4} \text{ s}^{-1}$, and under standardized climate conditions (23 °C / 50 % r.h.). Unless prior failure occurred, all tests were performed up to a compressive strain of 0.5.

In order to perform compressive tests on a universal testing machine, several modifications are necessary to ensure stable measurement conditions. To avoid wobbling of the loading pins around the center axis two options exist. One is to make use of a so-called reversal cage to apply compressive loads on the specimen with the testing machine itself working under tension [12]. While this configuration suppresses any misalignment from the mechanical set-up, it is disadvantageous in terms of the available working space and sight to the specimen, particularly when working with optical measurement devices to obtain transverse strain and full-field strain information. Another option, developed and applied in all test set-ups of this study, is the utilization of a special compression tool with aligning bars at each corner (Fig. 1^{*}). Due to the four ball linings and highly accurate aligning bars, a precise and reproducible movement of the upper and lower compression plate is guaranteed and any transverse forces and moments are avoided. As to the accurate determination of axial strain, an LVDT mounted between the two compression plates was used.

2.3. Test set-up and Data Reduction

2.3.1. Uniaxial Compression

The uniaxial compression test configuration with the cylindrical specimen between the two plates is shown in Fig.1. The specimen diameter d was 8 mm, the length l of the most frequently used standard specimen in this study was 12 mm, resulting in a l/d ratio of 1.5. This specimen geometry was chosen taking the expected

* All figures of this paper are collected at the end of the text.

failure mode according to [13] into account: buckling for $l/d > 5$, shear failure for $2.5 < l/d < 5$, and double barreling for $2 < l/d < 2.5$. Also according to [13], short specimens with $l/d < 1.5$ are strongly affected by friction. To study effects of friction, a series of specimens with an l/d ratio varying from 1 to 2 was prepared.

Even when highly polished plates and a PTFE lubricant are used, friction is evident in compression testing and influences the test results particularly at large strains. In order to reduce the influence of friction, the following measures were taken and evaluated:

- First, instead of utilizing a PTFE lubricant between the specimen and the compression plates, a direct method to solve the frictional problem is to use a PTFE tape. However, due to the compliance of the PTFE tape, the simultaneous measurement of the compressive modulus on the same specimen is not possible. In our investigation the equivalent PTFE tape of the type 3M-5480 (3M; St. Paul, MN, USA) used also in [14] was selected. The adhesive side of this single-side adhesive tape was positioned to face the specimen.
- The second approach applied was an indirect method to correct for frictional effects and was proposed originally by Cook and Larke [15]. Using a PTFE lubricant between specimen and compression plates, specimens with different l/d ratios were tested up to 50 % longitudinal strain. As frictional effects should decrease with increasing l/d ratios [15], a “friction-corrected” stress-strain curve may be obtained by extrapolating data obtained from various l/d ratios to $l/d = \infty$ (corresponding to $d/l = 0$ in a d/l diagram).
- The third approach followed to correct for frictional effects was suggested by Siebel [16-19] applying the so-called cone compression test, Fig. 2. In this test set-up the cone angle α is defined so that the lateral component of the longitudinal force becomes equal to the frictional force acting in the plane of the cone/specimen interface. Using the relationship $\tan \alpha = \mu$, where μ is the coefficient of friction, a value of 8° is derived for the cone angle α . For the material combination used, an “effective” average value for

μ was determined using a universal microtribometer (UMT2, Center for Tribology Inc.; Campbell, CA, USA), accounting for the acting normal stresses, the selected test temperature and the sliding speed. A disadvantage of this method is that neither the strain nor the strain rate are uniformly distributed along the specimen due to the diverse specimen length in the center and at the outer surface. Thus, by applying the displacement technique described above, the average of the maximum and minimum specimen length was taken for the strain calculation.

In addition to the measurement of the longitudinal force and the local displacement, simultaneous transverse strain measurements were performed in all experiments using a video extensometer system described in [20]. Hence, both nominal and true stress-strain relationships could be derived using the following equations:

The nominal longitudinal strain, $\varepsilon_{n,l}$, and the nominal transverse strain $\varepsilon_{n,t}$, are given by

$$\varepsilon_{n,l} = \frac{l - l_0}{l_0} \quad (1)$$

and

$$\varepsilon_{n,t} = \frac{d - d_0}{d} \quad (2)$$

where l_0 and d_0 are the original and l and d the actual length and width of the specimen, respectively. The true longitudinal strain, $\varepsilon_{t,l}$, and true transverse strain, $\varepsilon_{t,t}$ are given by

$$\varepsilon_{t,l} = \ln(1 + \varepsilon_{n,l}) \quad (3)$$

and

$$\varepsilon_{t,t} = \ln(1 + \varepsilon_{n,t}) \quad (4)$$

Note that the maximum nominal longitudinal strain in compression is -100 %, whereas the true strain at -100 % nominal strain is minus infinite, which implies that only true strain is symmetrical in tension and compression.

The nominal stress, σ_n , and true stress, σ_t , are given by

$$\sigma_n = \frac{F}{A_0} \quad (5)$$

and

$$\sigma_t = \frac{F}{A_0(1 - \varepsilon_{n,l} \nu_n)} = \frac{F}{A} \quad (6)$$

in which F is the force, A_0 the initial and A the actual cross-section of the specimen. The nominal Poisson's ratio, ν_n , is given as

$$\nu_n = -\frac{\varepsilon_{n,t}}{\varepsilon_{n,l}} \quad (7)$$

The true Poisson's ratio is calculated taking the true longitudinal and transverse strains according to

$$\nu_t = -\frac{\varepsilon_{t,t}}{\varepsilon_{t,l}} \quad (8)$$

For large strains, there is a significant difference between the nominal and the true strain. As the true axial strain in compression is larger than the nominal strain and the true transverse strain is smaller than the nominal strain, true Poisson's ratio values in the yield and post-yield regime can only be calculated via the true transverse and true axial strains, resulting in significant lower Poisson's ratio values than those obtained by nominal strains.

According to ISO 604 [21], values for the compressive modulus are defined for the strain range of 0.0005-0.0025. For a 12 mm long specimen this implies accurate deformation measurements for the first 30 μm , so that any initial misfits may result in a significant error of the compressive modulus value calculated. To provide the required accuracy, the surfaces of the specimens were polished to reduce the effect of friction as well as to ensure outer specimen surfaces perpendicular to the specimen axis.

2.3.2. Plane strain compression test

Two plane strain compression test methods were implemented and applied. Test method 1 (Fig. 3; “soft constraint”) consists of two compression dies of a width, w , of 6.50 mm and a length, l , of 50 mm. To avoid damaging of the material at the die edges, the radius of these edges was machined to 0.5 mm.

Specimens of 4 mm thickness, t , and 40 mm width, l , were cut out of injection-molded plates. These dimensions are in agreement to proposals elsewhere for plane strain conditions ($t/w > 4$ and $t \approx w$) [22-24]. A plane strain state is ensured by the undeformed material of the specimen outside the dies.

The plane strain compression test method 2 (“hard constraint”) was proposed in [25]. In this case the specimen is clamped between the two plates as displayed in Fig. 4. In this set-up the plane strain conditions are a consequence of the die shape and not of the specimen configuration (i.e., hardly any transverse strain is developed). A radius of 0.5 for the edges of the dies was again machined in order to avoid material damage at the die edges. The specimen dimensions were 20 x 10 x 4 mm, thus exhibiting the same thickness as the specimens for the plane strain test method 1 described above.

For both of these test set-ups, the nominal longitudinal strain, $\varepsilon_{n,l}$, is

$$\varepsilon_{n,l} = \frac{t - t_0}{t_0} \quad (9)$$

where t is the actual and t_0 the initial thickness of the specimen. True longitudinal strain was calculated according to eq. (3). As the area under load remains constant during testing, these plane strain configurations directly provide true stress values:

$$\sigma_t = \frac{F}{A} = \frac{F}{wl} \quad (10)$$

2.3.3. Confined compression test

The multiaxial confined compression test method used for this study corresponds to a method described in detail by Ravi-Chandar et al. [26, 27]. The test set-up used is shown in Fig. 5 along with a schematic illustration. The specimen is surrounded by a confining cylinder, which restrains the free lateral expansion

during loading without prohibiting it totally. Assuming a homogeneous deformation of the cylindrical specimen and a perfect fit between the specimen and the cylinder, the stress and strain field within the specimen and cylinder can be calculated via the Lamé solution for plane stress [28]. The measured values include the longitudinal force and displacement, and the hoop strain of the confining cylinder via strain gauges mounted on the outer cylinder surface. By varying the thickness of the cylinder or by using a cylinder material of different modulus, the stress state can be changed and adapted. Of special importance, this configuration allows for an inelastic as well as a viscoelastic characterization of polymers without a priori knowing the constitutive equation [26,29]. Furthermore, while in uniaxial compression testing an inhomogeneous specimen deformation may occur at high strains, in confined compression the strain localization is significantly reduced.

In this test set-up, cylindrical specimens of 20 mm in length, l , and of 10 mm in diameter, d , were used.

The maximum longitudinal strain is limited by the material that is squeezed out between the loading pin and the confining cylinder. In pre-tests, stopped at different strain levels, it was found that longitudinal strains below 20 % avoid material damage at the surface of the specimen by squeezed-out. Hence, all tests were stopped below 20 % longitudinal strain.

Confining cylinders of various diameters, D , were produced using polypropylene and steel. Outer diameters of 12 mm, 15 mm, 20 mm, 30 mm and 42 mm were used for polypropylene cylinders; the steel cylinder had a diameter of 28.5 mm. The moduli were determined to be 1.600 MPa and 210.000 MPa for polypropylene and steel, respectively.

Nominal and true longitudinal strain values were calculated by means of eqs. 2 and 3, respectively. As the area under load for this configuration remains constant, true stresses correspond to nominal stresses and are thus given by

$$\sigma_t = \frac{F}{A_0} = \frac{F}{r^2 \pi} \quad (11)$$

where r is the radius of the specimen.

3. RESULTS AND DISCUSSION

3.1. Small strain behavior in uniaxial compression

The two characteristic parameters describing the behavior of isotropic materials in the small strain regime are effective values of modulus and Poisson's ratio. In this context it is well-known that an accurate determination of these values under compression is significantly more complicated than under tension. For this reason only few reports on small strain compressive data for plastics are available [30].

As pointed out above, to ensure proper compression loading conditions, accurate specimen preparation, a perfect fit between the specimen and the compression plates and proper alignment of the specimen and load introduction devices are crucial. And yet, even when complying to these test quality requirements, the reduction of compressive modulus values according to ISO 604 for compressive testing and Poisson's ratio values analogous to ISO 527 for tensile testing in the strain range of 0.0005-0.0025 raises problems.

Small strain compressive data in the strain range up to 0.02 are shown in Fig. 6 in terms of diagrams depicting nominal longitudinal stress (Fig. 6a) and "apparent" compressive modulus (stress-strain derivative) (Fig. 6b) vs. longitudinal strain in both cases. The "apparent" compressive modulus values in Fig. 6b were obtained by first smoothing of the experimental data in Fig. 6a using a cubic spline and then calculating the derivative $d\sigma/d\varepsilon$. These apparent modulus values are seen to initially increase from about 500 MPa at just above 0 % strain to 2.000 MPa at about 0.8 % strain and then again decrease at higher strain levels. While the initial increase in the apparent modulus is related to deficiencies of load introduction in this range, the decrease at higher strain levels is due to viscoelastic nonlinearity.

Applying the above procedure, such peak compressive modulus values were determined for specimens of various l/d ratios and are plotted in Fig. 7. According to a proposal by Cook and Larke [15] these data were extrapolated to $d/l=0$, thus obtaining an "effective" value of the compressive modulus, which for the specific PP material investigated turned out to be about 2.350 MPa. For comparison, in tensile tests according to ISO 527 with the same material and at an equivalent strain rate, a tensile modulus of about 1.850 MPa was determined.

In Fig. 8 the nominal transverse strain (Fig. 8a) and the nominal Poisson's ratio (Fig. 8b) are plotted vs. the nominal longitudinal strain. At very low values of longitudinal strain, no transverse strain was detected thus, resulting in $\nu=0$ in this regime. Peak modulus equivalent Poisson's ratios may be derived at the same strain value of 0.8 % at which the peak in the apparent modulus in Fig. 6b was found. For the material investigated a value for ν of about 0.40 ± 0.03 was obtained (Fig. 8b). However, as the data scatter for ν with regard to various d/l ratios truncates any effects of specimen geometry, the deduction of a peak equivalent effective Poisson's ratio is not feasible.

3.2. Large strain behavior in uniaxial compression

A collection of photographs depicting the specimen appearance at various nominal strain levels for three uniaxial compression methods is shown in Fig. 9. Starting at higher strain levels (above about 10 %) significant differences in the lateral specimen deformation are observed. While in the case of the straight-forward uniaxial compression test (without a PTFE tape) significant specimen barreling takes place with increasing compressive strain, such an effect can hardly be detected when applying PTFE tapes to reduce friction between the specimen and the compression plates. As expected [19], the opposite was found for the cone compression test where the specimen is seen to deform in a concave manner with increasing strain thus leading to a reduced specimen cross-section in the specimen center.

The corresponding nominal stress-strain curves for the three types of uniaxial compressive tests are shown Fig. 10. While at small strain values up to about 5 % hardly any difference can be noticed, some differences in the nominal stress-strain response are visible at higher strain levels (i.e., yield and post-yield regime). Interestingly, the test with the PTFE tape exhibits the lowest stress values in the yield regime due to the friction reduction, while resulting in the highest nominal stresses at around 40 % nominal strain. The latter effect is probably due to the rather homogenous lateral deformation along the specimen length even at high post-yield deformations. Comparing the results of the cone compression test to the other two approaches and considering the necessity to optimize the cone angle

with regard to the coefficient of friction of the material combination used (compression plate and specimen; see previous section), no particular advantages of the cone compression test become apparent.

Nominal compressive stress-strain curves for specimens of different d/l ratios without using a PTFE tape for friction reduction are shown in Fig. 11 along with an extrapolated curve for $d/l=0$. As the contribution of frictional effects is considered to be reduced with decreasing d/l ratio, the extrapolated curve for $d/l=0$ is compared to the curve obtained by testing a finite specimen ($l/d=1.5$) with a PTFE tape in Fig. 12. While the differences in post-yield regime have yet to be elucidated further, differences in the relative contributions of friction at the specimen-compression plate interface and of barreling between finite ($l/d=1.5$ with PTFE) and quasi-infinite specimens ($d/l=0$ without PTFE) may play a role.

Curves of Poisson's ratio vs. longitudinal strain are plotted in Figs. 13 and 14 in terms of nominal and true values, respectively. While for compressive tests without PTFE, different measures of transverse strain obtained from video extensometer results were used for data reduction (i.e., maximum transverse strain at the specimen mid-section where barreling leads to the highest cross-section; minimum transverse strain at the specimen end where friction leads to the smallest cross-section; average transverse strain at half the distance between specimen end and specimen mid-section), only one measure of transverse strain was used for tests with PTFE as the lateral deformation was rather homogeneous over the entire test range. Of major importance, the results in Figs. 13 and 14 indicate that the frequently made assumption by many designers of a value of 0.5 for Poisson's ratio in the yield and post-yield regime may be erroneous [31, 32]. As in tensile testing, $\nu=0.5$ in compressive testing also implies deformation under constant volume. However, opposite to tensile testing, in compressive testing $\nu<0.5$ and $\nu>0.5$ imply volume decrease and volume increase, respectively. From the various curves depicted in Figs. 14 and 15, due to the overall homogeneous lateral deformation the one for the tests with PTFE in our opinion is the most plausible. Nevertheless, the other curves are depicted to indicate the wide range of Poisson's ratio values that may be deduced from such tests depending on the test procedure and the selection of a position to measure transverse strain. Paying

attention again to the true Poisson's ratio curve for the test with PTFE in Fig. 14, it may be noticed that the Poisson's ratio values in the yield and post-yield regime increase from about 0.43 at a true longitudinal strain of about 10 % to 0.50 at a true longitudinal strain of about 30 % up to 0.54 at 60 % strain. From 10 % to 30 % true strain, the volume decreases may be related to hydrostatic compaction, at least initially, and then to molecular rearrangements perhaps in the amorphous regime. The volume increase in the irreversible deformation regime beyond 30 % true compressive strain implies molecular and morphological restructuring processes of a different kind, possibly including partial destruction of crystallites (i.e., reduction of the degree of crystallinity and decrease in density). Both of these hypotheses need to be studied in future investigations.

Based on the quantitative results in Fig. 14, various true stress-true strain curves were deduced and are plotted in Fig. 15, again indicating the range of behavior to be expected depending on the test procedure and the selection of a position to measure transverse strain. The most plausible experimental true stress-strain curve for the test using PTFE for friction reduction is compared to further true stress-strain curves in Fig. 16. In one instance, using the data of the test with PTFE, however, by assuming a constant Poisson's ratio of 0.5 are shown. In the other case data for a test without PTFE again with the assumption of $\nu=0.5$ are depicted. These diagrams illustrate the variation of true stress-strain data between experiment based and assumption based ($\nu=0.5$) approaches.

3.3. Large strain behavior in multiaxial compression

True stress-strain curves were generated according to two plane strain compression methods described in section 2.3.2. and are compared in Fig. 17. The differences in the two curves in the pre-yield regime are possibly again related at least partly to load introduction deficiencies. In the yield and post-yield regime, in terms of the shape of the curves a similar behavior was found for both test methods, exhibiting some tendency for strain softening just after the yield point followed by subsequent strain hardening. However, as expected, test method 2 ("hard constraint") clearly led to higher stress levels, which is in agreement to the overall higher constraint level of this test configuration.

A further increase in the constraint level was achieved in the confined compression test methods, the results of which are shown for various confinement levels (different D/d ratios and PP vs. steel as cylinder material) again as true stress-strain diagrams in Fig. 18. When using PP cylinders of various diameters as confinement, the stress-strain diagrams in the yield and post-yield regime are shifted towards higher stress levels with increasing constraint (i.e., increasing D/d ratios). While no strain softening is observed for any of the D/d ratios, the tendency for strain hardening increases with higher constraint. When using a steel cylinder as confinement element, particularly high hydrostatic stresses may be generated in the specimen. The true stress-strain curve for this method depicted also in Fig. 18 is fundamentally different to those obtained with PP cylinders and reveals no signs of yielding up to a longitudinal stress of 300 MPa (corresponding to a hydrostatic stress of 200 MPa). In fact, even for axial stresses of more than 600 MPa (equivalent to a hydrostatic stress of 400 MPa), all deformations imposed on to the specimen turned out to be fully reversible.

3.4. Comparison of uniaxial and multiaxial test methods

In Fig. 19 the true stress-strain behavior of PP is compared for uniaxial compression and plane strain compression (method 2). Not surprisingly, the true yield stress increases with the level of constraint. The post-yield regime in the case of uniaxial compression is characterized by strain softening up to the highest strain level investigated. In contrast, following a slight tendency of strain softening just beyond the yield point, strain hardening is observed in the post-yield regime under plane strain compression. The morphological causes of this different behavior need yet to be investigated.

Finally, true stress-strain curves for the entire range of confinement levels investigated are depicted in Fig. 20. This diagram emphasizes the importance of characterizing polymeric materials under compression by applying proper constraint conditions and illustrates the wide range of compression behavior for PP, perhaps not untypical for plastics in general.

4. SUMMARY AND CONCLUSIONS

The objective of this paper was to develop, implement and compare a variety of compressive test methods and procedures for plastics covering a wide range of confinement levels (from uniaxial to fully confined compression). In total 5 test methodologies along with various data reduction procedures were investigated, using PP as a model material.

Applying various measures to reduce effects of load introduction deficiencies in uniaxial compression (specimen with various l/d ratios, without or with PTFE tape for friction control, cone loading device) to characterize the pre-yield regime, the use of cylindrical specimens without PTFE tape is suggested, and a proper procedure for data reduction to determine modulus values has been proposed based on a maximum slope definition. In the yield and post-yield regime, best results have been achieved using the same specimen configuration, however, with PTFE tape application for friction reduction.

In terms of yield and post-yield behavior, vast differences in the true stress-strain behavior were determined depending on the degree of confinement. While PP in uniaxial compression exhibits significant strain softening in the post-yield regime, this tendency was reduced (plane strain compression) and then reverted to strain hardening with increasing confinement level. For the fully confined test condition, using a steel cylinder as confinement, no signs of plastic deformation up to a true longitudinal stress of 600 MPa were detected. The wide range of compressive behavior found depending on the confinement level, emphasizes the need for a proper characterization of plastics under compressive loading conditions taking various constraint conditions into account.

Acknowledgements

The research work of this paper was performed at the Polymer Competence Center Leoben GmbH (PCCL, Austria) within the framework of the Kplus-program of the Austrian Ministry of Traffic, Innovation and Technology with contributions by *the University of Leoben* and *Borealis Polyolefine GmbH*. The PCCL is funded by the Austrian Government and the State Governments of Styria and Upper Austria.

References

- [1] M. Berer. Charakterisierung und Simulation des Verformungsverhaltens von Kunststoffrollen aus POM und PEEK. Diploma Thesis. Leoben, 2007.
- [2] D. Stahlberg, P. Junestam, M. Johansson, E.K. Gamstedt. Relaxation properties of particle filled coatings: Experimental study and modelling of a screw joint. *Prog. Org. Coat.* 2006; 55:112.
- [3] M.C. Dubourg, A. Chateauminois, B. Villechaise. In situ analysis and modelling of crack initiation and propagation within model fretting contacts using polymer materials. *Tribol. Int.* 2003; 36:109.
- [4] D.K. Baek, M.M. Khonsari. Fretting behavior of a rubber coating: Friction characteristics of rubber debris. *Wear* 2006; 261:1114.
- [5] N.K. Myshkin, M.I. Petrokovets, A.V. Kovalev. Tribology of polymers: Adhesion, friction, wear, and mass transfer. *Tribol. Int.* 2005; 38:910.
- [6] P.A. Kakavas, D.P.N. Kontoni. Numerical investigation of the stress field of particulate reinforced polymeric composites subjected to tension. *Int. J. Numer. Methods Eng.* 2006; 65:1145.
- [7] K.D. Pae. The macroscopic yielding behavior of polymers in multiaxial stress fields. *J. Mater. Sci.* 1977; 12: 1209.
- [8] J.A. Sauer, K.D. Pae. The flow of solid polymers under high pressure. *Colloid. Polym. Sci.* 1974; 252:680.
- [9] R. Quinson, J. Perez, M. Rink, A. Pavan. Yield criteria for amorphous glassy polymers. *J. Mater. Sci.* 1997; 32:1371.
- [10] M. Jerabek, Z. Major, B. Pukánszky, R.W. Lang. Micromechanical Deformation Mechanisms and Modeling of Particulate Filled Polypropylene Composites. To be published.
- [11] M. Jerabek, D. Tscharnuter, Z. Major, K. Ravi-Chandar, R. W. Lang. Relaxation behavior of neat and particulate filled polypropylene in uniaxial and multiaxial compression. To be published.
- [12] R. P. Brown. Handbook of plastics test methods. Longman, Scientific & Technical. 1984.

- [13] H. A. Kuhn. Mechanical testing and evaluation. Uniaxial compression testing. ASM handbook, Vol. 8.
- [14] E. T. J. Klompen. Mechanical properties of solid polymers – Constitutive modeling of long and short term behaviour. Technical University Eindhoven. 2005.
- [15] M. Cook, E. C. Larke. Resistance of copper and copper alloys to homogeneous deformation in compression. J. Inst. Metals 1945; 71:371.
- [16] E. Siebel, A. Pomp. Die Ermittlung der Formänderungsarbeit von Metallen durch den Stauchversuch. Mitteilungen Kaiser – Wilhelm Inst. für Eisenforschung 1927; 9:157.
- [17] M. Yoshizawa, H. Ohsawa. Evaluation of strain-rate sensitivity in superplastic compressive deformation. J. Mater. Process. Manu. 1997; 68:206.
- [18] E. Siebel. Die Prüfung der metallischen Werkstoffe. 2. Band. Springer Verlag, 1955.
- [19] R. Taprogge, H.-D. Kuske, E. Schmachtenberg, T. Krumholz. Bestimmung des Verformungs- und Versagensverhaltens von Kunststoffen unter einachsiger Druckbeanspruchung – Prüftechnik und zulässige Beanspruchungen. Kunststoffe 2003; 06:44.
- [20] E. Fauster, P. Schalk, P. L. O’Leary. Evaluation and calibration methods for the application of a video-extensometer to tensile testing of polymer materials. Proc. SPIE 2005; 5679:187.
- [21] Plastics – Determination of compressive properties. ISO 604. Third edition. 2002
- [22] A. B. Watts, H. Ford. On the basic yield stress curve for a metal. P. I. Mech. Eng. 1955; 169:1141.
- [23] J. G. Williams, H. Ford. Stress – strain relationships for some unreinforced plastics. J. Mech. Eng. Sci. 1964; 6:405.
- [24] J. G. Williams. Plane – strain compression testing of polymers. Trans. J. Plastics Inst. 1967; 6:505.

- [25] Z. Bartczak, M. Kozanecki. Influence of molecular parameters on high-strain deformation of polyethylene in the plane-strain compression. Part I. Stress-strain behavior. *Polymer* 2005; 42:8210.
- [26] Z. Ma, K. Ravi-Chandar. Confined compression: A stable homogeneous deformation for constitutive characterization. *Exp. Mech.* 2000; 40:38.
- [27] K. Ravi-Chandar, Z. Ma. Inelastic deformation in polymers under multiaxial compression. *Mechanics of Time-Dependent Materials* 2000; 4:333.
- [28] S. Timoshenko, J. Goodier. *Theory of Elasticity*. McGraw-Hill. 1934.
- [29] D. J. Qvale, K. Ravi-Chandar. Viscoelastic characterization of polymers under multiaxial compression, *Mechanics of Time Dependent Materials* 2004; 8:193.
- [30] H. D. Kuske. Bestimmung des Verformungs- und Versagensverhaltens von Kunststoffen unter einachsiger Druckbeanspruchung. Forschungsbericht Süddeutsches Kunststoff-Zentrum, 2002.
- [31] A. D. Mullikan, M. C. Boyce. Mechanics of the rate-dependent elastic-plastic deformation of glassy polymers from low to high strain rates. *Int. J. Solids Struct.* 2006; 43(5):1331.
- [32] B. A. G. Schrauwen. Deformation and failure of semi-crystalline polymer systems. Technical University Eindhoven, 2003.

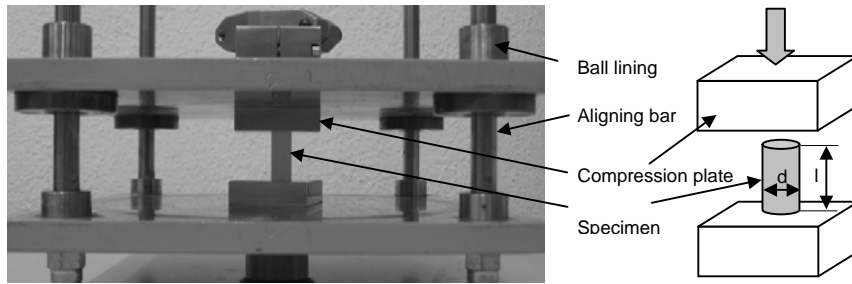


Fig. 1. Uniaxial compression set-up mounted in the compression tool used for all methods.

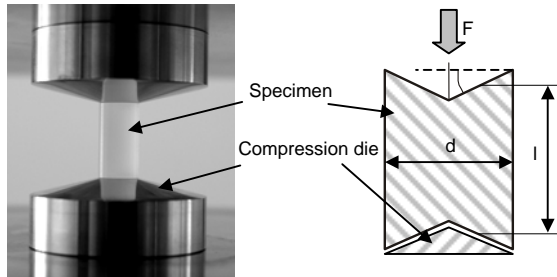


Fig. 2. Cone compression set-up.

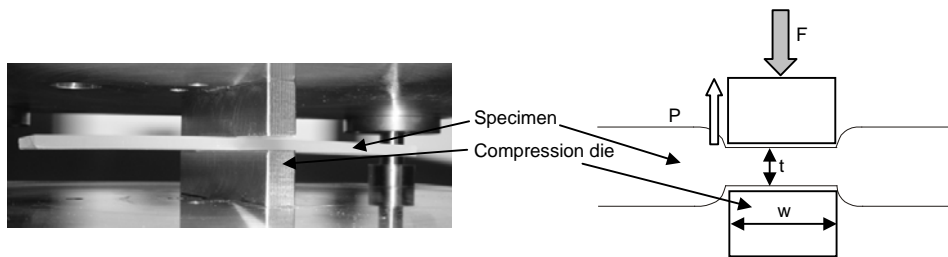


Fig. 3. Plane strain set-up method 1.

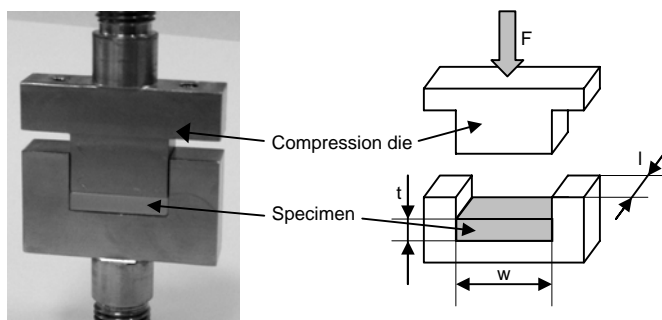


Fig. 4. Plane strain set-up method 2.

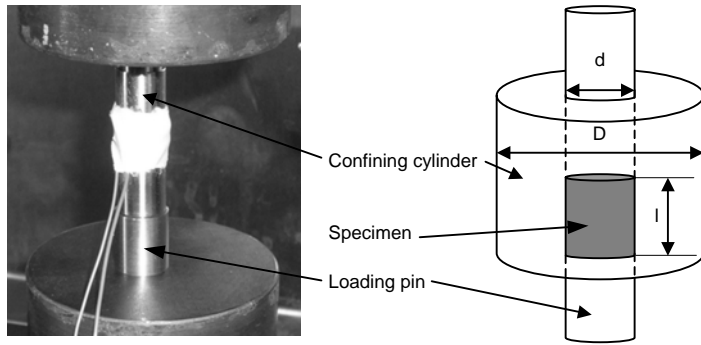


Fig. 5. Confined compression set-up.

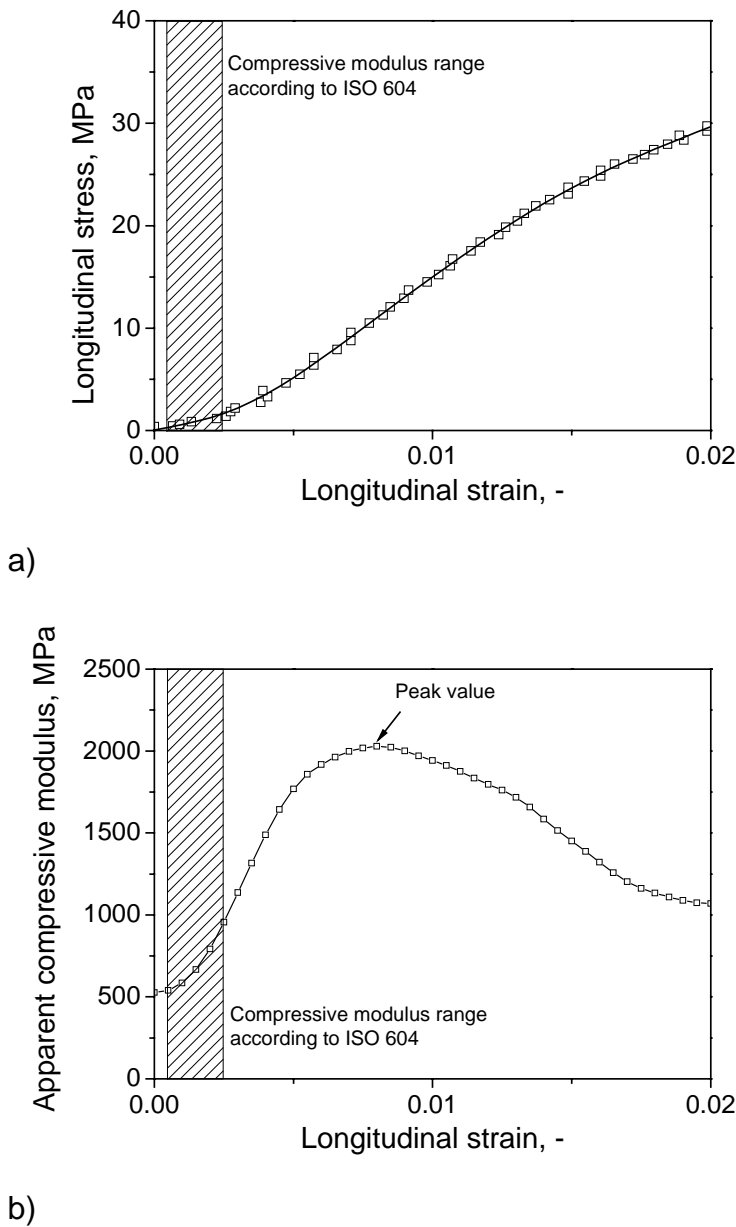


Fig. 6. Uniaxial compressive behavior in the small strain regime a) nominal longitudinal stress vs. nominal longitudinal strain and b) apparent compressive modulus ($d\sigma/d\varepsilon$) vs. nominal longitudinal strain.

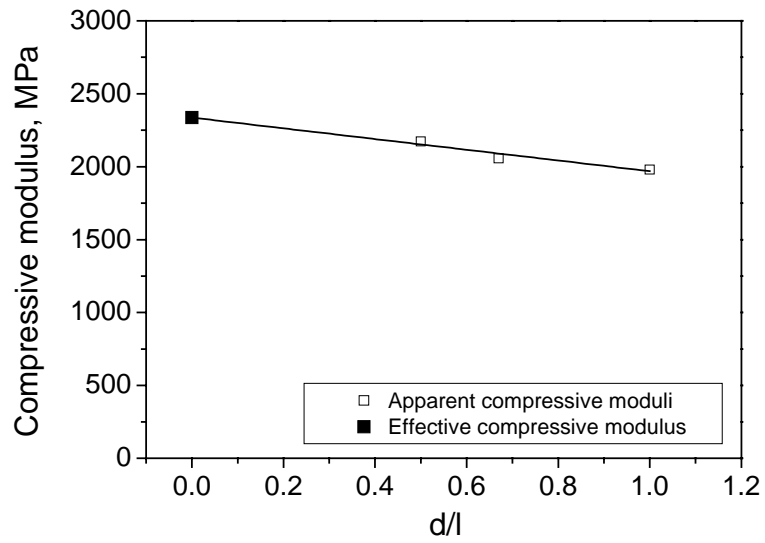
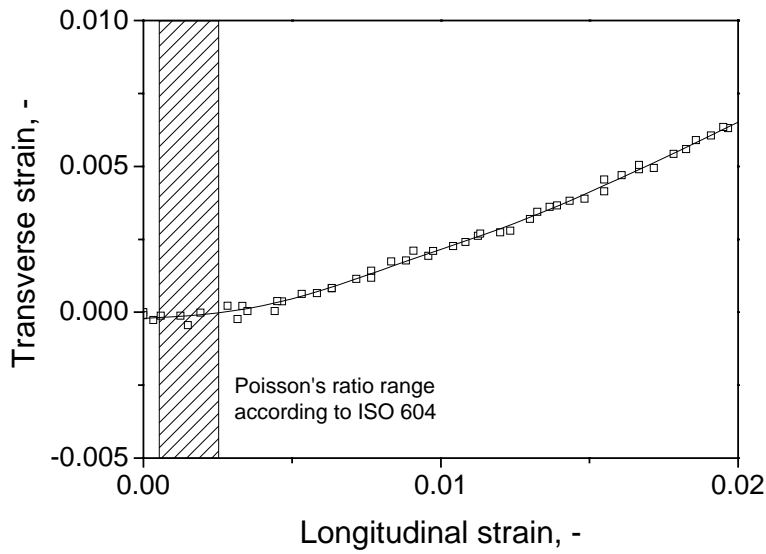
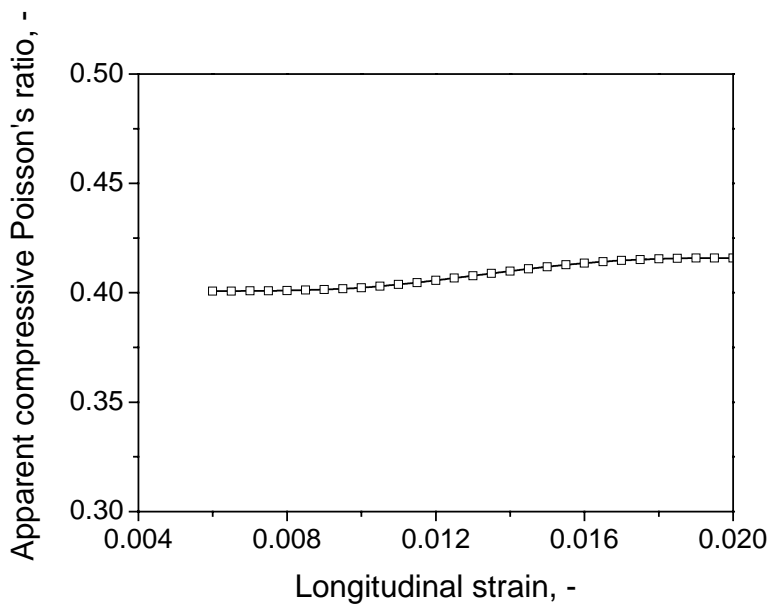


Fig. 7. Compressive modulus (peak value) vs. d/l ratio for three specimen lengths and extrapolation to infinite specimen length according to Cook and Larke.



a)



b)

Fig. 8. Uniaxial compressive behavior in the small strain regime a) nominal transverse strain vs. nominal longitudinal strain and b) apparent compressive Poisson's ratio vs. nominal longitudinal strain.

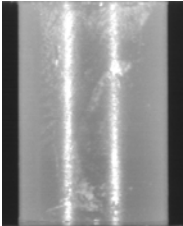
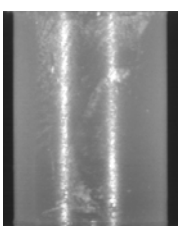
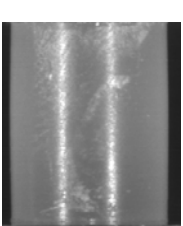
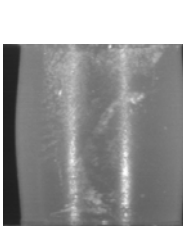
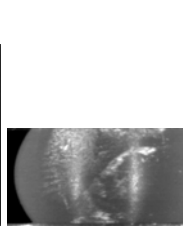
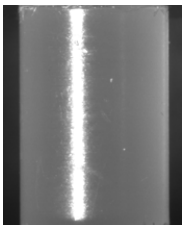
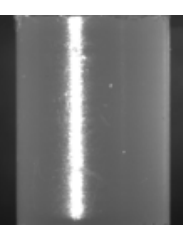
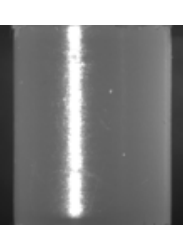
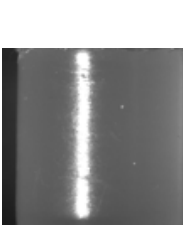
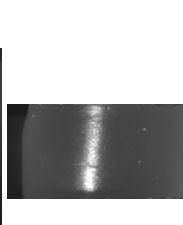
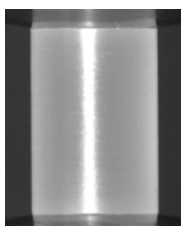

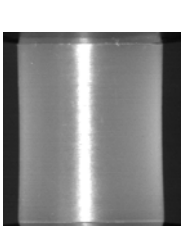
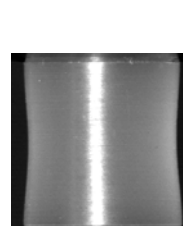
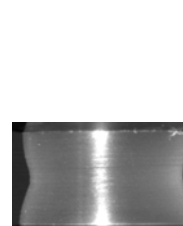
Test Method	Nominal strain in %				
	0 % strain	5 % strain	10 % strain	20 % strain	50 % strain
Uniaxial compression					
Uniaxial compression with PTFE tape					
Cone compression test					

Fig. 9. Illustration of the specimen appearance during compressive loading to increasing strains for three test methods (initial specimen length: 12 mm).

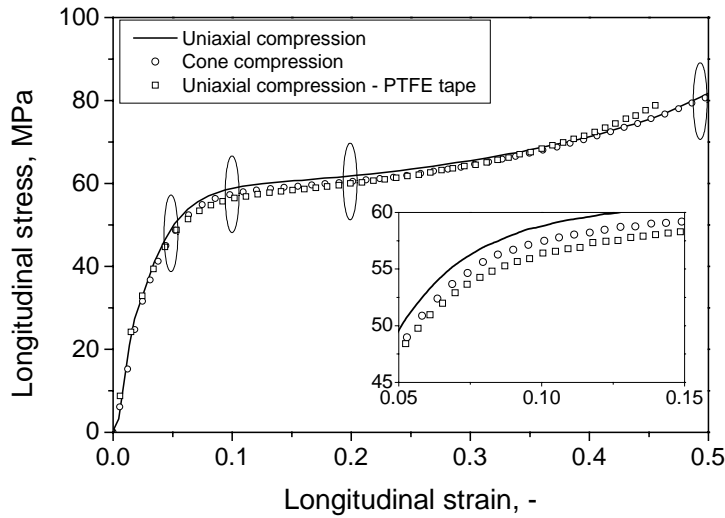


Fig. 10. Uniaxial compressive behavior of PP in terms of nominal compressive stresses vs. nominal longitudinal strains over a wide deformation regime including pre-yield, yield and post-yield deformations (initial specimen length: 12 mm).

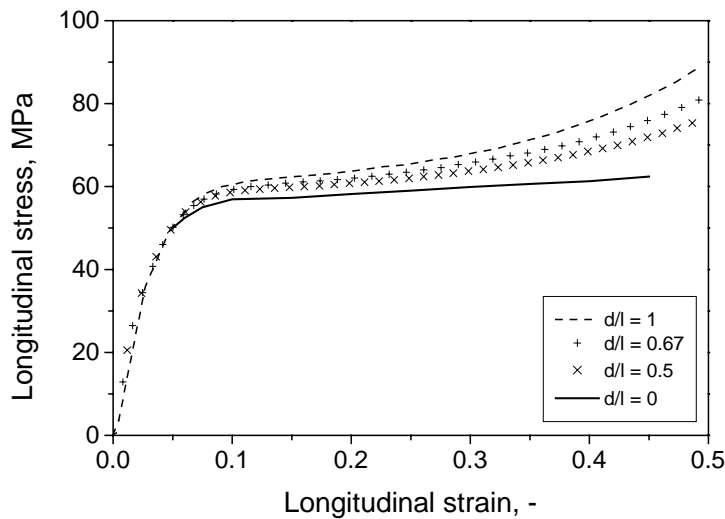


Fig. 11. Uniaxial compressive behavior of PP in terms of nominal compressive stresses vs. nominal longitudinal strains for various specimen geometries (d/l ratios) along with an extrapolated curve for $d/l=0$.

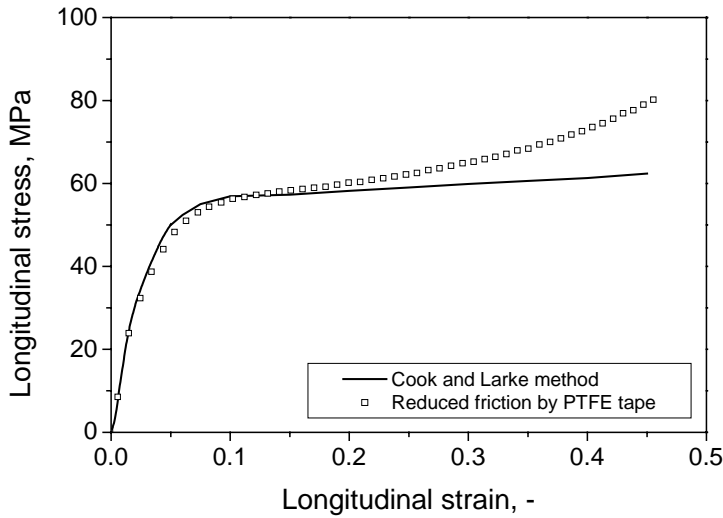


Fig. 12. Comparison of nominal compressive stress-strain curves of PP without PTFE, generated by extrapolation to a specimen geometry with $d/l=0$ (according to the Cook and Larke method), and with PTFE using a specimen geometry with $l/d=1.5$.

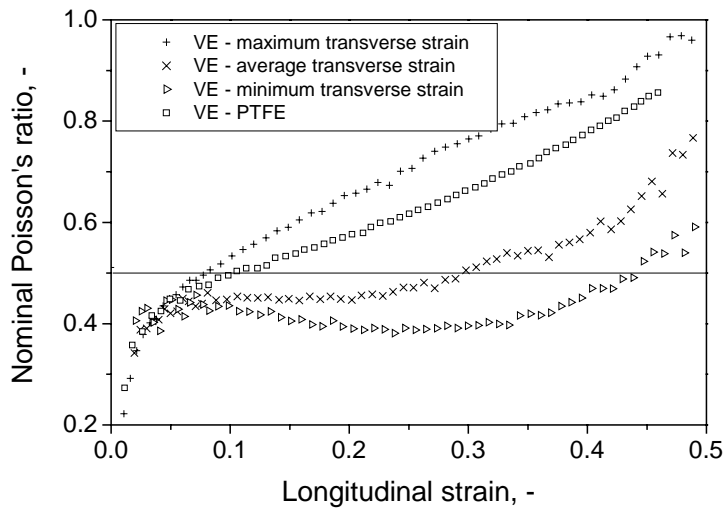


Fig. 13. Nominal Poisson's ratio vs. nominal strain in uniaxial compression for two test methods with and without PTFE; transverse strain measurement by video extensometer (VE) at various specimen positions (initial specimen length: 12 mm).

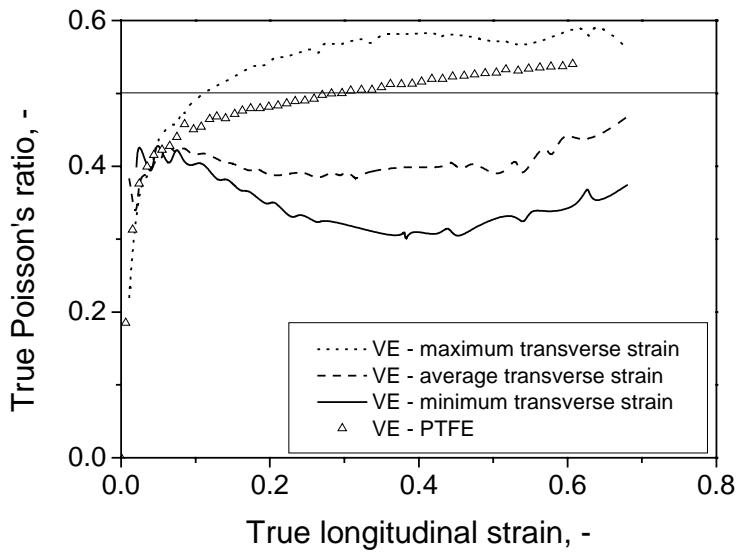


Fig. 14. True Poisson's ratio vs. true strain in uniaxial compression for two test methods with and without PTFE; transverse strain measurement by video extensometer (VE) at various specimen positions (initial specimen length: 12 mm).

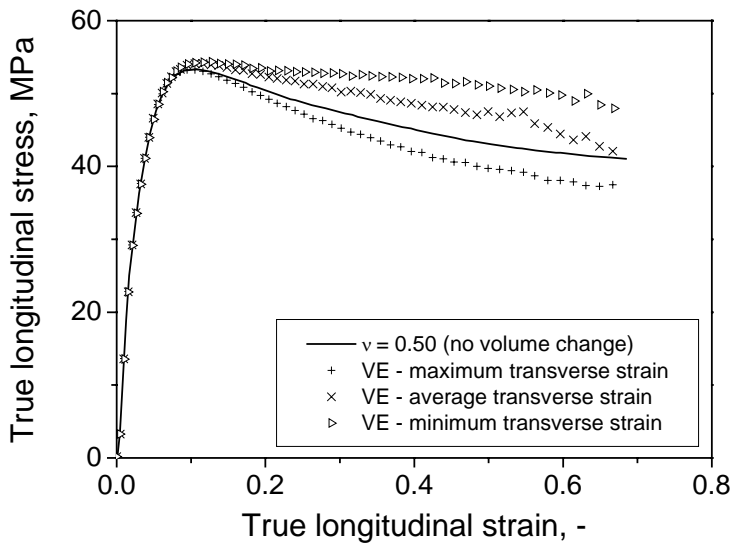


Fig. 15. True stress vs. true strain in uniaxial compression for two test methods with and without PTFE based on data in Fig. 14; (initial specimen length: 12 mm).

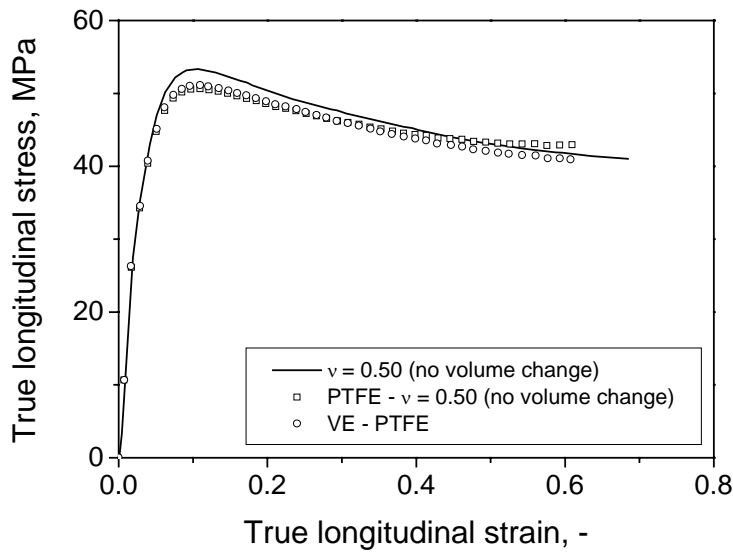


Fig. 16. True stress vs. true strain in uniaxial compression for two test methods with and without PTFE based on experimental transverse strain data and on the assumption of $\nu=0$; (initial specimen length: 12 mm).

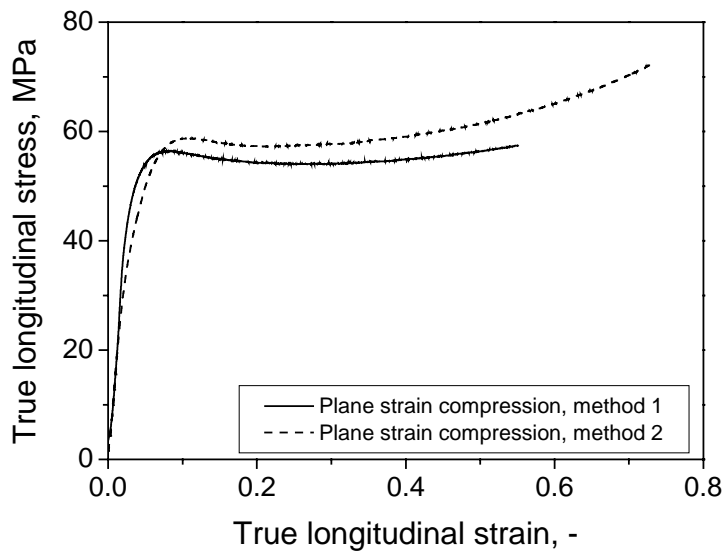


Fig. 17. Comparison of both plane strain configurations showing the influence of the configuration on the stress – strain curve.

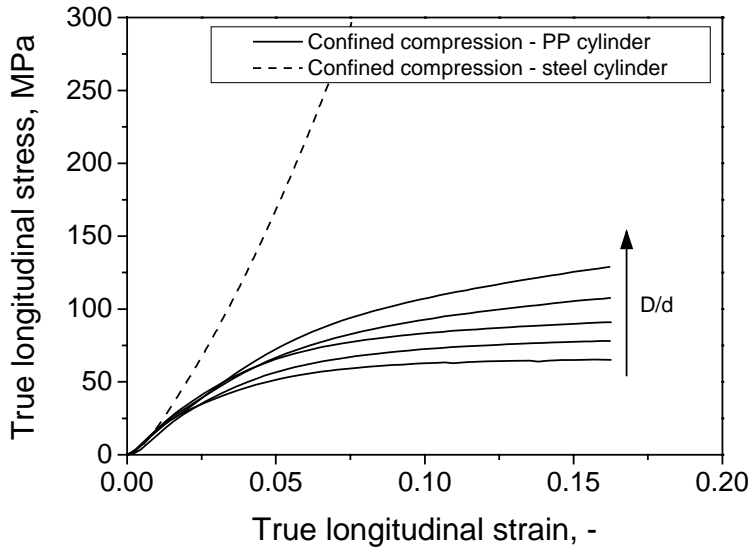


Fig. 18. True stress – true strain curves of the confined compression test for different levels of confinement.

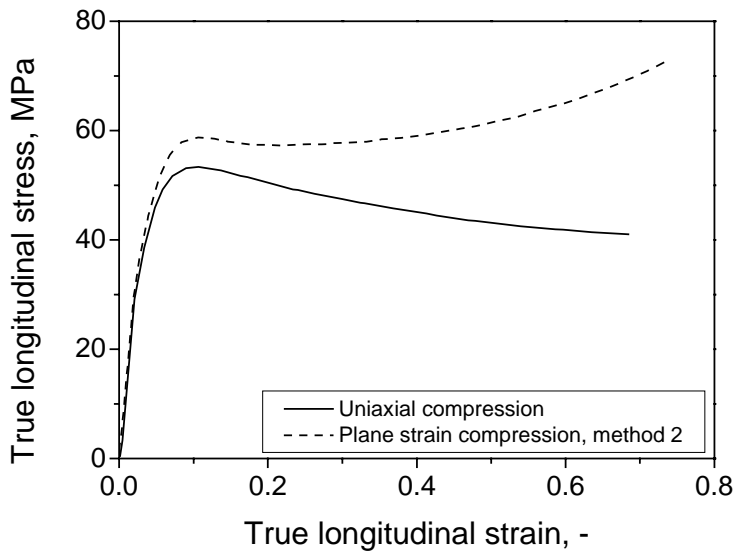


Fig. 19. Comparison of uniaxial and plane strain true stress versus true strain curves.

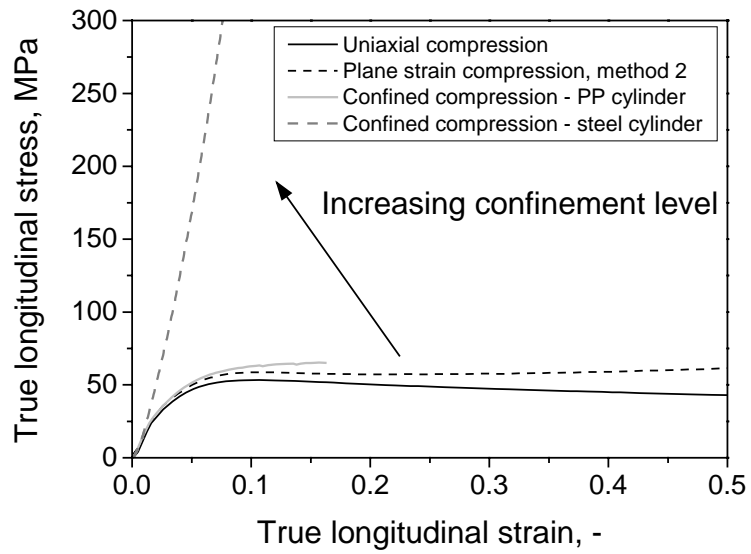


Fig. 20. True stress-true strain curves of the uniaxial, plane strain and confined compression test, showing the strong impact of hydrostatic pressure on the obtained stress levels.

PAPER 3^o**MECHANICS AND MODELING OF THE TENSILE YIELD BEHAVIOR OF PARTICULATE FILLED PP COMPOSITES**

M. Jerabek^{a,*}, Z. Major^b, B. Pukánszky^{c,d}, R.W. Lang^b

^a Polymer Competence Center Leoben GmbH, 8700 Leoben, Austria

^b Institute of Materials Science and Testing of Plastics, University of Leoben, 8700 Leoben, Austria

^c Laboratory of Plastics and Rubber Technology, Department of Physical Chemistry and Materials Science, Budapest University of Technology and Economics, H-1521 Budapest, P.O. Box 92, Hungary

^d Institute of Materials and Environmental Chemistry, Chemical Research Center, Hungarian Academy of Sciences, H-1525 Budapest, P. O. Box 17, Hungary

ABSTRACT

The tensile behavior of PP composites filled with glass beads and talc was studied in the strain rate range from $8.7 \times 10^{-5} \text{ s}^{-1}$ to $8.7 \times 10^{-3} \text{ s}^{-1}$ and in the temperature range from $-30 \text{ }^\circ\text{C}$ to $80 \text{ }^\circ\text{C}$. Two different sizes of glass beads were used, and composites were prepared with two different filler contents (3.5 v% and 7.0 v%). The results were interpreted in terms of particle size and shape, the importance of interfacial interactions and the deformation micro-mechanisms shear yielding and crazing. In agreement with theoretical models, for the glass bead composites the debonding stress was found to decrease with increasing particle size, also leading to a decrease of the yield stress. Because of their different temperature dependence, the debonding stress, which is substantially below the yield stress at low temperatures, approaches the yield stress at elevated temperatures (room

^o Paper will be submitted to Polymer.

* Corresponding Author: M. Jerabek

Tel.: +43 3842 42962 21; fax: +43 3842 42962 6; E-mail address: jerabek@pccl.at

temperature and above). In the low temperature regime, debonding, crazing and micro-cracking were determined as the dominating deformation micro-mechanisms, leading to brittle fracture. At elevated temperatures, the main micro-mechanisms of deformation change to shear yielding and crazing of the matrix, leading to ductile failure. As to the effect of temperature, similar results were obtained for the talc filled PP. However, while yield stress decreased with increasing filler loading at low temperatures, true reinforcement (increase of yield stress with filler content) was observed at elevated temperatures. Finally, the effect of interfacial interactions was expressed in quantitative terms by using a model proposed by Pukánszky and Vörös. The load-bearing capacity of fillers with different particle characteristics could be related to the dominating micro-deformation mechanisms and to the effects of test conditions.

Keywords: Particulate filled polypropylene; Micromechanical deformations; Debonding;

1. INTRODUCTION

Particulate filled polymeric composites have been used in increasing quantities in various applications in the automotive industry, for appliances or as garden furniture [1, 2]. The properties of these composites are basically determined by the behavior of the matrix, the properties of the filler, the composition, the particle spatial distribution and the interfacial interaction [3]. Although such heterogeneous systems are of scientific and practical interest, their behavior under external load is not fully understood. Further research is needed to understand and to predict the debonding of the particles properly. Debonding, i.e. failure at the interface and detachment of the particles from the matrix, is usually the dominating deformation mechanism of particulate filled polymers [4, 5].

Numerous studies have been carried out to determine the influence of particles on the stiffness, yield stress and tensile strength of such composites in uniaxial tension at a particular strain rate and temperature [6-9]. The results showed that the particle properties and the interfacial interaction mainly determine the response of the composite under tensile loading conditions and that the

micromechanics of particulate filled polymers is closely related to the size and shape of filler particles, which influence structure-property relationships considerably [10, 11]. The debonding stress of particles, as one of the key parameters for such heterogeneous systems, is strongly related to their size. Two models can be found in the literature to calculate the debonding stress of spherical particles, which are not chemically bonded to the matrix [12-14]. The first model derived by Vollenberg et al. [11, 12] is based on the assumption that the mechanically stored potential energy around a spherical inclusion is used for the creation of new surfaces at the moment of debonding. The authors assumed that debonding takes place around the poles of the spherical particles and proceeds to an angle of 25° instantaneously under the effect of a constant stress in this region. The second model developed by Pukanszky and Vörös [14] is also based on energy equalities but without the constant stress assumption made by Vollenberg et al. [12, 13]. It predicts the debonding stress, σ_D , as

$$\sigma_D = -C_1\sigma_T + C_2\left(\frac{W_{AB}E}{R}\right)^{\frac{1}{2}} \quad (1)$$

where C_1 and C_2 are constants having exact physical meanings, σ_T is the thermal stress induced by the different thermal expansion of the components, W_{AB} is the reversible work of adhesion, E is the tensile modulus of the matrix and R is the radius of the particles. Accordingly, smaller particles debond at larger stresses; moreover, debonding occurs over a broad stress range due to the inherently wide particle size distribution of natural fillers. The prediction of debonding stress is difficult with either model since their constants are not known and can not be determined by simple measurements.

Modulus as well as yield stress are strongly affected by particle shape and orientation [15-17]. The aspect ratio of particles can change from 1 (beads) up to 100 or more (needles). In order to obtain some reinforcing effect in the composite either very small particles or a minimum aspect ratio is needed [18]. Furthermore, anisotropic particles must be aligned in the loading direction to increase the mechanical properties of the composite. Usually significant weakening of the material can be observed, if the particles are orientated perpendicularly to the direction of the force [19].

Due to the viscoelastic nature of polypropylene (PP), mechanical properties depend significantly on time and temperature. Several studies focused on the mechanism of micromechanical deformations of neat PP under different testing conditions [20-22]. Much less work has been done to investigate the behavior of particulate filled composites at different temperatures [23] and only few studies determined the mechanical behavior over a wide temperature range, below and above the glass transition temperature (T_g), which changes the deformation mechanisms significantly also including the ductile-to-brittle transition [24]. The response of the polymeric matrix to local stress concentrations developing around the filler particles can vary from micro-cracking to shear yielding and thus may depend also on temperature and strain rate.

The objective of this research was to determine the mechanical properties of particulate filled composites as a function of temperature and strain rate. Glass beads with two different sizes and talc were used as fillers to investigate the effect of particle size, shape and orientation. The load-bearing capacity of the filler and thus the strength of interfacial interaction were investigated with respect to the viscoelastic behavior of the matrix.

2. EXPERIMENTAL MATERIALS AND PROCEDURE

The matrix material was a development grade PP homopolymer, provided by Borealis Polyolefine GmbH Linz (Linz, Austria) and delivered as injection molded tensile bars corresponding to ISO 3167 type B. The neat material as well as composites using this homopolymer as a matrix were extensively characterized in monotonic tension, under monotonic compression and in long-term compressive relaxation tests [25-27]. Two glass beads (GB) of different mean diameter (larger diameter: Spheriglass 3000 (GB-L); smaller diameter: Spheriglass 5000 (GB-S)) from Potters Europe (Barnsley, UK), were used as spherical fillers. Luzenac A7 talc provided by Luzenac Europe (Toulouse, France) was used as non-spherical filler in order to change particle shape. An overview of the nomenclature and composition of the composites studied is given in Table 1. The characteristics of the particles will be discussed in the next section in detail.

Table 1: Material designation and composition.

Material	Filler designation	Weight fraction of filler	Volume fraction of filler
PP	-	-	-
PP-G3.5S	GB-S	0.10	0.034
PP-G7.0S	GB-S	0.20	0.073
PP-G3.5L	GB-L	0.10	0.034
PP-G7.0L	GB-L	0.20	0.073
PP-T3.5	Talc	0.09	0.035
PP-T7.0	Talc	0.18	0.075

Tensile tests were carried out using the electromechanical universal testing machine type Instron 5500 (Instron LTD; High Wycombe, USA) at constant crosshead displacement rates covering five orders of magnitude from 0.0001 mm/s to 1 mm/s. A temperature chamber was mounted on the frame of the testing machine to carry out tests at -30 °C, -10 °C, 50 °C and 80 °C. The initial specimen length between the wedge grips was 115 mm. Axial strain was measured by an Instron 2630-112 mechanical clip-on extensometer with a initial gauge length of 50 mm.

3. RESULTS AND DISCUSSION

In the first part of this section the key particle characteristics determining the performance of the composites will be analyzed. In the second part, the effect of particle size and content on composite yield stress is discussed as a function of strain rate and temperature. The influence of particle shape and orientation on the same property is treated in the third part. Finally, a model is applied for the prediction of the composite yield stress, and the strength of particle-matrix interaction is estimated quantitatively.

3.1. Particle Characteristics

For micromechanical modeling purposes, volume fraction instead of mass fraction of fillers must be used. Similarly, the particle size distribution based on the number and not on the volume or weight of the particles must be determined. Many standard measurement procedures (e.g. sieving, Cilas Laser Particle Size Analyzers) give particle size distributions based on weight or volume, respectively. However, to properly characterize our fillers used, the particle size distributions were determined from scanning electron micrographs (SEM). Typical micrographs taken from two of the fillers studied are depicted in Fig. 1*, exhibiting the broad range of the filler particle size. Micrographs were taken at different resolutions to cover the entire range of sizes. The same number of particles was counted in each micrograph to eliminate any possible bias of the final distribution. The particle size distributions of the investigated fillers are depicted in Fig. 2. Only small differences can be found among the three fillers, although those small differences may change the performance of the composite significantly, as will be shown in the following sections. It is worth noting that more than 1000 particles were measured for each distribution. Since talc has a plate-like structure, its aspect ratio was also determined by measuring the length and thickness of the platelets. The distribution of the aspect ratio is plotted in Fig. 3, showing that the mean aspect ratio is approximately 8. The mechanical filler properties and other the particle characteristics are summarized in Table 2.

Talc is also known to act as a nucleating agent for PP. Compared to the neat PP matrix, this may change the crystallization of the polymeric matrix and its morphology significantly, which results in different mechanical properties of the two matrix state in the filled versus the unfilled case [28]. However, as was shown by Pukánszky et al. [29], the reinforcing effect of stiff particles overwhelms any effects of the modification in morphology (i.e., increase in the crystallinity or lamellar thickness) and thus has not been considered in this paper.

* All figures of this paper are collected at the end of the text.

Table 2: Mechanical properties and characteristics of the investigated particles. Tensile modulus and Poisson's ratio were obtained from data sheets.

Particle	Tensile modulus (GPa)	Poisson's ratio	Mean diameter (μm)	Specific surface area (m^2/g)	Aspect ratio	Coating
GB-S	70	0.21	1.31	1.0 ^{b)}	1	Yes
GB-L	70	0.21	1.58	0.6 ^{b)}	1	Yes
Talc	90 ^{a)}	0.21 ^{a)}	1.73	9.0 ^{c)}	8	No

a) Determined on the bulk material

b) Cilas Test Method

c) Determined by BET measurement

3.2. Effect of particle size on yield stress

The yield stress of particulate filled composites is determined by the constituent properties, the composition, the particle spatial distribution, and the particle/matrix interfacial interaction. The irreversible deformation processes in neat PP include shear-yielding and crazing followed by micro-cracking the relative contribution and importance depending on strain rate, temperature and stress state [30-32]. In particulate filled PP composites the dominating micromechanical deformation process is usually debonding often accompanied by shear yielding and/or crazing of the matrix [33]. Utilizing the tensile test it is possible to identify the primary micromechanical deformation process and under certain testing conditions allows for a quantitative description of the debonding process. The stress versus strain response of PP and PP-G7.0S below and above T_g are presented in Fig. 4 up to the yield stress to demonstrate the effect of the viscoelastic nature of the polymeric matrix. The yield stress of PP depends strongly on test temperature and increases from 14 MPa at 80 °C to 69 MPa at -30 °C with a simultaneous decrease of yield strain. At -30 °C the end of the stress-strain curve plotted in Fig. 4 corresponds to ultimate fracture of the specimen. Based on observations in separately carried out SEM in-situ tensile experiments, the primary deformation mechanisms at low temperature are crazing and micro-cracking followed by brittle failure of the specimen. Crazing and shear yielding under large strains (>100 %)

were observed at 23 °C and 80 °C indicating that the dominant deformation process changes around T_g for neat PP. The glass bead filled composite PP-G7.0S exhibits an increase in modulus, while for the yield stress the same values were obtained as for neat PP. Compared to the neat PP, the yield strain of the composite is lower at all temperatures investigated, the difference becoming smaller at higher temperatures. At -30 °C brittle fracture without necking was observed for the composite, whereas necking and shear yielding under large strains occurred at 23 °C and 80 °C.

As the debonding stress according to the above discussion strongly depends on particle size (Eq. 1) and considering the wide range of particle sizes according to the particle size distribution presented in Fig. 3, it follows that debonding does not occur at a certain stress level but over a wider stress range. The size distributions of the two glass bead fillers differ only slightly; a few large particles can only be observed in the large grade GB-L. Accordingly, the big particles may debond first from the matrix at lower stresses followed by the growth of voids around these particles. The tensile behavior of PP-G3.5S and PP-G3.5L is compared in Fig. 5 showing that the composite containing the large glass beads exhibits a lower yield stress. The two stress-strain curves deviate from one another at a stress level of about 20 MPa. The difference between the curves is increasing with strain, demonstrating that debonding and void growth reduces the effective cross-section and thus, the load-bearing capacity of the specimen. Comparing the response of the two composites it becomes evident that debonding of the large particles starts well before nominal macroscopic yielding of the composite.

The temperature dependence of the yield stress of PP-G3.5S and PP-G3.5L is plotted in Fig. 6. Obviously, the effect of particle size depends considerably on temperature. At temperatures below T_g much higher stresses develop during the tensile tests than at 23 °C and above. Debonding of large particles under large stresses occurs easily and the yield stress of the composites containing the two grades differs considerably. With increasing temperature the difference in yield stress becomes smaller and equal yield stress values were measured at 80 °C. This behavior can be explained again by Eq. 1, in which three parameters depend on temperature: (1) thermal stresses within the matrix σ_T , (2) reversible work of

adhesion W_{AB} , and (3) the modulus of the neat matrix E . In general, to obtain local stresses in the matrix, thermal stresses which decrease with increasing temperature are superimposed on the mechanically induced local stress field resulting from external specimen loads. Nevertheless, as internal thermal stresses in PP composites with a T_g at $-10\text{ }^\circ\text{C}$ may relax when stored at room temperature at least to some degree and compared to the magnitude of the external load induced stresses, the effect of the thermal stresses is neglected in the subsequent discussion. The reversible work of adhesion depends only slightly on temperature [34], thus it may not change the debonding stress as a function of temperature significantly. In contrast, the tensile modulus of the matrix strongly depends on temperature and decreases from 4452 MPa at $-30\text{ }^\circ\text{C}$ to 567 MPa at $80\text{ }^\circ\text{C}$ for a strain rate of $8.7 \times 10^{-3}\text{ s}^{-1}$. According to Eq. 1, the decrease of the modulus with temperature changes the debonding stress by a factor of approximately 2.8, while in the observed temperature range the yield stress changes by a factor of 4.7 from about 70 MPa to 15 MPa. Hence, the temperature dependence of the yield stress is more pronounced than that of the debonding stress. In other words, while at low temperatures debonding is the primary deformation process significantly prior to crazing and micro-cracking and macroscopic yielding, at elevated temperatures, the dominating deformation process may change from debonding of the particles to plastic deformation mechanisms (mainly shear yielding and crazing) of the matrix.

Matrix yield stress vs. temperature, not depicted in Fig. 6, is similar to the yield stress curve of the composite containing the small glass beads. If we assume debonding of some of the particles and as the yield stress remains unaffected by the filler, some load must be carried even by spherical particles to balance the effect of debonding. Strong interfacial interaction is required for an effective load transfer from the matrix to the filler.

The effect of strain rate on the yield stress at room temperature is depicted in Fig. 7 for all four glass bead filled composites. PP-G3.5S and PP-7.0S containing the small glass beads exhibit higher yield stress values than PP-G3.5L and PP-7.0L. No significant effect of filler volume fraction on the yield stress could be observed in the range investigated. Apparently, the decrease of the effective load-bearing

cross-section is compensated by the load carried by the particles fully attached to the matrix even at the yield point and by the dissimilar properties of the hard interphase forming between the matrix and the particles. Among other parameters (e.g., chemical reactions at the interface, physical adsorption of the polymer), the amount of interphase depends primarily on the specific surface area of the particles and on the particle content [35]. Despite the controversy related to the mechanical properties of the interphase [36, 37], the formation of a hard interlayer with reduced molecular mobility can be assumed in the case of stiff particles [38]. This interphase results in an increase in the overall stiffness and yield stress of the composites. In addition to the fully attached particles, it may thus compensate for the reduction of the effective cross-section. In the investigated strain rate range, the difference in the yield stresses of the composites containing the large and small glass beads is constant, indicating that only one deformation mechanism is dominant. As the modulus of the PP matrix compared to temperature effects only slightly depends on strain rate, the ratio of the debonding stress to the yield stress remains almost constant.

In order to support these findings, SEM investigations of fracture surfaces were performed. For low temperature tensile tests, the fracture surfaces were obtained directly from the tensile tests performed. At room temperature and elevated temperature, tensile tests were stopped at different strains and subsequently unloaded. To generate fracture surfaces for these specimens, the specimens were subsequently frozen in liquid nitrogen and then fractured in the cold condition. Two selected micrographs are presented in Fig. 8. The fracture surface of PP-G7.0L obtained at -30 °C and shown in Fig. 8a clearly exhibits interfacial failure around the glass bead. Furthermore, a smooth and completely matrix-free particle surface is observed, proving that the debonding of the particles takes place under these conditions. In contrast, different fracture surface characteristics were found for a specimen loaded at 23 °C up to the yield strain and then subsequently first unloaded and then fractured after exposing it to liquid nitrogen. While some of the differences are certainly due to the different temperature conditions at fracture, most notably, good adherence between the glass bead particle and the PP matrix is visible, indicating that no prior debonding in the tensile test at room temperature had occurred even though the specimen had been strained up to the yield strain.

3.3. Influence of particle shape and orientation on the yield stress

When comparing talc to glass beads, it is worth mentioning that the specific surface area of talc is about 10 times larger than that of the glass beads, leading to a corresponding difference to the amount of interphase formed in the respective composites. Yield stress values of the neat PP and talc filled PP-T7.0 are compared in Fig. 9 as a function of temperature. Analogous to the PP glass bead materials, debonding of talc particles might occur at low temperatures resulting in a decrease of the composite yield stress compared to that of the matrix. As similar yield stresses were measured for the composite and the matrix at 23 °C, the decrease in the effective cross-section is apparently compensated by the development of a hard interphase and by the load carried by bonded filler particles. At elevated temperatures, the yield stress of the composite exceeds that of the matrix, since the debonding stress becomes equal or even larger than the yield stress. Only a few large particles may debond from the matrix, which can easily be compensated by the load-bearing particles.

The influence of talc content on the yield stress is shown in Fig. 10 for two temperatures. While at -30 °C the yield stress decreases with increasing filler content, the opposite behavior was found for 80 °C. This can be attributed to the different dependence of yield and debonding stress on temperature. In agreement with models published elsewhere [39], a non-linear dependence of the yield stress on filler content was determined for both temperatures. In real materials superimposed may be effects of particle orientation distribution, which itself may depend on particle content [40].

3.4. Modeling of yield stress and particle-matrix interaction

A proper model of the yield process in particulate filled composites needs to account for the complexity of the micromechanical deformation processes described and discussed above. Hence, any analytical and semi-empirical model in which perfect bonding of the particles to the matrix is assumed up to the yield point are not capable to simulate the yield behavior adequately. A reasonably successful model for the prediction of the composition dependence of the yield stress in particulate filled composites has been developed by Pukánszky et al.

[41, 42]. This model consists of three parts; matrix yield stress, effective load-bearing cross-section, and particle-matrix interaction by expressing the load carried by the particles:

$$\sigma_{y,c} = \sigma_{y,m} \frac{1 - \phi_f}{1 + 2.5\phi_f} e^{B\phi_f} \quad (2)$$

where $\sigma_{y,c}$ and $\sigma_{y,m}$ are the yield stress of the composite and the matrix, respectively, and B is given by

$$B = (1 + l\rho_f A_f) \ln \frac{\sigma_{y,i}}{\sigma_{y,m}} \quad (3)$$

where l is the thickness of the interphase, ρ_f and A_f the density and specific surface area of the particles and $\sigma_{y,i}$ the yield stress of the interphase. The strength and thickness of the interphase can be calculated from parameter B , if the value is available for at least two different specific surface areas of the same filler. In order to calculate B Eq. 2 was rearranged to obtain the relative yield stress $\sigma_{y,rel}$:

$$\sigma_{y,rel} = \frac{\sigma_{y,c}}{\sigma_{y,m}} \frac{1 + 2.5\phi_f}{1 - \phi_f} = e^{B\phi_f} \quad (4)$$

As plotting the logarithm of the relative yield stress against the volume fraction of filler should give a straight line with the slope of B , it is plotted in this form at room temperature for one strain rate in Fig. 11. We must call attention to the fact that only three points are available for the linear fitting, thus the results must be treated with care. Since the relative yield stress increases as a function of filler content, some load must be carried by the particles ($B > 0$). While very good linear correlations were found for the composites containing the two glass beads, a non-linear relationship was obtained for the composites filled with talc. This may be associated with different orientations of the talc particles in the specimens at the two volume fractions studied.

The parameter B was calculated at different strain rates and temperatures to quantify the strength of interfacial interaction between the matrix and the particle. In Fig. 12 B is depicted as a function of strain rate for a test temperature of 23 °C. While a definite trend can be observed for the talc filled composite, the strain rate

dependence of the glass bead filled composites does not exhibit an obvious characteristic. In the talc filled composite the dominating micro-deformation process may change as B increases with decreasing strain rate. The tensile modulus of the matrix is the only strain rate dependent parameter in Eq. 1. The ratio of the yield to the debonding stress decreases monotonically with decreasing deformation rate. Thus, debonding initiates closer to the yield stress at low loading rates than at high loading rates. The primary deformation process of PP under fast loading conditions is crazing and micro-cracking followed by brittle fracture, while shear yielding and to some degree crazing dominate at moderate and low loading rates [30-32]. It is worth noting that at typical testing conditions (strain rate and temperature) micro-cracking and shear yielding can be observed simultaneously. The same processes can be observed in the composite, but debonding of the particles may occur additionally. Due to local stress concentrations around the particles, brittle fracture is favored in the composite and ductile fracture occurs at lower strain rates than in the neat matrix. The relative importance of the various micro-deformation processes (debonding, crazing and micro-cracking, and shear yielding and crazing) changes slowly with the rate of deformation and finally results in an increase of B with decreasing strain rate.

For the two glass bead filled composites, B increases slightly with decreasing strain rate, with the lowest B value measured at a strain rate of $8.7 \times 10^{-4} \text{ s}^{-1}$. Larger B values were measured for the composites containing the small glass beads with the larger specific surface area, which can be explained with larger debonding stresses. Even though the two glass beads have a specific surface area ten times smaller than talc, their B values are of the same magnitude. This can be related mainly to the surface modification and coupling of the glass beads, which is obviously quite effective and can compensate for the low specific surface area of the spherical filler.

Parameter B is depicted as a function of temperature in Fig. 13 for the fastest strain rate investigated. Again a clear tendency can be observed for the talc filled composite; B increases from values of about 2 up to 6 in the temperature range from $-30 \text{ }^\circ\text{C}$ to $80 \text{ }^\circ\text{C}$. This increase of B by a factor of 3 can be explained by a significant change of the dominating micro-deformation process from particle

debonding and matrix crazing and micro-cracking in the low temperature range to limited particle debonding and shear yielding with some crazing of the matrix at elevated temperatures. These findings are in agreement with the strain rate dependence shown in Fig. 12 and with the explanations given in previous sections above.

The behavior of the glass bead filled composites seems to be much more complicated. The parameter B increases up to 50 °C, with larger values for the small glass beads due to their larger specific surface area. The difference in the effect of the two glass beads decreases continuously with temperature and at 80 °C the composite containing the large glass beads has a larger B value than that prepared with the small beads. Moreover, B is reduced significantly at elevated temperatures for both glass bead filled composites. Three temperature dependent quantities describe B ; the thickness and yield stress of the interphase and matrix yield stress. Obviously, both yield stresses decrease with temperature. Because of the reduced mobility of the molecules adsorbed on the surface of the filler, we may assume a weaker temperature dependence for the yield stress of the interphase. Accordingly, the ratio of the interphase to matrix yield stress increases and so does B . However, with increasing temperature the strength of interaction decreases and the mobility of the molecules in the interphase increases. Thus, with further increase in temperature, the yielding of the matrix becomes dominant. The combination of all these effects may lead to the decrease of B at high temperatures. Naturally, this tentative explanation needs further study and proof.

4. CONCLUSIONS

The interpretation of the results in terms of particle size and shape proved the importance of interfacial interactions in the determination of composite properties measured at large deformations. The debonding stress decreased with increasing particle size, leading to a corresponding decrease also in the yield stress. Because of the different temperature dependences of the matrix properties, debonding stress values approached the yield stress with increasing temperature. At low temperatures, the dominating deformation micro-mechanisms were debonding and crazing associated with micro-cracking, leading to brittle fracture. As the

temperature was increased, the deformation micro-mechanisms change and were dominated by shear yielding of the matrix leading to ductile failure. A change in the dominating mechanism was also observed in composites filled with talc, which led to a different composition dependence at various temperatures. Yield stress values were found to decrease with increasing filler loading at low temperatures, but true reinforcement was observed for higher temperatures. The effect of interfacial interactions was expressed in quantitative terms by using an model proposed by Pukánszky and Vörös. The changing load-bearing capacity of fillers with different particle characteristics could be related to the dominating micro-deformation mechanisms and to their dependence on the experimental conditions (temperature and loading rate).

Acknowledgement

The research work of this paper was performed at the Polymer Competence Center Leoben GmbH (PCCL, Austria) within the framework of the Kplus-program of the Austrian Ministry of Traffic, Innovation and Technology with contributions by *the University of Leoben* and *Borealis Polyolefine GmbH*. The PCCL is funded by the Austrian Government, as well as by the State Governments of Styria and Upper Austria. The research was partly supported also by the National Scientific Research Fund of Hungary (OTKA Grant No. K 68748).

References

- [1] Markarian J. *Plast. Additives Compound* 2004;6:26.
- [2] Morieras G. *Ind. Miner.* 2001;6:29.
- [3] Pukánszky B. Particulate filled polypropylene: structure and properties. In: Karger-Kocsis J, editor. *Polypropylene: structure, blends and composites*, vol. 3. London: Chapman and Hall; 1995. p. 1.
- [4] Dubnikova IL, Oshmyan VG, Gorenberg AY. *J. Mater. Sci.* 1997;32:1613.
- [5] Bazhenov S. *Polym. Eng. Sci.* 1995;35:813.
- [6] Fu SY, Feng XQ, Lauke B, Mai YW. *Composites Part B* 2008;39:933.
- [7] Parsons EM, Boyce MC, Parks DM, Weinberg M. *Polymer* 2005;46:2257.
- [8] Leong YW, Ishak ZAM, Ariffin A. *J. Appl. Polym. Sci.* 2004;91:3327.
- [9] Yan W, Lin RJT, Bhattacharyya D. *Compos. Sci. Technol.* 2006;66:2080.

- [10] Dubnikova IL, Berezina SM, Antonov AV. *J. Appl. Polym. Sci.* 2004;94:1917.
- [11] Hadal RS, Dasari A, Rohrmann J, Misra RDK. *Mater. Sci. Eng., A* 2004;372:296.
- [12] Vollenberg P, Heikens D, Ladan HCB. *Polym. Compos.* 1988;9:382.
- [13] Vollenberg P. The mechanical behaviour of particle filled thermoplastics. PhD Thesis, Eindhoven University of Technology, Eindhoven, 1987.
- [14] Pukánszky B, Vörös G. *Compos. Interfaces* 1993;1:411.
- [15] Herbst, H. Modeling and Simulation of the Thermomechanical Behavior of Heterogeneous Polypropylene Compounds. Montanuniversitaet Leoben, Leoben, 2008.
- [16] Kamal MR, Song L, Singh P. *Polym. Compos.* 1986;7:323.
- [17] Mittal RK, Gupta VB, Sharma P. *J. Mater. Sci.* 1987;22:1949.
- [18] Pukánszky B, Fekete E. *Adv. Polym. Sci.* 1999;139:109.
- [19] Christie M. *Plast. Eng.* 1986;42:41.
- [20] G'Sell C, Dahoun A., Favier V, Hiver JM, Philippe MJ, Canova GR. *Polym. Eng. Sci* 1997;37(10):1702.
- [21] Pluta M, Bartczak Z, Galeski A. *Polymer* 2000;41:2271.
- [22] Dasari A, Rohrmann J, Misra RDK. *Mater. Sci. Eng., A* 2003;351:200.
- [23] Zhou Y, Mallick PK. *Polym. Eng. Sci.* 2002;42(12):2449.
- [24] Lapcik L, Jindrova P, Lapcikova B, Tamblyn R, Greenwood R, Rowson N. *J. Appl. Polym. Sci.* 2008;110:2742.
- [25] Jerabek M, Ravi-Chandar K, Major Z, Lang, RW. To be published.
- [26] Jerabek M, Tscharnuter D, Major Z, Ravi-Chandar K, Lang, RW. To be published.
- [27] Jerabek M, Major Z, Renner K, Móczó J, Pukánszky B. To be published.
- [28] Ferrage E, Martin F, Boudet A, Petit S, Fourty G, Jouffret F, Micoud P, De Parseval P, Salvi S, Bourgerette C, Ferret J, Saint-Gerard Y, Buratto S, Fortune JP. *J. Mater. Sci.* 2002;37:1561.

- [29] Pukánszky B, Belina K, Rockenbauer A, Maurer FHJ. *Compos.* 1994;25(3):205.
- [30] Karger-Kocsis J. *Polypropylene - An A-Z reference.* Dordrecht: Kluwer, 1999.
- [31] Friedrich K. *Adv. Polym. Sci.* 1983;52/53:226.
- [32] Narisawa I, Ishikawa M. *Adv. Polym. Sci.* 1990;91/92:354.
- [33] Dekkers MEJ, Heikens D. In: Ishida B, Koenig JL, editors. *Composite interfaces.* New York: Elsevier, 1987, pp. 161.
- [34] Fekete E, Móczó J, Pukánszky B. *J. Colloid Interface Sci.* 2004;269:143.
- [35] Pukánszky B. *Eur. Polym. J.* 2005;41:645.
- [36] Maurer FHJ, Kosfeld R, Uhlenbroich T, Bosveliev LG. Structure and properties of highly filled high-density polyethylene. In: 27th Intl Symp on Macromolecules, Strasbourg, France, 6–9 July 1981.
- [37] Vollenberg PHT, Heikens D. *Polymer* 1989;30:1656.
- [38] Kardos JL. In: Ishida H, Kumar G, editors. *Molecular Characterization of Composite Interfaces.* New York: Springer, 1985 p. 1.
- [39] Nicolais L, Narkis M. *Polym. Eng. Sci.* 1971;11:194.
- [40] Pukánszky B, Móczó J. *Macromol. Symp.* 2004;214:115.
- [41] Pukánszky B, Turcsányi B, Tüdös F. Effect of interfacial interaction on the tensile yield stress of polymer composites. In: Ishida H, editor. *Interfaces in polymer, ceramic, and metal matrix composites.* New York: Elsevier, 1988. p. 467.
- [42] Pukánszky B. *Compos.* 1990;21(3):255.

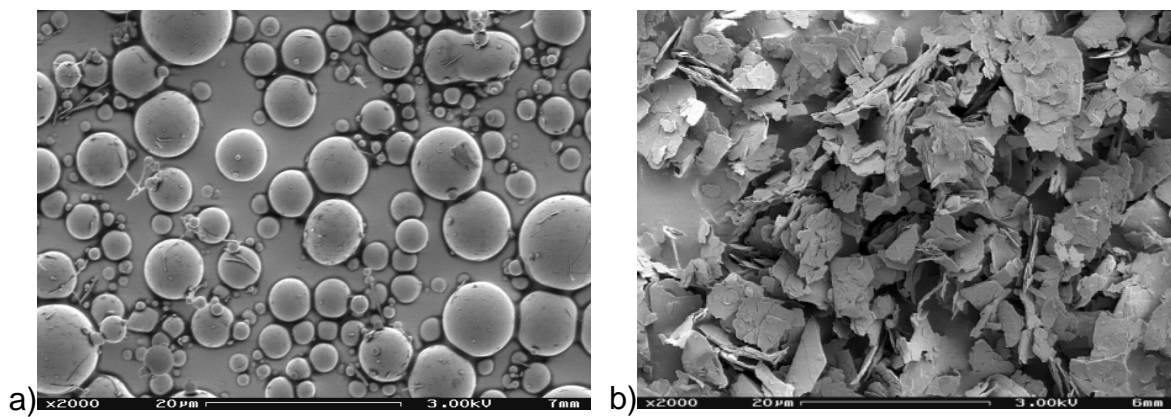


Fig. 1. SEM micrographs of the investigated fillers a) large glass beads and b) talc.

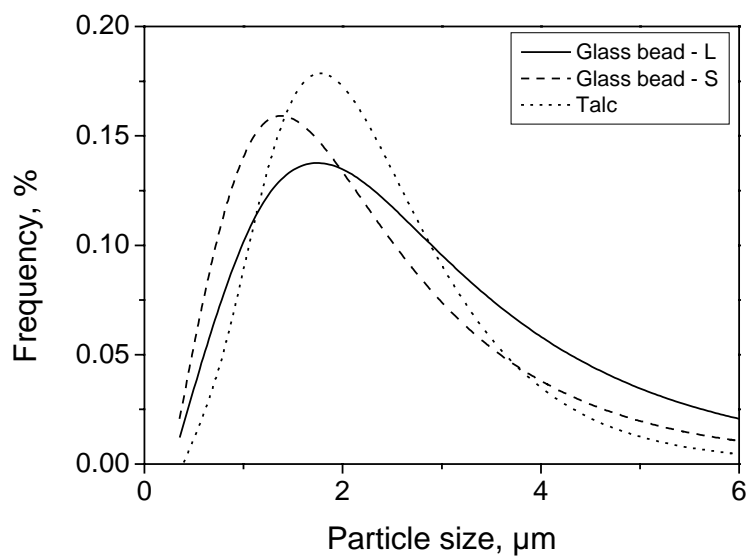


Fig. 2. Particle size distribution of the fillers.

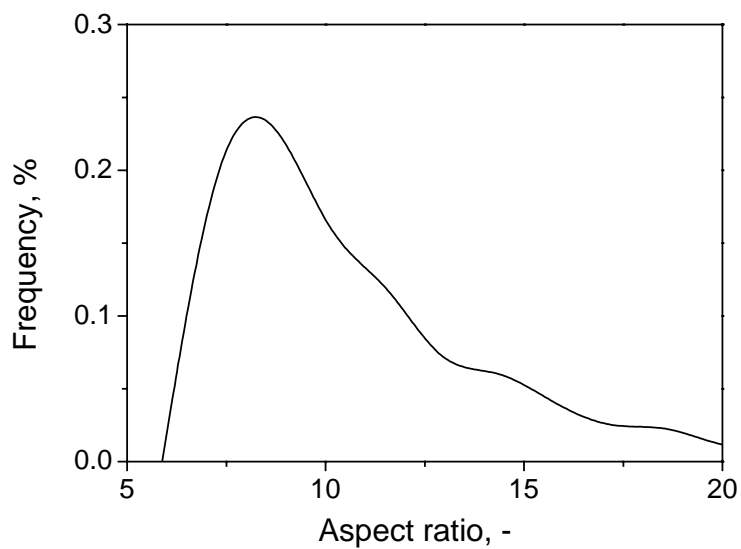


Fig. 3. Aspect ratio distribution of talc.

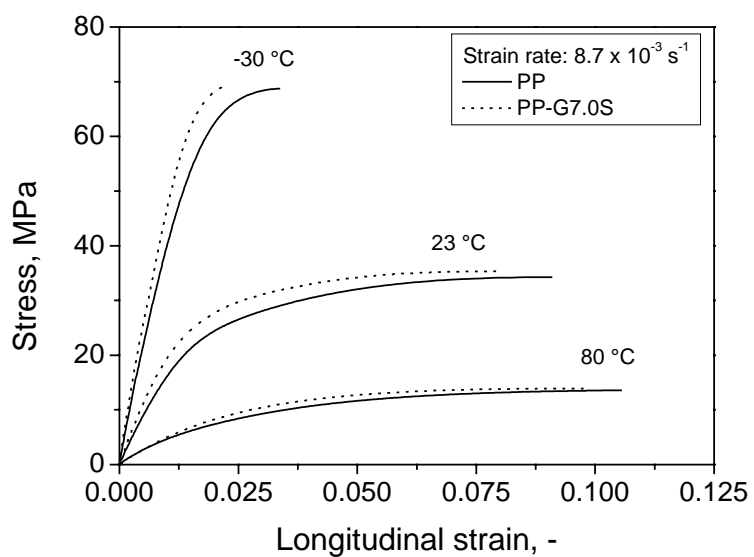


Fig. 4. Stress-strain curves of PP and PP-G7.0S measured below and above the glass transition temperature, up to the yield stress (23 °C and 80 °C) and to fracture (-30 °C), respectively.

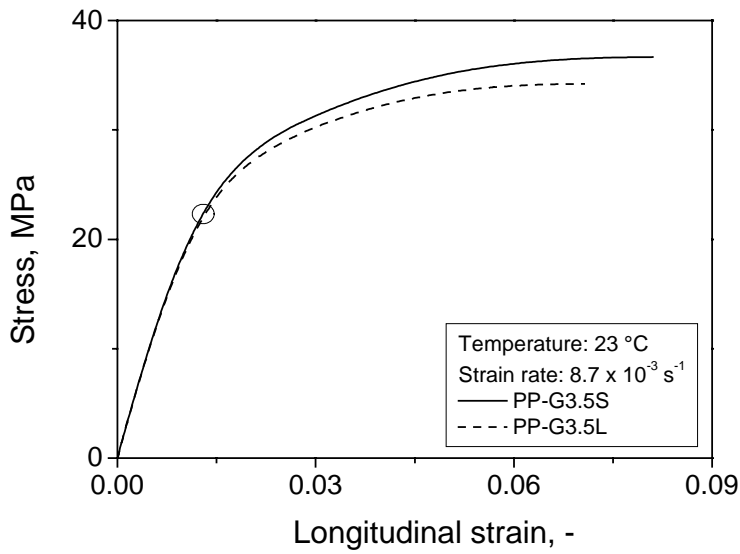


Fig. 5. Comparison of the stress-strain curves of PP containing two glass bead grades of different glass bead size distributions. The circle indicates the stress and strain level at which the curves deviate from each other.

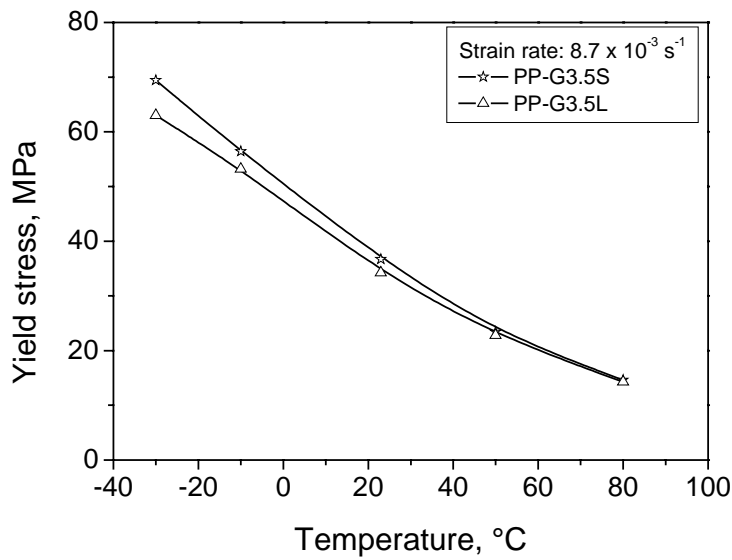


Fig. 6. Effect of particle size on the temperature dependence of the composite yield stress.

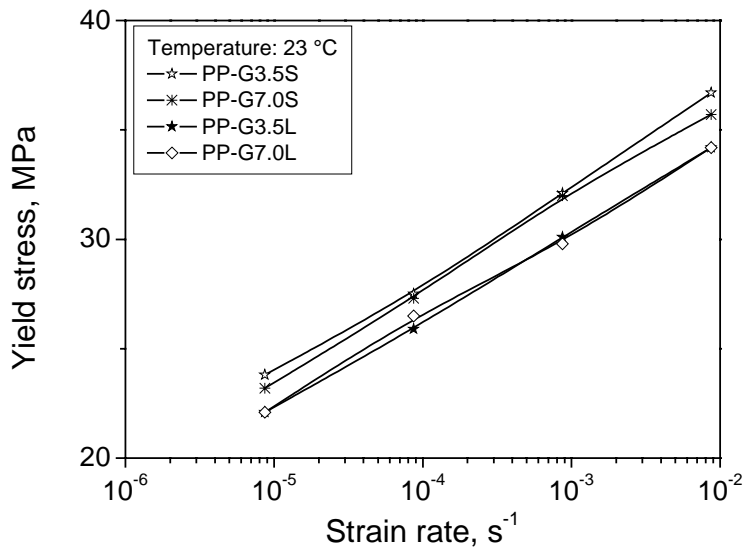
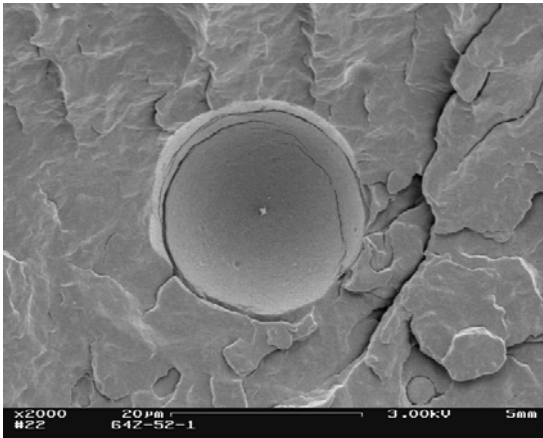


Fig. 7. Influence of particle size and content on the strain rate dependence of the composite yield stress.

a)



b)

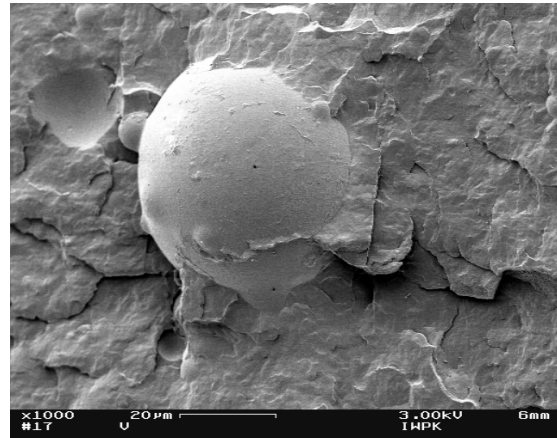


Fig. 8. SEM micrographs taken from the fracture surfaces of a) a tensile specimen tested at $-30\text{ }^{\circ}\text{C}$ and b) deformed at $23\text{ }^{\circ}\text{C}$ up to the yield point, subsequently unloaded and broken at liquid nitrogen temperature.

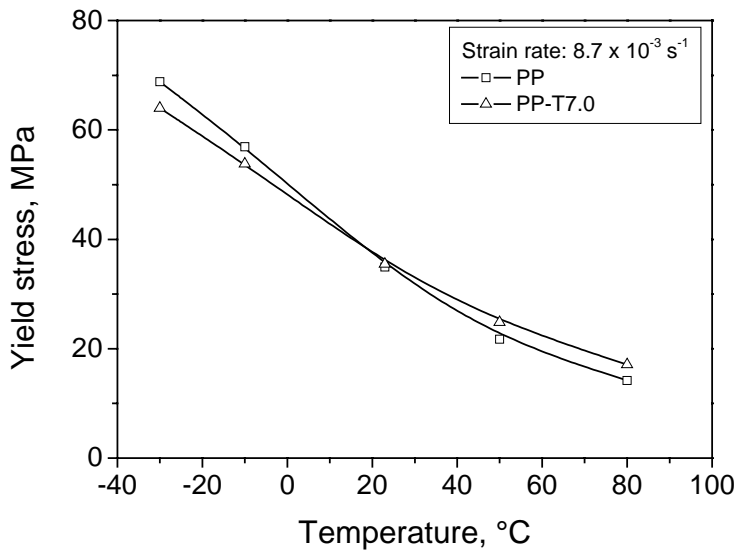


Fig. 9. Yield stress versus temperature for PP and PP-T7.0 showing the effect of particle shape.

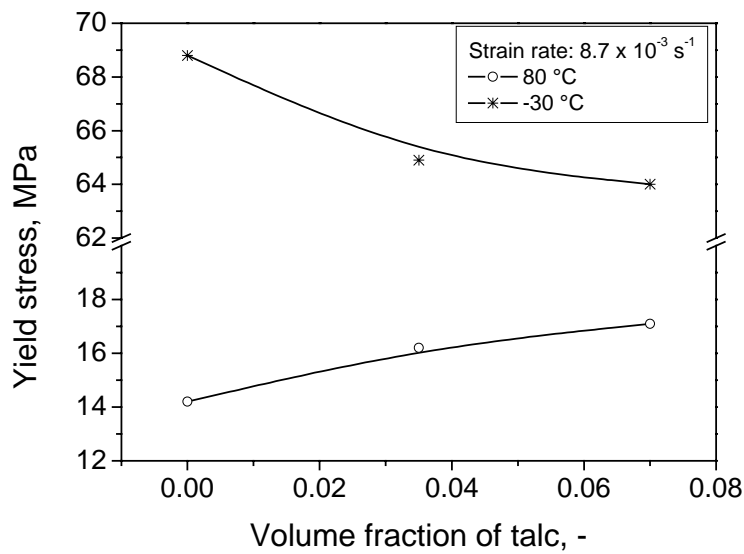


Fig. 10. Composition dependence of the yield stress of talc filled PP at two different temperatures.

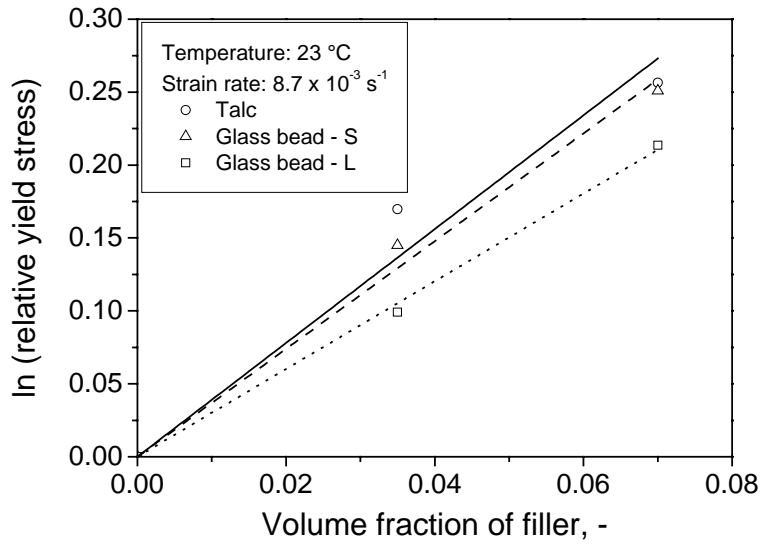


Fig. 11. The logarithm of relative yield stress plotted against volume fraction, the linear fit used for the calculation of parameter B is also shown.

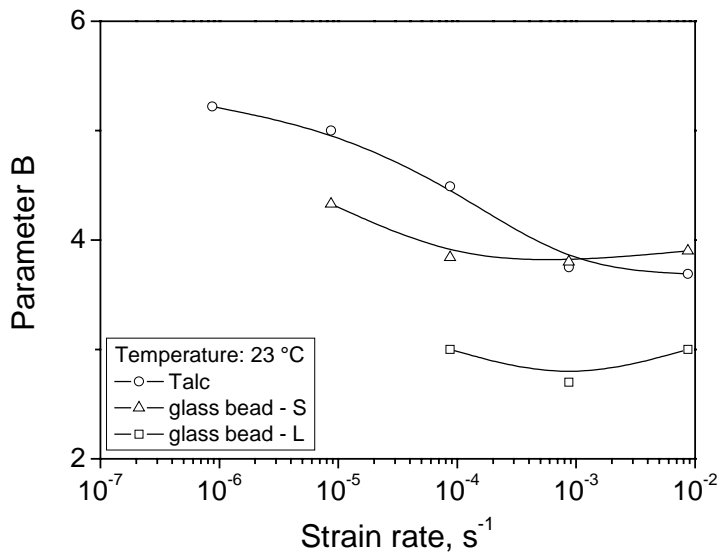


Fig. 12. Strain rate dependence of parameter B for the fillers studied.

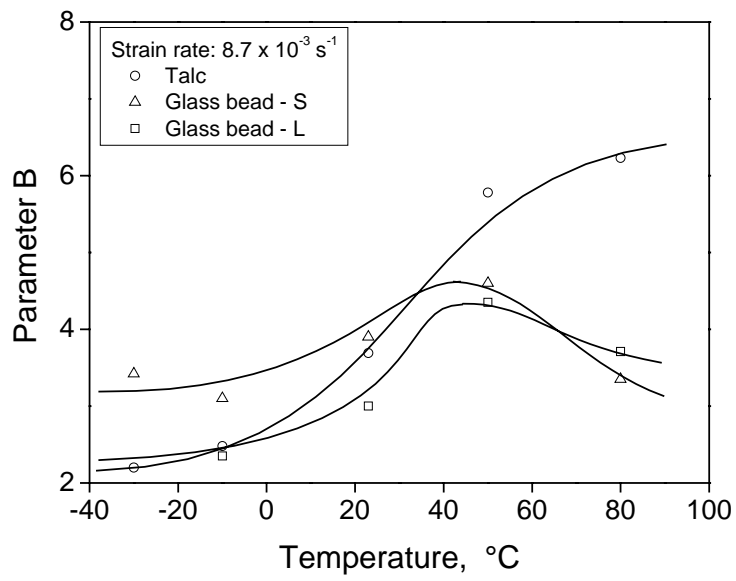


Fig. 13. Temperature dependence of parameter B for the three fillers used in this study.

PAPER 4^o**FILLER/MATRIX-DEBONDING AND MICRO-MECHANISMS OF DEFORMATION IN PARTICULATE FILLED PP COMPOSITES UNDER TENSION**

Michael Jerabek^{a,*}, Zoltan Major^b, Károly Renner^{c,d}, János Móczó^{c,d}, Béla Pukánszky^{c,d}, R.W. Lang^b

^a Polymer Competence Center Leoben GmbH, Rosegger Strasse 12, 8700 Leoben, Austria

^b Institute of Materials Science and Testing of Plastics, University of Leoben, Franz-Josef-Strasse 18, 8700 Leoben, Austria

^c Laboratory of Plastics and Rubber Technology, Department of Physical Chemistry and Materials Science, Budapest University of Technology and Economics, H-1521 Budapest, P.O. Box 92, Hungary

^d Institute of Materials and Environmental Chemistry, Chemical Research Center, Hungarian Academy of Sciences, H-1525 Budapest, P. O. Box 17, Hungary

ABSTRACT

Volume strain measurements of particulate filled polypropylene (PP) composites containing different glass beads and talc as filler were carried out in tension at two temperatures (23 °C and 80 °C) in the strain rate range from $8.7 \times 10^{-5} \text{ s}^{-1}$ to $8.7 \times 10^{-3} \text{ s}^{-1}$ to determine the micro-mechanisms of deformation. While local cavitation mechanisms (micro-voiding, crazing, and micro-cracking) and subsequent debonding of the particles dominated as failure mechanisms at high strain rates and at room temperature, a more significant contribution of local shear yielding was observed with a reduced contribution of cavitation mechanisms at low

^o Paper will be submitted to Polymer.

*Corresponding Author: M. Jerabek

Tel.: +43 3842 42962 21; fax: +43 3842 42962 6; E-mail address: jerabek@pccl.at

strain rates or at 80 °C. This change in the dominating micro-mechanisms of deformation resulted in smaller volume strains during the tensile loading of the composites than for the respective neat matrix. Moreover, a novel approach is introduced for the detection of debonding using volume strain measurements, which takes into account the dilatational and deviatoric behavior of the neat matrix polymer and the composite, respectively. The results are supported by acoustic emission measurements carried out simultaneously with the same specimens.

Keywords: Particulate filled polypropylene; Micro-mechanisms of deformation; Volume Strain;

1. INTRODUCTION

Particulate filled polymer composites have been used in increasing quantities in various applications e.g., in the automotive industry, for appliances or as garden furniture [1, 2]. The properties of these composites are basically determined by the behavior of the matrix, the properties of the filler, the composition, the particle spatial distribution and the interfacial interaction [3]. Although such heterogeneous systems are of large scientific and practical interest, their behavior under external load is not fully understood. Further research is necessary to understand and to predict properly the debonding of the particles, i.e., the failure at the interface and the detachment of the particles from the matrix, as well as other micro-mechanisms of failure including shear yielding, crazing and micro-cracking.

The debonding stress is one of the key parameters of particulate filled composites and it is strongly related to particle size. Two models have been proposed in the literature [4-6] to calculate the debonding stress of spherical particles, which are not bonded chemically to the matrix. The first model derived by Vollenberg et al. [4, 5] is based on the assumption that the mechanically stored potential energy around a spherical inclusion is used for the creation of new surfaces at the moment of debonding. The authors assumed that debonding takes place around the poles of the spherical particle and proceeds instantaneously at an angle of 25°. The second model developed by Pukánszky and Vörös [6] is also based on

energy equalities but without the assumptions made by Vollenberg et al. [4, 5] and gives the debonding stress, σ_D , as

$$\sigma_D = -C_1\sigma_T + C_2\left(\frac{W_{AB}E}{R}\right)^{\frac{1}{2}} \quad (1)$$

where C_1 and C_2 are constants having exact physical meanings, σ_T is the thermal stress induced by the different thermal expansion of the components, W_{AB} is the reversible work of adhesion, E is the tensile modulus of the matrix and R is the radius of the particles. Accordingly, smaller particles debond at higher stresses, moreover, debonding occurs over a broad strain range due to the inherently wide particle size distribution of commercial fillers. The prediction of debonding stress is difficult with either model since their constants are not known and can not be determined by simple measurements.

In order to detect the onset and to investigate the further progress of debonding, several methods have been proposed in the literature and applied in practice like in-situ tensile experiments [7], volume strain measurements [8-10] or the measurement of acoustic emission [11, 12]. One of the first studies aimed at the determination of debonding stress of stiff particles in polymer composites was carried out by Vollenberg [4], who performed tensile tests under light microscope and assigned the initiation of the debonding process to a “kink” in the stress-strain curve. Since this irregularity in the stress-strain curve was not confirmed in later experiments, volume strain measurements have been used more and more frequently. Different approaches exist in the literature for the determination of the initiation of debonding. A bilinear fitting was applied to the volume strain curve and the intersection of these linear regimes was related to the onset of debonding in one approach [13], which, however, completely neglects the differences in the dilatational and deviatoric responses of the matrix and the composite, respectively. Another approach defines the onset of debonding as the deviation of the dilatational from the overall volume strain [9]. The behavior of the matrix is not considered in this approach, but the results showed that the matrix might deviate from the dilatational behavior of the composites at small strains. In order to account for the dilatational deformation of the matrix, Sinien et al. [14] proposed to subtract the volume strain of the matrix from that of the composite. They justified

their approach with the help of high-precision volume strain measurements, but this method fails to predict the onset of debonding properly due to differences in Poisson's ratio and thus in the dilatational volume strain of the matrix and composite, respectively. To overcome the drawbacks of the approaches described above, Meddad and Fisa [8] suggested the subtraction of both the dilatational volume strain of the composite and the volume strain of the matrix from composite volume strain. The different local strain states (i.e., strain distribution and degree of constraint) in the matrix and in the composite are not considered in this procedure, so that this may lead to a significant error in the evaluation of the debonding stress. A model separating the dilatational, deviatoric and cavitational parts of the volume strain curve was developed by Heikens et al. [15], which may in principle also lead to reasonable results for the debonding stress in polymer composites deforming with a single, well defined mechanism. However, it must be emphasized that in filled polymer systems such as the particulate filled PP composites investigated in this study, several micro-mechanisms may contribute to an increase in the cavitational component of deformation (volume strain). This include debonding at the particle-matrix interface, and various mechanisms of void formation, crazing, and micro-cracking in the matrix [16, 17]. This, of course, complicates the experimental determination of the debonding stress via volume strain measurements.

In order to overcome the problems mentioned above and to make use of volume strain measurements for the characterization of the debonding process, a novel approach is introduced which is supported and verified by acoustic emission measurements. Hence, volume strain curves of the neat polymer, as well as talc and glass bead filled PP composites were determined and analyzed as a function of strain rate and temperature, and the dominating micro-mechanical deformation process under various conditions were deduced.

2. EXPERIMENTAL

2.1. Materials

The matrix material was a development grade PP homopolymer, provided by Borealis Polyolefine GmbH Linz (Linz, Austria) and delivered as injection molded tensile bars corresponding to ISO 3167 type B. The same material was extensively characterized under monotonic compression and in long-term compressive relaxation tests [18, 19]. Two glass beads (GB) with different sizes, Spheriglass 3000 (GB-L), large, and Spheriglass 5000 (GB-S), small, from Potters Europe (Barnsley, UK), were used as spherical fillers. Luzenac A7 talc provided by Luzenac Europe (Toulouse, France) was used as non-spherical filler in order to change particle shape. Glass beads and talc were added at two different volume fractions to PP in order to study the influence of particle content on the deformation behavior of the composites. An overview of the nomenclature and composition of the composites studied is given in Table 1.

Table 1: Nomenclature and composition of the materials investigated

Material	Filler	Weight fraction of filler	Volume fraction of filler
PP	-	-	-
PP-G3.5S	GB-S	0.10	0.034
PP-G7.0S	GB-S	0.20	0.073
PP-G3.5L	GB-L	0.10	0.034
PP-G7.0L	GB-L	0.20	0.073
PP-T3.5	talc	0.09	0.035
PP-T7.0	talc	0.18	0.075

The mean particle size was determined from scanning electron micrographs (SEM) by counting more than 1000 particles for each of the fillers. Due to the platy structure of talc, its aspect ratio was also determined by measuring the length and thickness of the platelets. Properties necessary for the understanding of the behavior of the composites are listed in Table 2. The size and aspect ratio distributions are discussed in detail elsewhere [20].

Table 2: Elastic properties and particle characteristics of the investigated fillers. Tensile modulus and Poisson's ratio were taken from the data sheets of the supplier.

Particle	Tensile modulus (GPa)	Poisson's ratio	Mean diameter (μm)	Specific surface area (m^2/g)	Aspect ratio	Coating
GB-S	70	0.21	1.31	1.0 ²⁾	1	Yes
GB-L	70	0.21	1.58	0.6 ²⁾	1	Yes
Talc	90 ¹⁾	0.21 ¹⁾	1.73	9.0 ³⁾	8	No

1) Determined on bulk material.

2) Cital Test Method

3) Determined by BET measurement

2.2. Experimental setup

Tensile tests were performed using an electromechanical universal testing machine Instron 5500 (Instron LTD, High Wycombe, USA) at constant crosshead displacement rates of 0.01 mm/s and 1 mm/s corresponding to strain rates of $8.7 \times 10^{-5} \text{ s}^{-1}$ and $8.7 \times 10^{-3} \text{ s}^{-1}$. Tests were performed at 23 °C and 80 °C. Initial gauge length was 115 mm. The 3D Digital Image Correlation (DIC) system Aramis (Gesellschaft für optische Messtechnik mbH, Braunschweig, D) was utilized for the accurate determination of volume strain. The equipment is described in detail in [21]. To allow for a sufficient optical signal detection and to avoid heating of the specimen during testing, the light directed onto the specimen was provided by the cold light system Dedocool (Dedo Weigert Film GmbH; Munich, D). The 3D-DIC system consists of two cameras, which record simultaneously the front surface of the specimen during the tensile test. The relative position of the two cameras to each other and the position of the specimen in the 3D-space are assured by the calibration of the system. Hence, the out-of-plane movement of the specimen is corrected automatically and has no impact on the accuracy of the strain measurement. The full strain field on the front surface of the specimen is determined as a function of the longitudinal and transverse strains. Since the main focus of this investigation is on the volumetric behavior of the composites up to or

only slightly beyond the yield point, the deformation monitored was completely homogeneous. In this case an average strain can be calculated by taking the mean of all sub-sets of the evaluated area, thus obtaining one average value for the longitudinal and the transverse strains, respectively. This averaging procedure increases the accuracy of the measurement significantly without any loss of information.

In addition to volume strain, the acoustic signals transmitted by the debonding of the particles were recorded for selected testing conditions and composites using a Sensophone AED 40/4 apparatus. Signals with amplitudes larger than 21 dB were recorded during the measurements. Volume strain and acoustic signals were recorded simultaneously on the same specimen to avoid errors coming from specimen-to-specimen variations.

2.3. Data reduction

The DIC system was applied in terms of technical strains to evaluate the essential data. True longitudinal strain $\varepsilon_{t,l}$ and true transverse strain $\varepsilon_{t,t}$ are given by

$$\varepsilon_{t,l} = \ln(1 + \varepsilon_{n,l}) \quad (2)$$

and

$$\varepsilon_{t,t} = \ln(1 + \varepsilon_{n,t}) \quad (3)$$

where $\varepsilon_{n,l}$ and $\varepsilon_{n,t}$ are the nominal longitudinal and nominal transverse strains, respectively. The Hencky strain definition enables us to calculate the volume strain ε_v by the combination of the three principal strains according to

$$\varepsilon_v = \varepsilon_{t,l} + 2\varepsilon_{t,t} \quad (4)$$

assuming that deformations are equal in the width and thickness of the specimen. Poisson's ratio, ν was obtained in the strain range of 0.0005-0.0025 according to

$$\nu = -\frac{\varepsilon_{n,t2} - \varepsilon_{n,t1}}{\varepsilon_{n,l2} - \varepsilon_{n,l1}} \quad (5)$$

and the dilatational volume strain, $\varepsilon_{v,dil}$, is given by

$$\varepsilon_{v,dil} = \varepsilon_{t,l}(1 - 2\nu) \quad (6)$$

Nominal stress, σ_n , and true stress, σ_t , are defined as

$$\sigma_n = \frac{F}{A_0} \quad (7)$$

and

$$\sigma_t = \frac{F}{A_0(1 - \varepsilon_{n,l}\nu_n)} = \frac{F}{A} \quad (8)$$

in which F is the force, A_0 the initial and A the actual cross-section of the specimen.

3. RESULTS AND DISCUSSION

3.1. Effect of particle size and content on deformation behavior

True strain vs. volume strain and true strain vs. true stress curves are presented in Fig. 1* for PP and PP-G3.5S at two different strain rates. As the strain rate decreases, lower stress levels are obtained both for the neat and the filled PP. The true strain-true stress curves are nonlinear from the very beginning of loading, thus no “kink” as suggested by Vollenberg et al. [4] can be detected on the curve and utilized for the determination of the onset of debonding. The volumetric response of neat PP in tension can be roughly divided into three stages or components [22-27]. The first component of increasing volume strain is caused by the negative hydrostatic pressure developing in tensile loading. The second component developing on a local scale initially is related to the compaction of amorphous chains (involving local strain induced crystallization) and to the destruction of crystalline order accompanied and followed by various cavitation mechanisms (void formation, crazing and micro-cracking). While amorphous chain compaction results in a decrease of effective volume, the destruction of crystalline order and

* All figures of this paper are collected at the end of the text.

the appearance of the various cavitation mechanisms decrease the density and thus increase volume. In this stage of deformation, cavitation is the dominating micromechanical deformation process, in which the increase in volume strain approaches the increase in longitudinal strain. Finally, in the third and last stage of post-yield deformation (regime of strain hardening prior to ultimate failure) strain induced re-crystallization and post-crystallization also involving volume changes may take place on a global scale. The various competitive processes described depend on test conditions (strain rate and temperature).

Regarding the deformation range performed as part of the study, the first two stages contribute to volume strain up to the strain levels investigated (Fig. 1). When strain rate decreases, volume strain decreases since (i) the hydrostatic pressure developed is smaller and (ii) the molecules have more time to get aligned in the direction of the load. In addition to the mechanisms described for neat PP, the debonding process increases the volume strain of the composites further. Comparing the volume strain curves of PP and PP-G3.5S at the higher strain rate, it becomes apparent that at a volume strain of about 0.02 the composite exhibits a significantly larger volume strain due to the debonding of the particles from the matrix (see Fig. 1). The difference between PP and the composite is remarkably reduced at the lower strain rate. However, the volume strain of PP-G3.5S is slightly smaller than that of PP at strains below 0.06 and almost identical values were determined for the two materials at the yield point. Void formation, crazing and micro-cracking occur in the neat PP before yielding of the specimen, which contributes to the volume increase. In the presence of particles, the stress fields change locally and thus may suppress cavitation deformation modes at least to some extent (as long as the matrix remains attached to the particles), and instead may initiate local shear yielding of the surrounding matrix [28].

The effect of particle size on the volumetric behavior is shown in Fig. 2 for the lowest strain rate of $8.7 \times 10^{-5} \text{ s}^{-1}$. The comparison of the traces obtained for PP, PP-G3.5S and PP-G3.5L clearly shows that the volume strain of both composites is smaller up to a strain of 0.05. It is worth noting that although this behavior is explained by the suppression of cavitation deformation modes in the composite, but it may be caused at least partly by the limited accuracy of the determination of

volume strain. The differences in the deformation of the matrix and composite are rather small. However, the volume strain-true strain traces of PP-G3.5L and PP-G3.5S coincide up to the strain of 0.03. Beyond this strain level the volume strain of PP-G3.5L is larger than that of PP-G3.5S, because of the lower debonding stress of larger particles as predicted by Eq. 1. As a result of the particle debonding, voids are created and volume strain increases. The yield stress of PP-G3.5L is smaller than that of PP-G3.5S, because of the smaller effective load-bearing cross-section of the specimen in the former case, as described in detail in [20].

Volume strain depends also on volume fraction of filler, which becomes evident if we compare the traces of PP-G3.5S and PP-G7.0S. At very low strains (<0.01), volume strain increases mainly because of the different dilatational behavior of the composites. Adding glass beads to PP decreases Poisson's ratio and increases the dilatational volume strain (see Eq. 6). Any further increase of the volume strain-true strain curve in the post-yield regime may be attributed to the debonding of particles. The slope in these curves at larger strains can be related to particle content [29, 30], since the number and size of voids created are proportional to the volume fraction of the filler.

The effect of temperature on the deformation behavior of the various materials investigated is shown in Fig. 3, in which the traces of PP, PP-G3.5S and PP-G7.0S are compared. The volume strain of neat PP is smaller at elevated temperature than at 23 °C (see Fig. 1). The decrease of volume strain is mainly associated to (i) the changing value of Poisson's ratio (close to 0.5 at 80 °C) and (ii) to the significant contribution of local deformations in the amorphous regime. The composite containing the lower volume fraction of filler has a considerably smaller volume strain than the neat PP. This may be explained again by the suppression of micro-cracks, but also by the relatively larger debonding stresses compared to the yield stress of the composite. According to Eq. 1, the debonding stress is proportional to the square root of the tensile modulus of the matrix. The yield stress decreases more significantly than the square root of the modulus, i.e., debonding takes place at stresses more closely to the yield stress at 80 °C than at 23 °C.

An increase in volume strain was detected for composites with the larger volume fraction of filler compared to 23 °C. Up to a strain of about 0.05, the shape of the volume strain-true strain curve is similar for PP-G3.5S and neat PP. The volume strain of composites increases significantly beyond this strain level due to debonding. Such behavior can be observed also at smaller volume fractions, but at larger strains. As the particle content increases, the local strain among the particles increases and various micro-deformation processes are initiated at lower global strains.

3.2. Effect of particle shape and orientation on deformation behavior

True strain vs. volume strain and true strain vs. true stress curves are presented in Fig. 4 for PP and PP-T3.5 at two different strain rates. Due to the plate like particle geometry of talc, strain localization at the edges of these particles is significantly larger than for spherical particles. These high local strains lead to a noticeable reduction in the yield strain of the composite and to subsequent strain softening as a result of debonding. The characteristics of the true stress-true strain and true strain-volume strain traces changes significantly when platelets are added instead of spheres. Although the volume strain of PP-T3.5 is larger than that of the neat PP at both strain rates, the difference decreases with decreasing strain rate. Minor differences were found in the volume strain of the two materials at yield, indicating that up to the yield point the dominating micro-mechanism of deformation is not debonding, but volume strain is determined by the general volumetric behavior of the matrix. Beyond the yield point, the effect of strain rate on volume strain of PP-T3.5 can be explained by the strain rate dependence of the debonding stress and by changes in the specific deformation mechanisms related to the matrix. Due to the higher matrix modulus for higher strain rates, debonding at the higher strain rate also occurs at higher stress levels, however, at slightly lower strain levels. More importantly, the slopes of the true volume strain vs. true strain curves in the post-yield regime indicate a stronger contribution for cavitation mechanisms and shear yielding mechanisms, respectively, for the higher and lower strain rate.

Volume strain-true strain curves measured at 80 °C are shown in Fig. 5 for PP and for composites with both talc contents. The behavior of the talc filled composites differs significantly from that of neat PP. At a strain value of about 0.01 the volume

strain of the composites deviates from the one recorded for neat PP. Furthermore, the volume strain decreases in a strain range from 0.03 to 0.08 and starts to increase slightly before yield for the composite with the smaller filler content. Such a decrease in volume strain has also been observed for neat PE and PP by other authors and was related to volume compaction mechanisms (strain induced crystallization of amorphous regions) during tension loading [22, 23]. However, in contrast, such a behavior was not detected for the neat PP in this study.

Nevertheless, the explanation that the reduction of volume strain may be associated with the compaction of amorphous chains in this specific strain range is supported by the prevailing local stress field in particulate filled composites. This behavior can not be related to the interphase in particle filled composites [31-33]. The interphase consists of molecules attached to both the matrix and the particles, thus their mobility is significantly reduced. As a consequence, the transverse deformation during longitudinal straining is reduced leading to an effective decrease in Poisson's ratio. This in turn increases the volume strain of particulate filled composites but, might not be the dominating micromechanical deformation process for the talc filled composite. The debonding of particles is obviously not the dominating process up to the yield point for PP-T3.5. According to Eq. 1, the debonding stress is closer to the yield stress of the composite at 80 °C than at 23 °C. Hence, debonding may start beyond the macroscopic yield point and result in a significant increase of volume strain in the post-yield regime.

The volume strain curve of PP-T7.0 shows the same characteristic behavior as PP-T3.5. Strain localization between the particles increases significantly due to the larger volume fraction of filler and thus reduces the overall yield strain of the composite. Moreover, the prevailing level of local constraint also increases in the matrix, which may partly hinder amorphous chain compaction. Most of the particles are aligned in the direction of loading in the tensile specimen [34]. However, the orientation distribution of the particles also depends on particle content, as the space available for rotation in the melt flow process during specimen production is reduced with increasing filler content.

The influence of particle shape on volume strain behavior is compared in Fig. 6 for the composites with 3.5 v% filler content at 23 °C and 80 °C. Significant reduction

of the volume strain can be observed with increasing testing temperature both for the neat PP and for the composites. While the dominating micromechanical deformation processes are apparently similar for the neat PP at both temperatures (similar shape of the volume strain-true strain curve) and the increased molecular mobility of the matrix results in the reduction of volume strain, the dominating deformation process changes significantly with temperature for the composites. This large change in behavior is caused by the difference in the ratio of debonding stress to yield stress at the two temperatures and by the increased molecular mobility of the matrix at 80 °C. The changing deformation mechanism may also explain the relative increase in the yield strain of PP-T3.5 compared to that of the neat PP as the temperature increases from 23 °C to 80 °C. The smaller volume strain of PP-T3.5 compared to that of PP-G3.5 may be attributed to the prevailing local stress field with higher shear stresses at the edges of the platelets in the talc filled composite [35]. The higher local stresses may initiate the local shear yielding of the matrix between two particles and suppress the cavitation modes of deformation. Since for PP-G3.5S no decrease of volume strain occurred in the strain range measured, amorphous chain compaction may not be of prime importance. On the other hand, in the talc filled composite a decrease in volume strain is clearly visible, indicating that amorphous chain compaction plays a role even outbalancing any destruction of crystalline order. The relative importance of chain compaction may be caused by increased crystallinity or thicker lamellae due to the nucleating effect of talc [36, 37].

3.3. Determination of the debonding stress from volume strain measurements

In this section a new approach is introduced for the determination of debonding stress in polymer composites, which takes into account both the dilatational and the deviatoric behavior of the matrix and the composite. The volume strain of a polymeric can result from deviatoric, dilatational or cavitation deformation [9]. An appropriate approach has to account for the behavior of the matrix and for the difference in the dilatational response of the neat matrix and the composite because of the presence of the particles. Since in most cases stiff particles have a Poisson's ratio different from that of the matrix, the dilatation volume strain

changes with particle content according to Eq. 6. Volume strain and dilatational volume strain are plotted as a function of true strain in Fig. 7. Dilatational deformation was detected for PP up to 0.02 true strain, while deviatoric deformation was observed subsequently up to 0.09 strain. Cavitation occurs in the post-yield regime. In order to decouple the influence of the different dilatational behavior of the matrix and the corresponding composites, the dilatational volume strain is subtracted from the overall volume strain. The resulting curve represents volume change due to deviatoric and cavitation deformation (also including debonding of the particles). As in the selected example it may also be negative, whenever the dilatational volume strain is larger in a certain strain range than the overall volume strain.

In order to subtract the deviatoric and cavitation volume strain of the matrix from that of the composite, a “corrected” true strain was calculated for the composites to account for the different global yield strains of the neat matrix and the composite, respectively. Since the local strain (and stress) is significantly larger in particle filled composites than in the neat matrix, yielding occurs at a smaller global strain. When comparing the yield strain of composites containing small and large glass beads, differences of the yield strain in the order of a few per cent caused by the dependence of debonding on glass bead size were obtained, which were neglected. Thus, to account for the different local strain states in the neat matrix and the composites and to obtain the “corrected” true strain value for a composite that corresponds to the true strain value of the neat matrix, the true strain of the composites was multiplied by the ratio of the matrix yield strain to the composite yield strain.

Subsequently the deviatoric and cavitation volume strain curves of the matrix were subtracted from that of the composite (true differential volume strain) using the “corrected” true strain. The true differential volume strain vs. true strain traces are shown in Fig. 8 for PP-G3.5L and PP-T3.5. Note that Fig. 8 is plotted as a function of true strain and not against “corrected” true strain. The latter quantity was necessary only to subtract the deviatoric and cavitation volume strain of the matrix from that of the composite. For practical engineering reasons, the original global strain values were applied for the determination of the debonding stress.

Two principal cases can be distinguished when determining the onset of debonding:

- If the dominating micromechanical deformation process is the same in the matrix and the composite, the increase in the differential volume strain is related to debonding. This behavior was found for PP-G3.5L and is shown in Fig. 8, where the circle indicates the onset of debonding. The rate of debonding increases with increasing strain up to a certain strain level.
- A change in the dominating micro-mode of deformation may also result in a decrease of the differential volume strain (e.g., cavitation deformation modes in the matrix and shear yielding in the composite), as shown in Fig. 8 for PP-T3.5. In this case the onset of debonding was assigned to the point of inflection which was determined from the second derivative of the differential volume vs. longitudinal strain curve.

Utilizing the approach presented above, debonding stresses were calculated for the studied composites at different strain rates and temperatures. The effect of strain rate on the debonding stress is presented in Fig. 9 for the small and large glass bead composites as well as for talc composites. While the effect of strain rate on the debonding stress is not very pronounced (keeping in mind that only two orders of strain rate were investigated), the overall increase of the debonding stress with strain rate are in good agreement with theoretical predictions (Eq.1). Also evident from Fig. 9 is the effect of particle size on debonding stress, indicating that even small differences in particle size may considerably influence the performance of particulate filled composites. The largest debonding stresses were determined for the talc filled composites, which may be related to some extent to the large specific surface area of this filler. The results are summarized in Table 3 listing values for debonding and yield stresses and their ratio for the composites at two different temperatures and at the strain rate of $8.7 \times 10^{-5} \text{ s}^{-1}$. As expected, the debonding stress is significantly closer to the yield stress at 80 °C than at 23 °C, irrespective of the filler type. For the talc filled composite, debonding stress and yield stress are approximately equal.

Table 3: Characteristic stress values of the studied composites determined at the strain rate of $8.7 \times 10^{-3} \text{ s}^{-1}$.

Composite	Temperature °C	Debonding stress σ_D , MPa	Yield stress σ_y , MPa	σ_D/σ_y %
G3.5S	23	22.8	27.5	83
G3.5S	80	10.0	11.0	91
G7.0S	23	23.5	27.3	86
G7.0S	80	9.5	11.0	86
G3.5L	23	17.5	26.5	66
G3.5L	80	9.3	10.9	85
T3.5	23	26.4	27.9	95
T3.5	80	12.3	12.3	100
T7.0	23	27.0	28.7	94
T7.0	80	12.0	13.2	91

3.4. Acoustic emission

In order to validate the results obtained from the volume strain measurements, acoustic emission signals were detected during tensile loading. A true stress-true strain curve is presented in Fig. 10 for PP-G3.5L together with the individual acoustic signals detected during deformation. The majority of the events were detected in the pre-yield regime of deformation. The cumulative number of events was differentiated according to true strain and the maximum of the derivative function is considered as the strain, at which the rate of particle debonding is maximized [11, 12]. A threshold amplitude of the signals was set to distinguish between background noise and particle-matrix interface failure. Also, small particles generate signals with significantly smaller amplitudes than large ones, which makes the identification of interfacial failure difficult. For the fillers investigated in this study, only the large glass beads provided a sufficient number of events during deformation. Despite several trials, no results of sufficient signal accuracy could be obtained when investigating composites containing the small glass beads and talc.

The cumulative number of acoustic events up to the yield stress is plotted as a function of strain rate for PP-G3.5L in Fig. 11. At 23 °C the number of signals

increased significantly with increasing strain rate from 700 up to 1700. Simultaneously, the number of recorded events for 80 °C is significantly below the one for 23 °C, which is consistent with the results from volume strain measurements (i.e., debonding stress approaches the yield stress and fewer particles debond from the matrix at elevated temperatures). It should be mentioned, that the number of hits detected also depends on the damping behavior of the matrix. Thus, fewer signals were detected by the sensor with increasing temperature due to the associated damping increase and modulus decrease.

Debonding stresses determined by volume strain and acoustic emission measurements are plotted as a function of strain rate for PP-G3.5L in Fig. 12. The maximum in the derivative function of the cumulative number of hits was used for the determination of debonding stress by acoustic emission. Debonding stress values increase with increasing strain rate at both test temperatures (23 °C and 80 °C). Both methods, acoustic emission and volume strain, yield significantly smaller debonding stress values at 80 °C than at 23 °C. At 23 °C the debonding stresses obtained by acoustic emission are about 20 % larger than those determined by volume strain measurements. Conversely, only insignificant differences were found at 80 °C, where at a strain rate of $8.7 \times 10^{-3} \text{ s}^{-1}$ the debonding stress determined from volume strain was 9.3 MPa, while a value of 10.0 MPa was obtained by acoustic emission measurements. The larger debonding stresses at 23 °C derived from acoustic emission results may be related to the data evaluation procedure. As has been pointed out above, the data reduction procedure of the acoustic emission technique leads to a debonding stress at which the rate of debonding is maximized, while the volume strain technique yields the debonding stress values corresponding to the onset of debonding. For future studies, the peak value of the second derivative of the cumulative number of hits in acoustic emission measurements may provide a better estimate of the initiation of the debonding process and thus a more reliable number for the debonding stress.

4. SUMMARY AND CONCLUSIONS

Tensile tests at two different temperatures (23 °C and 80 °C) in the strain rate range from $8.7 \times 10^{-5} \text{ s}^{-1}$ to $8.7 \times 10^{-3} \text{ s}^{-1}$ including volume strain measurements were carried out on PP containing glass beads of different size distributions and talc and on the neat PP used as matrix in the composite. The objective was to develop a methodology for the accurate characterization of the debonding process in these particulate filled composites and to determine the dominating micro-mechanisms of deformation. A significant increase in volume strain was recorded for composites containing the larger glass beads compared to those prepared with the smaller glass beads. The processes of local deformation in the matrix included various cavitation mechanisms (void formation, crazing and micro-cracking) and shear yielding all being initiated prior to the yield point. The cavitation failure mechanisms (voiding, crazing, micro-cracking and debonding) were favored by the lower temperature (23 °C) and higher strain rates. At the elevated temperature (80 °C) or lower strain rates the volume strain of the composites was even smaller than that of the matrix, indicating a change in the dominating micro-mechanisms of deformation from the various cavitation mechanisms to local shear yielding. The volume strain of composites containing talc was also smaller than that of the neat PP. Volume strain decreased considerably in the pre-yield regime, indicating a complete change of the dominating micro-deformation process. The observed decrease in volume strain was explained by the compaction process of amorphous molecules and by the absence of debonding in this specific strain range. Based on the experimental results, a new approach was introduced for the determination of debonding stress values, which accounts for the dilatational behavior of the matrix and the composite, respectively, on the one hand, and for the deviatoric and cavitation deformation mechanisms of the matrix, on the other. The debonding stress was found to decrease with decreasing strain rate and increasing temperature, a result that agrees well with the prediction of theoretical models. Acoustic emission measurements were carried out to validate these results. Debonding stress values deduced from the latter experiments changed in the same way as a function of strain rate and temperature as the debonding stresses determined from volume strain measurements. However, the values determined

by acoustic emission were somewhat larger, which was related to the data reduction procedure. Overall, the proper analysis of volume strain measurements in particulate filled composites provides useful information on the micro-mechanisms of deformation at various test conditions.

Acknowledgements

This research was performed at the Polymer Competence Center Leoben GmbH (PCCL, Austria) within the framework of the K_{plus}-program of the Austrian Ministry of Traffic, Innovation and Technology with contributions by the *University of Leoben*, and *Borealis Polyolefine GmbH*. The PCCL is funded by the Austrian Government and the State Governments of Styria and Upper Austria. The research on heterogeneous polymer systems was partly financed by the National Scientific Research Fund of Hungary (OTKA Grant No. K 68748 and F 68579), we appreciate the support very much. One of the authors is indebted also to the János Bolyai Research Scholarship of the Hungarian Academy of Sciences.

References

- [1] Markarian J. *Plast. Additives Compound* 2004;6:26.
- [2] Morieras G. *Ind. Miner.* 2001;6:29.
- [3] Pukánszky B. Particulate filled polypropylene: structure and properties. In: Karger-Kocsis J, editor. *Polypropylene: structure, blends and composites*, vol. 3. London: Chapman and Hall; 1995. p. 1.
- [4] Vollenberg P, Heikens D, Ladan HCB. *Polym. Compos.* 1988;9:382.
- [5] Vollenberg P. The mechanical behaviour of particle filled thermoplastics. PhD Thesis, Eindhoven University of Technology, Eindhoven, 1987.
- [6] Pukánszky B, Vörös G. *Compos. Interfaces* 1993;1:411.
- [7] Bai SL, Wang M, Zhao XF. *Compos. Interfaces* 2003;10:243.
- [8] Meddad A, Fisa B. *J. Appl. Polym. Sci.* 1997;64:653.
- [9] Naqui S, Robinson IM. *J. Mater. Sci.* 1993;28:1421.
- [10] Yilmazer U, Farris RJ. *Polym. Compos.* 1983;4:1.
- [11] Dányádi L, Renner K, Szabó Z, Nagy G, Móczó J, Pukánszky B. *Polym. Adv. Technol.* 2007;17:967.

- [12] Renner K, Henning S, Móczó J, Yang MS, Choi HJ, Pukánszky B. *Polym. Eng. Sci.* 2007;45:1235.
- [13] Pukánszky B, Van Es M, Maurer FHJ, Vörös G. *J. Mater. Sci.*,1994;29:2350.
- [14] Sinien L, Lin Y, Xiaoguang Z, Zongneng Q. *J. Mater. Sci.* 1992;27:4633.
- [15] Heikens D, Sjoerdsma SD, Coumans WJ. *J. Mater. Sci.* 1981;16:429.
- [16] Friedrich, K. *Adv. Polym. Sci.* 1983;52/53:226.
- [17] Narisawa, I, Ishikawa, M. *Adv. Polym. Sci.* 1990;91/92:354.
- [18] Jerabek M, Ravi-Chandar K, Major Z, Lang, RW. To be published.
- [19] Jerabek M, Tscharnuter D, Major Z, Ravi-Chandar K, Lang, RW. To be published.
- [20] Jerabek M, Major Z, Pukánszky B, Lang RW. To be published.
- [21] Jerabek M, Major Z, Lang RW. To be published.
- [22] Addiego F, Dahoun A, G'Sell C, Hiver JM. *Oil Gas Sci. Technol.* 2006;61:715.
- [23] Addiego F, Dahoun A, G'Sell C, Hiver JM. *Polymer* 2006;47:4387.
- [24] Na B, Lv R. *J. Appl. Polym. Sci.* 2007;105:3274.
- [25] Dasari A, Rohrmann J, Misra RDK. *Mater. Sci. Eng. A* 2003;351:200.
- [26] Kausch HH, Gensler R, Grein CH, Plummer CJG, Scaramuzzino P. *J. Macromol. Sci.* 1999;38:803.
- [27] Machado G, Denardin ELG, Kinast EJ, Goncalves MC, de Luca MA, Teixeira SR, Samios D. *Eur. Polym. J.* 2005;41:129.
- [28] Dekkers MEJ, Heikens D. *J. Appl. Polym. Sci.* 1985;30:2389.
- [29] Farris RJ. *Trans. Soc. Rheol.* 1968;12:315.
- [30] Farris RJ, Falabella R, Tsai YD. *ACS Symposium Series* 1978;95:233.
- [31] Pukánszky B. *Eur. Polym. J.* 2005;41:645-662.
- [32] Maurer FHJ, Kosfeld R, Uhlenbroich T, Bosveliev LG. Structure and properties of highly filled high-density polyethylene. In: 27th Intl Symp on Macromolecules, Strasbourg, France, 6–9 July 1981.

-
- [33] Kardos JL. In: Ishida H, Kumar G, editors. *Molecular Characterization of Composite Interfaces*. New York: Springer, 1985 p. 1.
- [34] Choi WJ, Kim SC. *Polymer* 2004;45:2393.
- [35] Herbst, H. *Modeling and Simulation of the Thermomechanical Behavior of Heterogeneous Polypropylene Compounds*. Montanuniversitaet Leoben, Leoben, 2008.
- [36] Ferrage E, Martin F, Boudet A, Petit S, Fourty G, Jouffret F, Micoud P, De Parseval P, Salvi S, Bourgerette C, Ferret J, Saint-Gerard Y, Buratto S, Fortune JP. *J. Mater. Sci.* 2002;37:1561.
- [37] Pukánszky B, Belina K, Rockenbauer A, Maurer FHJ. *Compos.* 1994;25:205.

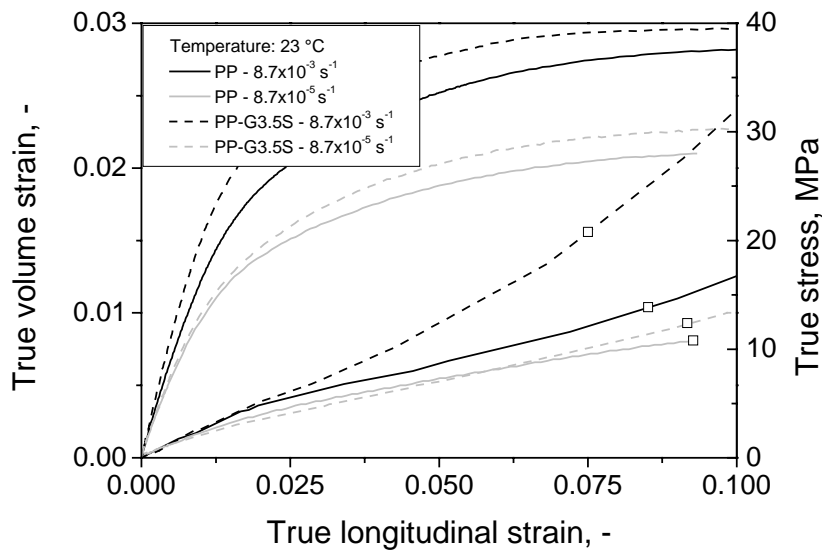


Fig. 1. True volume strain and true stress vs. true strain curves for PP and PP-3.5S recorded at two strain rates. The yield point determined on nominal stress-strain curves is also indicated by symbols (\square).

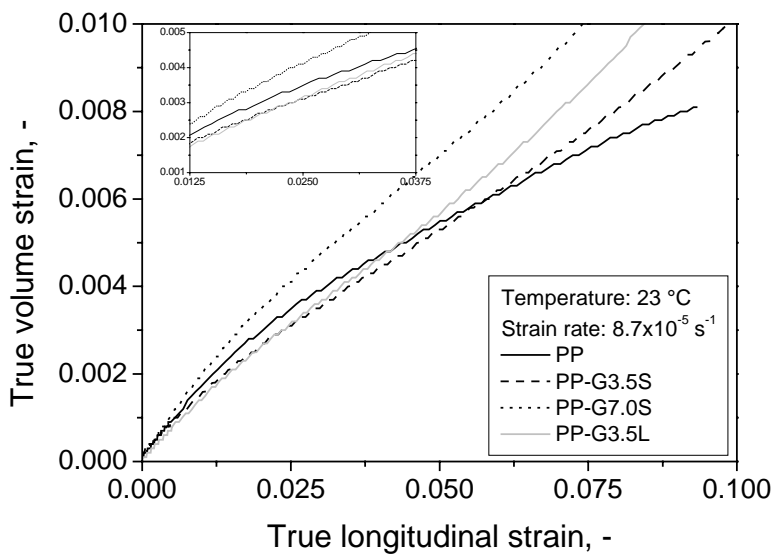


Fig. 2. Volume strain-longitudinal strain traces for neat and glass bead filled PP. Inset enlarges the strain range, in which the volume strain of the composites containing less filler is smaller than that of the neat PP.

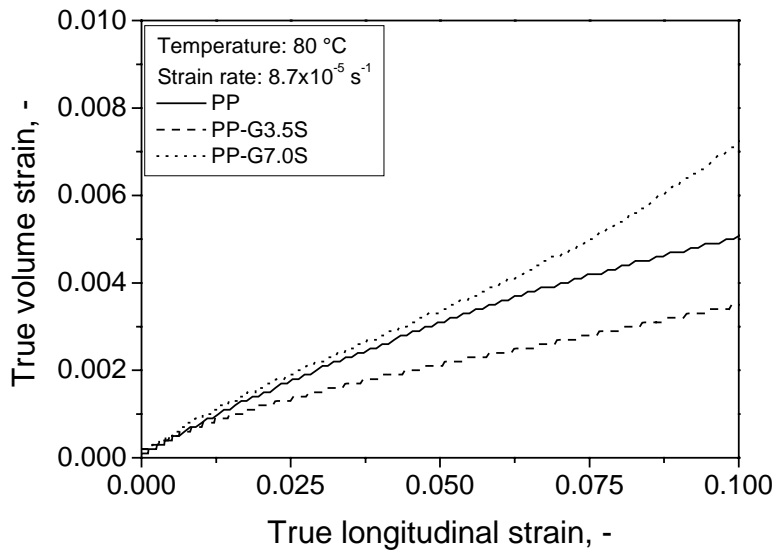


Fig. 3. Volume strain plotted as a function of longitudinal strain for PP and glass bead filled PP.

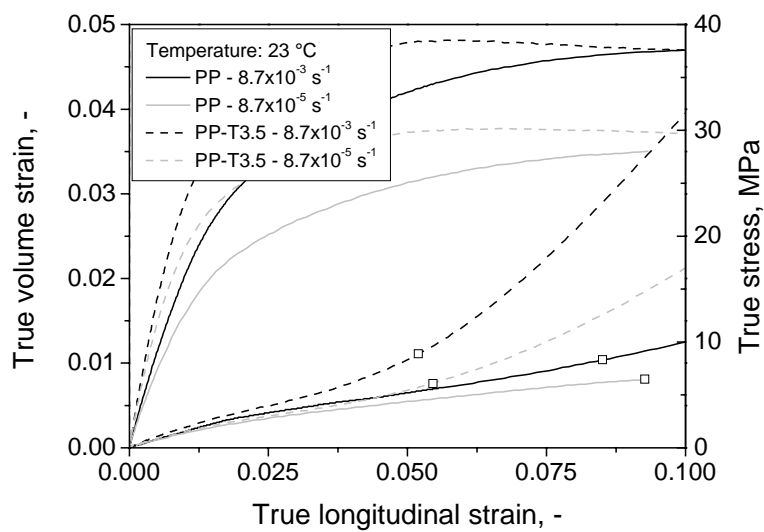


Fig. 4. True volume strain and true stress as a function of true longitudinal strain depicted for PP and talc filled PP; nominal yield point is indicated by symbols (□).

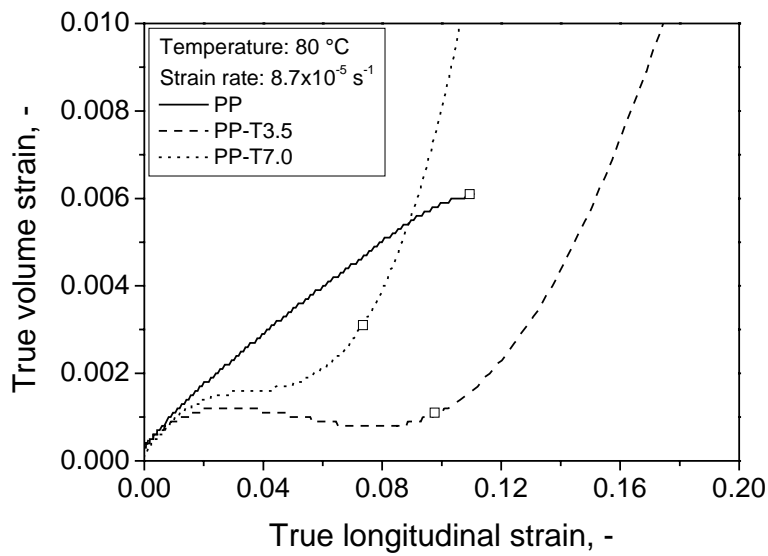


Fig. 5. Volume strain-longitudinal strain for neat PP and for composites containing different amounts of talc; nominal yield point is indicated by symbols (\square).

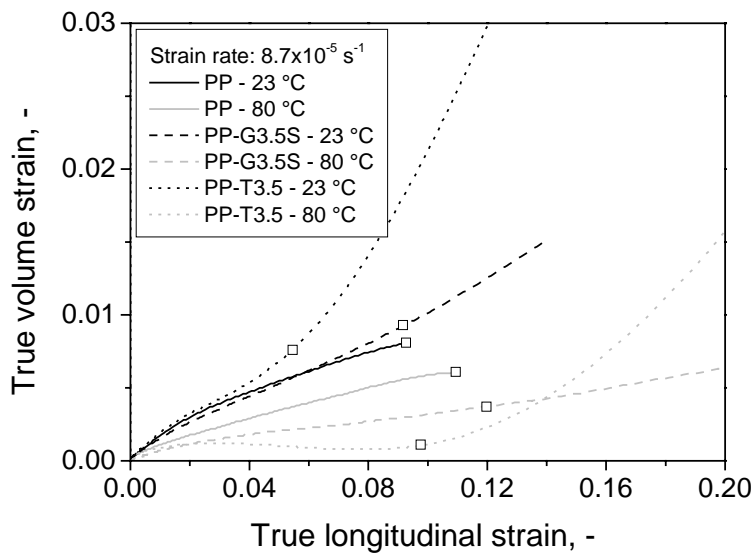


Fig. 6. Comparison of the deformation dependence of volume strain for PP composites at 23 °C and 80 °C; nominal yield point is indicated by symbols (\square).

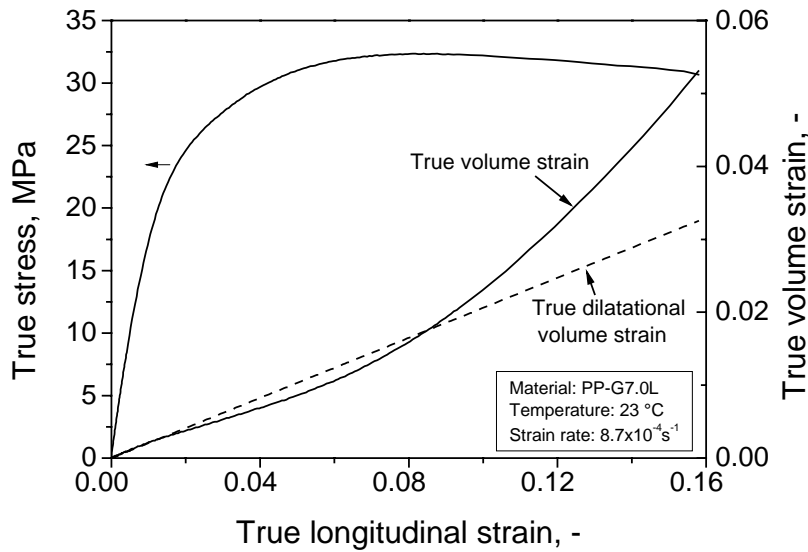


Fig. 7. Dilatational and overall volume strain plotted as a function of longitudinal strain; the stress-strain curve is also shown.

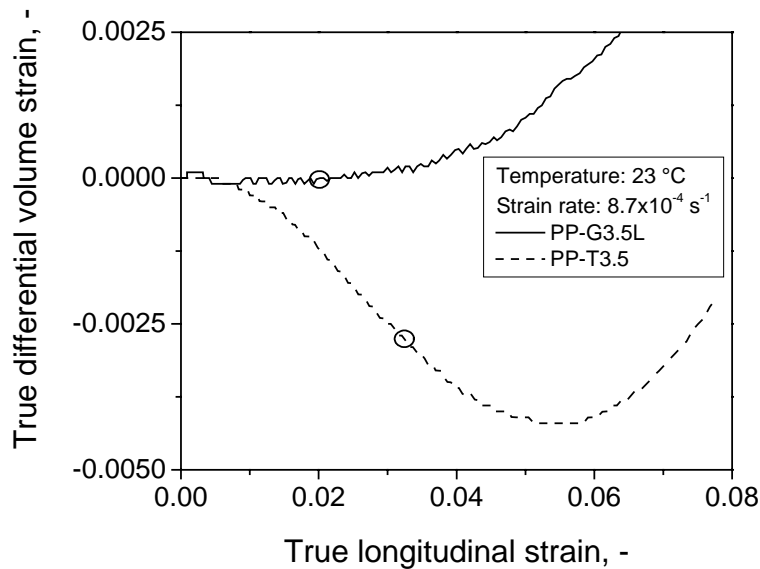


Fig. 8. True differential volume strain plotted as a function of true longitudinal strain for PP-G3.5L, which deforms with the same dominating micromechanical deformation mechanism as the neat PP, and for PP-T3.5 showing a significant change in the dominating micromechanical deformation. Circles indicate the onset of debonding.

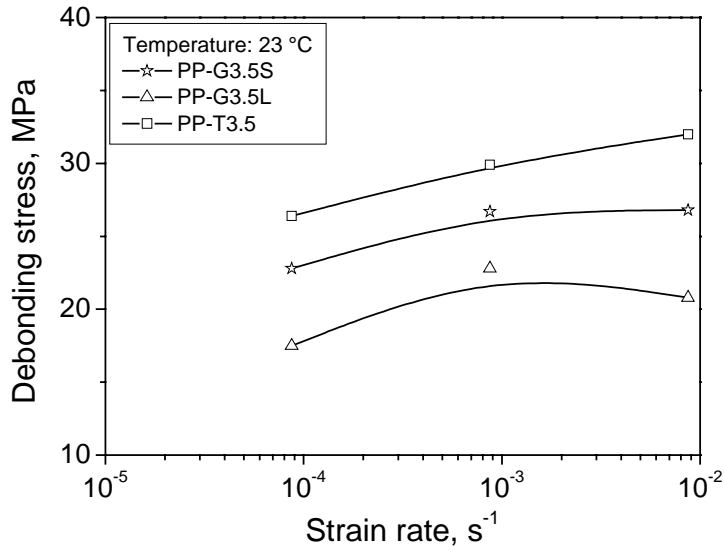


Fig. 9. Debonding stress plotted as a function of strain rate for the fillers studied.

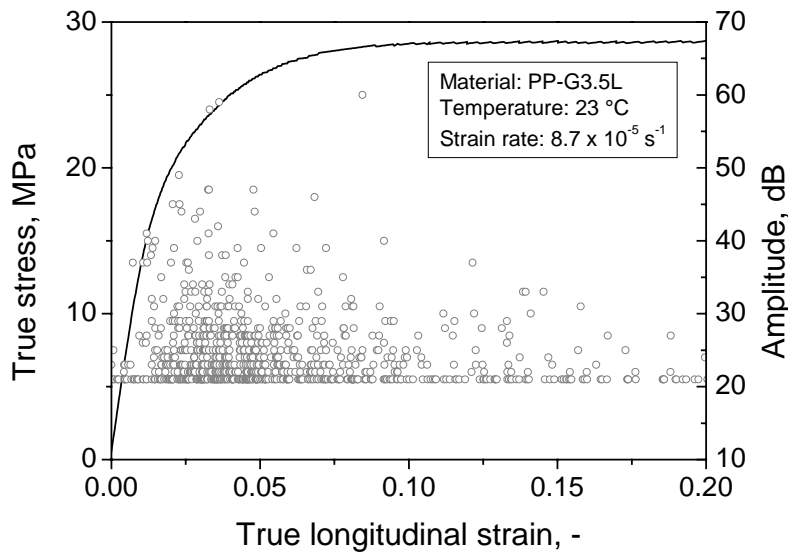


Fig. 10. True stress plotted against true strain together with the individual acoustic signals detected during the deformation of the sample.

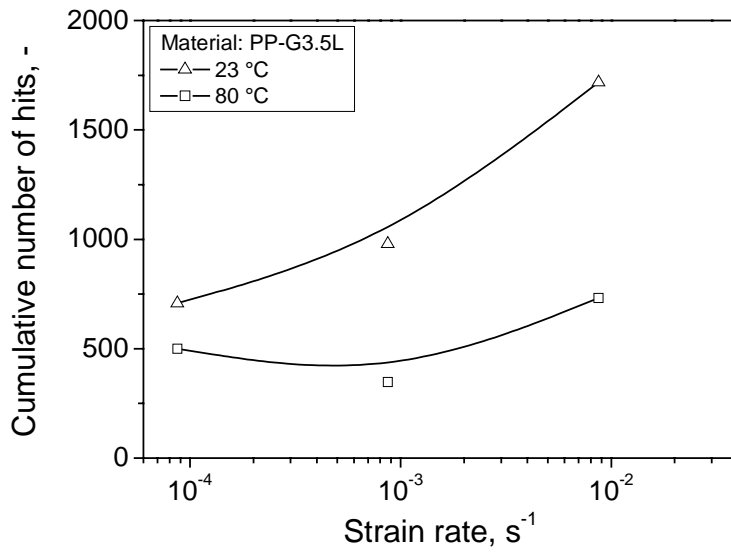


Fig. 11. Acoustic activity of PP-3.5L plotted against strain rate.

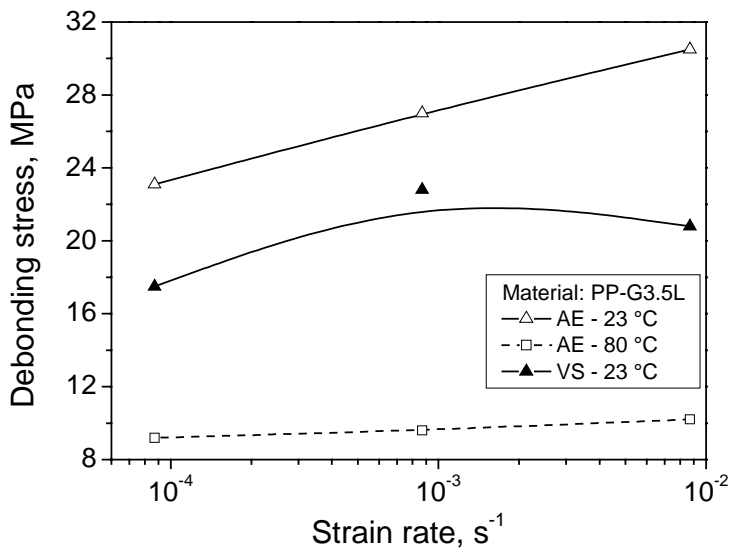


Fig. 12. Comparison of debonding stresses determined by acoustic emission and volume strain measurements at various strain rates.

PAPER 5[°]**MULTIAXIAL YIELD BEHAVIOR OF POLYPROPYLENE**

M. Jerabek¹, K. Ravi-Chandar², Z. Major³, R.W. Lang³

(1) *Polymer Competence Center Leoben GmbH, Roseggerstrasse 12, 8700 Leoben, Austria*

(2) *Center for Mechanics of Solids, Structures, and Materials, The University of Texas at Austin, 1 University Station, MC 6000, Austin, TX 78712-0235, U.S.A.*

(3) *Institute of Materials Science and Testing of Plastics, University of Leoben, Franz-Josef 18, 8700 Leoben, Austria*

Corresponding Author: M. Jerabek

Tel.: +43 3842 42962 21; fax: +43 3842 42962 6; E-mail address: jerabek@pccl.at

ABSTRACT

In order to characterize the yield behavior of polypropylene as a function of pressure and to verify the applicability of the Drucker-Prager yield function, various tests were conducted to cover the range of stress states from uniaxial tension and compression to multiaxial tension and confined compression. Tests were performed below and above the glass transition temperature, to study the combined effect of pressure and temperature. The experimental results were evaluated in terms of effective stress, to determine the equivalent stress vs. mean stress correlation and the pressure sensitivity index. An excellent linear relationship of equivalent stress vs. mean stress was found for all temperatures studied. To determine the pressure sensitivity as an intrinsic material parameter, normalized yield stresses were calculated with respect to the uniaxial tensile test. As expected, increasing pressure sensitivity values were found with increasing temperature, which was explained in terms of the free volume theory. The 3D Drucker-Prager yield function was fitted to the yield stresses and an average error between the predictions and the measurements of 8 % was obtained.

[°] Paper will be submitted to *Mechanics of Time Dependent Materials*.

Keywords: polypropylene; pressure dependent yielding; Drucker-Prager yield function; multiaxial compression

1. INTRODUCTION

In many engineering applications polymeric materials are exposed to complex multiaxial loading situations where in addition to tensile loads, compressive stresses may be dominant. Typical examples of multiaxial compressive loadings in practical applications of polymers include structural components exposed to direct compressive or bending loads like rollers, gears, bearings, damping materials and other similar applications. On a local scale, complex compressive stresses also play a major role in joint technologies (e.g., screw joints, clamping, fastening), in cutting processes and in tribological applications (i.e., friction, wear and scratch processes) also including fretting fatigue loads (Berer 2007; Stahlberg et al. 2006; Dubourg et al. 2003; Baek and Khonsari 2006; Myshkin et al. 2005). Another example for the development of multiaxial local stresses is in the area of polymer matrix composites, in which a multiaxial stress field develops on a local scale around the reinforcing phase, even though the external load applied to the material may be a uniaxial tensile load (Kakavas and Kontoni 2006).

Considering that the behavior of polymeric materials under tension and compression may differ particularly in the yield and post-yield regime (Sauer and Pae 1974; Sauer 1977; Dean and Crocker 2007; Rabinowitz et al. 1970), the need to characterize the whole range of stress states of plastics becomes evident. Moreover, the above examples indicate the importance of adequate test set-ups in a comprehensive manner and underline the need for appropriate test methodologies. Last but not least, adequate material data and material laws for multiaxial loadings are especially needed in advanced component design procedures and for structural reliability assessments based on modern simulation tools.

For the description of the 2D (plane stress) yield behavior of polymeric materials, von Mises or Tresca yield criteria modified to account for the pressure dependence have been widely used in recent investigations (Quinson et al. 1997;

Fasce et al. 2008; Ghorbel 2008). While these models are not capable to predict the onset of yielding in the 3D stress space under fully multiaxial loading conditions, reasonable results were obtained for plane stress states for amorphous and semicrystalline polymers unfilled and rubber-modified. To cover the whole range of real stress loadings, true multiaxial yield criteria must be applied to pressure dependent materials, in which the yield surface is shifted to larger values in the compression regime than those in the tensile domain (Bardenheier 1982; Pae 1977; Gol'dman et al. 1983). Moreover, it turned out that smooth yield functions (Drucker-Prager yield surface) inhibiting abrupt changes in the yield surface (e.g., Mohr-Coulomb yield function) are able to provide reasonably good results for viscoelastic materials (Kolupaev and Bolchoun 2008). As it has been applied successfully in recent studies, the Drucker-Prager yield criterion was used and applied to characterize the response of polypropylene (PP) in this investigation (Bardia and Narasimham 2006; Rittel and Dorogoy 2008).

In order to acquire sufficient experimental data for the evaluation of the yield surface, various test methods covering the whole stress range from biaxial and uniaxial tensile tests in the low pressure regime to fully confined compression tests in the high pressure regime were used. The latter provides true data values in the stress space and represents the deformation process of the bulk material. It completes the results of the uniaxial and plane strain compression tests and make the characterization of the pressure dependence of the deformation and yield behavior of polymers possible in the three principal axes. Thus, adequate material data for a pressure dependent yield criterion was determined and the methodology was applied to PP.

2. MATERIALS AND EXPERIMENTAL

The material investigated in this study was a development grade polypropylene (PP) homopolymer, manufactured and delivered by Borealis Polyolefine GmbH (Linz, A) either as injection molded plates, out of which all specimens were machined for the torsion test, biaxial tensile test and the various compression test set-ups, or as injection molded tensile specimens according to ISO 3167, type B. The identical material was characterized extensively under monotonic tensile

loading and in compressive relaxation tests (Jerabek et al. 2009). Further details as to the specimen geometries are described below. All tests were carried out at a strain rate of $8.7 \times 10^{-4} \text{ s}^{-1}$ and at ambient temperature. Tests at $80 \text{ }^\circ\text{C}$ and $-30 \text{ }^\circ\text{C}$ were performed for the various compression test set-ups and for the uniaxial tensile test. For all test set-ups only a brief introduction is given, as the reader is referred to the given literature for an in-depth explanation.

The biaxial *bulge* test was carried out, to investigate the behavior of the material in biaxial tension (Feichter et al. 2007). A round thin sheet of the material with a diameter of 140 mm and a thickness of 1 mm is clamped between two fixing grips and pressurized on one side by air, measuring simultaneously the exact pressure and the effective strain in the middle of the specimen system, where a biaxial stress state is guaranteed by the specimen geometry (Fig.1). Effective strain values were determined using a digital image correlation (DIC) system and nominal stress σ_n is given by

$$\sigma_n = \frac{\Delta p \cdot r_B \cdot \lambda^2}{2 \cdot t_0} \quad (1)$$

where Δp is the applied pressure, r_B is the bubble radius, λ is the extension ratio ($\lambda = \varepsilon + 1$), and t_0 is the initial thickness of the specimen. The true strain ε_t is defined as

$$\varepsilon_t = \ln(\varepsilon_n + 1) \quad (2)$$

where ε_n is the nominal strain. The true stress is given by

$$\sigma_t = \sigma_n (1 + \varepsilon_n) \quad (3)$$

where incompressibility of plastic deformation has been assumed. The uniaxial tensile tests were performed on an electro-mechanical universal testing machine of the type Instron 5500 (Instron LTD; High Wycombe, UK). The initial specimen length between the wedge grips was 115 mm. The axial strain was measured by a mechanical clip-on extensometer of the type Instron 2630-112 with an initial gage length of 50 mm. A temperature chamber was mounted on the frame of the testing

machine to carry out tests at $-30\text{ }^{\circ}\text{C}$ and at $80\text{ }^{\circ}\text{C}$. True stresses and strains were calculated according to Eqs. 2 and 3, respectively.

In order to characterize the torsion behavior of PP, an axial/torsional servo-hydraulic test system of the type MTS 359 (MTS Systems GmbH; Berlin, D) was utilized for these experiments, using the unnotched round bar specimen. The angle of twist, which is proportional to the shear strain, and the torque were measured to determine the shear strain vs. shear stress relationship and in terms of true strain and stress values, again Eqs. 2 and 3 were utilized.

In order to characterize the compression behavior of polymeric materials uniaxial and confined compression experiments were carried out using a recently developed compression device with aligning bars at each corner (Fig. 1) (Jerabek et al. 2009). Due to the four ball linings and highly accurate aligning bars, a precise and reproducible movement of the upper and lower compression plate is guaranteed and any transverse forces and moments are avoided. As to the accurate determination of axial strain, an LVDT mounted between the two compression plates was used. Again, all tests were carried out on the electro-mechanical driven universal testing machine of the type Instron 5500 (Instron LTD; High Wycombe, UK) also using the temperature chamber for non-ambient test temperatures.

As described in detail in (Jerabek et al. 2009), highly polished plates and a PTFE lubricant were used to minimize the effect of friction between the specimen surface and the compression plates. A uniform specimen deformation in the pre-yield regime up to the yield point was obtained, which was of prime interest in this investigation. For the determination of the true stress-true strain curve, a constant volume during deformation was assumed ($\nu=0.5$) applying Eqs. 2 and 3, as significant differences in the true stress values calculated taking the experimentally measured and the assumption based Poisson's ratio are only noticeable in the post-yield but not in the pre-yield regime.

The multi-axial confined compression test method used for this study corresponds to a method described in detail by Ma and Ravi-Chandar (2000) and Qvale and Ravi-Chandar (2004). The test set-up applied is shown in Fig. 2 along with a schematic illustration in Fig. 3. In this configuration the specimen is surrounded by

a confining cylinder, which restrains the free lateral expansion during axial loading without prohibiting it totally. Assuming a homogeneous deformation of the cylindrical specimen and a perfect fit between the specimen and the cylinder, the stress and strain field within the specimen and cylinder can be calculated via the Lamé solution, as shown in the next section. The measured values include the longitudinal force, local displacement provided by an LVDT, and the hoop strain of the confining cylinder determined via strain gauges mounted on the outer cylinder surface. By varying the thickness of the cylinder or by using a cylinder material of different modulus, the stress state applied on the specimen can be changed and adapted. Of special importance, this configuration allows for an inelastic as well as a viscoelastic characterization of polymers without a priori knowing the constitutive equation (Ravi-Chandar and Ma 2000; Qvale and Ravi-Chandar 2004). Furthermore, while in uniaxial compression testing an inhomogeneous specimen deformation may occur at high strains, in confined compression the strain localization is significantly reduced or eliminated.

In uniaxial and confined compression test set-ups, cylindrical specimens of 20 mm in length, l , and of 10 mm in diameter, $2a$, were used. It should be pointed out that specimens used for torsion, uniaxial and confined compression tests were machined from the 13 mm thick injection molded plates along the flow direction to avoid effects of different molecular orientations in the specimens. Confining cylinders of various diameters, $2b$, were produced out of rods made of a commercial polypropylene with outer diameters of 12 mm, 15 mm, 20 mm, 30 mm and 42 mm. For the analysis of the stress and strain field in the specimen, the mechanical behavior of the confining cylinder was determined via uniaxial tensile tests. The specimens were machined from the rods and tests were performed at the three different temperatures (23 °C, 80 °C -30 °C).

It should be noted that due to the limited accuracy in manufacturing the specimen and cylinder, a gap may exist at the start of the test and thus, the hoop strain at the outer surface of the cylinder may not develop from the onset of deformation when the axial load is applied on the specimen.

Definition of the Yield Point

Different approaches are described in the literature (Vincent 1960; Raghava et al. 1973; Mohanraj et al. 2006; Marano and Rink 2006) for the identification of the yield point, particularly in a monotonically increasing stress-strain curve. While several methods have no physical background (e.g., offset method, bilinear fit of the stress-strain curve), strain recovery experiments may predict the onset of yielding accurately based on irreversible deformation of the specimen (Marano and Rink 2001). As the number of test specimens increases significantly for the latter approach, a simple method was applied in this study. In uniaxial tension test, the first peak value in the stress-strain relationship was taken as the nominal yield point. In uniaxial compression the true stress-true strain curve was utilized to identify the strain at yield. Only slightly larger yield (true) strain was identified in compression than in tension tests. Due to the limited dependence of the yield strain on pressure, the yield strain values obtained in uniaxial compression were taken to be the yield strain to the confined compression experiments. The stress-state corresponding to the identified yield strain was calculated from the measurements in the confined compression scheme.

3. ANALYSIS OF THE COMPRESSION TESTS

Only a brief introduction into the analysis will be given in this paper, for a detailed description see Ma and Ravi-Chandar (2000) and Ravi-Chandar and Ma (2000). For the development of the strain and stress field a cylindrical coordinate system is utilized and the deformation of the specimen during the test is assumed to be uniform and homogeneous. The inner diameter of the specimen is $2a$ and the outer diameter of the cylinder is $2b$, as depicted in Fig. 3. The axial strain and stress applied on the specimen are

$$\varepsilon_n = \varepsilon_{zz}(r, \theta, z), \quad (4)$$

and

$$\sigma_n = \sigma_{zz}(r, \theta, z). \quad (5)$$

Different test methods can be compared only in terms of true strains and true stresses according to

$$\varepsilon_t = \ln(1 + \varepsilon_n) \quad (6)$$

and

$$\sigma_t = \sigma_n(1 + \varepsilon_n) \quad (7)$$

where again ε_t is the true longitudinal strain and σ_t the true longitudinal stress.

The confining cylinder provides a radial restraint on the deformation of the specimen. The pressures generated on the inner surface on the cylinder and on the outer surface of the specimen are equal and thus the stresses and displacements at the interface are given by

$$\sigma_{rr}(a) = \sigma_{rr}^c(a) = -\sigma \quad (8)$$

and

$$u_r(a) = u_r^c(a) > 0, \quad (9)$$

where the superscript c refers to the confining cylinder. Applying the Lamé solution (Timoshenko and Goodier 1934) of the stress field of an axisymmetric problem, the stresses, strains and displacements can be found to be functions of the unknown stress σ and can be related to the hoop strain measured at the outer surface of the cylinder. Furthermore, the hoop strain can be used to calculate the displacement at the inner surface of the cylinder. Due to the axial symmetry of the configuration the strains and stresses in the radial and circumferential direction are equal. Finally, by means of the boundary conditions the stress and strain fields can be calculated and are given by

$$\sigma_{rr} = \sigma_{\theta\theta} = -\frac{b^2 - a^2}{2a^2} E_c \varepsilon_h \quad (10)$$

$$\sigma_{zz} = \sigma_n \quad (11)$$

$$\varepsilon_{rr} = \varepsilon_{\theta\theta} = \frac{\varepsilon_h}{2} \left((1 - \nu^c) + (1 + \nu^c) \frac{b^2}{a^2} \right) \quad (12)$$

$$\varepsilon_{zz} = \varepsilon_n \quad (13)$$

where E_c and ν_c are the elastic modulus and Poisson's ratio of the cylinder and ε_h the measured hoop strain. From the equations 10-13 it is obvious that a complete description of the stress and strain field is given by only measuring three quantities (σ_n , ε_h , ε_n). The magnitude of the radial and circumferential stresses depends on the confinement level of the confining cylinder. The solution of the axisymmetric problem shown above (Eq. 10) corresponds to a fully elastic cylinder during the whole range of deformation. As indicated in the previous section, in some of the experiments reported here, polypropylene cylinders of different wall thickness were used as the confining cylinder. In order to account for the nonlinearity of the polypropylene cylinder, the results of the tensile tests were used for a numerical simulation performed with the commercial finite element code ABAQUS/Standard to obtain the hoop strain-pressure relationship. These data were then applied to calculate the radial and circumferential stresses using the hoop strain values measured at the outer surface of the cylinder. The simulations were performed for all testing temperatures and for all diameters of the cylinder.

Since the stresses and strains are obtained in the principal direction in the confined compression test, the characterization of the materials with respect to the deviatoric and dilatational behavior can be done in a straightforward manner. The dilatational and deviatoric parts of the stress and strain fields are

$$\sigma_m = \frac{\sigma_n + 2\sigma_{rr}}{3} \quad (14)$$

$$\varepsilon_v = \varepsilon_n + 2\varepsilon_{rr} \quad (15)$$

$$s_{ij} = \sigma_{ij} - \sigma_m \delta_{ij} \quad (16)$$

$$e_{ij} = \varepsilon_{ij} - \frac{\varepsilon_v}{3} \delta_{ij} \quad (17)$$

in which σ_m and s_{ij} are the mean and deviatoric stress components, δ_{ij} the Kronecker delta and ε_v and e_{ij} the volumetric and deviatoric strain components, respectively. Thus, the bulk and shear behavior of polymers can be characterized simultaneously under arbitrary pressure levels with the confined compression experiment. Due to the initial gap between specimen and cylinder and thus, the limited accuracy of the volume strain measurement, the dilatational behavior of the material was not considered in this research study.

For an accurate determination of the deviatoric behavior, the equivalent stress and equivalent strain definitions of Kachanov (Kachanov 1974) were applied, which enable the relation of the deviatoric strain to the deviatoric stress and are given by

$$\tau_e = \frac{1}{\sqrt{6}} \sqrt{(\sigma_{zz} - \sigma_{rr})^2 + (\sigma_{rr} - \sigma_{\theta\theta})^2 + (\sigma_{\theta\theta} - \sigma_{zz})^2 + 6(\tau_{zr}^2 + \tau_{r\theta}^2 + \tau_{\theta z}^2)} \quad (18)$$

$$\gamma_e = \sqrt{\frac{2}{3} \left[(\varepsilon_{zz} - \varepsilon_{rr})^2 + (\varepsilon_{rr} - \varepsilon_{\theta\theta})^2 + (\varepsilon_{\theta\theta} - \varepsilon_{zz})^2 + \frac{3}{2} (\gamma_{zr}^2 + \gamma_{r\theta}^2 + \gamma_{\theta z}^2) \right]} \quad (19)$$

where τ_e and γ_e are the equivalent stress and strain, respectively. For example, in the confined compression configuration this reduces to

$$\tau_e = \frac{1}{\sqrt{3}} |\sigma_{zz} - \sigma_{rr}| \quad (20)$$

$$\gamma_e = \frac{2}{\sqrt{3}} |\varepsilon_{zz} - \varepsilon_{rr}| \quad (21)$$

Relating the effective stress to the mean pressure acting on the specimen at the yield point, may provide a linear correlation with the slope being the pressure sensitivity index α according to

$$\tau_e = \tau_0 + \alpha \sigma_m \quad (22)$$

where τ_0 is the effective stress at zero pressure (torsion test).

4. RESULTS AND DISCUSSION

In the first part the behavior of the material in uniaxial tension, and uniaxial and confined compression is discussed in terms of stress-strain relationships. The pressure sensitivity index and the applicability of a 3D yield criterion for the prediction of the material response under arbitrary stress levels are presented in part two.

4.1. Uniaxial and Multiaxial Response of PP

The stress-strain curves of uniaxial tensile, uniaxial compressive and multiaxial compressive tests conducted at ambient temperature are depicted in Fig. 5. The tensile test is plotted up to the nominal yield point, thus the end of the curve does not represent ultimate failure of the specimen. Confined compression experiments were conducted to a value of longitudinal strain of 15 %, as up to this level the material does not get squeezed out between the loading pin and the confining cylinder. Beyond the initial seating effects seen in the two compression set-ups, the stress-strain curves surpass that of tension and considerably larger stress levels were observed depending on the level of confinement. This emphasizes the importance of characterizing polymeric materials under adequate testing conditions by applying proper constraint conditions and illustrates the wide range of compression behavior for PP. As to the determination of the yield stress, the simple approach described above was applied. In the post-yield regime, strain softening was observed in uniaxial compression. While no strain softening was determined for any of the b/a ratios, the tendency for strain hardening increases with higher constraint level.

True stress vs. true strain curves are depicted in Fig. 5 for three different test temperatures, comparing uniaxial tensile and compressive tests using an outer diameter of the confining cylinder of 20 mm. As expected, due to the viscoelastic nature of PP a significant increase in the stress values were obtained with decreasing temperature.

For the confined compression test, the constraint level was related to the radial stress applied to the specimen and is depicted as a function of true longitudinal

strain in Fig. 6. While no differences in the evolution of the radial stresses using different outer diameters of the cylinders were detected within the first 2 % of strain, nonlinear stress-strain curves developed after the specimen came into contact with the confining cylinder. The nonlinear stress-strain behavior is associated to the nonlinear stress-strain response of the PP specimen and confining cylinder, respectively. As expected, increasing radial stresses acted on the specimen with increasing confinement levels. These results indicate the significant pressure sensitivity of the PP investigated.

In order to determine and quantify the pressure sensitivity quantitatively, the deviatoric stress, given via Eq. 18, was calculated and plotted as a function of the equivalent strain in Fig. 7. Beyond the initial seating effects, higher confinement levels result in larger equivalent stresses, and strain softening is not observed. Appropriate dimensioning of the confining cylinder enables the variation of the stress state over a wide range of confinement levels from an almost uniaxial to a highly multiaxial stress state in the specimen. Relating these data to the predominant mean pressure in the specimen, enables the determination of the pressure sensitivity index necessary for pressure dependent yield criteria, as discussed in the next section.

4.2. Pressure Sensitivity and the Application to a 3D Yield Criterion

In principle, all mechanical properties i.e., modulus, yield stress, Poisson's ratio of polymeric materials depend on hydrostatic pressure (Tschoegl et al. 2002). In this investigation the yield stress as a function of pressure is considered and the applicability of the pressure dependent Drucker-Prager yield criterion (Drucker and Prager 1952) is analyzed. The equivalent stress as a function of mean stress is depicted in Fig. 8, calculated at the yield points. The pressure range covers a wide set of experiments from biaxial tension to fully confined compression. A linear relation between the equivalent stress and pressure was obtained for PP. This is similar to what is assumed in many publications to be the intrinsic material behavior (Quinson et al. 1997; Fasce et al. 2008), but bilinear and even nonlinear correlations have also been reported, depending on the stiffness, the molecular weight, and the crystallinity of the polymer (Sauer 1974; Sauer 1977). Moreover, the linear fit to the experimental data also shown in Fig. 8 provides the pressure

sensitivity index, an essential value used as input parameter for pressure dependent yield criteria (Bardia and Narasimhan 2006). The equivalent stress vs. pressure relation represents a part of the yield surface, i.e., while the applied load is below the obtained correlation, yielding of the material is inhibited. This yield surface is a characteristic for any material at a given deformation rate, temperature and physical aging state. It is worth noting, that the part of the yield surface plotted, is valid for monotonic loading conditions and may not predict the long-term failure of the material, which must be investigated on the one hand by long-term creep or relaxation tests and on the other by low and high cycle fatigue tests in the linear and nonlinear viscoelastic regime, respectively.

The maximum applied pressure in the confined compression test was about 60 MPa, which may not shift the glass transition temperature (T_g , about 0 °C for the PP studied) of PP above the ambient test temperature. As it turned out in previous investigations (Silano et al. 1977; Pae et al. 1986), T_g is shifted per 20 °C for 100 MPa of pressure, which may then considerably change the equivalent stress vs. pressure relationship. The significant effect of pressure may be related to the decrease of free volume and thus, to the reduced molecular mobility.

As the free volume is frozen below T_g and increases linearly with temperature above T_g (Ward 1971), a significantly enhanced pressure dependence may be expected at 80 °C, for which results of equivalent stress vs. pressure are depicted in Fig. 9. On the other hand, the pressure sensitivity should decrease for test temperatures below T_g , which is the case for a test temperature of -30 °C, for which equivalent stress is plotted as function of pressure in Fig. 10. For each of the two non-ambient test temperatures, an excellent linear correlation was obtained, also indicating that in the investigated pressure range only one molecular relaxation process is dominant. Equivalent stresses of more than 100 MPa were determined at -30 °C, which demonstrates the enhanced capabilities of polymeric materials under multiaxial compressive loading conditions.

In order to determine the effect of pressure as a function of temperature, the normalized equivalent stress was calculated based on the tensile equivalent stress. This procedure enables to calculate the pressure sensitivity free of

absolute values and allows for a determination of the intrinsic material behavior. The normalized equivalent stress is plotted as a function of mean stress in Fig. 11 for the two non-ambient test temperatures. As expected and explained above by the free volume and the molecular mobility, a significantly steeper slope of the linear fit was obtained for the elevated test temperature, while a reduced pressure dependence was noticed for -30 °C. The “normalized” pressure sensitivity index as a function of temperature is depicted in Fig. 12. An overall increase of the pressure dependence was obtained by a factor of 4 in the investigated temperature range. An appropriate function may be used to describe the pressure sensitivity vs. temperature relationship, but for an unambiguous determination obviously more test temperatures are necessary.

As to the prediction of the yield behavior of polymeric materials for arbitrary stress states, the pressure dependent 3D yield criterion of Drucker-Prager was utilized. This criterion can be given in the form

$$\sigma_e + \sigma_m \tan \alpha - \left(1 + \frac{\tan \alpha}{3}\right) \sigma_c = 0 \quad (23)$$

where $\sigma_e = \sqrt{3}\tau_e$ is the von Mises effective stress, and σ_c is the yield stress under uniaxial compression. In uniaxial compression, we see that $\sigma_e = \sigma$, $\sigma_m = \sigma/3$ satisfies the yield condition. If the pressure sensitivity index is zero, we recover the von Mises yield condition. For confined compression, $\sigma_e = (\sigma_{zz} - \sigma_{rr})$, and $\sigma_m = (\sigma_{zz} + 2\sigma_{rr})/3$; therefore, the Drucker-Prager criterion can be written as:

$$\sigma_{rr} = \frac{3 - \tan \alpha}{3 + 2 \tan \alpha} \sigma_{zz} + \frac{3 + \tan \alpha}{3 + 2 \tan \alpha} \sigma_c \quad (24)$$

The Drucker Prager yield function was fitted to the experimental test results and a best fit value of the pressure sensitivity index of about 31.5° was obtained, which is remarkably higher than those obtained for amorphous materials and for PP described in the literature (Quinson et al. 1997; Bardia and Narasimhan 2006). Note, that the pressure sensitivity indexes determined via Eq. 22 and 23 are two independent values and can not be compared to each other.

The resulting yield surface and the experimentally measured yield stresses in the various test set-ups are depicted in Fig. 13. The yield surface described by the Drucker-Prager criterion has a conical shape in the direction of but not axially symmetric to the hydrostatic axis. The criterion provides significantly larger yield stresses in the compressive than in the tensile regime. In fact, plastic deformation of the material is predicted under triaxial tensile loading conditions at a stress value of 72 MPa, while yielding under fully multiaxial compressive loading is prohibited. Intersection of the yield criterion with the plane-stress plane is also plotted, indicating the excellent agreement with the measured values. As the Drucker-Prager yield criterion has a conical shape, intersection with the plane-stress plane provides an ellipsoidal 2D yield surface, which is comparable to the modified von Mises yield criterion. The multiaxial confined compression test results are also shown in the 3D stress space in Fig. 13 along with the best-fit lines from the conical yield surface through the obtained multiaxial test results.

In order to quantify the prediction capabilities of the yield criterion, Table 1 provides an overview of the measured equivalent stresses and the calculated ones obtained from the best-fit yield surface. Except for the biaxial tensile test, all predictions for the various test set-ups are within a few percent with an average error of about 8 %.

Table 1: Summary of the equivalent stresses experimentally determined and predicted by the best fit Drucker-Prager yield function.

Test method	σ_e measured, MPa	σ_e calculated, MPa	Relative Error, %
Biaxial Tensile	26.0	33.4	26.8
Tensile	34.3	37.0	7.9
Torsion	39.6	44.0	11.3
Uniaxial Compression	55.4	55.4	0.0
Confined Compression (12 mm)	58.4	59.3	1.7
Confined Compression (15 mm)	62.4	64.4	2.6
Confined Compression (20 mm)	67.2	70.3	4.3
Confined Compression (30 mm)	69.6	75.8	8.7
Confined Compression (42 mm)	86.1	80.8	-6.3

As to the determination of the yield surface as a function of temperature and strain rate, suitable fitting functions may be applied to the pressure sensitivity vs. temperature (see Fig.11) and strain rate correlations to describe their behavior. The two effective parameters do not simply shift the yield surface to larger or smaller values, respectively, but may also change the slope of the yield surface significantly. Including the two fitting functions into the yield criterion, may allow for a complete description of the multiaxial yielding behavior of a viscoelastic material.

5. CONCLUSIONS

The objective of this paper is to characterize PP in different test configurations to cover a wide range of stress states and to apply a 3D yield criterion to predict yielding of the material in the 3D stress space. As to the determination of the yield point in various stress conditions, uniaxial and biaxial tensile tests, torsion tests, and uniaxial to confined compression tests were conducted. In order to characterize the effect of temperature, tests were performed at -30 °C, 23 °C and 80 °C.

As expected, vast differences in the true stress-strain behavior were determined depending on the degree of confinement, thus showing larger stress values in the compressive regime than in the tensile regime. In principle, the same trend was observed at all temperatures studied. Evaluation the equivalent stress at the yield point resulted in a linear correlation between the equivalent stress and the mean stress for all test temperatures. While the lowest equivalent stresses were obtained in the tensile regime (i.e., uniaxial and biaxial tensile tests) with a positive mean tensile stress upon the specimen, the highest equivalent stresses were found for the confined compression test with the largest mean compressive stresses investigated in this study. In order to calculate the pressure sensitivity index, normalized equivalent stresses were plotted against mean pressure and linear fittings were applied. As expected, the pressure dependency is seen to increase with temperature, which was attributed to the free volume in the amorphous phase and the macromolecular mobility.

In order to predict the onset of yielding in the 3D stress space, the Drucker-Prager yield criterion was utilized and fitted to the experimental values. A triaxial tensile yield stress of 72 MPa was predicted and a pressure sensitivity angle of 31.5° was obtained. The average error between the experimentally determined yield stresses and the 3D yield criterion is about 8 %, which clearly shows the applicability of the selected criterion for this class of materials. Moreover, the importance of adequate test methods and the determination of multiaxial data for accurate modeling of this class of materials are evident.

Acknowledgements

This research was performed at the Polymer Competence Center Leoben GmbH (PCCL, Austria) and at the Department of Aerospace Engineering and Engineering Mechanics at the University of Texas at Austin within the framework of the Kplus-program of the Austrian Ministry of Traffic, Innovation and Technology with contributions by *Borealis Polyolefine GmbH*. The PCCL is funded by the Austrian Government and the States Governments of Styria and Upper Austria.

References

- Bardenheier, R.: *Mechanisches Versagen von Polymerwerkstoffen*. Carl Hanser Verlag, München (1982)
- Bardia, P., Narasimhan, R.: Characterisation of Pressure-sensitive Yielding in Polymers. *Strain* 42, 187-196 (2006)
- Berer, M.: *Charakterisierung und Simulation des Verformungsverhaltens von Kunststoffrollen aus POM und PEEK*. Diploma Thesis. Leoben (2007)
- Baek, D.K., Khonsari, M.M.: Fretting behavior of a rubber coating: Friction characteristics of rubber debris. *Wear* 261, 1114-1120 (2006)
- Dean, G., Crocker, L.: Prediction of impact performance of plastics moulding Part 1: Materials models and determination of properties. *Plast. Rubber Compos.* 36, 1-13 (2007)
- Drucker, D.C., Prager, W.: Solid mechanics and plastic analysis for limit design. *Q. Appl. Math.* 10, 157-165 (1952)

- Dubourg, M.C., Chateauminois, A., Villechaise, B.: In situ analysis and modelling of crack initiation and propagation within model fretting contacts using polymer materials. *Tribol. Int.* 36, 109-119 (2003)
- Fasce, L.A., Pettarin, V., Marano, C., Rink, M., Frontini, P.M.: Biaxial Yielding of Polypropylene/Elastomeric Polyolefin Blends: Effect of Elastomer Content and Thermal Annealing. *Polym. Eng. Sci.* 48, 1414-1423 (2008)
- Feichter, C., Major, Z., Lang, R.W.: Method for Measuring Biaxial Deformation on Rubber and Polypropylene Specimens. In Proc. "13th International Conference on Experimental Mechanics" (2007)
- Ghorbel, E.: A viscoplastic constitutive model for polymeric materials. *Int. J. Plast.* 24, 2032-2058 (2008)
- Gol'dman, A.Y., Freidin, A.B., Lebedev, A.A.: Dependence of the Yield Point of Polymer Materials on Hydrostatic Pressure and Certain Plasticity Criteria. *Strength Mater.* 15, 373-377 (1983)
- Kachanov, L.M.: *Fundamentals of the Theory of Plasticity*. MIR Publishers, Moscow (1974)
- Kakavas, P.A., Kontoni, D.P.N.: Numerical investigation of the stress field of particulate reinforced polymeric composites subjected to tension. *Int. J. Numer. Methods Eng.* 65, 1145-1164 (2006)
- Kolupaev, V.A., Bolchoun, A.: Kombinierte Fließ- und Grenzbedingungen. *Forsch. Ingenieurwes.* 72, 209-232 (2008)
- Ma, Z., Ravi-Chandar, K.: Confined Compression: A Stable Homogeneous Deformation for Constitutive Characterization. *Exp. Mech.* 40, 38-45 (2000)
- Marano, C., Rink, M.: Viscoelasticity and shear yielding onset in amorphous glassy polymers. *Mech. Time-Depend. Mater.* 10, 173-184 (2006)
- Marano, C., Rink, M.: Shear yielding threshold and viscoelasticity in an amorphous glassy polymer: a study on a styrene-acrylonitrile copolymer. *Polymer* 42, 2113-2119 (2001)

- Mohanray, J., Barton, D.C., Ward, I.M., Dahoun, A., Hiver, J.M., G'Sell, C.: Plastic deformation and damage of polyoxymethylene in the large strain range at elevated temperatures. *Polymer* 42, 5852-5861 (2006)
- Myshkin, N.K., Petrokovets, M.I., Kovalev, A.V.: Tribology of polymers: Adhesion, friction, wear, and mass transfer. *Tribol. Int.* 38, 910-921 (2005)
- Pae, K.D.: The macroscopic yielding behaviour of polymers in multiaxial stress fields. *J. Mater. Sci.* 12, 1209-1214 (1977)
- Pae, K.D., Tang, C.L., Vijayan, K.: Effect of simple stress on the glass transition of polymers at high pressures. *J. Mater. Sci.* 21, 2901-2907 (1986)
- Quinson, R., Perez, J., Rink, M., Pavan, A. : Yield criteria for amorphous glassy polymers. *J. Mater. Sci.* 32, 1371-1379 (1997)
- Qvale, D., Ravi-Chandar, K.: Viscoelastic Characterization of Polymers Under Multiaxial Compression. *Mech. Time-Depend. Mater.* 8, 193-214 (2004)
- Rabinowitz, S., Ward, I.M., Parry, J.S.C.: The Effect of Hydrostatic Pressure on the Shear Yield Behaviour of Polymers. *J. Mater. Sci.* 5, 29-39 (1970)
- Raghava, R., Caddell, R.M., Yeh, G.S.Y.: The macroscopic yield behaviour of polymers. *J. Mater. Sci.* 8, 225-232 (1973)
- Ravi-Chandar, K., Ma, Z.: Inelastic Deformation in Polymers under Multiaxial Compression. *Mech. Time-Depend. Mater.* 4, 333-357 (2000)
- Rittel, D., Dorogoy, A.: A methodology to assess the rate and pressure sensitivity of polymers over a wide range of strain rates. *J. Mech. Phys. Solids* 56, 3191-3205 (2008)
- Sauer, J.A.: Deformation, Yield and Fracture of Polymers at High Pressure. *Polym. Eng. Sci.* 17, 150-164 (1977)
- Sauer, J.A., Pae, K.D.: The flow of solid polymers under high pressure. *Colloid. Polym. Sci.* 252, 680-695 (1974)
- Silano, A.A., Pae, K.D., Sauer, J.A.: Effects of hydrostatic pressure on shear deformation of polymers. *J. Appl. Phys.* 48, 4076-4084 (1977)

- Stahlberg, D., Junestam, P., Johansson, M., Gamstedt, E.K.: Relaxation properties of particle filled coatings: Experimental study and modelling of a screw joint. *Prog. Org. Coat.* 55, 112-118 (2006)
- Timoshenko, S.P., Goodier, J.N.: *Theory of Elasticity*. McGraw-Hill, New York (1934)
- Tschoegl, N.W., Knauss, W.G., Emri, I.: The Effect of Temperature and Pressure on the Mechanical Properties of Thermo- and/or Piezorheologically Simple Polymeric Materials in Thermodynamic Equilibrium – A Critical Review. *Mech. Time-Depend. Mater.* 6, 53-99 (2002)
- Vincent, P.I.: The necking and Cold-Drawing of Rigid Plastics. *Polymer* 1, 7-19 (1960)
- Ward, I.M.. *Mechanical Properties of Solid Polymers*. John Wiley & Sons Ltd., London (1971)



Fig. 1. Biaxial tensile test device also showing the specimen fixed between the two clamping devices

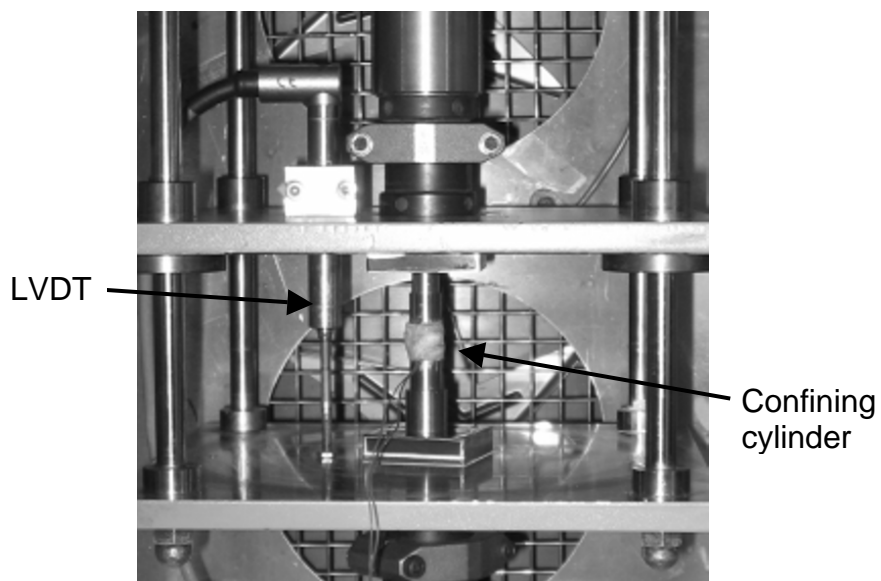


Fig. 2. Compression device utilized for the uniaxial and confined compression experiment. The four aligning bars at each corner and the set-up of the confined compression experiment can be seen.

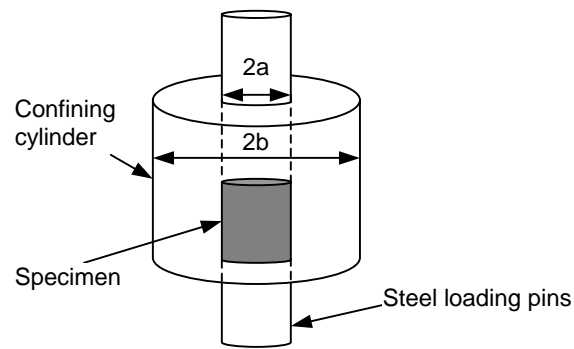


Fig. 3. Schematic diagram of the confined compression set-up

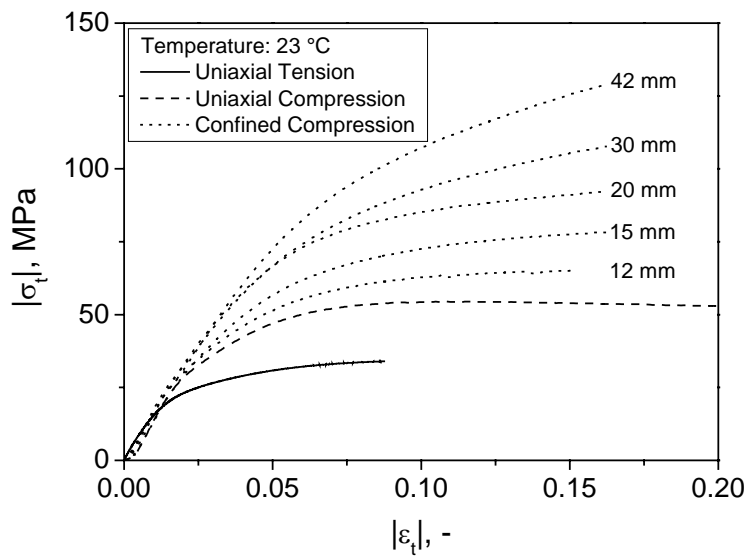


Fig. 4. True stress-true strain curves in uniaxial tension, uniaxial compression and confined compression measured at 23 °C. Each curve corresponds to the indicated diameter of the confining PP cylinder.

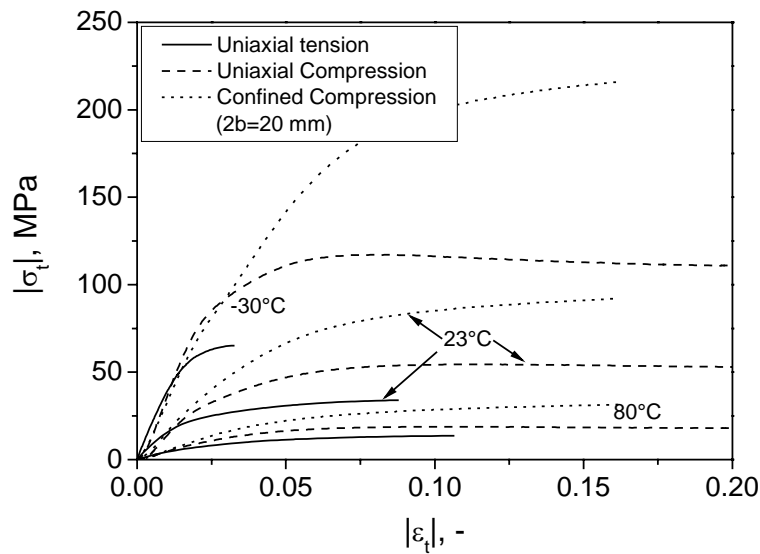


Fig. 5. Comparison of true stress-true strain curves of uniaxial tension, uniaxial compression and confined compression for all temperatures studied.

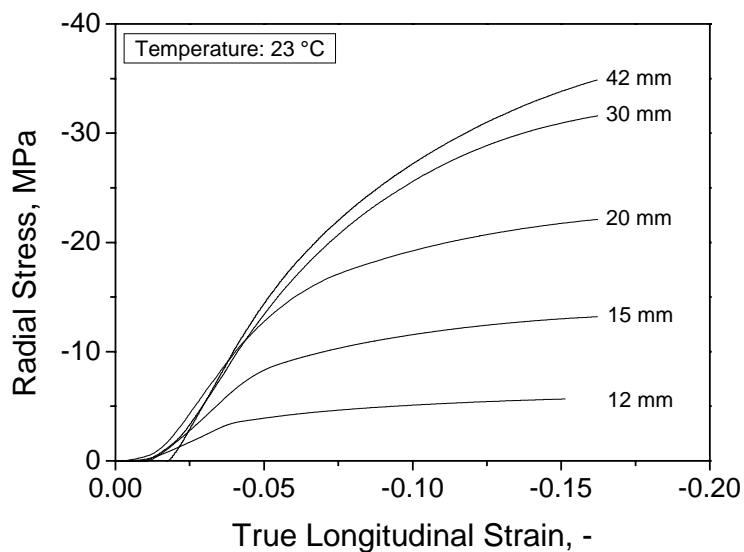


Fig. 6. Development of radial stress as a function of true longitudinal strain for the confined compression set-up. Each curve corresponds to the indicated diameter of the confining PP cylinder. Note that radial stress develops only after a small axial strain has been imposed; this is due to the initial clearance between the specimen and the confining cylinder.

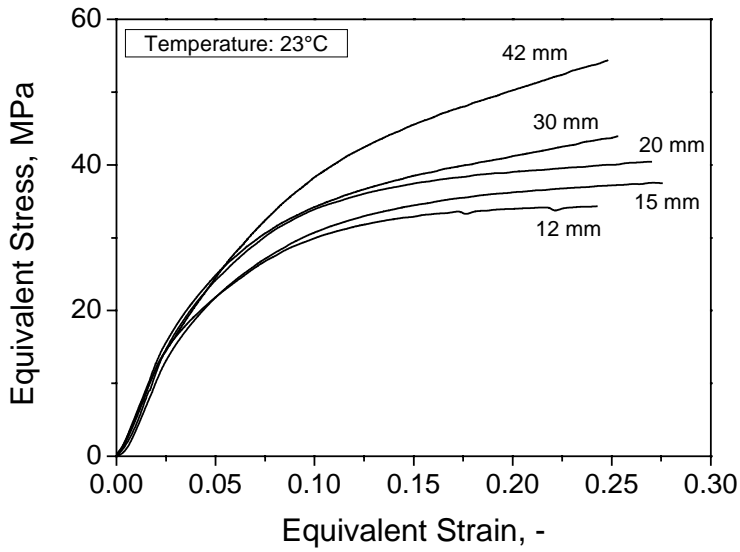


Fig. 7. Equivalent stress plotted against equivalent strain for the confined compression set-up. Each curve corresponds to the indicated diameter of the confining PP cylinder.

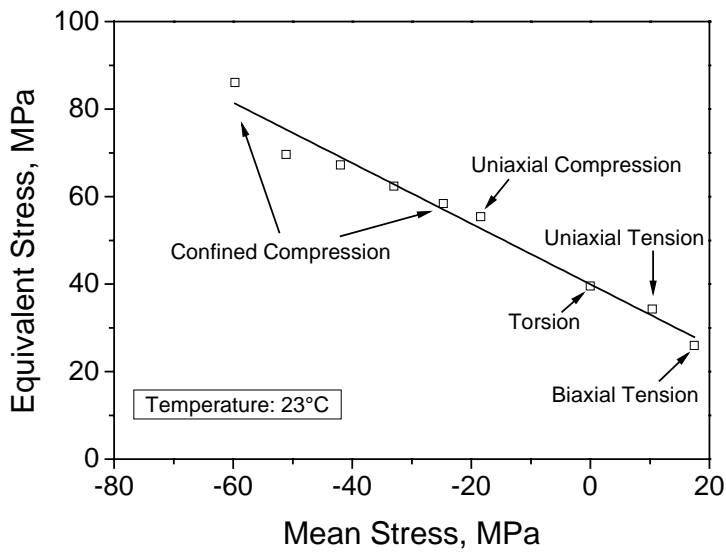


Fig. 8. Equivalent stress as a function a function of mean stress for 23 °C.

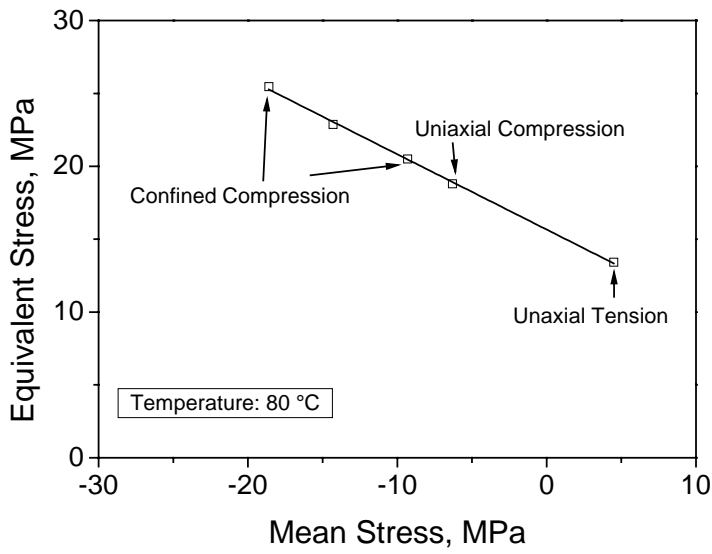


Fig. 9. Equivalent stress as a function a function of mean stress for 80 °C

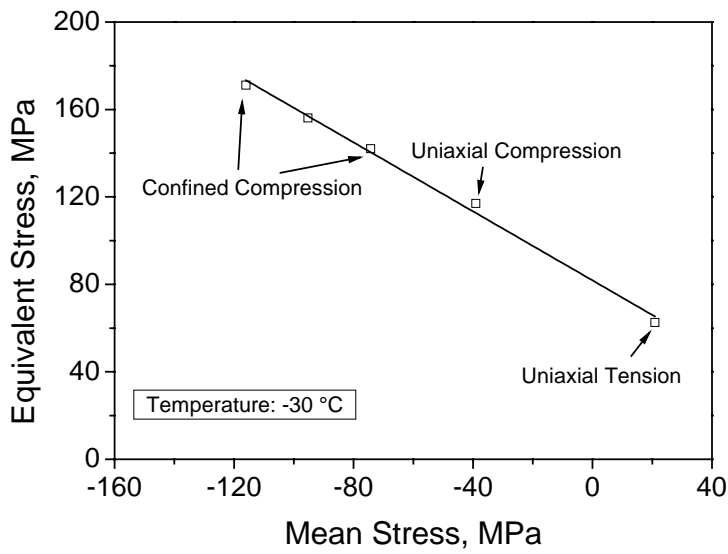


Fig. 10. Equivalent stress as a function a function of mean stress for -30 °C

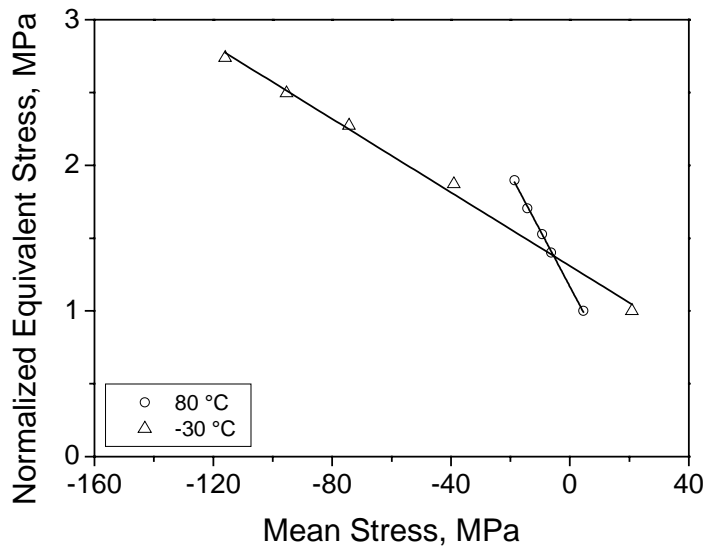


Fig. 11. Normalized equivalent stress plotted vs. mean stress for non-ambient temperatures

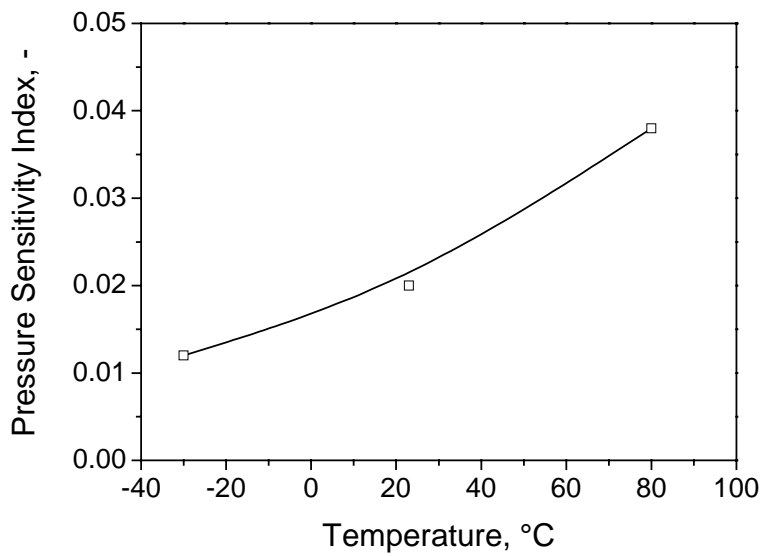


Fig. 12. Pressure sensitivity index as a function of temperature

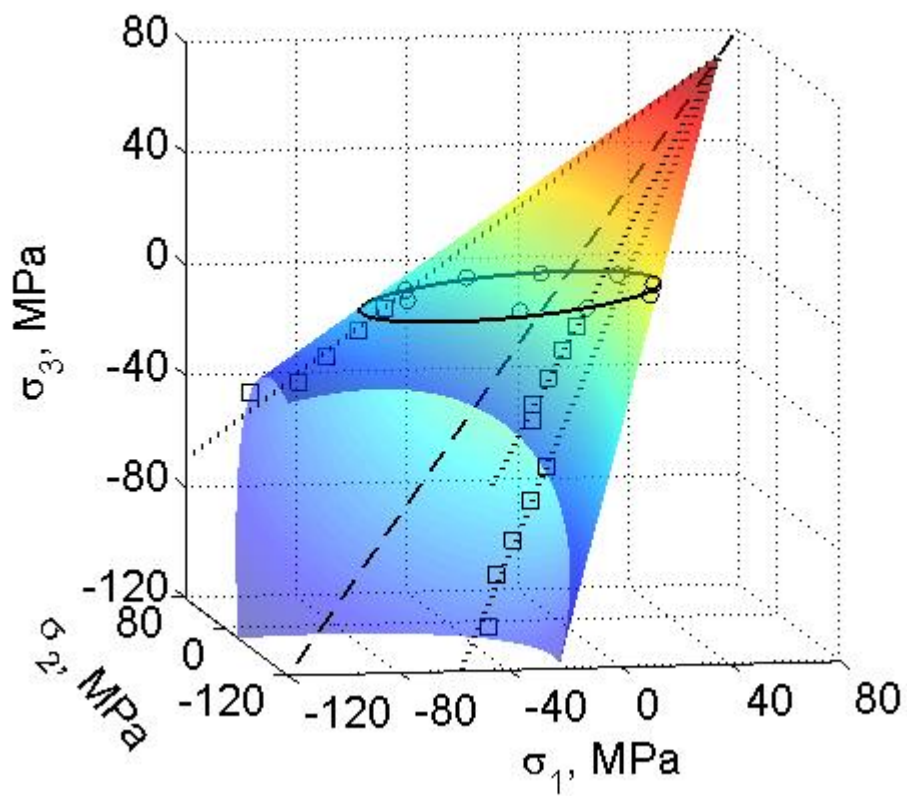


Fig. 13. Best fit Drucker-Prager yield function also indicating the hydrostatic axis and intersection with the plane-stress plane; experimental values are also depicted: (\square) confined compression, (\circ) plane stress values.

Paper 6[°]**RELAXATION BEHAVIOR OF NEAT AND PARTICULATE FILLED POLYPROPYLENE IN UNIAXIAL AND MULTIAXIAL COMPRESSION**

M. Jerabek¹, D. Tscharnuter¹, Z. Major², K. Ravi-Chandar³, R. W. Lang²

(1) *Polymer Competence Center Leoben GmbH, Roseggerstrasse 12, 8700 Leoben, Austria*

(2) *Institute of Materials Science and Testing of Plastics, University of Leoben, Franz-Josef-Strasse 18, 8700 Leoben, Austria*

(3) *Center for Mechanics of Materials, Solids and Structures, The University of Texas at Austin, 1 University Station, Austin, TX 78712, USA*

Corresponding Author: M. Jerabek

Tel.: +43 3842 42962 21; fax: +43 3842 42962 6; E-mail address: jerabek@pccl.at

ABSTRACT

The recently developed confined compression test was used to measure the viscoelastic bulk and shear relaxation moduli of neat, glass bead and talc filled polypropylene. In this paper further modifications of the test are introduced and a criterion for the assessment of the quality of experimental data is suggested. As expected, shear as well as the bulk relaxation moduli were found to increase with the addition of particles. In order to determine the pressure sensitivity of the material, unconfined compression tests were also performed and compared with the confined tests through interconversion of the measured moduli. In agreement with earlier results on other polymers, it turned out that the relaxation response is significantly retarded at higher confinement levels. It is shown that the effect of filler particles on the long-term behavior depends on the specific uniaxial or multiaxial stress state. Poisson's ratio was calculated by interconversion from the bulk and shear relaxation modulus; these results show that with a single test in the confined configuration, a complete viscoelastic characterization of the material can be obtained.

[°] Paper is submitted to Mechanics of Time Dependent Materials.

Keywords: relaxation test; uniaxial compression; confined compression; polypropylene; talc; glass beads; viscoelastic material functions; Poisson's ratio

1. INTRODUCTION

Determination of viscoelastic material functions dependent on time, temperature and pressure is of great importance for adequate modeling of polymeric materials. Commonly relaxation or creep experiments under uniaxial tensile loading conditions are performed and the corresponding creep compliance or the relaxation modulus is calculated. Performing experiments at different temperatures and making use of the time-temperature superposition principle gives rise to the master curve (Leaderman 1943), viscoelastic material models are developed assuming either a constant bulk modulus or a constant Poisson's ratio over the investigated temperature range to determine; interconversion yields all four viscoelastic material functions $[E(t), G(t), \nu(t), K(t)]$. As was shown by Lu (1997) and further by Tschoegl (2002) the determination of the bulk modulus is highly sensitive to the accuracy in measuring Poisson's ratio. Furthermore, according to the proposed methodology by Tschoegl (2002), two viscoelastic material functions should be measured in one test on the same specimen, i.e., determining relaxation modulus and Poisson's ratio in uniaxial relaxation experiments. Since from those measurements neither the shear nor the bulk modulus can be calculated with a high accuracy, experiments providing these values directly without the need for interconversion are necessary. Due to the complexity in the experimental configuration measuring particularly the bulk modulus, only few very special experiments of the two basic moduli – bulk and shear – can be found in literature (Deng and Knauss 1997; Kralj et al. 2001). Therefore Qvale and Ravi-Chandar (2004) adopted the recently developed confined compression setup (Ravi-Chandar and Ma 2000) for the viscoelastic characterization of polymers. In this experiment, the specimen is loaded under a multiaxial stress state and the bulk and shear moduli are calculated without interconversion.

In general the response of polymers on mechanical loading is strongly dependent on the hydrostatic pressure applied on the specimen (Rabinowitz et al. 1970). For this reason the yield stress measured in tension is lower than in compression

(Pae 1977). Therefore appropriate material modeling has to take into account the pressure sensitivity of the material, in addition to the usual effects of time and temperature (Knauss and Emri 1987). The confined compression configuration not only enables the direct measurement of the two basic viscoelastic material functions but also allows for the determination of the influence of pressure on the relaxation response. Interconversion of the shear and bulk moduli to the uniaxial modulus and comparison with uniaxial compression relaxation tests gives rise to the determination of the temperature dependent pressure sensitivity of the material.

Particulate filled polypropylene composites have been widely used in technical applications. There are a number of investigations of the micromechanics of such composites (Nemat-Nasser and Hori 1993; Vollenberg 1987; Renner et al. 2005) in order to determine the tensile properties (Pukanszky 1995; Fu et al. 2008) in comparison to the unfilled polymer. Few investigations have been carried out in the compression regime for unfilled polypropylene (PP) (Jerabek et al. 2009) and to our knowledge there is no study investigating the influence of particles on the compressive relaxation behavior. Thus, in this paper the properties of neat, glass bead filled (GB) and talc filled PP are investigated.

Hence, the main objectives of this work can be summarized as follows:

- Further development and application of the confined compression configuration for semicrystalline polymers.
- Calculation of all four viscoelastic material functions by interconversion of the shear and bulk moduli.
- Determination of the influence of pressure on the relaxation behavior of the investigated materials.
- Influence of particles on the relaxation behavior in the unconfined and confined compression tests.

2. MATERIALS

The matrix material was a development grade PP homopolymer from Borealis Polyolefine GmbH Linz (Linz, Austria), and as fillers Spheriglass 5000 from Potters Europe (Barnsley, UK) and Luzenac A7 talc provided by Luzenac Europe (Toulouse, France) were used. The specific compositions are listed in Table 1. The PP composites were provided from Borealis Polyolefine GmbH Linz as injection molded plates, from which the specimens were machined along the flow direction. The details of the processing of the composite as well as the results of the micromechanical simulations can be found in (Herbst 2008).

As can be seen from Table 1, two different volume fractions were tested for the glass bead filled composite in order to determine the influence of particle content on the moduli and particularly on the relaxation behavior. In order to characterize the influence of the particle shape and orientation on the properties of the materials, talc – which has a platelet like shape – is used as the filler in one of the materials investigated.

Table 1: Composite compositions investigated in this work.

Material	Filler	Volume fraction of filler
PP	-	-
PP-G3.5	Glass beads	0.035
PP-G7.0	Glass beads	0.070
PP-T7.0	Talc	0.070

One of the key characteristics of fillers that determines the debonding stress in the composite is the size and size distribution of the particles; large particles have a low value of the debonding stress (Pukanszky 1993). Therefore, the size distribution of the filler was determined and is shown in Fig. 1. Due to the platelet structure of talc its aspect ratio was also obtained by measuring the length and thickness of the platelets and the mean aspect ratio was determined to be about 8. The talc particles are mainly orientated along the axial direction of the specimen, which may reinforce the PP matrix. The specific particle surface area is significantly larger for talc than for the glass beads. Hence, the amount of PP

bonded to the particles and thus the interphase formed in the composite is larger for the talc filled composite and may have a significant effect on the mechanical properties. The mean particle size, the aspect ratio and the specific particle surface area are listed in Table 2.

Table 2: Characteristics of the investigated fillers.

	Mean particle size	Mean aspect ratio	Specific particle surface area
GB	1.31 μm	1	1 m^2/g ¹⁾
Talc	1.73 μm	8	9 m^2/g ²⁾

¹⁾ Cilas Laser Particle Size Analyzer

²⁾ Determined by BET measurement

3. EXPERIMENTAL SETUP

In order to characterize the compression behavior of polymeric materials a compression tool (see Fig. 2) was developed (Jerabek et al. 2009) and applied in this work. This tool consists of four aligning bars to ensure a correct uniaxial force transmission upon the specimen. Furthermore, local strain control was provided via a linear variable differential transducer (LVDT) for the uniaxial and the confined compression setup. This guarantees constant measurement constraints during the whole testing program. The displacement indicated in this paper refers to this local measurement via the LVDT (unless indicated otherwise).

In the confined compression setup a cylindrical specimen is placed inside a confining cylinder as shown in Fig. 3 and loaded in uniaxial compression in the special fixture discussed above. Assuming a perfect fit of the specimen and cylinder, the transverse strain of the specimen is restrained, dependent on the material and thickness of the confining cylinder. Proper dimensioning of the confining cylinder provides sufficient confinement level without inhibiting transverse strain entirely and without plastic deformation of the cylinder. The hoop strain of the cylinder is measured via a strain gauge mounted on the outer surface. As will be shown in the next section this method enables the determination of

the stress and strain of the specimen and cylinder simply by measuring the axial strain applied on the specimen, the force and the hoop strain on the cylinder.

In order to get reliable results there are some prerequisites for using this method. First, careful preparation of the specimen is absolutely necessary for compression testing and particularly when performing confined compression tests (Qvale and Ravi-Chandar 2004). For this purpose and to keep the testing constraints constant, specimens having equal dimensions are used in both methods with a diameter $2a$ of 10 mm and a length l of 20 mm. Attention was given to careful machining of the end surfaces of the specimen parallel to each other and perpendicular to the specimen axis. All dimensions are within ~ 0.005 mm. The confining cylinder was made of stainless steel, whose dimensions and material properties are given in Table 3. Accurate machining of the inner surface is necessary to get a perfect fit of the specimen and cylinder. Second, the contact surfaces have to be as smooth as possible to reduce the effect of friction during loading of the specimen. It was determined that friction may influence monotonic tests (Qvale 2003) but does not have a significant influence on long term relaxation loading, since frictional forces disappear few seconds after the loading. Third, tests below 0 °C may be influenced by ice formation, unless the humidity is controlled carefully. For this purpose a PTFE spray was used to reduce the generation of ice. Moreover, preloading of the specimen was performed to dissolve the ice between the steel loading pins and compression plates. Finally, at this highly confined stress state accurate temperature control is of crucial importance since even small variations may influence the test result. Proper test results could be obtained by ensuring the variation of the temperature to be within ± 0.5 °C.

In order to avoid any clearance between the specimen and cylinder a testing procedure based on different coefficients of thermal expansion between the specimen and the confining cylinder was applied. Due to the fact that polymers have a significantly higher thermal expansion coefficient than stainless steel, for the tests performed at temperatures above the room temperature a smaller specimen than the inner diameter of the steel cylinder was used. After the specimen was put into the cylinder the temperature was increased to a level below

the expected test temperature according to the initial specimen diameter and after reaching steady state an axial load was applied on the specimen. If the hoop strain develops immediately with the applied load then the specimen is in contact with the cylinder. Otherwise the axial loading was reversed, the temperature was increased by a few degrees and the procedure was repeated, until contact was established. This matches the specimen and confining cylinder to a particular test temperature and a relaxation test was performed at this condition. For tests performed below room temperature specimens having a larger diameter than the cylinder were used. Hence, in order to put the specimen into the cylinder the temperature was decreased below the testing temperature. Then the same procedure as described above was utilized to obtain contact between the specimen and the confining cylinder. This approach guarantees a perfect fit between the cylinder and the specimen at all test temperatures.

Table 3: Dimensions and material properties of the steel cylinder.

Inner Diameter	10.00 mm
Outer Diameter	11.75 mm
Modulus of Elasticity	210 GPa
Poisson's ratio	0.30

The specimen was loaded at a crosshead rate of 0.021 mm/s up to the final axial strain of 1 %. In order to avoid influences of the temperature on the thermal expansion of the test machine frame during the relaxation test, the crosshead bar was not kept constant during the test but was controlled by the local strain measurement. The measured crosshead displacement is shown in Fig. 4; keeping the crosshead constant obviously would result in a significant error.

4. DATA REDUCTION OF THE CONFINED COMPRESSION TEST

Only a brief summary of the analysis is given here; for a detailed description see Ma and Ravi-Chandar (2000), Ravi-Chandar and Ma (2000) and Qvale and Ravi-Chandar (2004). For the development of the strain and stress field a cylindrical

coordinate system is used and the deformation of the specimen during the test is assumed to be uniform and homogeneous. The inner diameter of the specimen is $2a$ and the outer diameter of the cylinder is $2b$, as depicted in Fig. 3. The axial strain and stress applied on the specimen are

$$\varepsilon_a = \varepsilon_{zz}(r, \theta, z), \quad (1)$$

and

$$\sigma_a = \sigma_{zz}(r, \theta, z). \quad (2)$$

The confining cylinder provides a radial restraint on the deformation of the specimen. The pressure that develops as a result of this constraint both on the inner surface on the cylinder and on the outer surface of the specimen is equal and the stresses and displacements at the interface are given by

$$\sigma_{rr}(a) = \sigma_{rr}^c(a) = -\sigma \quad (3)$$

and

$$u_r(a) = u_r^c(a) > 0, \quad (4)$$

where the superscript c refers to the confining cylinder. Applying the Lamé solution (Timoshenko and Goodier 1934) of the stress field of an axisymmetric problem the stresses, strains and displacements can be expressed as functions of the unknown stress σ and can be related to the hoop strain measured at the outer surface of the cylinder. Furthermore the hoop strain can be used to calculate the displacement at the inner surface of the cylinder. Due to the axisymmetric symmetry of the configuration the strains and stresses in the radial and circumferential direction are equal. Finally by means of the boundary conditions the stress and strain field can be calculated and is given by

$$\sigma_{rr}(t) = \sigma_{\theta\theta}(t) = -\frac{b^2 - a^2}{2a^2} E_c \varepsilon_h(t) \quad (5)$$

$$\sigma_{zz}(t) = \sigma_a(t) \quad (6)$$

$$\varepsilon_{rr}(t) = \varepsilon_{\theta\theta}(t) = \frac{\varepsilon_h(t)}{2} \left((1 - \nu^c) + (1 + \nu^c) \frac{b^2}{a^2} \right) \equiv \beta \varepsilon_h(t) \quad (7)$$

$$\varepsilon_{zz} = \varepsilon_a \quad (8)$$

where E_c and ν_c are the elastic modulus and Poisson's ratio of the cylinder and ε_h the measured hoop strain. From equations 5-8 it is obvious that a complete description of the stress and strain field is given by only measuring three quantities (σ_a , ε_h , ε_a).

Since the principal stresses and strains are obtained in the confined compression test, the viscoelastic characterization of the materials can be done in a straightforward manner. In order to calculate the bulk and shear moduli, the dilatational and deviatoric parts of the stress and strain field are calculated :

$$\sigma_m = \frac{\sigma_{zz}(t) + 2\sigma_{rr}(t)}{3} \quad (9)$$

$$\varepsilon_v = \varepsilon_{zz} + 2\varepsilon_{rr}(t) \quad (10)$$

$$s_{ij} = \sigma_{ij} - \sigma_m \delta_{ij} \quad (11)$$

$$e_{ij} = \varepsilon_{ij} - \frac{\varepsilon_v}{3} \delta_{ij} \quad (12)$$

in which σ_m and s_{ij} are the mean and deviatoric stress components, δ_{ij} the Kronecker delta and ε_v and e_{ij} the volumetric and deviatoric strain components. The bulk and shear behavior of a linear viscoelastic material are given by the following convolution integrals:

$$\sigma_{kk}(t) = 3\sigma_m(t) = 3 \int_{-\infty}^t K(t-\xi) \frac{\partial \varepsilon_v}{\partial \xi} d\xi \quad (13)$$

$$s_{ij}(t) = 2 \int_{-\infty}^t G(t-\xi) \frac{\partial e_{ij}}{\partial \xi} d\xi \quad (14)$$

where $K(t)$ and $G(t)$ are the viscoelastic bulk and shear moduli respectively. It is obvious from equation 5-8 that all values for the solution of the convolution integral are known.

As will be shown in the section 6.2., no significant changes in the hoop strain during the test were observed, thus, a constant hoop strain was assumed. Furthermore, to solve the convolution integrals with respect to the bulk and shear moduli, some kind of functional representation is necessary. It was shown that the series of decaying exponentials (Qvale and Ravi-Chandar 2004) provides an accurate fit of the experimental data:

$$K(t) = nK_{\infty} + \sum_{i=1}^n (K_i - K_{\infty}) e^{-\frac{t}{\tau_i}} \quad (15)$$

$$G(t) = nG_{\infty} + \sum_{j=1}^n (G_j - G_{\infty}) e^{-\frac{t}{\tau_j}} \quad (16)$$

K_{∞} , K_i , G_{∞} , G_j and τ_i , are determined for each temperature from the experimental data. A value of 4 was found to be the optimum value for n . The initial loading is assumed to be a step loading function since the loading sequence is very short compared to the testing duration. For this reason experimental data within the first 60 s of relaxation are not used for the data reduction. With these constraints the final equations for the viscoelastic characterization can be found.

$$\sigma_m(t) = nK_{\infty}[\varepsilon_a + 2\beta\varepsilon_h(t)] + \sum_{i=1}^n (K_i - K_{\infty}) e^{-\frac{t}{\tau_i}} [\varepsilon_a + 2\beta I_i(t)] \quad (17)$$

$$s_{zz}(t) = \frac{4}{3}nG_{\infty}[\varepsilon_a - \beta\varepsilon_h(t)] + \frac{4}{3}\sum_{j=1}^n (G_j - G_{\infty}) e^{-\frac{t}{\tau_j}} [\varepsilon_a - \beta I_i(t)] \quad (18)$$

with

$$I_i(t) = \int_0^t \frac{\partial \varepsilon_h(\xi)}{\partial \xi} e^{-\frac{\xi}{\tau_i}} d\xi \quad (19)$$

Equations 17 and 18 can be fit to the experimental data by an iterative process varying the constants from equation 15 and 16 characterizing the moduli. This

optimization was done by a MATLAB script. It was found out that the error between the fit and the measured data is less than 1 % and can therefore be neglected.

5. INTERCONVERSION OF THE SHEAR AND BULK MODULI

In theory, from any two viscoelastic material functions the remaining material functions of a homogeneous isotropic material can be determined by interconversion. Whether or not the interconversion leads to reasonable results depends strongly on the quality of the experimental data. Large errors may arise from specimen-to-specimen variations or non-identical test conditions when data from multiple tests are used in the interconversion (Lu et al. 1997). In this regard the simultaneous measurement of the two material functions in the confined compression test provides a key requirement for successful interconversion to determine the remaining material functions: the Poisson's ratio and the uniaxial relaxation modulus. The confined compression test scheme avoids errors arising from specimen-to-specimen variations and ensures identical experimental conditions for the two measured material functions.

For the following interconversion method the bulk modulus $K(t)$ and the shear modulus $G(t)$ are represented by a Prony series,

$$K(t) = K_{\infty} + \sum_{i=1}^{n_K} K_i e^{-t/\tau_{K,i}} \quad (20)$$

$$G(t) = G_{\infty} + \sum_{i=1}^{n_G} G_i e^{-t/\tau_{G,i}} \quad (21)$$

where the subscript ∞ denotes the equilibrium values. Their Laplace transforms are

$$K(s) = K_{\infty} \frac{1}{s} + \sum_{i=1}^{n_K} K_i \frac{1}{s + 1/\tau_{K,i}} \quad (22)$$

$$G(s) = G_{\infty} \frac{1}{s} + \sum_{i=1}^{n_G} G_i \frac{1}{s + 1/\tau_{G,i}} \quad (23)$$

where s is the transform variable. For an elastic material there exist relations between the four material constants. In the case of a linear viscoelastic material similar relations can be defined using the correspondence principle (Tschoegl 1989). According to this principle, the linear viscoelastic relations are obtained by substituting the Laplace transform of the linear viscoelastic quantity times the transform variable for the elastic quantity in the elastic relations, i.e. substitute $sG(s)$ for the elastic shear modulus G . Even though the interconversion method is the same for both the relaxation modulus and Poisson's ratio, the underlying relation for the latter is simpler and therefore more instructive to consider in detail. The elastic relation between bulk and shear modulus and Poisson's ratio for isotropic materials is

$$\nu = \frac{3K - 2G}{6K + 2G} \quad (24)$$

and therefore the relation for the linear viscoelastic Poisson's ratio is (Tschoegl et al., 2002)

$$\nu(s) = \frac{1}{s} \frac{3K(s) - 2G(s)}{6K(s) + 2G(s)} \quad (25)$$

Using the Laplace transforms of the moduli as defined in equations 22 and 23 this yields

$$\nu(s) = \frac{1}{s} \frac{3K_{\infty} \frac{1}{s} + \sum_{i=1}^{n_K} 3K_i \frac{1}{s + 1/\tau_{K,i}} - 2G_{\infty} \frac{1}{s} - \sum_{i=1}^{n_G} 2G_i \frac{1}{s + 1/\tau_{G,i}}}{6K_{\infty} \frac{1}{s} + \sum_{i=1}^{n_K} 6K_i \frac{1}{s + 1/\tau_{K,i}} + 2G_{\infty} \frac{1}{s} + \sum_{i=1}^{n_G} 2G_i \frac{1}{s + 1/\tau_{G,i}}} \quad (26)$$

When the Prony series parameters are determined by a least-squares fit, it is common practice to simplify the optimization problem by using predefined relaxation times which are usually logarithmically spaced on the time range covered by the data, with one or two relaxation times per decade in time. In this case only the respective relaxation strengths have to be determined. From the experience of the authors this approach leads to a larger number of parameters

than necessary in case the relaxation times are optimized as well, but it is still capable of providing a good fit. In the specific case of the relation for Poisson's ratio predefined relaxation times allow a simplification of the cumbersome eq. 26. We choose to define a common set of fixed relaxation times for both moduli, $\tau_{K,i} = \tau_{G,i} \equiv \tau_i$. Using this set of relaxation times, eq. 26 becomes

$$\nu(s) = \frac{\frac{1}{s} (3K_\infty - 2G_\infty) + \sum_{i=1}^n (3K_i - 2G_i) \frac{1}{s + 1/\tau_i}}{\frac{1}{s} (6K_\infty + 2G_\infty) + \sum_{i=1}^n (6K_i + 2G_i) \frac{1}{s + 1/\tau_i}} \quad (27)$$

To further simplify this equation, we introduce the abbreviations $a_i = 3K_i - 2G_i$ and $b_i = 6K_i + 2G_i$ and remove the fractions by multiplying the numerator and the denominator with $s \prod_{i=1}^n s + 1/\tau_i$.

$$\nu(s) = \frac{\frac{1}{s} a_\infty \prod_{i=1}^n s + 1/\tau_i + \sum_{i=1}^n a_i s \prod_{j \neq i}^n s + 1/\tau_j}{b_\infty \prod_{i=1}^n s + 1/\tau_i + \sum_{i=1}^n b_i s \prod_{j \neq i}^n s + 1/\tau_j} \quad (28)$$

By expanding the products and collecting terms of equal degree in s one can see that the numerator is a polynomial of degree n whereas the denominator is a polynomial of degree $n+1$.

Thus $\nu(s)$ is a rational function with $n+1$ poles s_j and is analytic in $\mathbb{C} \setminus \{s_j\}$. Clearly there also exist constants M and $p > 0$ such that

$$|\nu(s)| \leq \frac{M}{|s|^p} \quad (29)$$

The inverse Laplace transform is given by the integral

$$\nu(t) = \frac{1}{2\pi i} \int_{\gamma-i\infty}^{\gamma+i\infty} \nu(s) e^{st} ds \quad (30)$$

with $\lambda > \max_j \Re(s_j)$. It can be shown that for functions that satisfy the condition 29, the integral along a special circular contour vanishes (Schiff 1999). Consequently

the residue theorem (Schiff 1999) can be used to calculate the inverse Laplace transform.

$$\nu(t) = \frac{1}{2\pi i} \int_{\gamma-i\infty}^{\gamma+i\infty} \nu(s) e^{st} ds = \sum_j \text{Res}(\nu(s)e^{st}; s_j) = \sum_j e^{s_j t} \text{Res}(\nu(s); s_j) \quad (31)$$

where the sum extends over all poles. Finally the residues of the rational function $\nu(s)$ turn out to be simple poles, so that the residues can be calculated by

$$\text{Res}(\nu(s); s_j) = \frac{P(s_j)}{Q'(s_j)} \quad (32)$$

Here P and Q are the numerator and denominator polynomials respectively, see eq.28.

The ' denotes derivative with respect to s and the formula holds when $P(s_j) \neq 0$. By comparing equation (31) with equation (20) we note that the inverse Laplace transform yields $\nu(t)$ as a Prony series, where the inverse relaxation times are given by the poles s_j and the spectral strengths are given by the corresponding residues. Thus we introduce $\nu_j = -\text{Res}(\nu(s); s_j)$ and $\theta_j = -\frac{1}{s_j}$ to finally express

Poisson's ratio as the Prony series

$$\nu(t) = \nu_0 - \sum_j \nu_j e^{-t/\theta_j} \quad (33)$$

We found that the residues at all poles except for $s = 0$ are negative. The ν_j are therefore positive and the obtained Poisson's ratio is a monotonically increasing function of time.

The Prony series fits to the moduli were performed with a MATLAB script. The script was designed to create a Maple program. Subsequently the CAS Maple was called to execute this program, which performed the algebraic manipulations that were outlined above. With the exception of the root-finding to determine the poles the calculation of Poisson's ratio is thus done analytically.

The uniaxial relaxation modulus can be determined from

$$E(s) = \frac{9K(s)G(s)}{3K(s) + G(s)} \quad (34)$$

The inverse transform can be calculated as described for Poisson's ratio with Prony series for the bulk and shear moduli and the uniaxial relaxation modulus is finally expressed as

$$E(s) = \frac{9}{s} \frac{K_\infty G_\infty \prod_{k=1}^n (s + 1/\tau_k) \prod_{l=1}^n (s + 1/\tau_l) + \sum_{i=1}^n (K_i G_\infty + K_\infty G_i) s \prod_{k \neq i}^n (s + 1/\tau_k) \prod_{l=1}^n (s + 1/\tau_l) + \sum_{i=1}^n \sum_{j=1}^n K_i G_j s^2 \prod_{k \neq i}^n (s + 1/\tau_k) \prod_{l \neq j}^n (s + 1/\tau_l)}{(3K_\infty + G_\infty) \prod_{k=1}^n (s + 1/\tau_k) \prod_{l=1}^n (s + 1/\tau_l) + \sum_{i=1}^n (3K_i + G_i) s \prod_{k \neq i}^n (s + 1/\tau_k) \prod_{l=1}^n (s + 1/\tau_l)} \quad (35)$$

6. RESULTS AND DISCUSSION

In the first part further progress of the confined compression setup is described and a quality criterion is introduced to distinguish between tests that provide adequate results and tests yield unacceptable results. In the second part, the viscoelastic characterization of the confined compression mode is presented. In the last part, the unconfined compression relaxation response is compared to the response obtained by interconversion of the confined compression data; this comparison also shows the impact of particles on the relaxation behavior.

6.1. Progress on the Confined Compression Setup

Relaxation tests can in principle be divided into two stages; the initial loading of the specimen, followed by the relaxation stage. In Fig. 5a the displacement of the first 100 s of a selected relaxation test is depicted. After the linear loading stage the displacement was kept constant within ± 0.01 mm. The resulting output load and hoop strain are shown in Figs. 5b and 5c. Due to the local strain control and the corresponding control speed of the testing machine, the load and the hoop strain both show some amount of overshooting at the end of the loading stage. Due to the fact that the first 60 s of relaxation were not used for the data reduction, the effect of overshooting can be neglected.

Due to inaccuracies of the loading pin and specimen geometry, the initial loading portion of the load-displacement curve in compression shows an increasing slope, as illustrated in Fig. 6a for the confined setup. This indicates that the specimen

and the compression plate is not perfectly aligned and in full contact along the whole specimen surface. With exact machining of cylindrical specimens the initial portion of the load-displacement curve can be minimized to be less than 30 μm (Jerabek 2009). In the confined compression configuration the overall error is larger due to the application of steel loading pins and the confining cylinder. For this reason the initial phase is about 100 μm , as depicted in Fig. 6a. To correct for this misfit a linear function was fitted to the linear range of the load-displacement curve (the arrows in Fig.6 indicate the fitting range), and extrapolated to the beginning of the test. Thus, the true axial strain applied on the specimen can be deduced. It is worth noting that the actual strain applied varied from test to test between 0.6 % and 0.9 % depending on the accuracy of the whole measurement system. The same procedure was also utilized on the hoop strain vs. displacement curve to correct for the true hoop strain (Fig. 6b). Both correction procedures are essential in compression testing in order to obtain accurate results. Therefore, the adjustment of the force was also applied in the uniaxial compression test.

During the testing program it turned out that despite the fact that the starting procedure of the measurement was similar for all tests, not all measurements provided reliable results. It turned out that the load vs. hoop strain relation during the loading of the specimen can be used as a quality criterion of the test. In Fig. 7 an example of a perfect linear relation between the axial load and hoop strain in the cylinder is shown. Additionally the linear fit is plotted; it was determined that a coefficient of determination higher than 0.995 yield in reliable test results. An example of a poor relation of the load vs. hoop strain curve can be found in Fig. 8. Note that one must still account for the initial nonlinearity that arises from seating effects discussed above.

6.2. Viscoelastic Characterization of the Confined Compression

Experiment

The two important measurements of the relaxation test are the axial stress and the hoop strain. In Fig. 9 selected results of the axial stress for PP at various temperatures are shown. Typically two to three decades of time were covered in one test. The corresponding hoop strain curves are plotted in Fig. 10. It is obvious

that there is no clear trend of the hoop strain at different temperatures. This finding is in accordance with Qvale and Ravi-Chandar (2004). Due to the fact that the hoop strain is almost constant during the test, the influence of the small fluctuations seen in Fig. 10 on the calculations is negligible; therefore, we considered the hoop strain to be constant in time.

The axial stress and hoop strain are used for the calculation of the mean and deviatoric stress as explained in Section 4. Then the bulk and shear moduli are determined by using equation 17 and 18. This procedure is repeated for each test at a certain test temperature. For a proper and smooth generation of the master curves in the linear viscoelastic range only horizontal shifting of the several results is necessary. The bulk and shear master curves for the neat PP shown in Fig. 11 were obtained by horizontal and vertical shifting, which is common for the nonlinear viscoelastic range. The linear viscoelastic limit of polymers depends on temperature and hydrostatic pressure and is significantly higher below the glass transition temperature (T_g) than above T_g . In order to avoid significant post-crystallization in the relaxation tests, the maximum testing temperature for all materials was limited to about 70 °C. Nevertheless, it was noticed that some post-crystallization may have occurred at 50 °C and above.

For the neat PP, the linear viscoelastic limit in tension at 23 °C is below 5 MPa (Retting and Laun 1991). Since compression testing at such low stresses is difficult due to initial misfits, the specimen was loaded up to 1 % axial strain. This results in axial stresses significantly larger than the linear viscoelastic limit (Fig. 9). For this purpose tests conducted at elevated temperatures were vertically shifted to obtain a smooth master curve. The strain range of the initial misfit has a significant impact on the stress and strain level the specimen experiences and thus on the applied vertical shifting. Another effect contributing to the vertical shifting particularly of the bulk modulus arises from variations in the specimen geometry. A misfit of 0.01 mm between specimen and cylinder results in errors in the bulk modulus of up to 30 %. However, the amount of horizontal and vertical shifting was only chosen by visual inspection of the master curve assuming that the trend of the bulk and shear relaxation modulus is not affected by nonlinear viscoelastic behavior.

For the generation of the bulk and shear relaxation master curves the same horizontal shift factors for both functions were used although the mechanisms of relaxation are different in shear and bulk (Ward 1971). Due to the limited bulk relaxation and the applied vertical shifting of the curves conclusions about the time shifting are not possible. In Fig. 12 the relaxation master curves for all investigated materials are shown, using equal time shift factors for the bulk and shear moduli. It should be noted that the Prony series fitted to the master curves is shown, rather than the raw data points. This Prony series is then used in the next section for the interconversion of the bulk and shear relaxation moduli. As expected, rigid particles increase the stiffness of PP; higher volume fractions of filler result in higher bulk and shear modulus values. Comparing the moduli of the composites containing the glass beads and talc, the effect of particle shape is evident. Due to the reinforcing effect of the aligned talc particles, a significant increase of the shear relaxation modulus was observed, while a limited influence on the bulk relaxation modulus was determined. However, the particles do not appear to affect the short time relaxation response of the materials significantly, but may influence the approach to long-term response. We will return to this in the next section with a discussion of the interconverted uniaxial relaxation modulus.

6.3. Unconfined Compression Results and Interconversion of Relaxation Moduli

In order to determine the pressure dependence of viscoelastic material functions unconfined compression experiments were also performed and the corresponding master curves are shown in Fig. 13. For the generation of the master curves, tests were carried out from -30 °C up to 70 °C to have the same temperature range as for the confined tests. For comparison, all test results are shown in Fig. 16 for the talc filled PP composite. Obviously, only minor scatter in the data was observed. Vertical shifting was not applied on the data since the measured stress levels are significantly smaller than in the confined mode, specifically above T_g due to the lower hydrostatic pressure.

In order to compare the confined results with the unconfined measurements, the interconversion of the shear and bulk relaxation moduli is necessary as described

in Section 5. The result of the interconversion in terms of the uniaxial modulus is depicted in Fig. 14 for neat and talc filled PP. In the confined mode a significant retardation of the relaxation was determined. In the glassy state below T_g only a minor influence of the hydrostatic pressure on the relaxation function can be found. This is in good agreement with the literature (Qvale and Ravi-Chandar 2004), where the pressure sensitivity of the stiffness and strength of polycarbonate and polymethylmethacrylate were investigated. The high pressure sensitivity above T_g can be explained by the free volume in the amorphous phase. High hydrostatic pressure reduces the free volume and thus the mobility of molecules, which gives rise to the reduced relaxation in the confined setup. Below T_g the free volume is frozen and hence, the influence of hydrostatic pressure is limited. This results in almost equal uniaxial relaxation modulus values in the glassy state. Furthermore, the confined compression experiment shows the material behavior not only at increased hydrostatic pressure levels but also at multiaxial stress states. Relaxation at complex stress states is retarded and uniaxial results used as input data in numerical simulations result in an underestimation of the mechanical properties.

For PP filled with low volume fraction of glass beads a uniaxial tensile relaxation test at 23 °C was carried out additionally (Fig. 15). The test was shifted horizontally using the time shift factor from the uniaxial compression test for a test temperature of 23 °C. The influence of hydrostatic pressure increases the relaxation modulus at a reduced time of 10^{10} s from 1115 MPa in the tensile loading to 1445 MPa in uniaxial compression up to 2125 in the confined compression mode. This again reinforces the need for testing under adequate stress states to determine the viscoelastic properties of polymers specifically in creep and relaxation.

As it was already shown, rigid particles have an influence on the long-term behavior of polymers (Fig. 12). For the purpose of quantifying this influence for different stress states, the relative relaxation in % was calculated and plotted for the unconfined and confined mode in Figs. 16 and 17, respectively. This allows for a comparison that is free of absolute values and gives rise to the pure amount of relaxation. The relaxation behavior of PP and glass bead filled PP is almost similar

in the unconfined mode, as illustrated in Fig. 16. Thus, small volume fraction of fillers influence the modulus values, but have no effect on the overall relaxation. This may be explained by different effects both increasing and decreasing the relaxation moduli. First, retardation of the relaxation may generally be observed due to the rigid elastic filler. Second, the most important contribution arises from the spontaneously formed interphase between particle and matrix, which has a property different from that of the matrix (Pukanszky 2005). This is associated with the reduced molecular mobility of the macromolecular chains connected to the particle surface and leads to delayed relaxation. Third, the complex multiaxial stress state around the particles also results in a reduced relaxation. Finally, interfacial failure and subsequent debonding of the particles from the matrix reduces the effective cross-section of the specimen and thus, the load-bearing capability. The stress distribution around spherical inclusions as derived by Pukanszky (1993) shows the maximum radial tensile stress responsible for initiation of the debonding process at the equator of the spheres when loaded in uniaxial compression. Taking the axial stresses applied in the uniaxial compression relaxation test, local tensile stresses of 20 MPa (for test temperatures below T_g) can be obtained. Comparing this with debonding stresses derived from uniaxial tensile tests (Jerabek 2009), interfacial failure may occur in uniaxial compression relaxation tests. For the glass bead filled composite all mechanisms described can be detected simultaneously. Interfacial failure is mainly compensated by interphase formation and to a lesser extent by hydrostatic pressure.

For the talc filled PP a significant retardation of the relaxation was found mainly due to two effects: first, the amount of interphase formed is significantly larger than for the glass bead filled PP due to the specific surface area of talc and second, the debonding stress for the talc filler investigated is larger than for the glass bead grade studied, as was shown in (Jerabek et al. 2009).

The behavior described above is further corroborated by the result obtained in the confined mode, depicted in Fig. 17. The relaxation curves for the various composites are similar, but differ significantly from that of the unfilled PP. The local tensile stresses at the equator of the spheres are compensated by the radial

stresses applied by the confining cylinder in the confined compression test. The maximum compressive stress at the pole of the sphere is about 5 times the value of the tensile stress at the equator, calculated according to (Pukanszky 1993). As the ratio of the axial stress to the radial stress in the confined compression test is smaller than 3 for the configuration applied, local tensile stresses around the particles can not develop and interfacial failure is inhibited. It is worth noting that in addition to differences in the end values of the relative relaxation of both methods by a factor of 2, the trend of the relaxation also differs from exponential decay in the unconfined mode to a power-law decay in the confined mode.

The bulk and shear relaxation modulus can be used to calculate Poisson's ratio, as described in Section 5. The time-dependent Poisson's ratio for all materials investigated is shown in Fig. 18. The Poisson's ratio for polymers increases with time and temperature from about 0.3 below the secondary transition temperature up to the limit of 0.5 (corresponding to incompressibility) at high temperatures (Tschöegl et al. 2002). For the unfilled PP a Poisson' ratio of 0.33 at $-30\text{ }^{\circ}\text{C}$ was measured and increases up to 0.45, which corresponds to a testing temperature of about $70\text{ }^{\circ}\text{C}$ or reduced time of 10^{15} . As with other viscoelastic material functions, Poisson's ratio is also dependent on the pressure (Masubuchi et al. 1998). Below the glass transition temperature pressure increases Poisson's ratio since the free volume is frozen and the applied hydrostatic pressure enforces the material to deform in the transverse direction like an incompressible fluid. Above T_g Poisson's ratio will be decreased by hydrostatic pressure due to the reduced molecular mobility. Comparison with experiments at different stress states will be presented elsewhere (Tscharnuter et al. 2009).

Since rigid particles have a Poisson's ratio of about 0.21 for glass beads and 0.21-0.27 for talc, which is lower than the value for unfilled PP, addition of fillers reduce the Poisson's ratio of the filled composite, as shown in Fig. 18. The properties of elastic fillers are constant within the temperature range investigated. Hence, the difference in the Poisson's ratio between filler and matrix is not constant and is increasing with temperature and time. This explains that the curves for the unfilled and glass bead filled PP coincide at the beginning followed by an increasing difference at large times. It should be noted that the difference in the Poisson's

ratio at low temperatures is beyond the accuracy of the test method and data should be treated with care. As already mentioned for the talc filled composite, ice formation could not be avoided entirely resulting in a higher relaxation of the bulk modulus as expected (Fig. 12). This affects the result of the Poisson's ratio significantly. Nevertheless, a trend can be deduced that due to an aspect ratio of 8, talc particles have a more pronounced influence on the Poisson's ratio than glass beads.

7. CONCLUSIONS

In this paper the confined compression test was applied to PP and particulate filled PP composites to determine the long-term shear and bulk relaxation moduli. In order to obtain reliable and reasonable test results an advanced testing procedure was introduced to correct for initial misfits and to allow for the implementation of a quality criterion. Furthermore, it was pointed out that local strain control with high temperature stability within the temperature chamber is absolutely necessary to perform valid relaxation tests.

For the generation of the bulk and shear modulus master curves horizontal and vertical shifting was applied. A significant relaxation of the shear modulus was found within the temperature range investigated in comparison to the limited relaxation of the bulk modulus. Rigid particles increase both the bulk as well as the shear relaxation modulus. Moreover, particles change the relaxation behavior and significantly retard the relaxation in case of talc filler. By interconversion of viscoelastic material functions the uniaxial relaxation modulus and the Poisson's ratio were calculated. Through comparison of the unconfined and confined compression relaxations, the pressure sensitivity of the viscoelastic PP matrix was determined and discussed with respect to the free volume theory. Comparison of the relative relaxation reveals the influence of interfacial failure on the long-term performance of particulate filled composites. Furthermore, it was shown that the trend of the relaxation changes from exponential to power-law form indicating the strong influence of pressure on relaxation.

The time dependent Poisson's ratio was calculated by interconversion of the bulk and shear relaxation modulus. As expected, an increasing Poisson's ratio with time was found. The addition of rigid particles results in a lower value of Poisson's ratio. Thus it was demonstrated that with the test configuration applied, all viscoelastic material functions can be accurately determined with one test.

Acknowledgement

This research was performed at the Polymer Competence Center Leoben GmbH (PCCL, Austria) and at the Department of Aerospace Engineering and Engineering Mechanics at the University of Texas at Austin within the framework of the Kplus-program of the Austrian Ministry of Traffic, Innovation and Technology with contributions by the *University of Leoben* and *Borealis Polyolefine GmbH*. The PCCL is funded by the Austrian Government and the States Governments of Styria and Upper Austria.

References

- Deng, T.H., Knauss, W.G.: The Temperature and Frequency Dependence of the Bulk Compliance of Poly(Vinyl Acetate). A Re-Examination. *Mech. Time-Depend. Mater.* 1 33-49 (1997)
- Fasce, L. A., Pettarin, V., Marano, C., Rink, M., Frontini, P.M.: Biaxial yielding of polypropylene/elastomeric polyolefin blends: Effect of elastomer content and thermal annealing. *Polym. Eng. Sci.* 48, 1414-1423 (2008)
- Fu, S.Y., Feng, X.Q., Lauke, B., Mai, Y.W.: Effects of particle size, particle/matrix interface adhesion and particle loading on mechanical properties of particulate-polymer composites. *Composites Part B* 39, 933-961 (2008)
- Herbst, H.: Modeling and Simulation of the Thermomechanical Behavior of Heterogeneous Polypropylene Compounds. *Montanuniversitaet Leoben, Leoben* (2008)
- Knauss, W.G., Emri, I.: Volume Change and the Nonlinearly Thermo-Viscoelastic Constitution of Polymers. *Polym. Eng. Sci.*, 27, 86-100 (1987)
- Kralj, A., Prodan, T., Emri, I.: An apparatus for measuring the effect of pressure on the time-dependent properties of polymers. *J. Rheol* 45, 929-943 (2001)
- Leaderman, H.: Elastic and Creep Properties of Filamentous Materials and Other High Polymers. The Textile Foundation, Washington (1943)

- Lu, H., Zhang, X., Knauss, W.G.: Uniaxial, Shear and Poisson Relaxation and Their Conversion to Bulk Relaxation: Studies on Poly(Methyl Methacrylate). *Polym. Eng. Sci.* 37, 1053-1064 (1997)
- Ma, Z., Ravi-Chandar, K.: Confined Compression: A Stable Homogeneous Deformation for Constitutive Characterization. *Exp. Mech.* 40, 38-45 (2000)
- Masubuchi, Y., Matsuoka, H., Takimoto, J., Koyama, K., Ohta, Y.: Measurement of Young's modulus and Poisson's ratio of Polymers under High Pressure. *Mater. Sci. Res. Int.* 4, 223-226 (1998)
- Nemat-Nasser, S., Hori, M.: micromechanics: overall properties of heterogeneous materials. Elsevier Science Publishers B.V., Amsterdam (1993)
- Pae, K.D.: The macroscopic yielding behaviour of polymers in multiaxial stress fields. *J. Mater. Sci* 12, 1209-1214 (1977)
- Pukánszky, B.: Interfaces and interphases in multicomponent materials: past, present, future. *Eur. Polym. J.* 41, 645-662 (2005)
- Pukánszky, B.: Interfacial Interactions in Particulate Filled Thermoplastics: Mechanism, Strength, Properties. *Makromol. Chem., Macromol. Symp.* 70/71, 213-223 (1993)
- Pukánszky, B.: Particulate filled polypropylene: structure and properties. In: Kocsis, K. (ed.) *Polypropylene: Structure, Blends and Composites*, pp. 1-70. Chapman and Hall, London (1995)
- Pukánszky, B., Vörös, G.: Mechanism of interfacial interactions in particulate filled composites. *Compos. Interfaces* 1, 411-427 (1993)
- Qvale, D.: Viscoelastic Material Characterization of Polymers Under Multiaxial Compression. The University of Texas at Austin, Austin (2003)
- Qvale, D., Ravi-Chandar, K.: Viscoelastic Characterization of Polymers Under Multiaxial Compression. *Mech. Time-Depend. Mater.* 8, 193-214 (2004)
- Rabinowitz, S., Ward, I.M., Parry, J.S.C.: The Effect of Hydrostatic Pressure on the Shear Yield Behaviour of Polymers. *J. Mater. Sci* 5, 29-39 (1970)
- Ravi-Chandar, K., Ma, Z.: Inelastic Deformation in Polymers under Multiaxial Compression. *Mech. Time-Depend. Mater.* 8, 333-357 (2000)
- Renner, K., Yang, M. S., Móczó, J., Choi, H.J., Pukánszky, B.: Analysis of the debonding process in polypropylene model composites. *Eur. Polym. J.* 41, 2520-2529 (2005)

- Retting, W., Laun, H.M.: *Kunststoff-Physis*. Hanser, Muenchen (1991)
- Schiff, J.L.: *The Laplace Transform: Theory and Applications*. Springer, New York (1999)
- Tschoegl, N.W.: *The Phenomenological Theory of Linear Viscoelastic Behavior*. Springer-Verlag, Heidelberg (1989)
- Tschoegl, N.W., Knauss, W.G., Emri, I.: Poisson's Ratio in Linear Viscoelasticity – A Critical Review. *Mech. Time-Depend. Mater.* 6, 3-51 (2002)
- Timoshenko, S.P., Goodier, J.N.: *Theory of Elasticity*. McGraw-Hill, New York (1934)
- Vollenberg, P.H.T.: *The Mechanical Behaviour of Particle Filled Thermoplastics*. Technische Universiteit Eindhoven, Eindhoven (1987)
- Ward, I.M. *Mechanical Properties of Solid Polymers*. John Wiley & Sons Ltd., London (1971)

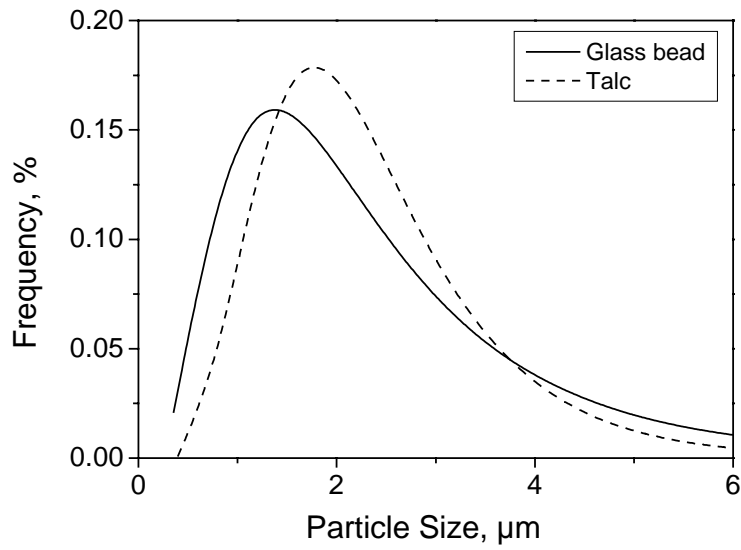


Fig. 1. Particle size distribution for glass bead and talc filler

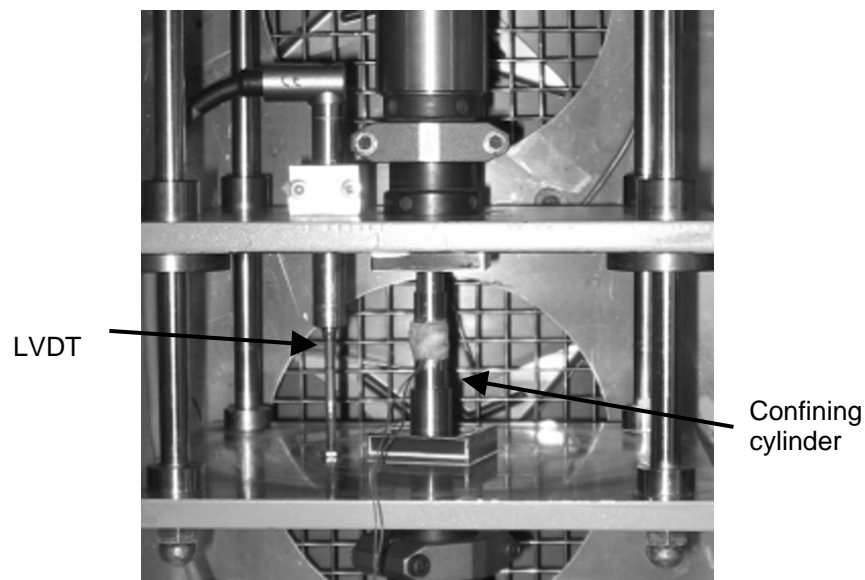


Fig. 2. Photograph of the compression tool showing the four aligning bars at each corner and the LVDT for the local strain measurement. The confining cylinder between the two compression plates can be seen.

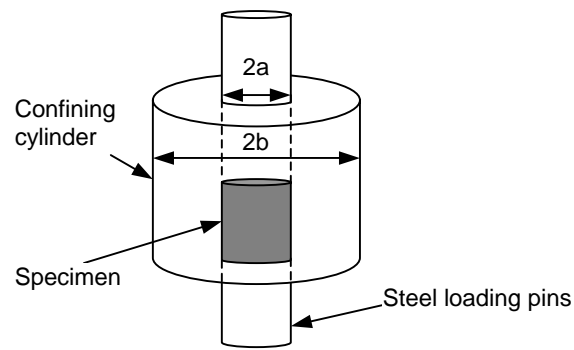


Fig. 3. Schematic of the confined compression test, $2a$ and $2b$ representing the radius of the specimen and confining cylinder

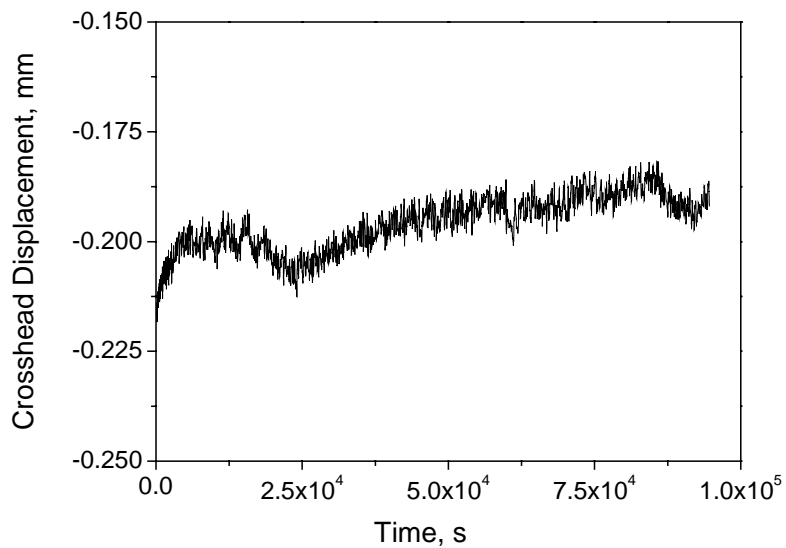
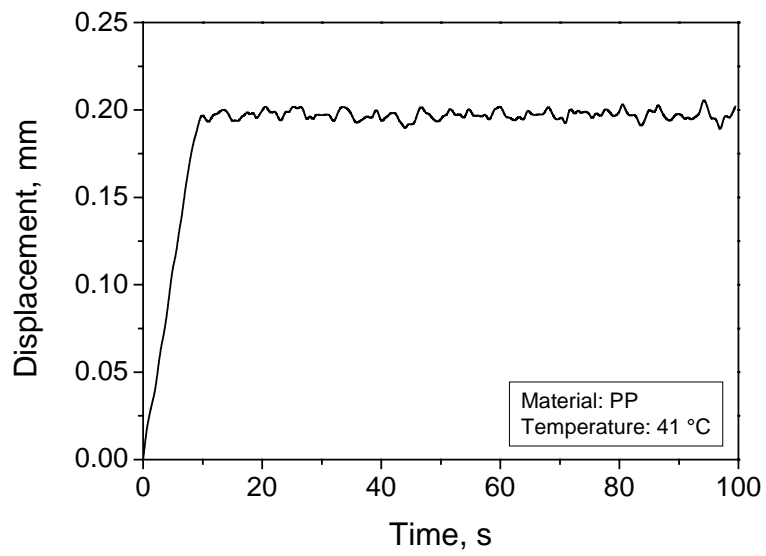
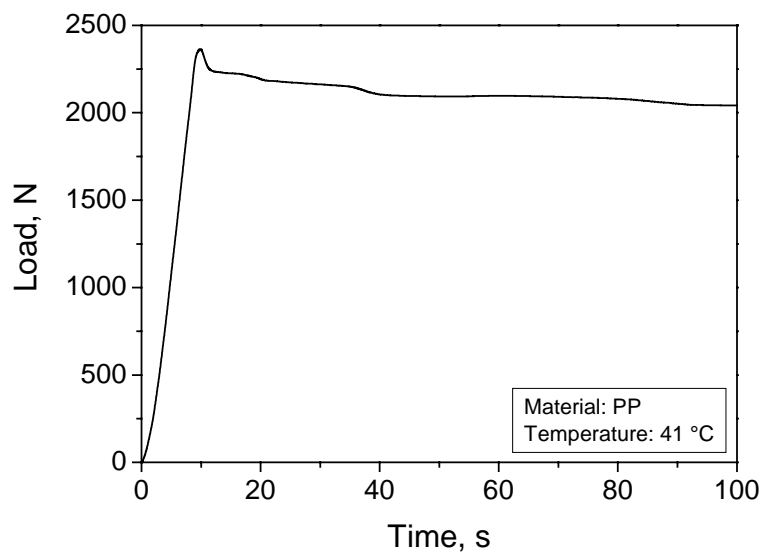


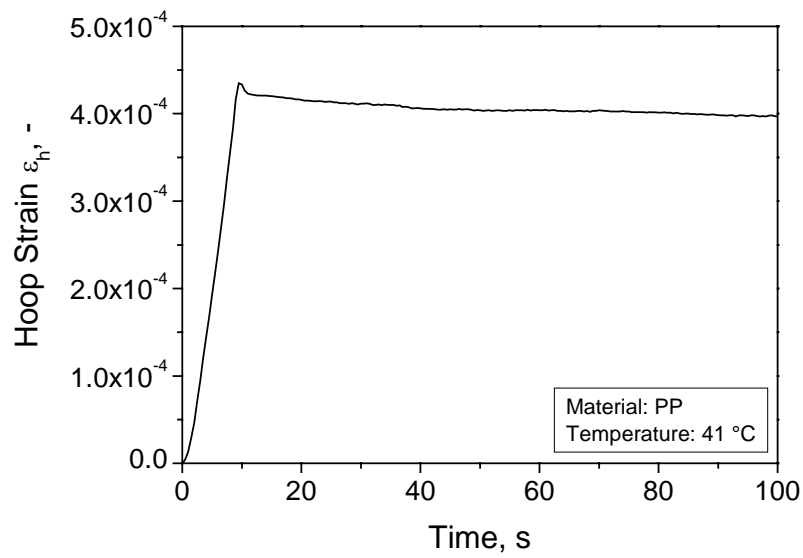
Fig. 4. Displacement of the crosshead during relaxation testing when keeping the local strain (LVDT) constant. Overall changes in the displacement are from temperature variations in the environment.



a)

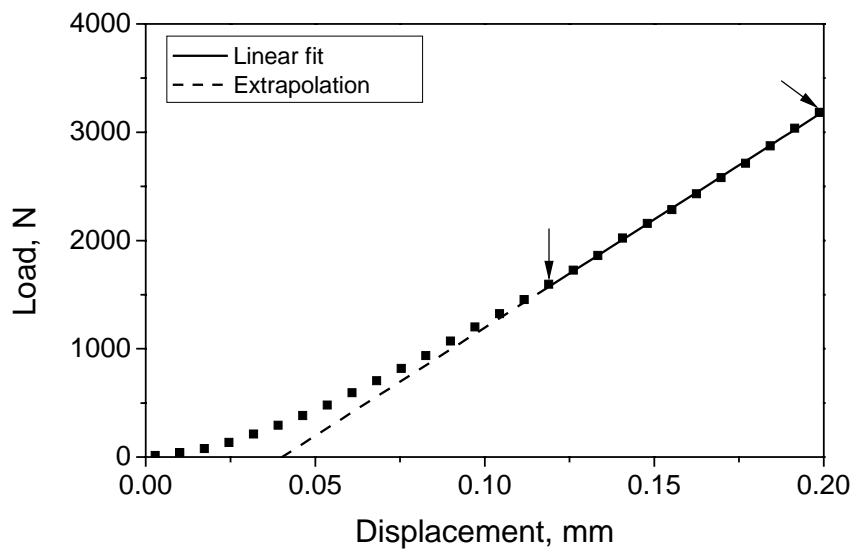


b)

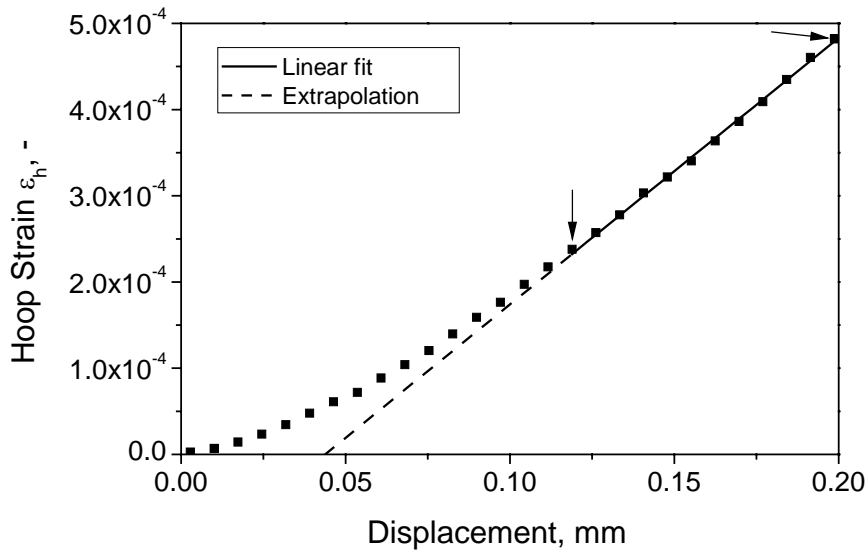


c)

Fig. 5. Loading and initial specimen relaxation in a confined compression relaxation test a) local displacement vs. time, b) load vs. time and c) hoop strain vs. time.



a)



b)

Fig. 6. Loading of the specimen in the confined compression configuration depicting the initial misfit between specimen and compression plates, arrows indicate the linear range a) load vs. displacement and b) hoop strain vs. displacement.

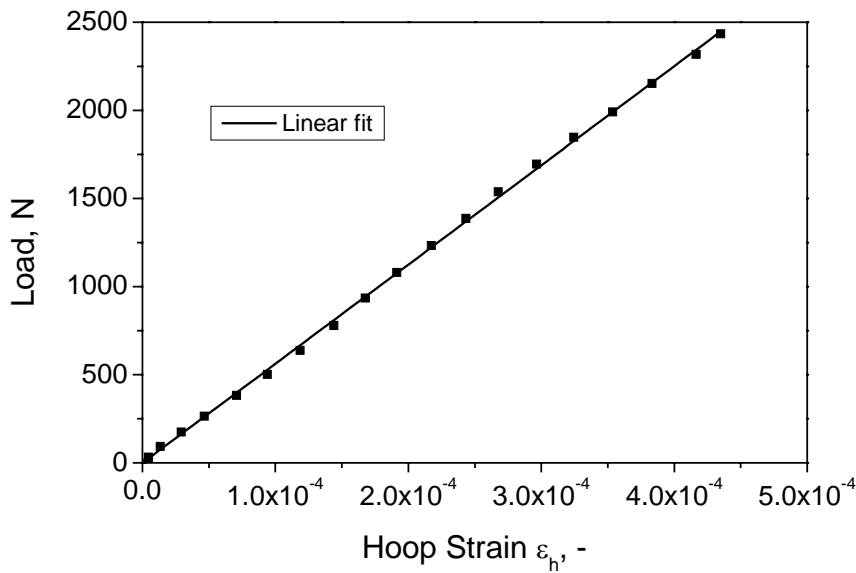


Fig. 7. Load versus hoop strain curve showing a linear relation

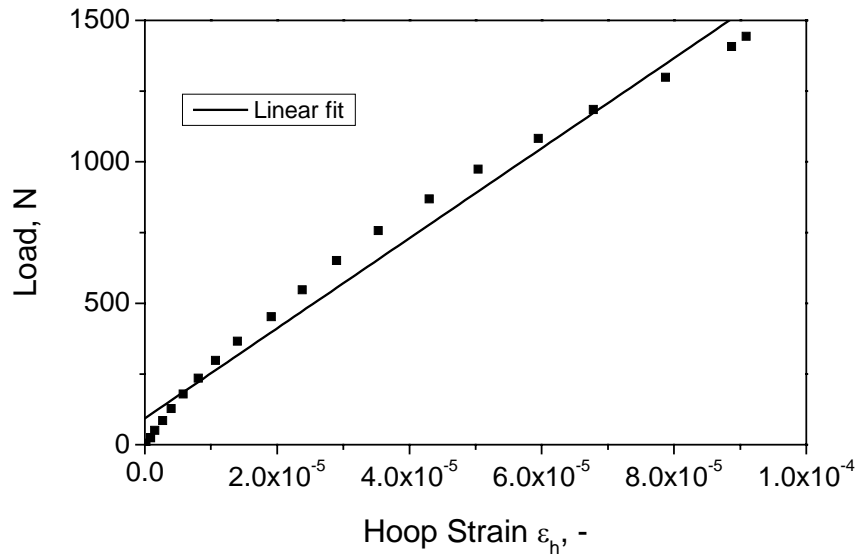


Fig. 8. Load versus hoop strain curve showing a nonlinear relation. This test may not give reliable results.

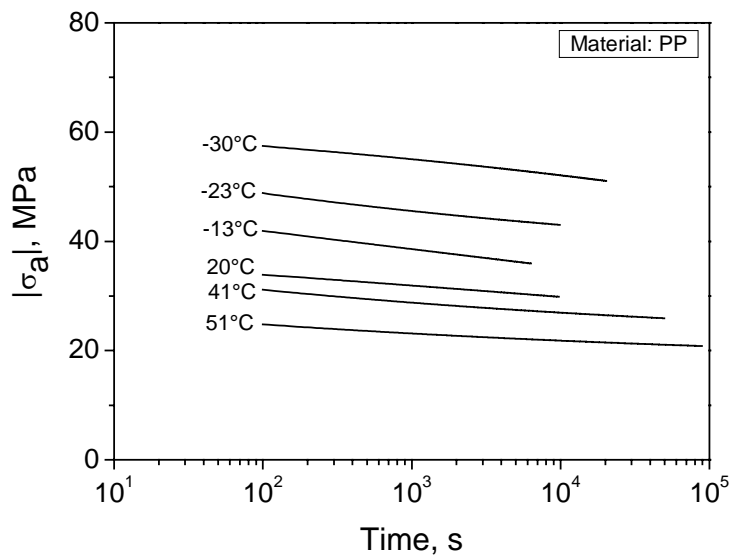


Fig. 9. Relaxation of axial stress for selected temperatures

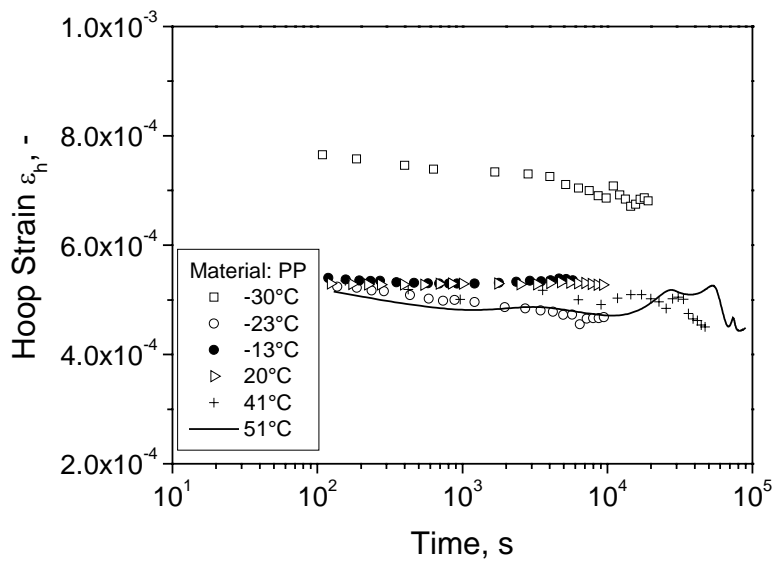


Fig. 10. Hoop strain variation during relaxation for selected temperatures

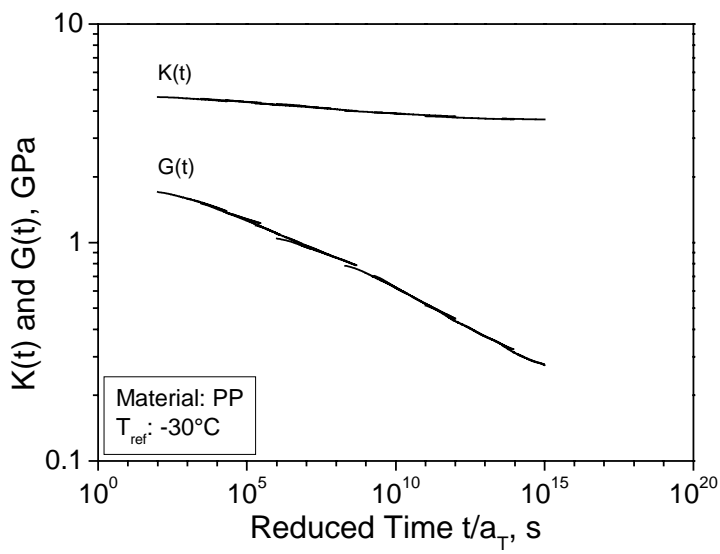


Fig. 11. Bulk and shear relaxation master curve for the unfilled PP. Tests were performed from -30 °C up to 70 °C.

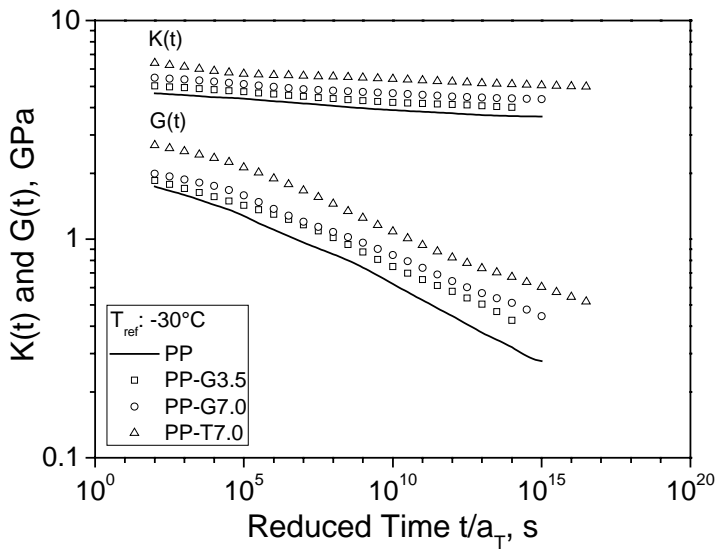


Fig. 12. Relaxation master curves for all materials investigated showing a significant influence of rigid particles on the modulus values

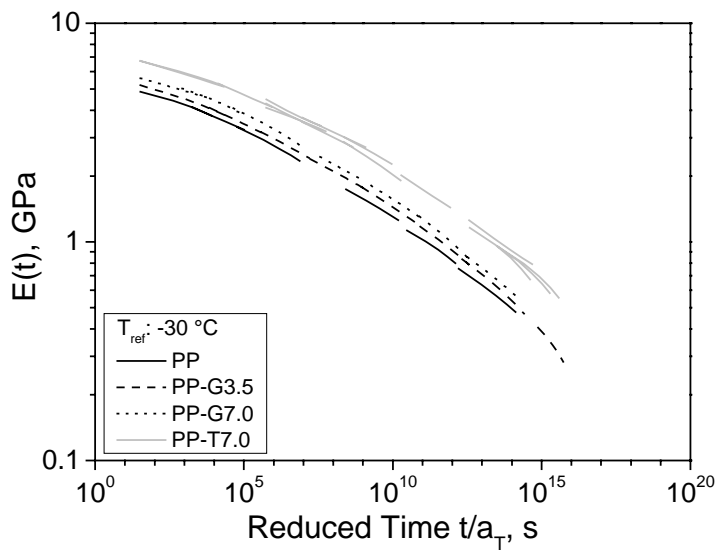


Fig. 13. Uniaxial relaxation modulus master curves representing the same temperature range as the confined master curve

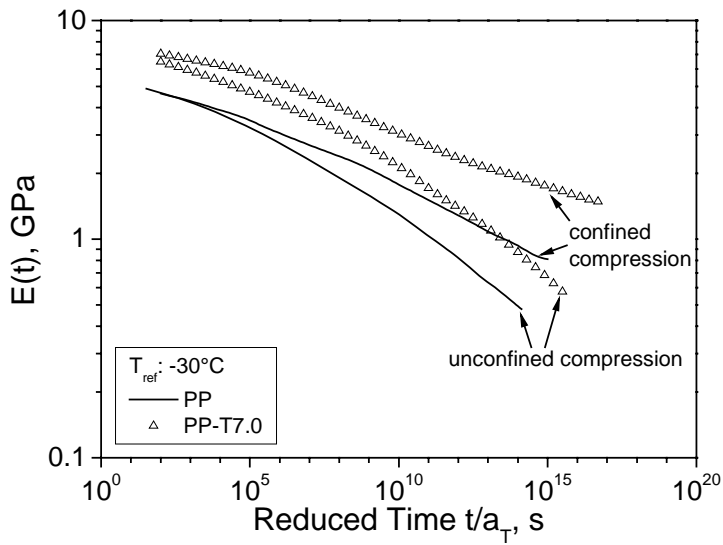


Fig. 14. Comparison of the unconfined and confined compression relaxation. A significant dependency on the confinement level can be seen.

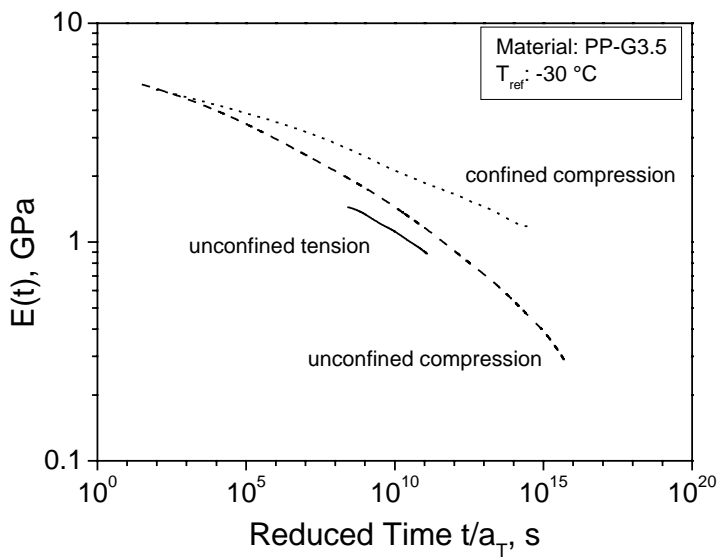


Fig. 15. Comparison of uniaxial tensile (23 °C), unconfined and confined compression relaxation experiments showing the influence of pressure on the long-term relaxation behavior

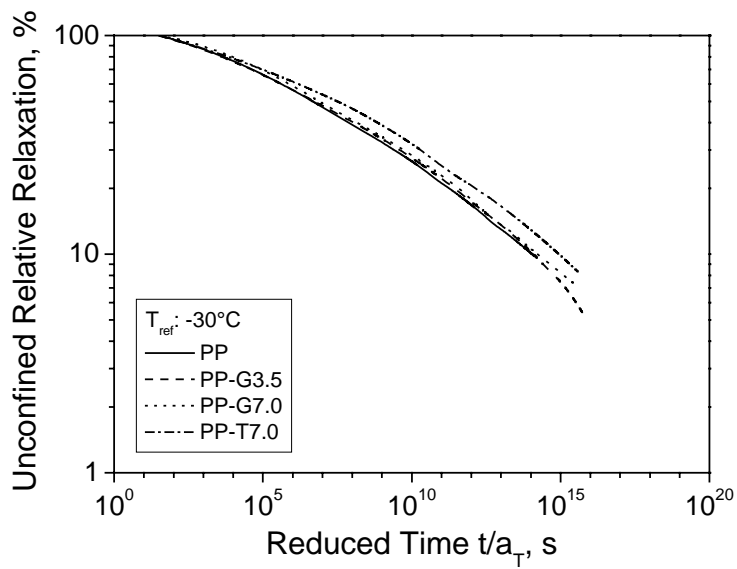


Fig. 16. Unconfined relative relaxation master curves for all investigated materials. Retarded relaxation for the talc filled PP can be seen

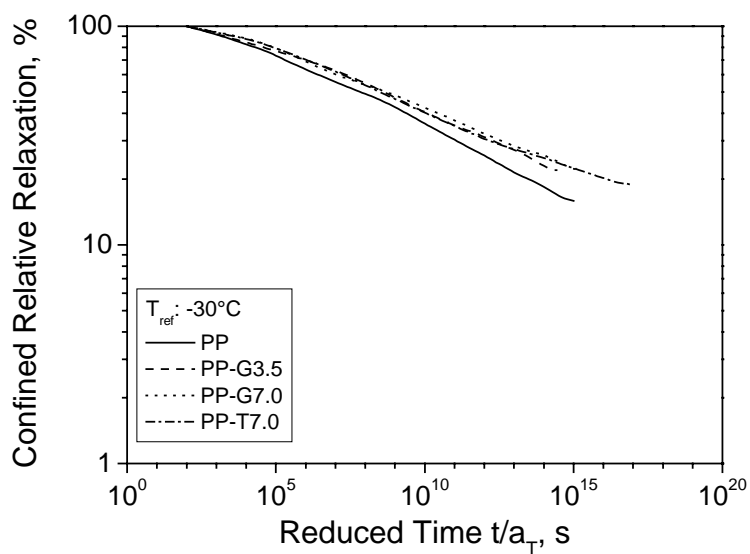


Fig. 17. Confined relative relaxation master curves for all investigated materials. Retarded relaxation was found for the particle filled composites in comparison to the unfilled PP.

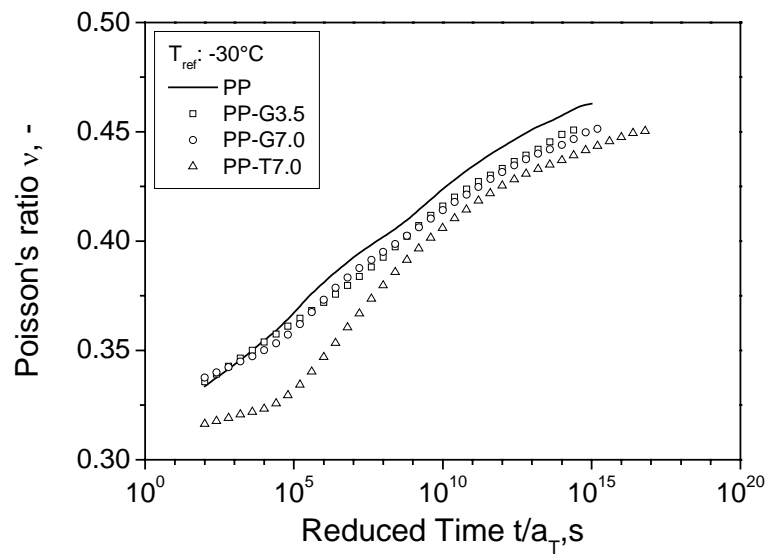


Fig. 18. Plot of the master curve of the Poisson's ratio calculated by interconversion